Sandro Oswald, BSc

Influences Of Meteorological Factors And Instrumentation On The Accuracy Of Solar Radiation Measurements In Graz

MASTER'S THESIS

to achieve the university degree of

Diplom-Ingenieur

Master's degree programme: Space Sciences and Earth from Space

submitted to

Graz University of Technology

Supervisor

Ass.-Prof. Mag. Dr. Harald Rieder

Wegener Center for Climate and Global Change and
Institute of Geophysics, Astrophysics and Meteorology (IGAM)/Institute of Physics (IP)

Graz, October 2015

AFFIDAVIT

I declare that I have authored this thesis independently, that I have not used other than the declared sources/resources, and that I have explicitly indicated all material which has been quoted either literally or by content from the sources used. The text document uploaded to TUGRAZonline is identical to the present master's thesis dissertation.

Graz, _____ _____

Date Signature

Acknowledgment

I want especially to thank my advisor Ass.-Prof. Mag. Dr. Harald Rieder for the opportunity to write my master thesis in his group and his mentoring and scientific advise. Through his scientific curiosity, problem solving skills and open door policy he became an academic role model for me.

Furthermore I want to thank Mag. Helga Pietsch and Mag. Dietmar Baumgartner for their steady support, particularly during the measurement campaign. I am grateful that they shared their extensive knowledge on technical aspects of radiation measurements with me and for their advise through the writing stage of this thesis.

I want to thank Ao. Univ.-Prof. Mag. Dr. Erich Mursch-Radlgruber from the Institute of Meteorology of the University of Natural Resources and Applied Sciences (BOKU) Vienna for providing an ‚all-in-one' meteorological observing system (WS600 UMB by Lufft GmbH) and Dr. Marc Olefs and Dr. Martin Mair (both ZAMG) for providing essential measurement devices (two CMP 21 pyranometers, two Eigenbrodt SBL 480 housings) during the measurement campaign at ARAD site Graz/University in January 2015.

I also want to thank the Austrian Central Institute for Meteorology and Geodynamics (ZAMG) for providing data from TAWES site Graz/University and ARAD site Graz/University. I want to thank the University of Graz's Institute of Geophysics, Astrophysics and Meteorology/Institute of Physics and Wegener Center for Climate and Global Change for workspace and support provided.

I wish to acknowledge the *R-Project* and *Latex-Project* development teams and their great work which have been a huge help for my thesis.

Last but not least I would like to thank my parents, Sabine and Peter Oswald, and my girlfriend Jasmin Saleh for all their support and being always by my side.

Abstract

This thesis investigates potential reasons for the observed nighttime offset between two pyranometers, measuring global and diffuse solar radiation, at the Austrian RADiation monitoring network (ARAD) site Graz/University. The two pyranometers concerned are of the same type (CMP 21 by manufacturer Kipp&Zonen) though contained in different housings (Eigenbrodt SBL 480 and a self-built housing manufactured by the staff of Kanzelhöhe Observatory (University of Graz)). The analysis of operational nighttime measurements of these two pyranometers indicates a constant offset of about $2\,\mathrm{W\,m^{-2}}$. Although nighttime pyranometer measurements are of no particular importance for the determination of the global energy balance they are an important indicator for instrument stability/performance according to the operational guidelines of the Baseline Surface Radiation Network (BSRN), which are closely adopted within the ARAD framework.

Measurements of surface radiative fluxes of highest accuracy are particularly important for the development and evaluation of satellite retrievals and climate model parametrizations. Furthermore the most recent assessment report of the Intergovernmental Panel on Climate Change (IPCC) quantifies total anthropogenic radiative forcing for 2011 relative to 1750 with 2.29 [1.13 to 3.33] $\mathrm{W\,m^{-2}}$. This (‚small‘) value indicates that high accuracy measurements of radiative fluxes are needed to accurately determine changes in radiative forcing.

Therefore the aim of this thesis was to identify potential causes for the observed nighttime offset. Potential causes for the observed instrument offset were hypothesized to be: (1) differences in instrument configuration i.e., the housing systems containing the pyranometers; and (2) external influences such as ambient meteorology (precipitation, changes in wind speed and/or temperature).

The analysis of routine ARAD measurements along with co-located meteorological measurements indicated a potential influence of meteorological factors on the radiation measurements. To determine if such influence indeed occurs a series of experiments aiming to simulate meteorological events, i.e., spray-test representing precipitation events and cover-tests representing abrupt changes in wind speed, have been performed under stable ambient conditions. As the set of preliminary experiments confirmed the hypothesis regarding the influence of meteorological factors an extensive field campaign has been performed in January 2015 to further investigate and quantify individual effects. Within the course of this campaign more than 60 experiments with pyranometers contained in different housing systems and configurations were carried out.

The results of the campaign showed that the offset observed at ARAD site Graz/University can be repeated for two pyranometers of the same type when operated in different housing systems. In contrary pyranometers operated simultaneously in the same type of housing (and housing configuration) showed strongly reduced offsets, indicating that operation of one uniform housing system would be preferential for routine monitoring sites. Furthermore all experiments simulating meteorological effects triggered instrument responses (although of different magnitude depending on housing configuration), indicating a significant influence of ambient meteorology on instrument

performance. The detailed comparison of pyranometers contained in different housing systems indicated that pyranometer output agreed best among instruments contained in the Eigenbrodt SBL 480 housing in standard configuration and the ventilated but unheated KSO housing. Given this rather surprising result a detailed comparison of pyranometer performance throughout all types of housing systems used within the ARAD framework as well as potential further adjustments of the KSO housing are suggested for future work.

Zusammenfassung

Im Rahmen dieser Masterarbeit wurden potentielle Ursachen für nächtliche Offsets zwischen zwei an der Station Graz/Universität des Austrian RADiation monitoring networks (ARAD) eingesetzter Pyranometer, welche die Global- und Himmelsstrahlung messen, untersucht. Dabei handelt es sich um baugleiche Instrumente (CMP 21 von Kipp&Zonen) welche jedoch mit unterschiedlichen Heizungs- und Ventilationsgehäusen (Eigenbrodt SBL 480 bzw. Eigenbau des Observatorium Kanzelhöhe (KSO)) betrieben werden. Die Analyse der nächtlichen Messwerte zeigte einen konstanten Offset von $2\,\mathrm{W\,m^{-2}}$. Obwohl die Messwerte in der Nacht keine wesentlichen Größen bei der Betrachtung der Energiebilanz darstellen, gelten sie im Rahmen der Empfehlungen des Baseline Surface Radiation Networks (BSRN), welchen ARAD folgt, als wichtige Kennwerte für die Qualität der Messungen.

Präzise Messungen der bodennahen Strahlungsflüsse sind von entscheidender Bedeutung für die Entwicklung und Validierung von Satelliten Retrievals sowie der Parametrisierung von Klimamodellen. Der jüngste Bericht des Weltklimarates (IPCC) weist einen anthropogenen Strahlungsantrieb von etwa 2.3 [1.13 bis 3.33] $\mathrm{W\,m^{-2}}$ für 2011, relativ zu 1750, aus. Dieser (‚kleine') Wert verdeutlicht die Notwendigkeit hochgenauer Strahlungsmessungen zur exakten Bestimmung des Strahlungsantriebs.

Aus diesem Grund war das Hauptziel dieser Masterarbeit die Identifikation möglicher Gründe für den am Standort Graz auftretenden nächtlichen Pyranometer-Offset. Zwei Arbeitshypothesen wurden verfolgt: (1) Der Offset wird durch Unterschiede im instrumentellen Aufbau (Gehäusetyp) verursacht; (2) meteorologische Einflüsse (Niederschlag, Lufttemperatur, Windgeschwindigkeit) verursachen den Offset.

Statistische Untersuchungen der ARAD Datenreihe sowie paralleler meteorologischer Messreihen zeigten einen möglichen Einfluss meteorologischer Größen auf. Um diese Hypothese zu untersuchen wurde eine Reihe von Experimenten mit dem Ziel, meteorologische Ereignisse (Sprühversuche als Niederschlagssimulation, Abdeckungsversuche als Simulation sich rasch ändernder Windbedingungen, Veränderungen der Heizleistung als Simulation sich rasch ändernder Umgebungstemperatur) nachzubilden, durchgeführt. Die Auswertung der Versuchsreihen bestätigte die Vermutung, dass meteorologische Einflüsse die Strahlungsmessung beeinträchtigen.

Um die tatsächlichen Auswirkungen einzelner Größen besser quantifizieren zu können, wurde im Jänner 2015 eine mehrtägige Messkampagne mit mehr als 60 Versuchsreihen, in direkter Nachbarschaft zur ARAD Station Graz/ Universität durchgeführt. Die Ergebnisse dieser Messkampagne zeigten, dass der beobachtete Offset zwischen zwei baugleichen Pyranometern, die in unterschiedlichen Gehäusen betrieben werden, reproduzierbar ist. Hingegen zeigten die selben Pyranometer beim Betrieb in baugleichen Gehäusen keinen nennenswerten Offset. Von diesem Ergebnis wird die Empfehlung abgeleitet an Monitoringstationen möglichst baugleiche Systeme einzusetzen. Des Weiteren verursachten alle Experimente, die meteorologische Einflüsse simulieren, deutliche Signalausschläge sowohl in der Gehäusetemperatur der Pyranometer als auch im Messwert selbst.

Dieses Ergebnis bestätigt die Vermutung eines deutlichen Einflusses der Umgebungsbedingungen auf die Qualität von Strahlungsmessungen. Die detaillierte Auswertung der Messkampagne zeigte, dass die verwendeten Pyranometer, wenn sie in unterschiedlichen Gehäusen betrieben werden, die geringsten Abweichungen aufweisen wenn eine Kombination aus Eigenbrodt Gehäuse in Standardkonfiguration und ein ungeheiztes aber ventiliertes KSO Gehäuse verwendet wird. Dieses doch überraschende Ergebnis führt zur Schlussfolgerung, dass weiterführende Untersuchungen der Pyranometerstabilität mit allen von ARAD eingesetzten Gehäusetypen notwendig sind. Zudem werden weitere Untersuchungen sowie Entwicklungsarbeiten für das KSO Eigenbaugehäuse empfohlen.

Contents

1 Introduction and Motivation 1

2 Theoretical principles 3
2.1 Radiation laws . . . 4
2.1.1 Lambert's cosine law . . . 4
2.1.2 Application of Lambert's cosine law . . . 5
2.1.3 Planck's law . . . 6
2.1.4 Stefan-Boltzmann law . . . 8
2.1.5 Kirchhoff's law of thermal radiation . . . 9
2.2 Interaction of radiation and matter . . . 9
2.2.1 Extinction . . . 10
2.2.2 Reflection . . . 12
2.2.3 Transmission . . . 12
2.3 Radiative transfer equation . . . 12
2.4 Radiation balance . . . 13
2.4.1 Greenhouse effect . . . 14
2.5 Components of radiation . . . 16
2.5.1 Short-wave radiation . . . 16
2.5.2 Long-wave radiation . . . 17
2.5.3 Components of radiation at ARAD site Graz/University . . . 18
2.5.4 Global and diffuse radiation . . . 19
2.6 Measurements of global and diffuse radiation . . . 19
2.7 Fundamental meteorological properties . . . 21
2.7.1 Pressure . . . 21
2.7.2 Temperature . . . 23
2.8 Ideal gas law . . . 23
2.8.1 Humidity . . . 24
2.9 Energy balance . . . 25
2.10 Evaporation . . . 26

3 Instruments, Data and Methods 27
3.1 The Austrian RADiation Monitoring Network (ARAD) . . . 27
3.1.1 Aims of the ARAD network . . . 27
3.1.2 Instrumentation of ARAD sites . . . 28
3.2 Radiation measurements at ARAD site Graz/University . . . 28
3.2.1 The pyranometer CMP 21 . . . 29
3.2.2 Sensing element . . . 30
3.2.3 Glass-dome . . . 31
3.2.4 Drying cartridge . . . 32
3.2.5 Zero offset A . . . 32

3.2.6 Zero offset B . . . 32
3.2.7 Temperature dependence of CMP 21 output . . . 33
3.2.8 Housing for global and diffuse radiation sensors at ARAD site Graz/University 33
3.2.9 The pyranometer setup for measurements of diffuse radiation at ARAD site Graz/University (HIM) . . . 33
3.2.10 The pyranometer setup for measurements of global radiation at ARAD site Graz/University (GLO) . . . 34
3.2.11 Heating levels of the KSO housing . . . 35
3.3 Routine meteorological measurements at TAWES site Graz/University . . . 36
3.4 Additional instrumentation used during the measurement campaign of January 2015 36
3.4.1 Pyranometers, instrument housings and housing modifications . . . 36
3.4.2 Mobile meteorological observation platforms . . . 37
3.4.3 Thermoelements . . . 37
3.5 Experiments and laboratory analysis . . . 37
3.5.1 Experiments . . . 37
3.5.2 Laboratory analysis . . . 38
3.6 Data sets and data analysis . . . 38

4 Results 41
4.1 Preliminary investigations . . . 41
4.1.1 Consideration of meteorological factors . . . 44
4.1.2 Statistical investigations . . . 49
4.1.3 Initial experiments . . . 52
4.2 Measurement campaign . . . 61
4.2.1 The whole time series of the measurement campaign . . . 65
4.2.2 Analysis of measurements with both pyranometers contained in Eigenbrodt SBL 480 housings . . . 66
4.2.3 Analysis of measurements for pyranometers contained in an Eigenbrodt SBL 480 (reference) and KSO original (experimental) housing . . . 76
4.2.4 Analysis of measurements for pyranometers contained in an Eigenbrodt SBL 480 (reference) and KSO modified (experimental) housing . . . 82
4.2.5 Statistical analysis of spray-tests . . . 91
4.2.6 Comparison of pyranometer body temperature(s) with ambient air temperature 94
4.2.7 Theoretical black body radiative exchange . . . 100
4.2.8 Comparison of meteorological records obtained during the measurement campaign . . . 104

5 Summary and Conclusions 111

List of Figures 115

List of Tables 121

Abbreviations 123

Symbols 125

Bibliography 133

Appendices 137
Appendix A 137
Appendix B 140
Appendix C 143

1 Introduction and Motivation

Earth's climate is largely determined by the global energy balance (Wild et al., 2013). Therefore a precise knowledge of the surface energy budget, which includes the solar and terrestrial radiation fluxes, is essential for understanding the Earth's planetary circulation and climate system (Ramanathan, 1987; Augustine and Dutton, 2013; Wild et al., 2015).

The surface radiation budget represents the absorbed energy at the Earth's surface and is defined by the difference of downward and upward components of short-wave and long-wave irradiance (Augustine and Dutton, 2013). In-situ measurements of solar radiation on the Earth's surface, more precisely global radiation which is the sum of the direct and diffuse components, began in the 1920s (in Sweden), but became more widespread with the advent of thermopile pyranometers and through initiatives of the International Geophysical Year 1957/58 (Wild, 2009). Around the turn of the century a series of studies (Dutton et al., 1991; Gilgen et al., 1998; Ohmura et al., 1998; Stanhill and Cohen, 2001; Liepert, 2002) reported on negative trends in global radiation based on in-situ measurements, a phenomenon commonly referred to as ‚global dimming' (Wild et al., 2005; Wild, 2009). Average trends of -6 to $-9\,\mathrm{W\,m^{-2}}$ between 1960-1990 have been reported in the literature (Wild et al., 2005), but estimates vary depending on location, record length and time period considered (Wild et al., 2013).

The growing interest of the scientific community in surface radiation trends and limitations in the accuracy of historic records led in the early 1990s to the establishment of the Baseline Surface Radiation Network (BSRN) under the auspices of the World Climate Research Programme (WCRP) (Ohmura et al., 1998). BSRN sites are (and have been) equipped with instruments of highest accuracy and to date more than 50 anchor sites are operational around the globe. Besides BSRN a series of national monitoring networks was established at this time operating at (or close) to BSRN standards. Data from several of these networks was used in the seminal study of Wild et al. (2005) documenting that in the period 1990-2000 the negative trends previously observed could (over most parts of the globe) no longer be found, and have been replace with widespread increases in surface solar radiation since the 1980s. A phenomenon termed ‚global brightening' by the authors.

Radiative flux estimates on global scale are available from satellite platforms since the early 1980s. Radiation trends from these long-term data sets confirm ‚global dimming' and ‚global brightening' during the last decades of the 20^{th} century reported for in-situ records but regional differences in magnitude, seasonality and sign have been reported (Pinker et al., 2005).

Changes in the global energy balance are of central importance to understand the Earth's past and future climate and changes therein. From a physical point of view, anthropogenic climate change is first of all a perturbation of the global energy balance through changes in atmospheric composition (Wild et al., 2013). While traditional climate variables such as temperature or precipitation represent the atmosphere's lagged response to climate change they reveal little about its underlying cause. Drivers of climate change such as changes in e.g., the concentration of (well-mixed) greenhouse gases, aerosols or cloud cover may be better reflected in surface heat

fluxes and the surface radiation budget (Augustine et al., 2005). The Intergovernmental Panel on Climate Change (IPCC) states in its Fifth Assessment Report (AR5) that ‚total radiative forcing is positive, and has led to an uptake of energy by the climate system'. As summarized in AR5 the largest contribution to total radiative forcing is caused by the increase in the atmospheric concentration of CO_2 since 1750, resulting in an estimated total anthropogenic radiative forcing for 2011 relative to 1750 of 2.29 [1.13 to 3.33] W m^{-2} (IPCC, 2014).

Despite its central importance substantial uncertainties exist in the quantification of the different components of the global energy balance (Wild et al., 2013). While advent in remote sensing platforms such as e.g., the Clouds and Earth's Radiant Energy System (CERES) (Wielicki et al., 1996), and Solar Radiation and Climate Experiment (SORCE) (Anderson and Cahalan, 2005) provides information on the top of the atmosphere radiative fluxes with unprecedented accuracy (Loeb et al., 2012) much less is known about the energy distribution at the surface as surface radiative fluxes cannot be directly measured by satellite platforms (Wild et al., 2013).

Therefore surface measurements of the solar and terrestrial radiation fluxes, of highest possible accuracy, are needed for retrieval optimization and satellite product validation (Pinker et al., 2005; Gupta et al., 2003; Zhang et al., 2010; Yan et al., 2011; Wang et al., 2014; Zhou et al., 2007) and the evaluation and/or parametrization of radiative fluxes in global and regional climate models (Wild et al., 1998; Marty et al., 2003; Kuipers Munneke et al., 2011; Freidenreich and Ramaswamy, 2011; Donner et al., 2011) and reanalysis products (Allan, 1999).

Over the last decades a series of national and international monitoring networks for solar and terrestrial radiative fluxes has been establish supporting these efforts. In Austria the so-called Austrian RADiation Monitoring Network (ARAD) has been established in 2010 by a consortium of the Central Agency of Meteorology and Geodynamics (ZAMG), the University of Graz, the University of Innsbruck, and the University of Natural Resources and Applied Sciences, Vienna (BOKU). ARAD aims to provide long-term monitoring of radiation budget components at highest accuracy and to capture the spatial patterns of radiation climate in Austria (Olefs et al., 2015).

To date the ARAD Network comprises one BSRN site (Sonnblick) and four additional sites (Kanzelhöhe, Graz/University, Innsbruck/University, Wien Hohe Warte). All ARAD sites are equipped with instrumentation according to BSRN standards (McArthur, 2005). Despite BSRN class equipment and regular instrument maintenance radiation measurements are influenced by meteorological conditions and instrumentation effects leading occasionally to so-called zero B offsets. Within this thesis the influence of meteorological factors and instrumentation on the accuracy of radiation measurements at ARAD site Graz/University is investigated, supporting the ARAD mission of providing continuous high accuracy data on radiative fluxes for satellite/model calibration and evaluation and climate monitoring.

2 Theoretical principles

Solar radiation is a key variable in the Earth's climate system. In physical terms radiation can be described as an electrodynamic process which has two forms: electromagnetic waves and particles. In this thesis the focus lies on the electromagnatic waves and resulting flux.
The main radiative flux Φ in the Earth's atmosphere stems from the sun, its energy bulk E_{Solar} [J] per time t [s] is

$$\Phi = \frac{E_{Solar}}{t} \quad [\mathrm{J\,s^{-1}} = \mathrm{W}] \tag{2.1}$$

Considering the solar flux received on an area A [$\mathrm{m^2}$] in an distance d from the sun, yields the solar irradiance

$$F_{Solar} = \frac{\Phi}{A} \tag{2.2}$$

In case of the Earth $d = 1$ astronomical unit $(AU) \approx 150 \cdot 10^9$ m and the solar flux per unit area is commonly referred to as the solar constant

$$S_0 = \frac{\Phi}{A} = \frac{3.85 \cdot 10^{26}\,\mathrm{W}}{4\pi\, AU^2} = 1368\,\mathrm{W\,m^{-2}} \tag{2.3}$$

(Hantel, 2013).

In reality S_0 is not a constant as it is influenced by several varying factors such as e.g. the motion around the sun based on the orbital eccentricity $\varepsilon_o = 0.0167$ of the Earth and the eleven-year sun cycle (sunspot cycle). Considering the extreme values of the distance between Sun and Earth (perihelion in January with $1413\,\mathrm{W\,m^{-2}}$, aphelion in July with $1321\,\mathrm{W\,m^{-2}}$), one sees that S_0 varies by about 3.3% (Kraus, 2004).

Another important scientific parameter is the radiance L [$\mathrm{W\ m^{-2}\ sr^{-1}}$]. This quantity does not only consider the radiation flux per area, but also the solid angle ω which has the unit steradian [sr]. The whole solid angle of a sphere gives 4π sr, so the upper half space amounts 2π sr. Thus radiance is given by:

$$L = \frac{\Phi}{A\,\omega} \tag{2.4}$$

The big advantage of L is independence of the geometry, as it is solely a property of the radiation source because if one nears the radiation source, irradiance F increases but L does not. Further the differential form of the solid angle $\mathrm{d}\omega$ can be expressed with the proportion of the considered differential area $\mathrm{d}A$ and the radius r or with the azimuth φ and the altitude angle (commonly referred to as zenith angle) ϑ:

$$\mathrm{d}\omega = \frac{\mathrm{d}A'}{r^2} = \sin\vartheta\,\mathrm{d}\vartheta\,\mathrm{d}\varphi \tag{2.5}$$

(Hantel, 2013).

2.1 Radiation laws

The following paragraphs provide a summary of important radiation laws.

2.1.1 Lambert's cosine law

The physical law describing the connection between the radiation flux Φ and the radiance L is named after the physicist Johann Heinrich Lambert (Darmstaedter, 1908). Figure 2.1 shows the radiation source $\mathrm{d}A'$ in a distance $\mathbf{r}$ to the radiation receiver $\mathrm{d}A$. If one considers the angle ϑ between $\mathbf{r}$ and the lot of the upper half space one yields the following proportions:

$$\mathrm{d}\Phi \propto \mathrm{d}A' \qquad \mathrm{d}\Phi \propto \mathrm{d}A \qquad \mathrm{d}\Phi \propto \cos\vartheta \qquad \mathrm{d}\Phi \propto \mathbf{r}^{-2} \tag{2.6}$$

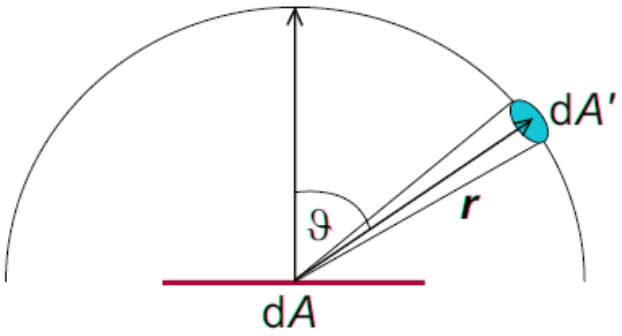

Figure 2.1: The area $\mathrm{d}A'$ transmits radiation to the ground area $\mathrm{d}A$ under the altitude angle ϑ. The distance between $\mathrm{d}A'$ and $\mathrm{d}A$ is the vector $\mathbf{r}$. The semicircle symbolises the upper half space. Source: (Hantel, 2013)

The first two proportions in Eq. 2.6 state that, the larger the area $\mathrm{d}A$ or $\mathrm{d}A'$ is, the larger the receiving radiation flux $\mathrm{d}\Phi$ is. The third proportion illustrates the dependency of the radiation intensity on the entry angle, and the last proportion gives the decrease in intensity with the square of the distance. All four together result in *Lambert's cosine law*:

$$\mathrm{d}\Phi = L\,\mathrm{d}A\cos\vartheta\,\frac{\mathrm{d}A'}{\mathbf{r}^2} \tag{2.7}$$

Here L is a proportional constant and the factor $\frac{\mathrm{d}A'}{\mathbf{r}^2}$ is the differential solid angle $\mathrm{d}\omega$ from Eq. 2.5. From the definition of the irradiance $\mathrm{d}F = \frac{\mathrm{d}\Phi}{\mathrm{d}A}$ (Eq. 2.2) and the integral of the azimuth φ and the altitude angle ϑ, the irradiance can be calculated as

$$F = \int_{\varphi_1}^{\varphi_2}\int_{\vartheta_1}^{\vartheta_2} L(\varphi,\vartheta)\cos\vartheta\sin\vartheta\,\mathrm{d}\vartheta\,\mathrm{d}\varphi \tag{2.8}$$

(Hantel, 2013).

2.1.2 Application of Lambert's cosine law

There are two simple but realistic examples for the calculation of the irradiance F from Eq. 2.8: (1) the isotropic radiation from the upper half space and (2) the parallel radiation (Hantel, 2013).

Case 1: Isotropic radiation from the upper half space

Isotropic radiation from the upper half space is also called diffuse sky radiation because if the sky is full of clouds or high fog there is no appreciable lightness source, so the radiance L can be moved in front of the integral. The azimuth and the altitude angles can be defined by a half sphere:

$$F_{iso} = L_{iso} \int_{\varphi=0}^{2\pi} \int_{\vartheta=0}^{\frac{\pi}{2}} \cos\vartheta \sin\vartheta \, \mathrm{d}\vartheta \, \mathrm{d}\varphi \tag{2.9}$$

with the simple integration of $\mathrm{d}\varphi$ and a substitution of $\mathrm{d}(\sin\vartheta) = \cos\vartheta \, \mathrm{d}\vartheta$, one yields

$$F_{iso} = 2\pi \, L_{iso} \int_{\sin\vartheta(\vartheta=0)}^{\sin\vartheta(\vartheta=\frac{\pi}{2})} \sin\vartheta \, \mathrm{d}(\sin\vartheta) = \pi L_{iso} \tag{2.10}$$

so the radiance L_{iso} differs only by the factor π from the irradiance F_{iso} considering an isotropic upper half space radiator (Hantel, 2013).

Case 2: Parallel radiator

In the case of a parallel radiator the rays of the sun can be considered under a very small solid angle, which can be calculated by an finite difference with

$$\Delta\omega = \frac{\pi \, r_{Solar}^2}{AU^2} \tag{2.11}$$

where r_{Solar} is the radius of the Sun. Because of the Earth's large distance to the Sun, ϑ is approximately constant and Eq. 2.8 (Eq. 2.5 introduced) reads

$$F = \int L \cos\vartheta \, \mathrm{d}\omega = L \cos\vartheta \, \Delta\omega \tag{2.12}$$

If the Sun is in zenith ($\cos\vartheta = 1$), another form of expression for the solar constant results

$$S_0 = L_{Solar} \, \Delta\omega \tag{2.13}$$

where L_{Solar} is the radiance of the sun. From this simple equation, a unique formula can be derived for planets in our solar system. L_{Solar} is only a property of the sun, it doesn't matter how far away the radiated object is. Eq. 2.3 gives the final result with

$$L_{Solar} = \frac{S_0}{\Delta\omega} = \frac{\Phi}{4\pi \, AU^2} \frac{AU^2}{\pi \, r_{Solar}^2} \approx 2 \cdot 10^7 \, \mathrm{W\,m^{-2}} \tag{2.14}$$

(Hantel, 2013).

2.1.3 Planck's law

For statements about the spectral distribution of the transmitted radiation, more specifically a black-body radiation, *Planck's law* has to be considered.

A black body is a body which absorbs all received radiation, so it neither reflects nor transmits. Furthermore a black body emits at a given temperature at all wavelengths the maximum of the possible radiance; i.e. L turns into B when considering a black body (Kraus, 2004).

Various scientists including Baron Rayleigh, Sir James Jeans and Wilhelm Wien tried to find an analytic function of the spectral radiance $B_\lambda(\lambda, T)$ [W m^{-2} nm^{-1} sr^{-1}] of a black body as a function of wavelength λ [m] and temperature T [K].

In the year 1900, Max Planck achieved such formulation making the assumption that the radiation energy is quantised and that there exists a quantum of action of finite size. The formulation of *Planck's law* in dependence of wavelength is

$$B_\lambda(\lambda, T) = \frac{\partial B(\lambda, T)}{\partial \lambda} = \frac{2hc^2}{\lambda^5(e^{\frac{hc}{k_B \lambda T}} - 1)} \tag{2.15}$$

whereby
$h = 6.62612 \cdot 10^{-34}$ J s is Planck's constant,
$c = 2.99792 \cdot 10^{8}$ m s^{-2} is the speed of light and,
$k_B = 1.38065 \cdot 10^{-23}$ J K^{-1} is the Boltzmann constant (Kraus, 2004).

In plain terms $B_\lambda(\lambda, T)$ is the energy of unpolarised radiation which a black body transmits in normal direction per unit time, area, solid angle and wavelength. If the radiation is polarised, it would only be half (Kraus, 2004).

Figure 2.2 shows *Planck's law* as a function of the wavelength λ for specific temperatures in a linear coherence. One can see that the magnitudes are too different and an optimal settlement is not found. However, if a logarithmic scale is used, a linear relationship between the maxima for individual temperatures does exist.

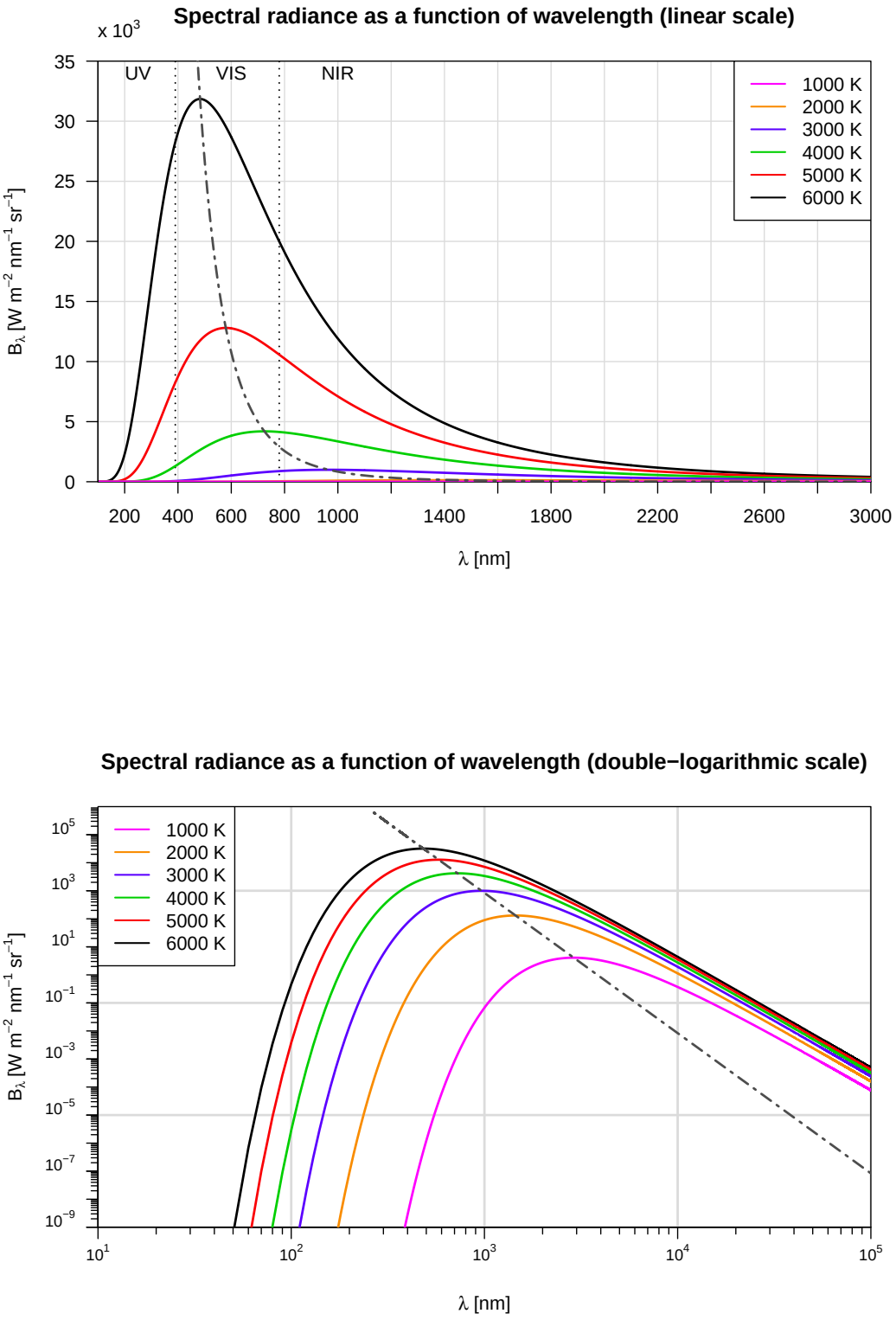

Figure 2.2: The spectral radiance of a black body as a function of wavelength for different temperatures in linear (top) and double-logarithmic scale (bottom). The grey dashed line connects maximum. Note: Scales of x and y axis differ between panels. Computed following Eq. 2.15.

2.1.4 Stefan-Boltzmann law

The *Stefan-Boltzmann law* is one of the most prominent laws in physics. It states that the irradiance of a body depends only on the fourth power of its temperature. The integration of *Planck's law* over the wavelength λ and the solid angle ω yields the radiation flux which a black body transmits to the upper half space (Kraus, 2004).

Eq. 2.15 will get into Eq. 2.8 and looks like

$$F(T) = \int_{\omega=0}^{2\pi} \left(\int_{\lambda=0}^{\infty} B_\lambda(\lambda, T) \mathrm{d}\lambda \right) \cos\vartheta \, \mathrm{d}\omega \tag{2.16}$$

As shown in subsection 2.1.2 the spectral radiance B_λ transmits radiation isotropic, as the radiance L_{iso}, thus Eq. 2.16 can be rearranged to

$$F(T) = \overbrace{\int_{\lambda=0}^{\infty} \frac{2hc^2}{\lambda^5 (e^{\frac{hc}{k_B \lambda T}} - 1)} \mathrm{d}\lambda}^{1} \overbrace{\int_{\varphi=0}^{2\pi} \int_{\vartheta=0}^{\frac{\pi}{2}} \cos\vartheta \sin\vartheta \, \mathrm{d}\vartheta \, \mathrm{d}\varphi}^{2} \tag{2.17}$$

The second term in Eq. 2.10 was already solved; thus the first solution yields $F(T) = B(\lambda, T)\, \pi$ (Hantel, 2013).

The first term in Eq. 2.17 is an improper integral and can only be solved by substitution

$$x = \frac{hc}{\lambda k_B T} \quad \Rightarrow \quad \frac{\mathrm{d}x}{\mathrm{d}\lambda} = -\frac{hc}{\lambda^2 k_B T} \quad \Rightarrow \quad \mathrm{d}\lambda = -\lambda^2 \frac{k_B T}{hc} \, \mathrm{d}x \tag{2.18}$$

Substituting and using the conversion of $\lambda = \frac{hc}{x k_B T}$, yields

$$F(T) = \int_{x=0}^{\infty} \left[\frac{x k_B T}{hc} \right]^3 \frac{2 c k_B T}{e^x - 1} \, \pi \, \mathrm{d}x = \int_{x=0}^{\infty} \frac{2\pi k_B^4 T^4}{h^3 c^2} \left[\frac{x^3}{e^x - 1} \right] \mathrm{d}x \tag{2.19}$$

The first term can be brought in front of the integral and applying the solution for the improper integral $\left[\frac{x^3}{e^x - 1} \right]$ from a table, yields

$$F(T) = \frac{2\pi k_B^4}{c^2 h^3} \, T^4 \, \frac{\pi^4}{15} = \underbrace{\frac{2\pi^5 k_B^4}{15 c^2 h^3}}_{\equiv \sigma} \, T^4 \tag{2.20}$$

The variable σ in front of T^4 is a constant, named after the two physicists Josef Stefan and Ludwig Boltzmann, with the value $5.67 \cdot 10^{-8}$ W m^{-2} K^{-4}, leading to the well-known form of *Stefan-Boltzmann law*

$$F(T) = B(T)\, \pi = \sigma \, T^4 \tag{2.21}$$

(Kraus, 2004).

2.1.5 Kirchhoff's law of thermal radiation

The previous sections have focused on the physical concept of a black body and its received and/or transmitted radiation.

However, real bodies differ from the idealistic concept of a black body and have further interactions with radiation like reflection and/or scattering. In other words such bodies have an emissivity of $0 < \varepsilon(\lambda) < 1$. Hence, the radiance of these random bodies will be denote as $L_\lambda(\lambda, T)$ and the emissivity can be defined by

$$\varepsilon(\lambda) = \frac{L_{\lambda,emitted}(\lambda, T)}{B_\lambda(\lambda, T)} \tag{2.22}$$

Thus *Kirchhoff's law* describes the coherence of emissivity and absorptivity $\alpha(\lambda)$, which reads

$$\alpha(\lambda) = \frac{L_{\lambda,absorbed}(\lambda, T)}{L_{\lambda,incoming}(\lambda, T)} \tag{2.23}$$

under the assumption of a thermal equilibrium in the body or medium. In contrary if the body temperatures would be in- or decreasing, one can set $L_{\lambda,emitted}(\lambda, T) = L_{\lambda,absorbed}(\lambda, T)$ and retain:

$$\varepsilon(\lambda) B_\lambda(\lambda, T) = \alpha(\lambda) L_{\lambda,incoming}(\lambda, T) \tag{2.24}$$

In radiative balance the received radiation of the real body $L_{\lambda,incoming}(\lambda, T)$ is equal to the emitted radiation of the black body, so from Eq. 2.24 one yields *Kirchhoff's law*

$$\varepsilon(\lambda) B_\lambda(\lambda, T) = \alpha(\lambda) B_\lambda(\lambda, T) \qquad \Rightarrow \qquad \varepsilon(\lambda) = \alpha(\lambda) \tag{2.25}$$

which states that every body emits the same part of black-body radiation which he absorbs for a given wavelength and a given temperature. Especially a black body emits and absorbs a maximum of radiation at every wavelength if $\varepsilon(\lambda) = \alpha(\lambda) = 1$ (Hantel, 2013).

2.2 Interaction of radiation and matter

As the concept of a black body, outlined in the previous section, describes only radiative interactions at the surface of a medium, the following section extends considerations to the interaction of radiation as it passes through a medium, e.g., air (Zmarsly et al., 2002).

In this respect it is important to distinguish between absorption, scattering, transmission and reflection if radiation impinges on matter. Absorption and scattering together are referred to as *extinction*.

In general

$$\alpha(\lambda) + \varrho(\lambda) + T_\lambda = 1 \tag{2.26}$$

whereby $\alpha(\lambda) =$ absorptivity, $\varrho(\lambda) =$ reflectivity and $T_\lambda =$ transmittance and all three terms are dimensionless (Zmarsly et al., 2002).

2.2.1 Extinction

Extinction is the selective weakening of a radiation flux in a medium like the atmosphere, which composes of absorbtion and scattering (Zmarsly et al., 2002). The word *selective* means that the weakening depends on the wavelength of the radiation. As shown in Figure 2.3 the direction of the radiation has to be considered. Before entering a medium the spectral radiance is referred to as L_λ^I and after it is transmitted as L_λ^{II}. Mathematically this yields

$$L_\lambda^{II} = L_\lambda^I + \mathrm{d}L_\lambda \tag{2.27}$$

where $\mathrm{d}L_\lambda$ is the extinction, which is negative; and one can set the following proportions:

$$\mathrm{d}L_\lambda \propto \mathrm{d}s \qquad \mathrm{d}L_\lambda \propto \rho \qquad \mathrm{d}L_\lambda \propto -L_\lambda^I \tag{2.28}$$

The first proportion states that the longer the way $\mathrm{d}s$ [m] through a medium, the stronger is the extinction. The second proportion describes the decrease of radiance dependent on the density of particles ρ [kg m^{-3}] in a medium and the third proportion states that the more radiance enters a medium, the more can be extinct.
With no radiance source inside the medium ($\mathrm{d}L_\lambda < 0$) and by using a proportional constant k, one yields

$$\mathrm{d}L_\lambda = -L_\lambda^I \, k(\lambda) \, \rho \, \mathrm{d}s \tag{2.29}$$

where the proportional constant k is the mass-specific extinction coefficient and has the unit [m^2 kg^{-1}] (Hantel, 2013).

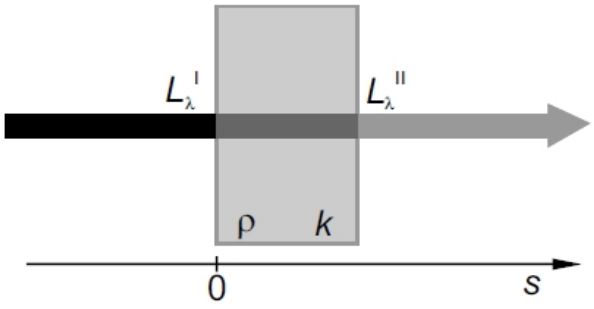

Figure 2.3: Extinction of the spectral radiance L_λ^I in a medium (grey rectangle) with the density ρ and the mass-specific extinction coefficient k. Source: (Hantel, 2013)

To obtain the radiance after passing through the medium $L_\lambda^{II} = L_\lambda(s)$, one has to integrate Eq. 2.29 considering that the density is constant in the whole medium ($\rho \neq \rho(s)$), which yields

$$\int_{L_\lambda(s=0)}^{L_\lambda(s)} \frac{\mathrm{d}L_\lambda}{L_\lambda^I} = -k(\lambda)\,\rho \int_0^s \mathrm{d}s \tag{2.30}$$

where $L_\lambda(s=0)$ is the radiation flux before entering the medium. The solution of the integral yields

$$\ln \frac{L_\lambda(s)}{L_\lambda(s=0)} = -k(\lambda)\,\rho\,(s-0) \tag{2.31}$$

Reformulation of Eq. 2.31 yields the *Bouger-Lambert-Beer law*

$$L_\lambda(s) = L_\lambda(s=0)\, e^{-k(\lambda)\rho s} \tag{2.32}$$

where the term in the exponential is the optical depth $\tau(\lambda, s) = k(\lambda)\rho s$. As extinction already begins at the top of the atmosphere (TOA) some important proportions are given below (Hantel, 2013).

Absorption

If absorption (in the medium) takes place the intensity of the radiation will mitigate and the energy is transformed into heat. If Eq. 2.29 is used only for absorption, the mass-specific extinction coefficient turns into the absorption cross section σ_a [cm^2] and the concentration of particles n [cm^{-3}] hence has the same unit as the product $k(\lambda)\rho$, yielding

$$\mathrm{d}L_\lambda = -L_\lambda^I\, n\, \sigma_a\, \mathrm{d}s \tag{2.33}$$

(Petty, 2006).

Scattering

Scattering is another form of interaction between radiation and matter. When an atom absorbs energy from the incoming radiation, the electron jumps into a larger orbit and reaches a higher energy state. Subsequently radiation will be emitted in all directions and the electron collapses back into its inertial state.

The scattering strength and scattering direction depend on the diameter of the particle d_P and the wavelength λ. Commonly two cases, named after the physicists Lord Rayleigh and Gustav Mie, are considered (Kraus, 2004):

- $d_P \ll \lambda$: Assuming that the wavelength of the radiation is much bigger than the diameter of a particle, *Rayleigh scattering* occurs:

  $$\sigma_{scat} \propto \lambda^{-4} \tag{2.34}$$

  Rayleigh theory states that the smaller the particles the more scattering occurs.

- $d_P \geq \lambda$: If particles have equal or similar size as the wavelength like e.g. dust particles or aerosols, *Mie scattering* occurs:

  $$\sigma_{scat} \propto \lambda^{-1.3} \tag{2.35}$$

  Mie theory states that the dependence on the wavelength λ of the scattering radiance is very small, on average -1.3 but values between -0.5 and -3.0 are possible in real environments.

2.2.2 Reflection

Reflection is the discontinuous alteration of the propagation direction of waves when contacting boundary layers. There are two extreme cases, (1) mirroring reflection at a smooth and (2) diffuse reflection at a very abrasive surface (Zmarsly et al., 2002). The reflectivity is dependent on the wavelength thus one yields

$$\varrho(\lambda) = \frac{L_{\lambda,reflected}(\lambda, T)}{L_{\lambda,incoming}(\lambda, T)} \tag{2.36}$$

In case of a black body the reflectivity would be 0. In case of the Earth a variety of surfaces with different kinds of reflectivity need to be considered. Experience has shown that the use of a planetary albedo a (reflectivity for visible light) is useful for practical applications, which has the value 0.3. (Zmarsly et al., 2002).

2.2.3 Transmission

The part of the incoming radiation which hasn't been absorbed or scattered by a medium and wouldn't reflect at a boundary layer, passes through the medium or transmits. This process can be described with the transmittance from Eq. 2.26 and is wavelength dependent:

$$T_\lambda = \frac{L_{\lambda,transmitted}(\lambda, T)}{L_{\lambda,incoming}(\lambda, T)} = \frac{L_\lambda(s)}{L_\lambda(s=0)} \tag{2.37}$$

By using Eq. 2.32, the expression above turns into

$$T_\lambda = e^{-\tau(\lambda,s)} \tag{2.38}$$

(Petty, 2006).

2.3 Radiative transfer equation

The *radiative transfer equation* (RTE) combines transmission and emission in one equation. As basis conduces the differential form of the *Bouger-Lambert-Beer law*.

$$\mathrm{d}L_\lambda = (J_\lambda - L_\lambda)\ \mathrm{d}\tau \tag{2.39}$$

The term J_λ in Eq. 2.39 denotes the source function, describing the intensification of radiation in a medium with varying density. In outer space ρ, J_λ and hence τ would be zero, thus eventually $\mathrm{d}L_\lambda = 0$, which states that the spectral radiance of the Sun and of all other stars is constant. If one considers a medium without any radiation source but with varying density, one yields a modification of the *Bouger-Lambert-Beer law*:

$$\int_{L_\lambda(\tau_1)}^{L_\lambda(\tau_2)} \frac{\mathrm{d}L_\lambda}{L_\lambda} = -k(\lambda) \int_{s_1}^{s_2} \rho(s)\,\mathrm{d}s = \tau_2 - \tau_1 \qquad \Rightarrow \qquad L_\lambda(\tau_2) = L_\lambda(\tau_1)\, e^{-(\tau_2 - \tau_1)} \tag{2.40}$$

where the term $e^{-(\tau_2-\tau_1)}$ describes the transmission after passing through the medium (Hantel, 2013).

Applying Eq. 2.39 in the case of $J_\lambda \neq 0$ and multiplying with e^τ yields:

$$e^\tau(\mathrm{d}L_\lambda + L_\lambda \, \mathrm{d}\tau) = e^\tau \, J_\lambda \, \mathrm{d}\tau \tag{2.41}$$

Using the product rule and the fact that $e^\tau \, \mathrm{d}\tau = \mathrm{d}(e^\tau)$, one can rewrite the formula above, yielding

$$\mathrm{d}\left(e^\tau \, L_\lambda\right) = J_\lambda \mathrm{d}\left(e^\tau\right) \tag{2.42}$$

Now integration with the limits τ_1 until τ_2 yields

$$e^{\tau_2} \, L_\lambda(\tau_2) - e^{\tau_1} \, L_\lambda(\tau_1) = \int_{\tau'=\tau_1}^{\tau'=\tau_2} J_\lambda(\tau') \, e^{\tau'} \, \mathrm{d}\tau' \tag{2.43}$$

Transformation of Eq. 2.43 yields the general solution of the *radiative transfer equation*:

$$L_\lambda(\tau_2) = L_\lambda(\tau_1) \, e^{-(\tau_2 - \tau_1)} + \int_{\tau'=\tau_1}^{\tau'=\tau_2} J_\lambda(\tau') \, e^{-(\tau_2 - \tau')} \, \mathrm{d}\tau' \tag{2.44}$$

where $J_\lambda(\tau')$ is considered inside the integral because radiation can be created in the medium (Hantel, 2013).

2.4 Radiation balance

Within this section the entire radiation flux which comes from the Sun to the Earth is considered. Parts of this flux are reflected and emitted from Earth into space, resulting in the radiative equilibrium temperature of the Earth T_E (Hantel, 2013).

If the Sun is considered a black body, the radiation equilibrium temperature T_{Solar} can be calculated from Eq. 2.21:

$$F_{Solar} = \frac{3.85 \cdot 10^{26}\,\mathrm{W}}{4\pi r_{Solar}^2} = 6.33 \cdot 10^7\,\mathrm{W\,m^{-2}} = \sigma T_{Solar}^4 \quad \Rightarrow \quad T_{Solar} = 5780\,\mathrm{K} \tag{2.45}$$

To get the radiative equilibrium temperature of the Earth, one has to equal the incoming Φ_{in} and the outgoing radiative flux Φ_{out}. Φ_{in} can be calculated with the solar constant S_0, the albedo a and the fact that the Sun radiates only the cross section area of the Earth, i.e. a fourth of the whole surface area:

$$\Phi_{in} = S_0(1-a)\pi r_E^2 \tag{2.46}$$

where r_E is the Earth's radius (Hantel, 2013).

Now the Stefan Boltzmann law can be used to determine the outgoing radiation of the Earth

$$\Phi_{out} = 4\pi r_E^2 \sigma T_E^4 \tag{2.47}$$

Eqs. 2.46 and 2.47 need to equal as otherwise the Earth would cool or warm

$$S_0(1-a) = 4\sigma T_E^4 \tag{2.48}$$

Transformation for T_E yields

$$T_E = \sqrt[4]{\frac{1368\,\mathrm{W\,m^{-2}}}{4 \cdot 5.67 \cdot 10^{-8}\,\mathrm{W\,m^{-2}\,K^{-4}}}(1-0.3)} = 255\,\mathrm{K} = -18\,^{\circ}\mathrm{C} \tag{2.49}$$

It is obvious that T_E depends only on the distance to the radiative source. At first glance $T_E = 18\,^{\circ}$C seems too low (considering the Earth's surface temperature T_s as reference), but in fact it accurately represents the average temperature in the middle troposphere (Hantel, 2013).

2.4.1 Greenhouse effect

To understand the Earth's temperature one needs to consider the greenhouse effect. As shown in Figure 2.4 T_s represents the temperature of the boundary layer below, the Earth's surface will equal a black-body radiator and its emission $\varepsilon = 1$. The upper layer is the atmosphere and is considered entirely transparent for solar irradiance (Hantel, 2013).

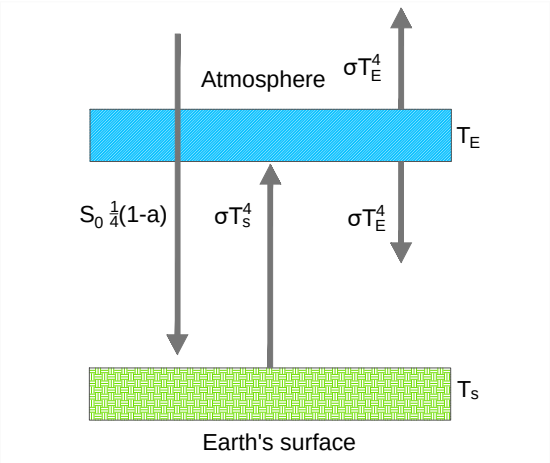

Figure 2.4: The atmosphere and the Earth's surface should be two infinitely thin areas (for illustrative purposes they are drawn extensive) and can't save any form of physical energy. The variables T_E and T_s besides represent their temperatures. In analogy to (Hantel, 2013, p. 21).

From the radiative fluxes illustrated in Figure 2.4 the two following balances can be inferred:

Balance atmosphere: $$\sigma T_s^4 = 2\sigma T_E^4 \tag{2.50}$$

Balance Earth's surface: $$\frac{S_0}{4}(1-a) + \sigma T_E^4 = \sigma T_s^4 \tag{2.51}$$

Together they yield

$$T_s = \sqrt[4]{\frac{S_0(1-a)}{2\sigma}} \tag{2.52}$$

and in analogy with Eq. 2.48

$$T_s = \sqrt[4]{2}\, T_E \approx 303\,\mathrm{K} \approx 30\,^\circ\mathrm{C} \tag{2.53}$$

(Hantel, 2013).

This model yields a much higher temperature than expected from day to day experience. From a physical perspective an important term, the emissivity of the Earth, emissivity is missing in the considerations above.

Considering this emissivity one can rewrite Eqs. 2.50 and 2.51 with emissivity $0 < \varepsilon < 1$

$$\text{Balance atmosphere:} \qquad \varepsilon\sigma T_s^4 = 2\varepsilon\sigma T_E^4 \tag{2.54}$$

$$\text{Balance Earth's surface:} \qquad \frac{S_0}{4}(1-a) + \varepsilon\sigma T_E^4 = \sigma T_s^4 \tag{2.55}$$

Transformation yields

$$T_s = \sqrt[4]{\frac{S_0(1-a)}{4\sigma(1-\frac{\varepsilon}{2})}} \tag{2.56}$$

with Eq. 2.48

$$T_s = \sqrt[4]{2}\, T_E \sqrt[4]{\frac{1}{2-\varepsilon}} \tag{2.57}$$

ε is initially unknown for the Earth's surface but T_s can be measured and considering the global average temperature of $15\,^\circ$C yields an emissivity $\varepsilon \simeq 0.77$ (Kraus, 2004).

2.5 Components of radiation

The next two sections consider the most important variables in radiation physics for this master thesis: the components of vertical radiative fluxes and their measurement principles.

The vertical radiative fluxes can be described for a multi-layered atmosphere by considering the up- and downward directed short-wave solar radiation F_{sw} (sw stands for short-wave), and up- and downward long-wave radiation F_{lw} (lw stands for long-wave):

$$F_{sw} = F_{sw}^{\downarrow} + F_{sw}^{\uparrow} \tag{2.58}$$

$$F_{lw} = F_{lw}^{\downarrow} + F_{lw}^{\uparrow} \tag{2.59}$$

where

$F_{sw}^{\downarrow}$ = downwelling short-wave radiation **transmitted** through the air
$F_{sw}^{\uparrow}$ = upwelling **reflected** short wave (solar) radiation
$F_{lw}^{\downarrow}$ = long-wave **diffuse** IR radiation downward directed and
$F_{lw}^{\uparrow}$ = long-wave IR radiation **emitted** (upward directed) (Stull, 1988).

Together all four components give the net radiative flux

$$F_N = F_{sw}^{\downarrow} + F_{sw}^{\uparrow} + F_{lw}^{\downarrow} + F_{lw}^{\uparrow} \tag{2.60}$$

By definition the upward fluxes are negative, while the downward fluxes are positive because these contribute a positive value to the radiation balance. Each of these terms represents the sum of direct and diffuse radiation components crossing a locally horizontal plane at the surface (Stull, 1988).

2.5.1 Short-wave radiation

Initially one considers the incoming short-wave radiation from the Sun, in other words the direct solar radiation, which depends on the following variables (Stull, 1988):

- Solar constant S_0
- Angle of entry Ψ [rad] of the Sun, which depends on:
  - Geographic latitude φ_g [rad]
  - Geographic longitude λ_g [rad]
  - Time of day t_h [h]
  - Season of the year, realised through the declination angle δ_{Solar} [rad] of the Sun above the equator, which depends on the current day d_y [#] of the year

- Transmittance T_Ψ of the atmosphere, which depends on:
  - Angle of entry Ψ
  - Cloud coverage (high, middle and low) height σ_{c_H}, σ_{c_M} and σ_{c_L}

The individual variables are discussed in detail in the following paragraphs.

The declination angle δ_{Solar} can be calculated by the latitude of the Tropic of Cancer ($23.45\,^\circ = 0.409$ radians), the day of the summer solstice ($= 173$) and the day of the year (e.g. June $19 =$ day 170) divided by the sidereal year:

$$\delta_{Solar} = 0.409 \cos\left(2\pi \frac{d_y - 173}{365.25}\right) \tag{2.61}$$

The calculation of the local angle of entry is a geometric consideration resulting in

$$\sin\Psi = \sin\varphi \sin\delta_{Solar} - \cos\varphi \cos\delta_{Solar} \cos\left(\frac{\pi\, t_h}{12} - \lambda\right) \tag{2.62}$$

Burridge and Gadd (Burridge, 1974) developed a parametrisation for the transmittance which includes the specific values for different cloud heights

$$T_\Psi = (0.6 + 0.2 \sin\Psi) \cdot (1 - 0.4\,\sigma_{c_\mathrm{H}}) \cdot (1 - 0.7\,\sigma_{c_\mathrm{M}}) \cdot (1 - 0.4\,\sigma_{c_\mathrm{L}}) \tag{2.63}$$

If the Sun is directly in the zenith and the sky is cloud-free, T_Ψ would be 0.8. In the same case but with clouds (in all three layers), T_Ψ would be approximately a factor 10 smaller (Stull, 1988).

The equation for short-wave radiation can be separated in two cases dependent on the angle of entry:

$$F_{sw}^{\downarrow} = S_0\, T_\Psi(\Psi(\varphi, \lambda, \delta_{Solar}(d_y), t_h), \sigma_{c_\mathrm{H}}, \sigma_{c_\mathrm{M}}, \sigma_{c_\mathrm{L}}) \sin\Psi(\varphi, \lambda, \delta_{Solar}(d_y), t_h) \quad \sin\Psi > 0 \tag{2.64}$$

$$F_{sw}^{\downarrow} = 0 \quad \sin\Psi \leq 0 \tag{2.65}$$

where the case $\sin\Psi \leq 0$ represents nighttime conditions (Stull, 1988).

Finally the outgoing short-wave radiation can be easily calculated if $F_{sw}^{\downarrow}$ is known, as it depends only on the albedo a (which is highly variable 0.95 over fresh snow and 0.1 over coniferous forest)

$$F_{sw}^{\uparrow} = -aF_{sw}^{\downarrow} \tag{2.66}$$

(Stull, 1988).

2.5.2 Long-wave radiation

As described in section 2.4.1 the outgoing long-wave radiation can be described with the *Stefan-Boltzmann law*. With the negative sign and with the emissivity ε one yields

$$F_{lw}^{\uparrow} = -\varepsilon\sigma T_s^4 \tag{2.67}$$

The downward long-wave radiation is much more difficult to calculate because one has to integrate the equations for radiative flux divergence (Stull, 1988).

Ångstrom developed a simple model for the counter-radiation based on empirical datasets and showed that $F_{lw}^{\downarrow}$ depends on the partial pressure of water vapour e [kg m^{-1} s^{-2} = 1 pascal (Pa)] and air temperature T_a

$$F_{lw}^{\downarrow} = \left[0.804 - 0.236 \cdot 10^{-0.052e}\right] \sigma T_a^4 \tag{2.68}$$

(Liljequist and Cehak, 1984).

A simpler way to derive F_{lw} is the combination of outgoing and incoming long-wave radiation in one formula which depends only on cloud coverage at different heights. Using a baseline value of -100 W m^{-2} one yields

$$F_{lw} = -100 \text{ W m}^{-2} \cdot (1 - 0.6\,\sigma_{c_\text{H}} - 0.3\,\sigma_{c_\text{M}} - 0.1\,\sigma_{c_\text{L}}) \tag{2.69}$$

This leads to two extreme cases (Stull, 1988):

- $\sigma_{c_\text{H}} = \sigma_{c_\text{M}} = \sigma_{c_\text{L}} = 0$; which means that there are no clouds and F_{lw} is at its minimum $-100\,\text{W m}^{-2}$.
- $\sigma_{c_\text{H}} = \sigma_{c_\text{M}} = \sigma_{c_\text{L}} = 1$; which means complete cloud coverage and F_{lw} is at its maximum $0\,\text{W m}^{-2}$.

2.5.3 Components of radiation at ARAD site Graz/University

Figure 2.5 shows calculated surface radiation budget components ($F_{sw}^{\uparrow}$, $F_{sw}^{\downarrow}$, F_{lw} and F_N) at ARAD site Graz/University (47° 04' 41.5" N, 15° 26' 55.0" E) on the 19$^{\text{th}}$ of June 2015.

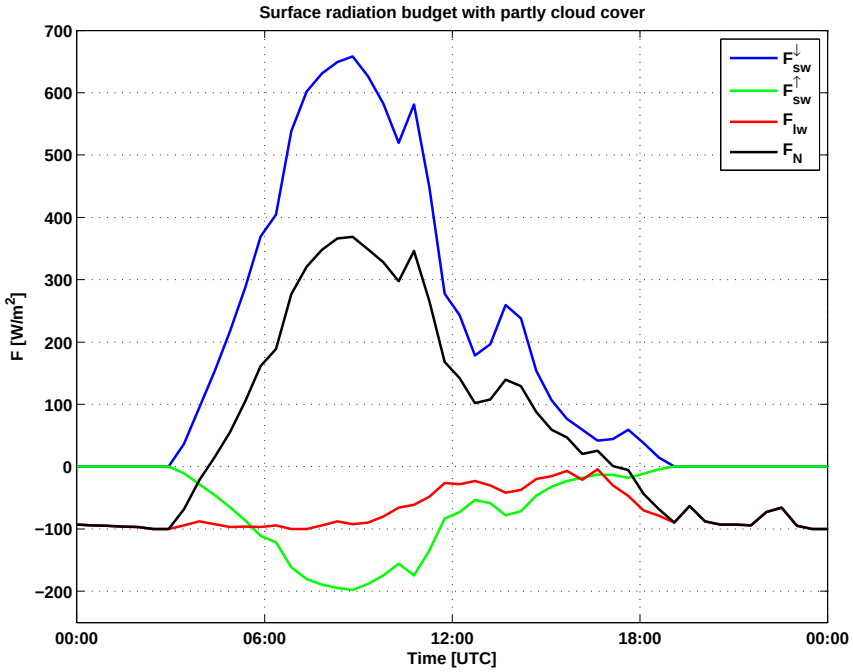

Figure 2.5: Calculated surface radiation budget components at ARAD site Graz/University for 2015-06-19. In the morning only few clouds are present, while in the early afternoon convective clouds emerge and reduce the incoming short-wave radiation. Calculations performed following Eqs. 2.60, 2.64, 2.66 and 2.69.

2.5.4 Global and diffuse radiation

Finally it is useful to have a mathematical expression for the *global radiation* (*GLO*) and the *incoming diffuse radiation* (*HIM*). *GLO* is the sum of the direct solar radiation $F_{sw}^{\downarrow}$ and *HIM*

$$GLO = S_0 \, T_\Psi \sin \Psi + HIM \tag{2.70}$$

To obtain the diffuse radiation one must introduce two absorption coefficients, one for water vapour $\tau_{wv} = 0.07$ and one for ozone $\tau_o = 0.02$.

$$HIM = 0.5 \cdot (1 - 0.07 - 0.02) \, S_0 \sin \Psi - F_{sw}^{\downarrow} \tag{2.71}$$

The factor 0.5 in Eq. 2.71 implies that half of the incoming diffuse radiation scatters to the Earth's surface and the other half scatters back to space (Williams et al., 1972).

2.6 Measurements of global and diffuse radiation

The following section describes the measurement principle used for observations in state-of-the art meteorological surface networks. Other methods such as caloric, chemical or remote sensing techniques are not discussed here as they are not central to this master thesis.

The focus lies on the radiative fluxes described in section 2.5 which impinge on a horizontal area. All these fluxes refer to the upper half space (2π sr) and can be measured as outlined below. Figure 2.6 shows a sketch of a *pyranometer*, the standard meteorological device to measure *GLO* from ground (Kraus, 2004).

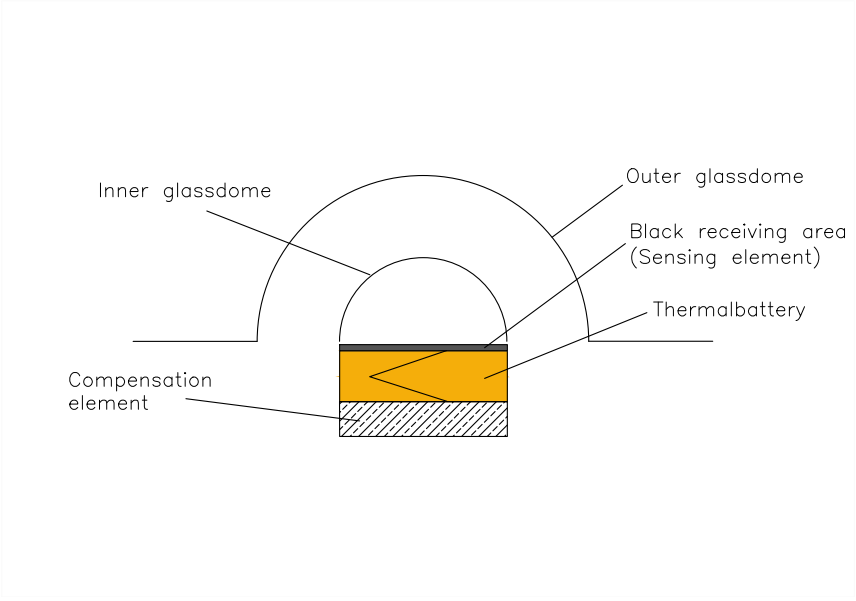

Figure 2.6: Cross-section of a pyranometer. The radiative flux passes through the outer and the inner glass-dome and impinge the sensing element. The orange rectangle represents the thermal battery, the dashed area symbolises the ‚cold' junction. A more detailed illustration is shown in chapter 3.2.1. In analogy to (Kraus, 2004, p. 133).

First a pyranometer with only one glass-dome is considered (note: the more complicated two glass-dome pyranometer is described further below). The incoming short-wave radiation passes the glass-dome and impinges the black receiving area which is called sensing element or ‚active' junction. The thermal battery is directly below this sensing element and has a large number of thermocouple junctions connected electrically in series. Finally it's connected with a thermal sluggish compensation element, referred to as ‚cold' junction. Now the energy balance of the receiving area in the glass-dome must be considered:

$$F_N - F_G - F_S - F_L = 0 \tag{2.72}$$

where F_G = ground heat flux, F_S = sensible heat flux and F_L = latent heat flux, which are detailed in section 2.9 (Kraus, 2004).

As the receiving area is assumed dry, the latent heat flux F_L of the water vapour can be set zero. For F_N one can use Eq. 2.60 and subsequent equations (where RA stands for receiving area):

$$F^{\downarrow}_{sw,RA} = \mathit{GLO} = S_0\, T_\Psi \sin\Psi + \mathit{HIM} \tag{2.73}$$

Eq. 2.73 describes the measurement of the whole radiative flux coming from 2π sr.

$$F^{\uparrow}_{sw,RA} = 0 \tag{2.74}$$

$F^{\uparrow}_{sw,RA}$ can be set zero because a black body has no reflectivity in an ideal case.

$$F^{\uparrow}_{lw,RA} = -\sigma T^4_{RA} \tag{2.75}$$

Eq. 2.75 represents *Kirchhoff's law* ($\varepsilon(\lambda) = \alpha(\lambda) = 1$), so the receiving area emits entirely long-wave radiation.

$$F^{\downarrow}_{lw,RA} = \sigma T^4_d \tag{2.76}$$

For simplification the glass-dome is considered as a black body for infrared radiation (the index d marks the glass-dome) (Kraus, 2004).

Finally one yields the equation for the net radiation F_N inside the glass-dome

$$F_N = F_{sw,RA} - \sigma T^4_{RA} + \sigma T^4_d \tag{2.77}$$

Now F_G and F_S must be described with two coefficients which represent the proportion between the heat flux and the thermodynamic force for this flux, i.e. a temperature difference ΔT

$$\alpha_a = \frac{F_S}{T_{RA} - T_a} \tag{2.78}$$

$$\beta = \frac{F_G}{T_{RA} - T_C} \tag{2.79}$$

where α_a is the heat transfer coefficient between the receiving area (RA) and the air (a) inside the dome, β is the heat transfer coefficient between the receiving area and the compensation element (C). Introducing both equations and Eq. 2.77 in Eq. 2.72 yields

$$F_{sw,RA} - \sigma T^4_{RA} + \sigma T^4_d - \alpha_a(T_{RA} - T_a) - \beta(T_{RA} - T_C) = 0 \tag{2.80}$$

If the temperatures and both coefficients are known, $F_{sw,RA}$ can be calculated (Kraus, 2004).

A simpler way to obtain $F_{sw,RA}$ is to include a second glass-dome (inner) in the pyranometer (see Figure 2.6). After this modification the heat transfer between the black receiving area and the dome will be minimized and the long-wave radiative fluxes can be set equal $-\sigma T_{RA}^4 = \sigma T_d^4$ (Kraus, 2004).

Additionally the turbulent air flow is approximately zero and F_S disappears. Thus in Eq. 2.80 only one term remains and it simplifies to

$$F_{sw,RA} = \beta(T_{RA} - T_C) = \frac{\beta}{\varsigma} U \tag{2.81}$$

$U = \varsigma(T_{RA} - T_C)$ is valid, when the measured voltage U of the thermal battery depends directly on the thermoelectric power ς. In plain terms the whole solar radiation from the upper half space can be derived solely from the temperature difference between the ‚active' and ‚cold' junction; consequently the voltage U. The factor $\frac{\beta}{\varsigma}$ has the unit (W m^{-2}) V^{-1} and is determined directly at the gauging (Kraus, 2004).

But $F_{sw,RA}^{\downarrow}$ in Eq. 2.73 has a second term, the incoming diffuse radiation *HIM*, which can be directly measured with a simple modification to the observational system. A small sphere, mounted with the instrument on an electric powered sun tracker, intercepts the direct solar radiation and allows that only diffuse radiation is measured. This small black sphere has to cover the pyranometer´s glass-dome completely and throughout whole day, which is achieved by the sun tracker following the Sun´s position (Kipp&Zonen, 2010).

2.7 Fundamental meteorological properties

In this section some physical base items or properties are presented which are important in the context of this thesis due to their influence on radiation measurements. Properties are items which describe the current condition for every position in space in coordinates x, y and z and for every temporal moment t of a physical system. In atmospheric sciences properties like temperature T, pressure p or relative humidity RH can be described as a field which depends of space and time, e.g., $T = T(x, y, z, t)$ (Kraus, 2004).

2.7.1 Pressure

Before the pressure of a medium can be defined, one has to look at the mass M [kg] (physical perspective) and the amount of substance M^* [mol] (chemical perspective). The combination of both yields the molar mass m^* [kg mol^{-1}] (= mass of the amount of a substance of one mol)

$$M = m^* M^* \tag{2.82}$$

m^* is constant for every single substance like oxygen $m_{O_2}^* = 32$ kg kmol^{-1}, but differs for a mixture of gases (Hantel, 2013).

A further important parameter is the *Avogadro constant* N_A when expressing the amount of a substance through the number of particles N

$$N = N_A \, M^* \tag{2.83}$$

N_A has the value of $6.022 \cdot 10^{23}$ mol^{-1} and is constant for all substances (Hantel, 2013).

Now the pressure p [Pa] can be defined by the force F_A [N] acting normally on an area A

$$p = \frac{F_A}{A} \tag{2.84}$$

A force is the product of a mass and a gravitational acceleration g [m s^{-2}]. Mass is the product of density ρ_i and the volume V_c [m^3], so Eq. 2.84 can be reformulated to

$$p = \frac{M_i \, g}{A} = \frac{\rho_i \, V_c \, g}{A} = \frac{\rho_i \, l \, A \, g}{A} = \rho_i \, l \, g \tag{2.85}$$

Next one has to consider a volume with different gases, all having individual partial pressures p_i. The whole mass of a group of molecules can be expressed as the product of the number of particles and the mass m of a single molecule

$$M = N \, m \tag{2.86}$$

One particle of a given gas has a velocity v [m s^{-1}] and travels a certain way s in a certain time t. Figure 2.7 illustrates these velocities and shows a cube with the side-length L_m. The number of particles ΔN which arrive at the cubes wall within time t (under the assumption that every particle can travel in six directions; positive and negative x, y and z), one yields

$$\frac{\Delta N}{N} = \frac{1}{6} \frac{v \, t}{L_m} \tag{2.87}$$

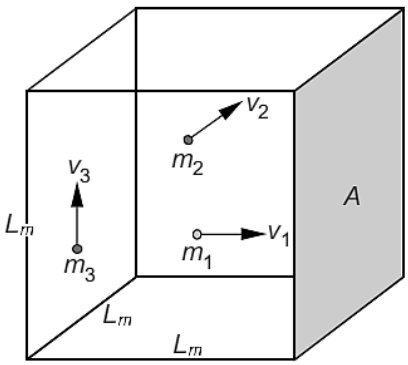

Figure 2.7: Conceptional model for partial pressure p_i with the mass m_i, the side-length L_m and an area A of a cube. Every particle has its own velocity v_i and moves along the six directions parallel to the side edge. Source: (Hantel, 2013)

Every collision of a particle with a wall transfers momentum I to the wall

$$\Delta I = 2 \, m \, v \tag{2.88}$$

The factor 2 in Eq. 2.88 illustrates that the wall obtains momentum from the particle; but returns the same momentum back to the particle (Hantel, 2013).

The increasing momentum of colliding particles can be expressed as an impulse (force times time)

$$\Delta N \, \Delta I = F_A \, t \tag{2.89}$$

which introduced in Eq. 2.84 yields

$$p = \frac{F_A}{A} = \frac{\Delta N \, \Delta I}{A \, t} \tag{2.90}$$

Now, ΔN can be replaced by transformation of Eq. 2.87 and ΔI by Eq. 2.88, yielding

$$p = \frac{1}{6} \, \frac{v \, t \, N}{L_m} \, \frac{2 \, m \, v}{A \, t} = \frac{1}{3} \, \frac{m \, v^2 N}{V_c} \tag{2.91}$$

With $n = \frac{N}{V_c}$, Eq. 2.91 can be transformed to

$$p = \frac{m v^2 n}{3} \tag{2.92}$$

which states that pressure: (1) depends on the concentration of particles n; (2) is proportional to the square of the velocity; (3) can only exist with moving particles (Hantel, 2013).

Figure 2.7 shows more than one kind of molecule with the index i. All these molecules contribute a partial pressure and the sum yields *Dalton's law*:

$$p = \sum_i p_i \tag{2.93}$$

(Hantel, 2013). Thus the partial pressure of any single component of a mixture of an ideal gas is independent of the existence of other molecules (Kraus, 2004).

2.7.2 Temperature

Temperature T [K] is understood as kinetic energy of a molecule. In this context one can define the *principle of thermodynamic equilibrium*. In thermodynamic equilibrium the kinetic energy $\frac{mv^2}{2}$ is equal for every molecule and the temperature is defined by:

$$\frac{3}{2} k_B T = \frac{1}{2} m v^2 \tag{2.94}$$

(Hantel, 2013).

2.8 Ideal gas law

All gases without molecule interactions can be described by a single equation of state, where Eq. 2.94 combined with Eq. 2.92 yields a product of temperature, concentration of particles and the Boltzmann constant, commonly referred to as the *ideal gas equation*:

$$p = n k_B T \tag{2.95}$$

This equation can be easily transformed in a universal gas equation according to Avogadro's hypothesis (equal volumes contain equal numbers of molecules at the same temperature and pressure) and yields multiplied with $\frac{N_A}{N_A}$

$$p = \frac{N}{V_c} k_B T \qquad \Rightarrow \qquad p\,V_c = \overbrace{\frac{N}{N_A}}^{M^*} \overbrace{k_B\,N_A}^{R^*} T = M^* R^*\,T \tag{2.96}$$

where R^* is the *universal gas constant* of $8.31\,\mathrm{J\ mol^{-1}\ K^{-1}}$ (Hantel, 2013).

If one divides the equation above through the volume V_c and introduces the amount concentration $\rho^* = \frac{M^*}{V_c}$, one yields

$$p = \rho^* R^* T \tag{2.97}$$

The universal gas constant can be used for any *specific* gas and can be written as the expression of mass/amount of substance (Eq. 2.82)

$$R = \frac{R^*}{m^*} \qquad \Rightarrow \qquad p = \rho\,R\,T \tag{2.98}$$

(Hantel, 2013). The specific gas constant for dry air with its molar mass m_d^* is expressed as

$$R_d = \frac{R^*}{m_d^*} = \frac{8.3144\,\mathrm{J\,mol^{-1}\,K^{-1}}}{28.965 \cdot 10^{-3}\,\mathrm{kg\ mol^{-1}}} = 287\,\mathrm{J\,kg^{-1}\,K^{-1}} \tag{2.99}$$

(Kraus, 2004).

2.8.1 Humidity

Dalton's law can be used to introduce the *partial pressure of the water vapour* e. Taking the sum of the partial pressures of dry air p_d and water vapour e yields

$$p = \sum_i p_i = p_d + e \tag{2.100}$$

Water vapour is independent of other components in the gas and has its own ideal gas equation:

$$e = \rho_v\,R_v\,T \tag{2.101}$$

where ρ_v is the density of water vapour and $R_v = \frac{R^*}{m_v^*}$ is the specific gas constant of water vapour with $m_v^* = 18.016 \cdot 10^{-3}\,\mathrm{kg\,mol^{-1}}$ (Kraus, 2004).

Specific humidity

The specific humidity q [$\mathrm{kg\,kg^{-1}}$] expressed as proportion of the densities of water vapour and whole moist air (i.e., the sum of densities of dry and moist air; $\rho = \rho_d + \rho_v$):

$$q = \frac{\rho_v}{\rho} = \frac{\rho_v}{\rho_d + \rho_v} \tag{2.102}$$

Reformulation of Eq. 2.100 and introducing it with Eq. 2.101 and in Eq. 2.102 yields

$$q = \frac{\frac{e}{R_v T}}{\frac{p-e}{R_d T} + \frac{e}{R_v T}} = \frac{R_d}{R_v} \frac{e}{p - (1 - \frac{R_d}{R_v})e} = 0.622 \frac{e}{p - 0.378e} \approx 0.622 \frac{e}{p} \tag{2.103}$$

This formulation can be achieved as $0.378e$ is always much smaller than p (Kraus, 2004).

Relative humidity

The partial pressure of water vapour has a ceiling which is called the saturation vapour pressure e_s which depends only on air temperature T_a. The case of $e = e_s$ means that the air is saturated and the proportion of both variables can be expressed by the relative humidity RH:

$$RH = \frac{e}{e_s(T_a)} \cdot 100 \tag{2.104}$$

(Kraus, 2004).

2.9 Energy balance

The energy balance at the surface comprises four important radiative fluxes (Eq. 2.105): In this expression only the vertical components are considered because horizontal fluxes have a very small gradient regarding temperature and humidity.

$$F_N - F_G - F_S - F_L = 0 \tag{2.105}$$

The value and algebraic sign of each parameter depends on various factors (Kraus, 2004):

- Net radiation flux F_N: see section 2.5
- Ground heat flux F_G, depends on the temperature gradient in the ground, and the grounds material properties like the specific heat capacity c_p at constant pressure and the thermal conductivity κ. If temperature decreases with depth, the heat flux is directed away from the surface (positive flux), conversely if the top layer receives heat from underneath temperature increases with depth (negative flux).
- Sensible heat flux F_S, depends on meteorological properties such as wind velocity and the vertical temperature gradient. Furthermore it depends on the moisture content of the ground which supplies the energy of the flux.
- Latent heat flux F_L, depends on the gradient of the specific humidity q. When q decreases with height, the flux is upward directed and positive. Additionally the wind velocity in and the relative humidity of a layer of air are crucial for the strength of this flux.

2.10 Evaporation

Evaporation denotes a transport of water vapour from a surface in the atmosphere; note from a living surface this process would be called *transpiration*. The process of evaporation can be described with the flux of the latent heat F_L or with the heat of vaporisation L_w for water. $L_w = 2.6 \cdot 10^6$ J kg^{-1} which is the energy needed for a phase transition from liquid water to water vapour. To calculate the evaporation one can choose from three different approaches (Kraus, 2004):

1. By using the energy balance from Eq. 2.105 one can calculate F_L if other parameters are known.

2. F_L can be described by the difference of specific humidity at the surface q_0 and the overlying air q_a, expressed in *Dalton's law of evaporation*:

$$F_L = \frac{\alpha_a}{c_p} L_w \left(q_0 - q_a\right) \tag{2.106}$$

3. By the vertical specific humidity gradient and the appropriate eddy diffusion coefficient K_z [m^2 s^{-1}]:

$$F_L = -L_w \, \rho \, K_z \frac{\partial q}{\partial z} \tag{2.107}$$

   where the index z of K indicates that it has the same height above the surface as $\frac{\partial q}{\partial z}$.

3 Instruments, Data and Methods

This thesis focuses on the influence of meteorological factors and instrumentation on the accuracy of global and diffuse radiation measurements at the Austrian RADiation Monitoring Network (ARAD) site Graz/University. The subsections of this chapter provide an overview about the ARAD network (Section 3.1), the instruments used for radiation measurements at ARAD site Graz/University (Section 3.2), co-located meteorological measurements at TAWES site Graz/University (Section 3.3), additional instrumentation used during an extensive measurement campaign performed in January 2015 (Section 3.4), experiments and laboratory analysis (Section 3.5), data obtained from routine and campaign measurements analysed within this thesis, and programs and software for data analysis (Section 3.6).

3.1 The Austrian RADiation Monitoring Network (ARAD)

3.1.1 Aims of the ARAD network

The Austrian RADiation Monitoring Network (ARAD), founded in 2010, is a joint effort of the Austrian Central Institute for Meteorology and Geodynamics (ZAMG), the University of Graz, the University of Innsbruck and the University of Natural Resource and Applied Sciences, Vienna (BOKU) for high precision long-term monitoring of solar and terrestrial surface radiation to assess temporal and spatial changes of radiative fluxes at/to the surface. ARAD's mission comprises three major requirements: (1) to provide a state-of-the-art climate monitoring network; (2) to provide data for atmospheric model/satellite calibration and validation; (3) to provide high-precision data for further technical developments in the field of solar energy utilization (Olefs et al., 2015).

To date ARAD comprises five monitoring sites:

- Sonnblick (3109 m a.s.l.)
- Kanzelhöhe (1540 m a.s.l.)
- Innsbruck/University (578 m a.s.l.)
- Graz/University (398 m a.s.l.)
- Wien Hohe Warte (198 m a.s.l.)

A geographical overview about station locations is provided in Figure 3.1. In its current extent, ARAD covers four out of five so-called Coarse-Resolution Subregions (CRS) defined in the Historical Instrumental climatological Surface Time series (HISTALP) project (Auer et al., 2007).

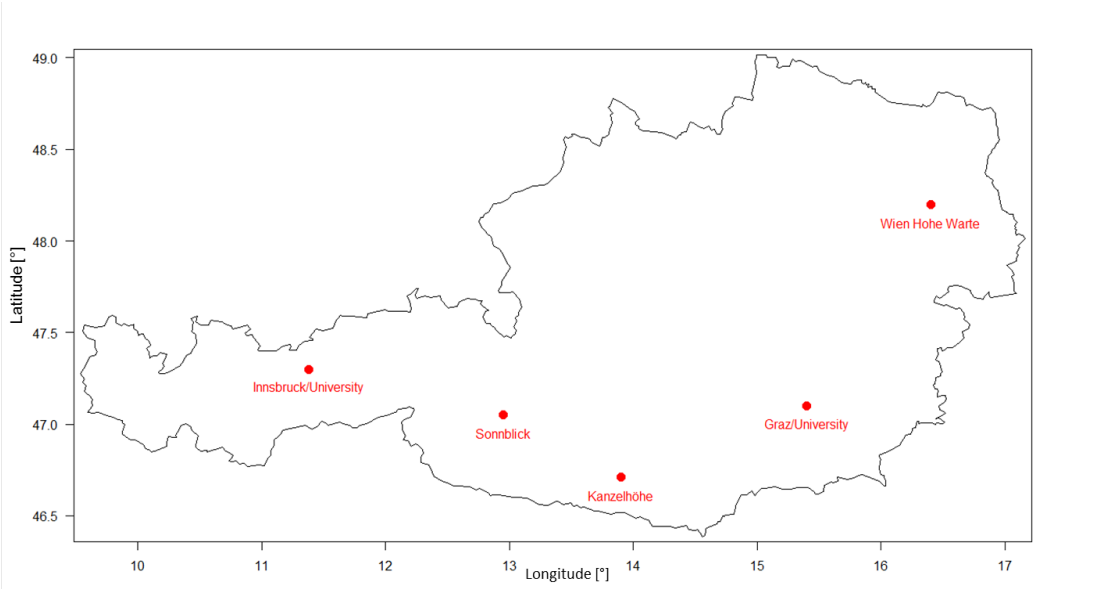

Figure 3.1: Overview of the Austrian RADiation (ARAD) station locations.

3.1.2 Instrumentation of ARAD sites

ARAD sites are equipped with state-of-the-art broadband radiometers for measurements of global, direct, and diffuse solar radiation and downwelling long-wave radiation. All ARAD sensors are suitable to BSRN requirements; according to ISO 9060 all pyranometers are secondary standard instruments and all pyrheliometers are first class instruments. All horizontally mounted sensors are contained in ventilated and heated housing units to reduce solar loading and thermal offsets (Olefs et al., 2015).

At each ARAD site radiometers are mounted on a sun tracker, ensuring the continuous alignment of the pyrheliometer and continuous shading of the pyranometer measuring diffuse solar radiation and the pyrgeometer for measurements of downwelling long-wave radiation (Olefs et al., 2015).

3.2 Radiation measurements at ARAD site Graz/University

ARAD site Graz/University is operated by the Institute of Geophysics, Astrophysics and Meteorology (IGAM)/Institute of Physics (IP) of the University of Graz in cooperation with ZAMG.

The following subsection describes the pyranometer CMP 21 of Kipp&Zonen which is used for radiation monitoring at the ARAD site Graz/University, and whose sensitivity to the influence of meteorological factors is investigated within this thesis.

3.2.1 The pyranometer CMP 21

The devices of the CMP series are premium radiometer to measure the incoming short-wave radiation $F^{\downarrow}_{sw,RA}$ (see Eq. 2.73). These pyranometers are complying with the ISO 9060 standard and the guidelines of the World Meteorological Organization (WMO).

The CMP 21 is composed of two glass-domes, a black receiving area or sensing element, a thermal battery or thermopile, a thermalisation resistance/compensation element in the body (see Figure 2.6), a thermistor, a sun-shield and a drying cartridge. A cross-section and a schematic outside illustration of the CMP 21 are shown in Figures 3.2 and 3.3, while technical specifications are provided in Table 3.1. Individual instrument parts are described in detail in subsections 3.2.2 to 3.2.4 below.

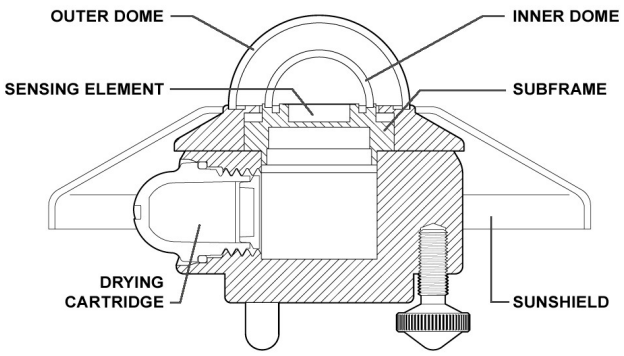

Figure 3.2: Cross section of the CMP 21, indicated are the outer and inner glass-dome, the sensing element with the thermopile, the drying cartridge, the subframe and the white sun-shield. Source: (Kipp&Zonen, 2010)

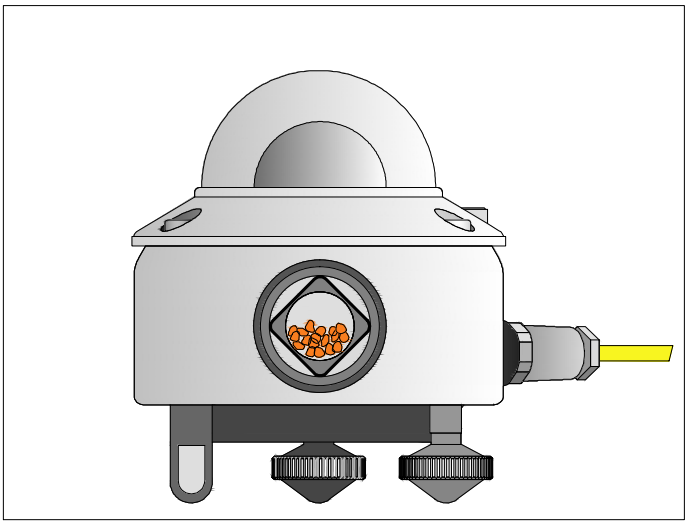

Figure 3.3: Schematic outside illustration of a CMP 21 with two glass-domes. The orange pellets represent the silica-gel in the drying cartridge to regulate the humidity level inside the radiometer. The yellow cable is a low noise type cable for signal transmission. In analogy to (Kipp&Zonen, 2010, p. 7)

Table 3.1: Technical specifics of the CMP 21 pyranometer. Source:(Kipp&Zonen, 2010)

Specification	**Unit**	**CMP 21**	**Definition**
Spectral range	nm	$285-2800$	50% response point
Sensitivity	μV (W^{-1} m^{-2})	$7-14$	Signal output for 1 W m^{-2} irradiance
Impedance	ω	$10-100$	At instrument housing connector
Response time	s	<5	95% of final value
Non-linearity	%	<0.2	From 0 to 1000 W m^{-2} irradiance
Temperature dependence of sensitivity	%	<1	Variation in range $-20\,^{\circ}$C to $50\,^{\circ}$C from value at $20\,^{\circ}$C
Tilt error	%	<0.2	Deviation when facing downwards
Zero offset A	W m^{-2}	<7	At 0 to -200 W m^{-2} of IR net radiation
Zero offset B	W m^{-2}	<2	At 5 K h^{-1} temperature change rate
Operating temperature	°C	-40 to 80	Storage temperature is the same
Field of view	°	180	Hemispherical
Directional error	W m^{-2}	<10	At $80\,^{\circ}$ with 1000 W m^{-2} irradiance
Maximum irradiance	W m^{-2}	4000	Level above which damage may occur
Non-stability	%	<0.5	Variation in sensitivity per year
Humidity	%	$0-100$	Relative humidity
Uncertainty in daily total	%	<2	95% confidence level

3.2.2 Sensing element

The black receiving area bases on a passive sensing element which is called thermopile. This thermopile consists of 16 thermocouple junction pairs connected electrically in series. The temperature of one of these thermocouple junctions, called active or ‚hot' junction, as in section 2.6, increases with the absorption of thermal radiation. A reference or ‚cold' junction, fixed in the lower part of the thermopile is held at a constant temperature and serves as reference for the ‚hot' junction. The differential temperature between the ‚hot' and ‚cold' junction produces an electromotive force which is directly proportional to the difference in temperature and can be converted in a output voltage linearly to the absorbed thermal radiation. This process is referred to as Seebeck effect. As every thermal battery has its own physical properties and structure, every radiometer has its specific and individual calibration factor. The black receiving area has a very rough surface structure with micro-cavities that effectively absorbs more than 97% of the short-wave radiation in a broad spectral range (see Figure 3.4) (Kipp&Zonen, 2010).

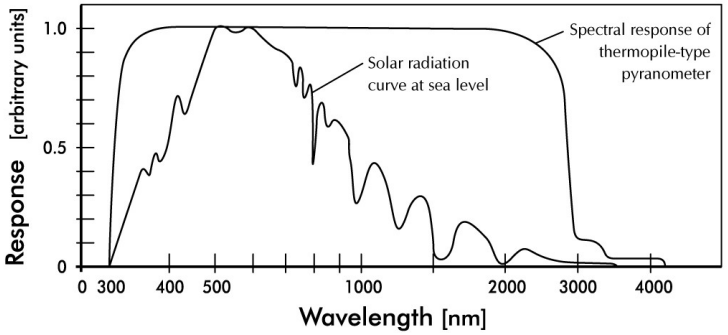

Figure 3.4: Illustration of the solar irradiance spectrum at the Earth's surface with specific absorption lines of diverse molecules in the atmosphere and corresponding pyranometer response. Note: the spectral response of a thermopile-type pyranometer shows a large range of possible absorption wavelengths for short-wave radiation. Source: (Kipp&Zonen, 2010)

For convenience $F^{\downarrow}_{sw,RA}$ is in practice transformed in the variable R [W m^{-2}] and its value can be calculated with the output voltage U_{out} [μV] divided by the sensitivity of the radiometer S [μV (W^{-1} m^{-2})] (Kipp&Zonen, 2010); the reciprocal of $\frac{\beta}{\varsigma}$ in Eq. 2.81:

$$R = \frac{U_{out}}{S} \tag{3.1}$$

3.2.3 Glass-dome

As outlined above the black receiving area absorbs over 97% of the arriving short-wave radiation, consequently the glass-domes have to transmit this amount. In fact manufacturer specifics show that the high quality concentric glass-domes with 2 mm thickness transmit 97-98% of the solar radiation spectrum. Furthermore the domes are manufactured to minimize errors in radiation measurements at all angles which follow the *Lambert's cosine law* (see Eq. 2.7).
Another important part to be considered is the instruments field of view. ISO 9060 and the guidelines of the WMO require that the view regarding the black receiving area has to be clear 180° in all directions (Kipp&Zonen, 2010). Figure 3.5 shows a calculated view in the upper half space as seen from a pyranometer at ARAD site Graz/University.

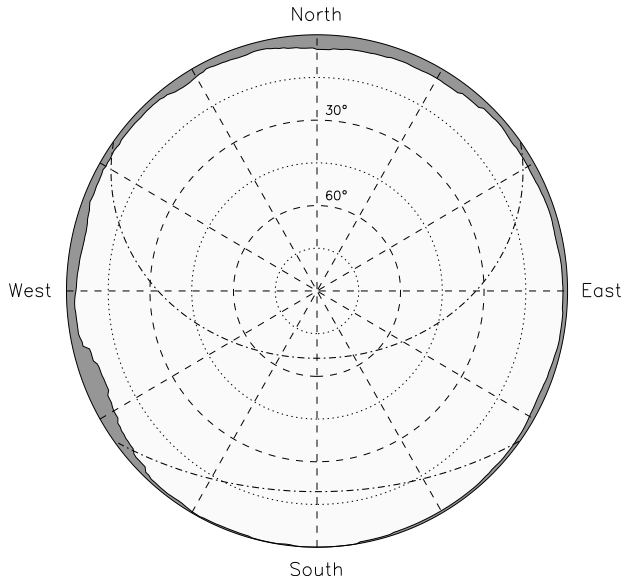

Figure 3.5: Schematic illustration of the upper half space as seen from a pyranometer at ARAD site Graz/University. This geometric horizon was designed with a high-resolution digital elevation model by staff of Kanzelhöhe Observatory.

3.2.4 Drying cartridge

The drying cartrige contains a silica-gel desiccant needed to absorb moisture if it enters the radiometer body. At the time the color of the initially orange silica-gel becomes clear (transparent), the desiccant is saturated with moisture and has to be replaced (Kipp&Zonen, 2010).

3.2.5 Zero offset A

As detailed in section 2.1 any body with a certain temperature has a specific irradiance and this irradiance is exchanged with the environment. Considering the CMP 21 the main exchange occurs between the glass-dome and the cold atmosphere above. During cloudless night the atmosphere can be up to 50 °C ‚colder' than the Earth's surface thus the radiometer dome loses energy to the atmosphere through radiative transfer. This means that the temperature of the glass dome decreases to a level which is lower than the rest of the radiometer and a small negative output signal will be generated which is commonly referred to as *Zero Offset type A*. The second (inner) glass dome serves as a radiation buffer to minimize this effect, as illustrated in Figure 3.6. Additionally a ventilation unit, detailed in section 3.2.8, is used in pyranometer operation helping to mitigate a *Zero Offset type A* (Kipp&Zonen, 2010).

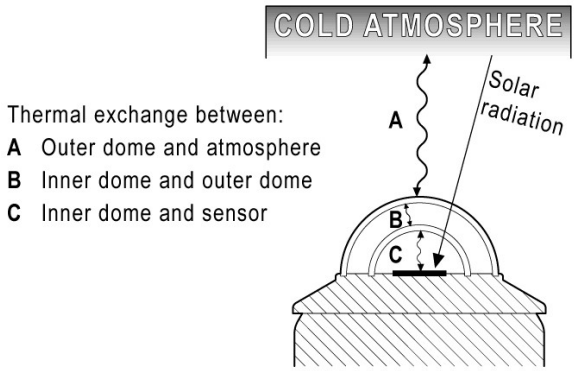

Figure 3.6: Illustration of the radiative transfer between the CMP 21 and the (‚cold') atmosphere. Source: (Kipp&Zonen, 2010)

3.2.6 Zero offset B

The body temperature of the CMP 21 is measured by a thermistor (type: YSI 44031 $10\,\mathrm{k\Omega}$ @ $25\,^{\circ}\mathrm{C}$) (Kipp&Zonen, 2010). This body temperature is directly proportional to the ambient air temperature whereby the possibility of the emergence of heat currents in the radiometer has to be considered, causing a so-called *Zero Offset type B*. This *Zero Offset type B* is specified by the manufacturer, to occur following a $5\,\mathrm{K\,hr^{-1}}$ change in ambient air temperature (Kipp&Zonen, 2010).

3.2.7 Temperature dependence of CMP 21 output

The physical and thermodynamic properties of the individual instrument parts define the range of the body and/or operating temperature of a pyranometer. The CMP 21 has a specific range from $-20\,°$C to $50\,°$C with an interval of $10\,°$C. The aforementioned internal thermistor allows for sensitivity corrections of the pyranometer output. The Kipp&Zonen manual states: „The temperature dependence is given as percent deviation with respect to the calibrated sensitivity at $20\,°$C.“ Thus every single CMP 21 (or any other pyranometer) has its own temperature dependence curve which must be calculated directly at the gauging (Kipp&Zonen, 2010).

3.2.8 Housing for global and diffuse radiation sensors at ARAD site Graz/University

Pyranometers are during routine operation contained in housing units equipped with a ventilation and heating unit. In the following section the specific properties of the housings and their inner life used for ARAD sensors at Graz/University are described. Figure 3.7 shows the ARAD platform at the rooftop of the chemical institute of the University of Graz (Heinrichstraße 28) with the pyranometers for the monitoring of diffuse (*HIM*) and global radiation (*GLO*) marked. In this image also another radiation monitoring instrument within the ARAD setup, a pyrgeometer for the measurement of atmospheric long-wave radiation, here type CGR 4 of Kipp&Zonen (right-hand side, unmarked) and two small, black spheres which obliterate the direct solar radiation for *HIM* and pyrgeometer measurements, are shown. The entire measurement equipment (two pyranometers, one pyrgeometer and one pyrheliometer) is mounted on a power-driven Sun tracking device (at ARAD site Graz/University of type 2 AP by Kipp&Zonen).

3.2.9 The pyranometer setup for measurements of diffuse radiation at ARAD site Graz/University (HIM)

HIM stands as a synonym for the pyranometer monitoring diffuse radiation at ARAD site Graz/University contained in a housing unit of type SBL 480 by Eigenbrodt GmbH & Co. KG. The SBL 480's housing cast is made of aluminium and contains an electronic controlled fan and five heating elements which shelter pyranometers like the CMP 21 from meteorological effects like snow or frost.
The heating elements are located at the height of silica-gel roughly $5\,$cm below the onset of the glass-dome (see Figure 3.8). The heating elements are powered with $10\,$W in routine operation (though other settings are available for operation under rough outside conditions, such as present e.g., at the high altitude ARAD site Sonnblick). The SBL 480 housing is white stove-enamelled, which is standard for housing units to prevent pyranometers from heating-up through solar influence.

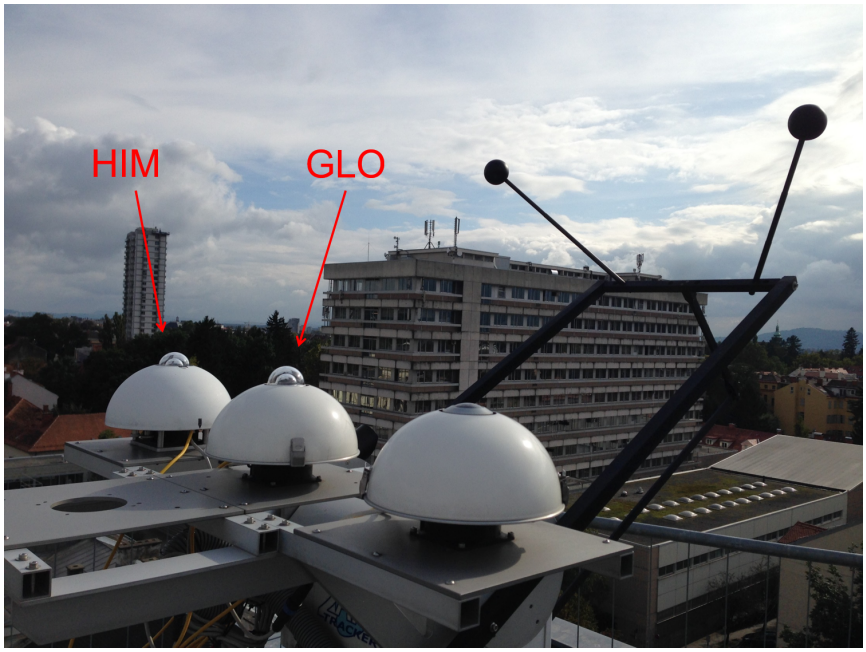

Figure 3.7: ARAD monitoring site Graz/University on top of the roof of Heinrichstraße 28, 8010 Graz. The two pyranometers for the monitoring of global (*GLO*) and diffuse (*HIM*) radiation, marked, as well as a pyrgeometer for the monitoring of downward long-wave radiation are mounted on a horizontal plane on top of a sun-tracking device.

3.2.10 The pyranometer setup for measurements of global radiation at ARAD site Graz/University (GLO)

GLO stands as synonym for the pyranometer measuring global radiation at ARAD site Graz/University, contained in a self-built housing unit, which has been designed and developed by the staff of Kanzelhöhe Observatory. This housing unit consists of a stainless steel bowl of similar size as the SBL 480, with two base plates, a ventilation unit and six heating elements (see Figure 3.8). As the SBL 480 and other standard pyranometer housings the ‚KSO housing' is white stove-enamelled.

The main difference between the SBL 480 and the ‚KSO housing' is the number of heating elements (five vs. six) and the location of these in the housing. The six heating elements of the ‚KSO housing' are mounted on the same baseplate as the operated pyranometer. Heating power in standard operation is 10 or 5 W depending on air temperature inside the housing. Table 3.2 lists the main differences between *HIM* and *GLO*.

Table 3.2: Housing properties of *HIM* and *GLO*.

Item	**HIM**	**GLO**
Manufacturer	Eigenbrodt GmbH & Co. KG	self-built by KSO
Material of sun-shield	high quality aluminium	stainless steel bowl
Heating elements		
Number	five	six
Electrical resistance	three times 12 Ω, two times 50 Ω	six times 12 Ω
Position	at height of drying cartridge	on baseplate

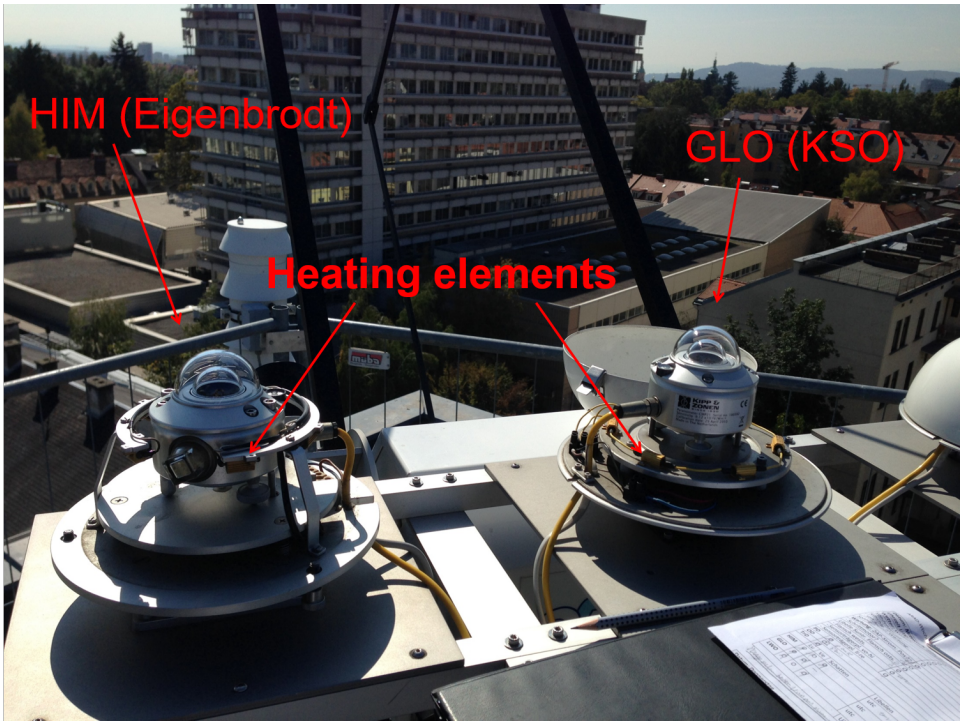

Figure 3.8: Heating elements of housings for *HIM* and *GLO* at ARAD site Graz/University: Eigenbrodt SBL 480 (left, *HIM*, five heating elements at the height of the drying cartridge); self-built KSO housing (right, *GLO*, six heating elements mounted at the upper baseplate).

3.2.11 Heating levels of the KSO housing

The staff of Kanzelhöhe Observatory thought that dynamic heating steps, i.e. switching heating levels dependent on ambient air temperature could improve the accuracy of the solar radiation measurement. A *Zero Offset B* occurs if the body temperature of the pyranometer is proportional to the ambient air temperature, i.e. the pyranometer is also directly proportional to the thermal output of the six heating elements. Therefore KSO scientist Dietmar Baumgartner installed a thermal cut-out which ensures the shift of the heating levels HL_1 and HL_2 inside the KSO housing. This disc insulated thermostat is distributed by Farnell GmbH, Austria.

The heating power of HL_1 is $5\,\mathrm{W}$ and its response temperature is $15\,^{\circ}\mathrm{C}$ with a tolerance of $\pm 3\,^{\circ}\mathrm{C}$ at an ambient temperature $T_a < 100\,^{\circ}\mathrm{C}$. HL_2 has a heating power of $10\,\mathrm{W}$ with a response temperature of $5\,^{\circ}\mathrm{C}$ at same tolerance. The design of the thermal cut-out means that the heating power has a strong dependence on the season of the year and in times where the air temperature varies between 5 and $15\,^{\circ}\mathrm{C}$ the thermal cut-out could switch very often, if such frequent switching occurs, the heating level will be denoted as HL_v (v for various) in this thesis work. To avoid vibrations, the thermal cut-out has built-in a hysteresis (or reset temperature) working at a $10\,^{\circ}\mathrm{C} \pm 4\,^{\circ}\mathrm{C}$ temperature range under an ambient temperature $T_a < 100\,^{\circ}\mathrm{C}$ (Farnell, 2013).

3.3 Routine meteorological measurements at TAWES site Graz/University

The data base of the ZAMG TAWES system (**T**eil **A**utomatisches **W**etter **E**rfassungs **S**ystem - semi-automatically weather monitoring system) captures meteorological measurements in 1-minute resolution and transfers them in 10 minute intervals to the central TAWES data base at ZAMG.

After transmission the measurements are quality controlled and quality flags (*FL*) of *FL* type 0 (unverified), *FL* type 1 (measured and correct), *FL* type 2 (measured and incorrect), *FL* type 3 (measured and doubtful), *FL* type 255 (not measured/missing value) are assigned and archived, along with the measured values, in the database (ZAMG, 1984).

3.4 Additional instrumentation used during the measurement campaign of January 2015

3.4.1 Pyranometers, instrument housings and housing modifications

As ARAD site Graz/University is a continuous monitoring site additional pyranometers and instrument housings have been used for experiments during the measurement campaign.

Two CMP 21 pyranometers by manufacturer Kipp&Zonen, which are the same type of pyranometers operated at ARAD site Graz/University in routine operation, have been used as experimental and reference systems. The two CMP 21 pyranometers have been provide by Dr. Marc Olefs and Dr. Martin Mair (both ZAMG) for the measurement campaign.

The pyranometer housing types used during the campaign have been identical to the two housing systems used at ARAD site Graz/University in routine operation: the SBL 480 housing of manufacturer Eigenbrodt and the self-built cost-effective standard KSO housing designed and manufactured by Mag. Dietmar Baumgartner and colleagues from Kanzelhöhe Observatory (University of Graz). As a major focus of this thesis is to identify potential reasons for offsets of nighttime irradiance measurements by pyranometers of the same type but operated in different housings, one pyranometer was contained in an Eigenbrodt SBL 480 housing in standard configuration (10 W heating level, ventilated), serving as undisturbed reference during the whole campaign.

As the configuration of the heating system was identified as a possible cause for nighttime offsets (see Section 4.1 below) adjustments to the heating level have been performed during the campaign. A simple electronic switch allowed changing the heating level of experimental housings to 10 W, 5 W and 0 W (no heating) during operation. In addition a modified setup (see Section 4.2) allowed raising the heating ring of the KSO housing (by 5, 10 and 15 mm) during the campaign.

3.4.2 Mobile meteorological observation platforms

Two mobile meteorological observation platforms, WS600 UMB by Lufft GmbH (hereinafter referred to as LUFFT; provided by Prof. Dr. Erich Mursch-Radlgruber from BOKU) and a self-built mobile observation platform (hereinafter referred to as MobMet; provided by the Institute of Physics of the University of Graz), have been operated during the measurement campaign of January 2015 to monitor ambient meteorological conditions. Both mobile observation platforms measured ambient air temperature, relative humidity, wind speed and wind direction.

Further one of the mobile observation platforms, LUFFT, was placed at different locations during the campaign to investigate a possible influence of air emitted (at room temperature) by ventilation shafts, in proximity to the ARAD platform, on radiation measurements. Further details on the mobile meteorological observing platforms and their application are provided in subsection 4.2 of this thesis.

3.4.3 Thermoelements

During the campaign measurements of ambient air temperature inside the Eigenbrodt SBL 480 and KSO housings as well as the temperature near the pyranometer glass-domes have been performed using standard PT100 elements. These measurements were needed to identify changes in temperature/heat flow following experimental work (see below). Further details on the PT100 elements and their installation in the different housing systems are provided in Section 4.2 of this thesis.

3.5 Experiments and laboratory analysis

3.5.1 Experiments

A series of experiments were conducted during this thesis to simulate the effect of meteorological events and/or instrument configuration on the radiation sensors. These experiments included:

- Variable and standardized spray-tests: a defined (experiment depending) number of strokes of distilled water was sprayed from a distance of $2 - 4$ cm on the pyranometer(s) glass-dome(s) to simulate precipitation events.
- Coverage-tests: an aluminium cap was fit on the instruments glass-dome(s) to simulate abrupt changes in wind speed.
- Combined spray- and coverage-test to simulate highly variable ambient conditions.
- Adjustments of heating level: to simulate abrupt changes in ambient air temperature and to investigate instrument performance/robustness under different heating levels.
- Adjustments of heating element height: to investigate the influence of different instrument configurations on measurement performance/robustness.

Further details on the individual experiments performed are provided, along with the analysis of sensor responses to experiments, in the individual subsections of Chapter 4.

3.5.2 Laboratory analysis

As described above a series of spray-test were performed previously and during the campaign experiments. While spray-tests have not been ‚standardized' during preliminary investigations, to determine sensor responses to different amounts of water (defined by the number of strokes), uniform spray-tests have been performed during the measurement campaign. The amount of water impacting on the glass-domes of the pyranometers during these standardized spray-tests (30 strokes from $2-4$ cm distance) was determined in laboratory analysis.

To this aim 30 strokes of distilled water have been sprayed into a standard petri dish (from $2-4$ cm distance) and weighed with an analytical laboratory accuracy scale at the Institute of Chemistry at the University of Graz. The procedure was repeated five times to provide statistical uncertainties, yielding an average amount of water released per trial of 3.35 g which corresponds roughly to 3.35 ml, a quantity released within short-term moderate precipitation events.

Table 3.3 provides the summary of the five laboratory trials including average $\overline{x}$, standard deviation σ_x, absolute error $\pm\Delta x$ and relative error $\pm\delta x$, of the amount of distilled water.

Table 3.3: Statistical summary (average, standard deviation, absolute error and relative error) of laboratory trials for five spray tests x_i, each performed with 30 strokes of distilled water.

Item	**Value** [ml]
x_1	3.1953
x_2	3.5221
x_3	3.3992
x_4	3.4971
x_5	3.1752
$\overline{x}$	3.3578
σ_x	0.1642
$\pm\Delta x$	0.0734
$\pm\delta x$	2.2%

3.6 Data sets and data analysis

All data analyses in this thesis are based on 1-minute averages. Besides ARAD data from station Graz/University the following data sets are analysed within this thesis:

- global radiation from the CMP 21 pyranometers (reference and experimental);
- body temperature of the CMP 21 pyranometers (reference and experimental);
- glass-dome temperature of the CMP 21 pyranometers (by PT100 elements);
- air temperature in the Eigenbrodt SBL 480 and KSO housings (by PT100 elements);
- meteorological information on ambient air temperature, relative humidity, wind speed and wind direction from mobile meteorological observation platforms (LUFFT and MobMet);
- supplemental meteorological information (temperature, wind speed and wind direction, precipitation amount, precipitation sensor output) from TAWES site Graz/University.

ARAD data was retrieved directly from the ARAD data portal and/or internal data base at the University of Graz. TAWES data was retrieved directly from the TAWES data base of ZAMG. All data recorded during the measurement campaign were stored on CR3000 and CR1000 data logging systems by manufacturer Campbell Scientific Inc., or directly retrieved from internal instrument logging systems.

All data analyses within this thesis were performed within the General Public License software R Version 3.1.0.

4 Results

In this chapter the results of the analyses of pyranometer measurements (for global and diffuse radiation) and co-located meteorological measurements (air temperature T, wind speed V, wind direction D, relative humidity RH, precipitation sum P and the output of a precipitation sensor PS) are presented. Subsection 4.1 details analyses for the period June 2013 to May 2014. During this time period potential causes for non-physical values or fluctuations between the global and diffuse radiation sensors have been investigated, motivating further measurements and analyses during an extensive measurement campaign detailed in subsection 4.2.

All data analysed in this thesis is of one minute temporal resolution. Due to database properties of the automated recording system used at ARAD site Graz/University the radiation measurements for diffuse (HIM) and global radiation (GLO) are rounded to full digit values. Campaign measurements of global radiation have been recorded with an external data logging system and are available with one decimal digit resolution. The following color code is used throughout all figures of the results section for radiation quantities and meteorological factors:

- Diffuse radiation sensor at ARAD site (*HIM*): red
- Global radiation sensor at ARAD site (*GLO*): blue
- Reference global radiation sensor during the measurement campaign (*PYRANO A*): green
- Experimental global radiation sensor during the measurement campaign (*PYRANO B*): orange
- Difference between two variables shown in the same graph: brown; note: for radiation measurements absolute differences are shown
- Ambient air temperature (T): red
- Wind speed (V): blue
- Wind direction (D): violetred
- Relative humidity (RH): orange
- Precipitation sum (P): magenta
- Precipitation sensor (PS): green

4.1 Preliminary investigations

During routine measurements of *GLO* and *HIM* at ARAD site Graz/University it was identified that the difference $|\Delta R|$ of the nighttime values between *GLO* and *HIM* is frequently (in more than 82% of the individual measurements in the period June 2013 - May 2014) equal or greater than

$2\,\mathrm{W\,m^{-2}}$. The problem seems to be related to *GLO* as this device shows most of the time values around $-2\,\mathrm{W\,m^{-2}}$, while *HIM* is frequently close to the expected value of $0\,\mathrm{W\,m^{-2}}$. This nighttime zero offset is of particular interest for the quality of the ARAD measurements, i.e., whatever is the cause for the offset may also lead to erroneous observations during daytime conditions. Therefore initial analyses of this thesis work focused solely on nighttime values and the identification of meteorological conditions possibly leading to this offset and/or a potential instrumentation effect.

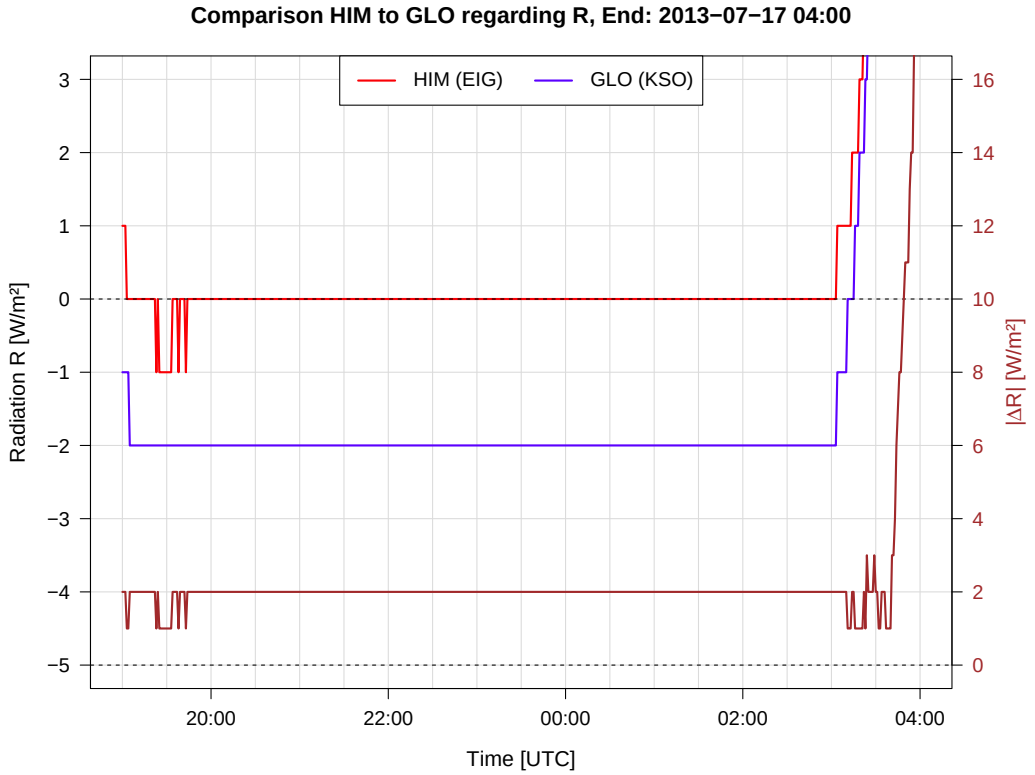

Figure 4.1: Comparison of radiation R [$\mathrm{W\,m^{-2}}$] measured at ARAD site Graz/University with sensors for diffuse (*HIM*: CMP 21, Eigenbrodt housing, red curve) and global radiation (*GLO*: CMP 21, KSO housing, blue curve) between 2013-07-16 19:00 UTC and 2013-07-17 04:00 UTC. For convenience the absolute difference between measurements of *HIM* and *GLO* $|\Delta R|$ [$\mathrm{W\,m^{-2}}$] is shown along with the individual instrument measurements (brown curve, right-hand axis). The black dashed horizontal lines mark $0\,\mathrm{W\,m^{-2}}$ for R and $|\Delta R|$, respectively.

Figure 4.1 shows the time series of radiation R (*HIM* (red) and *GLO* (blue), left-hand axis; absolute difference between *HIM* and *GLO* (brown), right-hand axis) measured at ARAD site Graz/University between 2013-07-16 19:00 UTC and 2013-07-17 04:00 UTC.
One can see that *HIM* remains (almost) throughout the entire period at the expected value of $0\,\mathrm{W\,m^{-2}}$ while *GLO* shows values of $-2\,\mathrm{W\,m^{-2}}$ during this time; consequently $|\Delta R|$ is at $2\,\mathrm{W\,m^{-2}}$ almost throughout the night. Shortly after 03:00 UTC dawn starts and the signals of both radiation sensors rise. The observations illustrated in Figure 4.1 are representative for nighttime measurements of *GLO* and *HIM* at ARAD site Graz/University between June 2013 and May 2014. The big open question is, what causes this nighttime offset?

- A first hypothesis is that an environmental effect, e.g., heat flow, near/at the ARAD site could influence the radiation measurements and cause this offset. This hypothesis was developed as 8 shafts (see Figure 4.56) are located in proximity to the ARAD site on the roof top of Heinrichstraße 28. This shafts emit air at approximately room temperature, on arbitrary schedules depending on lab working hours and work load, and because of the concrete slab directly over these shafts, the air flows horizontally in all directions.
- A second hypothesis is that the housing units (i.e., differences in ventilation and heating systems, material of the shields) affect the observations and that the zero offset is triggered through differences in material/instrumentation properties.
- A third hypothesis is that neither heat flow nor instrument properties are responsible for the zero offset but that one or multiple meteorological factors such as e.g., precipitation, wind direction and wind speed, ambient temperature, relative humidity, influence the ARAD measurements.
- The fourth hypothesis developed is that the zero offset is caused by a combination of all or multiple of the factors described above.

During the chronological analysis of nighttime measurements of *GLO* and *HIM* several interesting cases of different behaviour of the sensors could be identified.

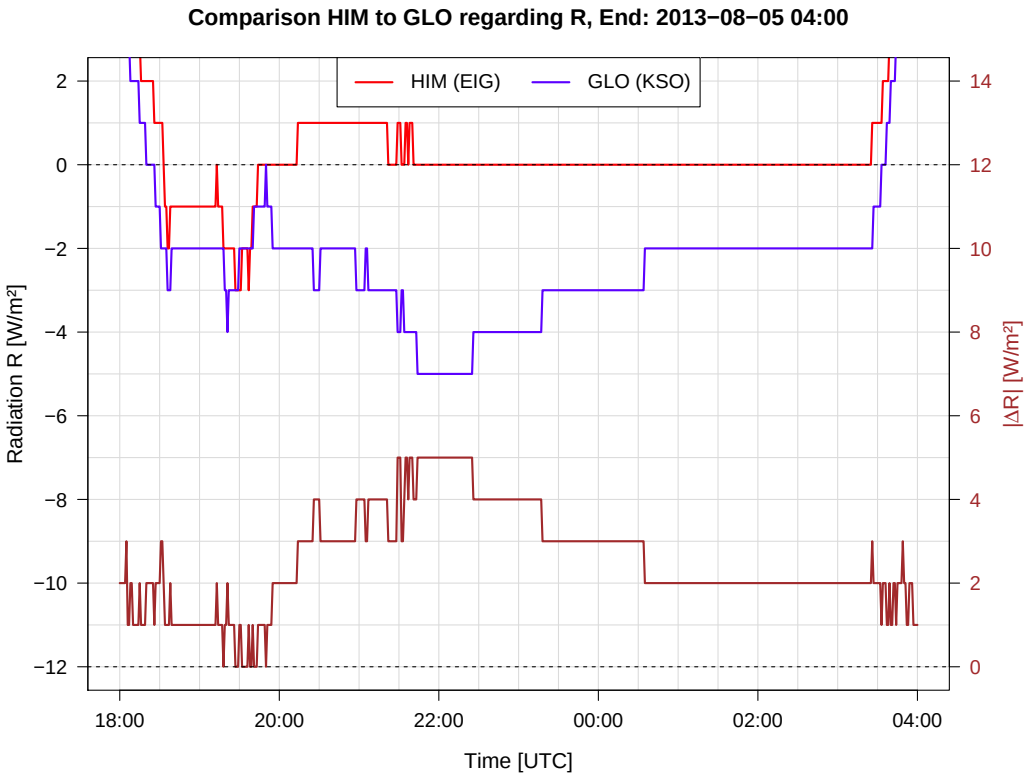

Figure 4.2: As Figure 4.1 but for measurements between 2013-08-04 18:00 UTC and 2013-08-05 04:00 UTC.

Figure 4.2 shows one of these cases, the nighttime series of *HIM* and *GLO* between 2013-08-04 18:00 UTC and 2013-08-05 04:00 UTC. With dusk a constant offset of $|\Delta R| = 1\,\mathrm{W\,m^{-2}}$ occurred lasting from 18:30 UTC to 19:15 UTC. Then at 19:15 UTC suddenly both radiation sensors declined to a strong negative output signal (*HIM*: $R = -3\,\mathrm{W\,m^{-2}}$ and *GLO*: $R = -4\,\mathrm{W\,m^{-2}}$). After a couple of minutes *HIM* recovered, reaching a signal of $0\,\mathrm{W\,m^{-2}}$. *GLO* recovered initially too but relapsed to a negative output signal of $R = -5\,\mathrm{W\,m^{-2}}$ within 2 hours. In the second half of the night *GLO* increased to $R = -2\,\mathrm{W\,m^{-2}}$ and remained at this level for the rest of the night, resulting in the common offset of $|\Delta R| = 2\,\mathrm{W\,m^{-2}}$.

Given the parallel evolution of the sensor output signals around sunset and sunrise and the signal divergence during the night it is hypothesized that one of the sensors, *GLO*, might react more sensitive to changes in meteorological conditions. To test this hypothesis a joint analysis of nighttime radiation measurements at ARAD site Graz/University and co-located meteorological observations (TAWES site Graz/University, located in the weather garden (wg) at Universitätsplatz and the rooftop of Heinrichstraße 28) has been performed. In the following, examples for the influence of meteorological variables on the ARAD measurements at site Graz/University are discussed in detail.

4.1.1 Consideration of meteorological factors

Case 1

Figure 4.3 shows the time series of radiation components at ARAD site Graz/University (*HIM* and *GLO*) along with time series of selected meteorological factors such as relative humidity RH_{wg} [%], precipitation sensor output PS_{wg} [-], ambient air temperature T_{wg} [°C] recorded at TAWES site Graz/University, located in the weather garden (wg) in front of the university's main building and wind speed V_{Sonic} [$\mathrm{km\,h^{-1}}$] measured, $10\,\mathrm{m}$ above ground, at the rooftop of Heinrichstraße 28 between 2013-06-15 20:00 UTC and 2013-06-16 02:00 UTC. The precipitation sensor output data PS_{wg} is the only binary (0 or 1) data considered and is included in the analysis as it is expected that already a few rain drops could have an influence on an operating pyranometer.

At the beginning of the night *HIM* and *GLO* showed a constant offset of $|\Delta R| = 2$ to $3\,\mathrm{W\,m^{-2}}$. From 20:40 to 21:00 UTC the precipitation sensor PS_{wg} registered two short rain events. Shortly after these precipitation events *HIM* declined while *GLO* remained at a constant level of $-2\,\mathrm{W\,m^{-2}}$. During the same night at 22:29 UTC a major precipitation event started (marked with the dark grey solid line in Figure 4.3). Right with the onset of this precipitation event *HIM* began to fall by $3\,\mathrm{W\,m^{-2}}$ while *GLO* declined by only $1\,\mathrm{W\,m^{-2}}$. Simultaneously with the onset of the precipitation event relative humidity rose by about 20% (see Figure 4.3b) and the precipitation sensor responded (see Figure 4.3c). Wind speed variation was marginal between 22:00 UTC and 23:00 UTC (see Figure 4.3d) and the *Zero Offset B* (a response in $\mathrm{W\,m^{-2}}$ following a 5 $\mathrm{K\,hr^{-1}}$ change in ambient temperature) was most likely not the reason for declining R because ambient air temperature T_{wg} changed only about $2\,°\mathrm{C}$ (see Figure 4.3e) in the same time period. Interestingly *HIM* recovered during the duration of the precipitation event, reaching shortly after midnight a value of $0\,\mathrm{W\,m^{-2}}$, leading to the hypothesis that the decline was triggered by the initial impulse of the rain event rather than its duration or effect on ambient meteorological conditions i.e., RH_{wg} and/or T_{wg}. *GLO* recovered too, faster than *HIM*, reaching its initial value of $-2\,\mathrm{W\,m^{-2}}$ already 15 minutes after the onset of the precipitation event.

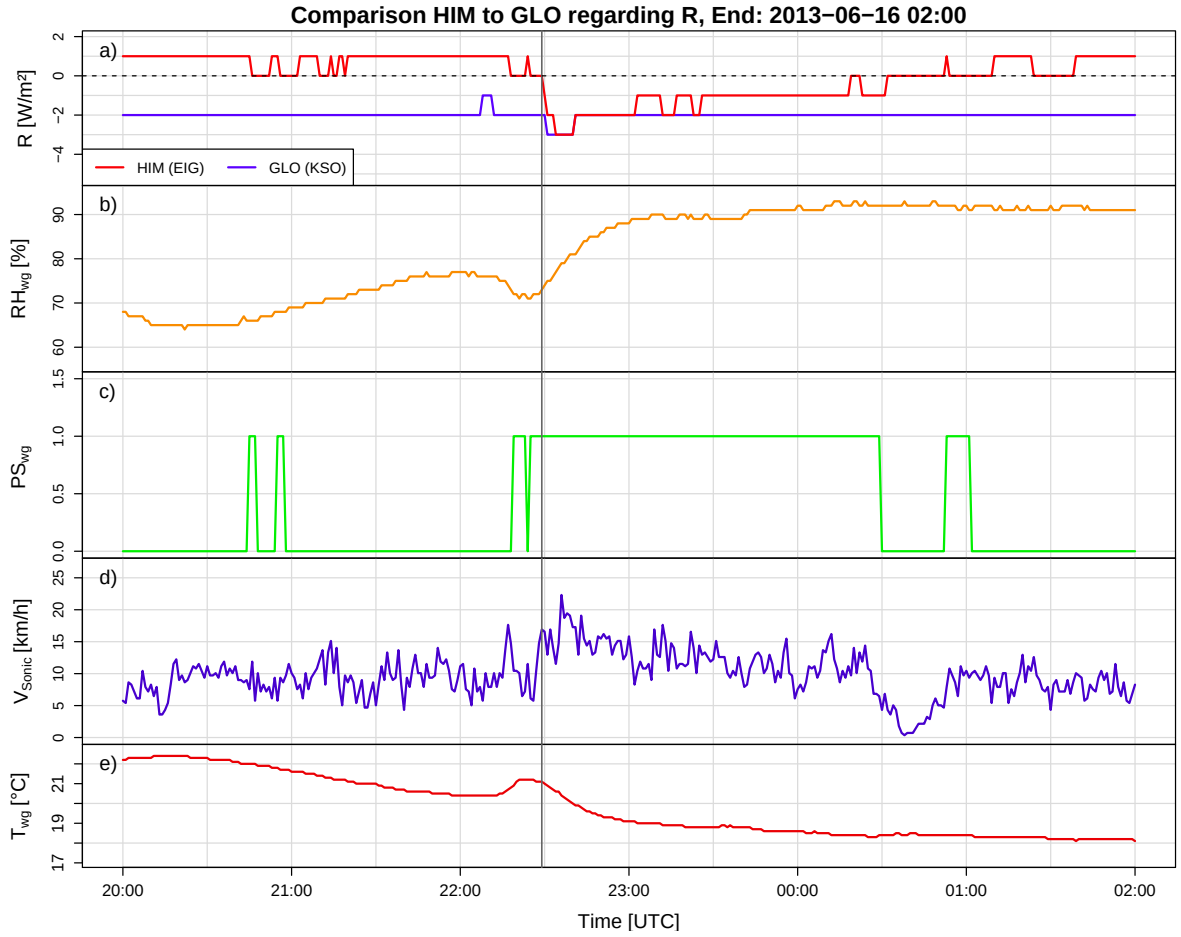

Figure 4.3: Measurements of radiation components at ARAD site Graz/University and meteorological variables (co-located) between 2013-06-15 20:00 UTC and 2013-06-16 02:00 UTC. (a) Radiation R [W m^{-2}] measured at ARAD site Graz/University with sensors for diffuse (*HIM*: CMP 21, Eigenbrodt housing, red curve) and global radiation (*GLO*: CMP 21, KSO housing, blue curve). (b)-(e) measurements of meteorological variables at co-located TAWES site Graz/University: (b) relative humidity RH_{wg} [%], (c) precipitation sensor PS_{wg} [-], (d) wind speed V_{Sonic} [km h^{-1}], (e) ambient air temperature T_{wg} [°C]. Superscripts near meteorological variables in (b)-(e) indicate location of TAWES sensors (wg: weather garden, Sonic: rooftop, 10 m above ground). Note: Precipitation data is binary (0 or 1) as output of a precipitation sensor is considered instead of absolute amounts. The black dashed horizontal line in (a) marks 0 W m^{-2}. The dark gray solid line throughout the graph marks 22:29 UTC when *HIM* begins to fall.

Case 2

Figure 4.4 shows a segment of the time series illustrated in Figure 4.2 above but now extended for simultaneously measured meteorological variables. Between 2013-08-04 18:45 UTC and 2013-08-05 19:15 UTC *HIM* and *GLO* had a nearly constant difference of $1\,\mathrm{W\,m^{-2}}$. During the same time period the relative humidity RH_{wg} (see panel b) increased, while the wind speed V_{Sonic} (see panel d) remained roughly constant and the ambient air temperature T_{wg} declined about $7\,^{\circ}\mathrm{C}$. Curiously both radiation sensors held their initial output signal despite these varying meteorological conditions.

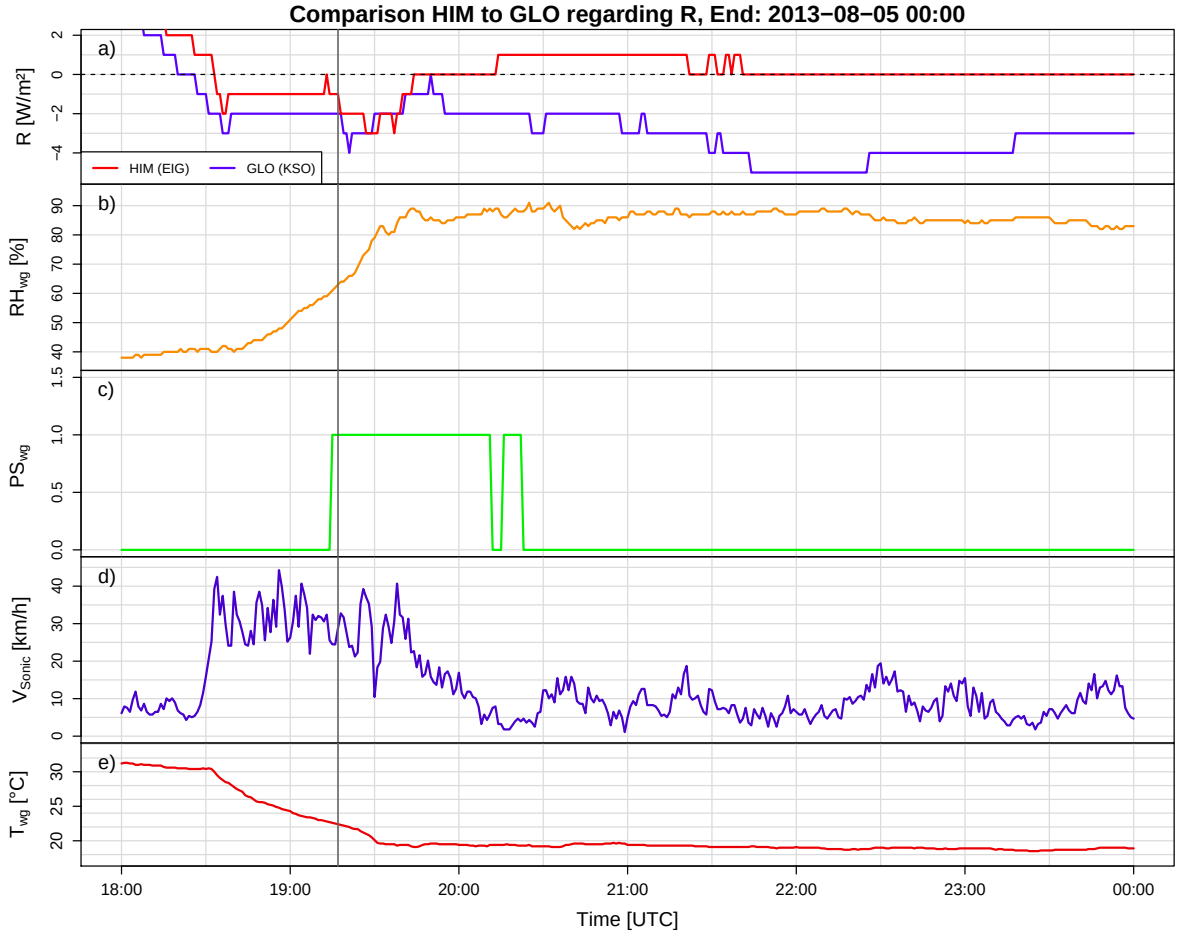

Figure 4.4: As Figure 4.3 but for measurements between 2013-08-04 18:00 UTC and 2013-08-05 00:00 UTC. The dark gray solid line throughout the graph marks 19:17 UTC when *HIM* and *GLO* begin to fall.

At 19:17 UTC (marked with the dark gray solid line throughout Figure 4.4) the precipitation sensor registered the first rain drops to fall (panel c) and relative humidity increased to approximately 90% over the next 15 minutes. The physical cause for the response of *HIM* and *GLO* could be that the raindrops are colder than the outer glass-dome and quench its temperature. Another hypothesis is that the evaporation of raindrops on the glass-dome, i.e., the required energy of phase transformation, decreases the glass-dome temperature. From theoretical considerations, both effects could create a strong negative signal in R.

Case 3

Figure 4.5 shows radiation and meteorological data between 2013-09-10 19:00 UTC and 2013-09-11 00:00 UTC. During the initial hours of this night *HIM* and *GLO* showed a difference of $|\Delta R| = 2 - 3\,\mathrm{W\,m^{-2}}$. At 20:40 UTC (marked with the dark gray solid line) rain began to fall (see panel c) and wind speed increased about $15\,\mathrm{km\,h^{-1}}$ (see panel d). With the onset of the precipitation event *HIM* started to decline (by $4\,\mathrm{W\,m^{-2}}$) while *GLO* remained pretty constant at the $-2\,\mathrm{W\,m^{-2}}$ level (see panel a). In contrast to case 2, where *HIM* needed more than 6 hours to recover, the recovery to the $0\,\mathrm{W\,m^{-2}}$ line lasted only 1.5 hours. Ambient air temperature declined by about $4\,^{\circ}\mathrm{C}$ (see panel e) between 20:40 UTC to 21:40 UTC, however *HIM* had already recovered by the time T_{wg} reached $13\,^{\circ}\mathrm{C}$, thus a *Zero Offset B* response is not the dominating factor.

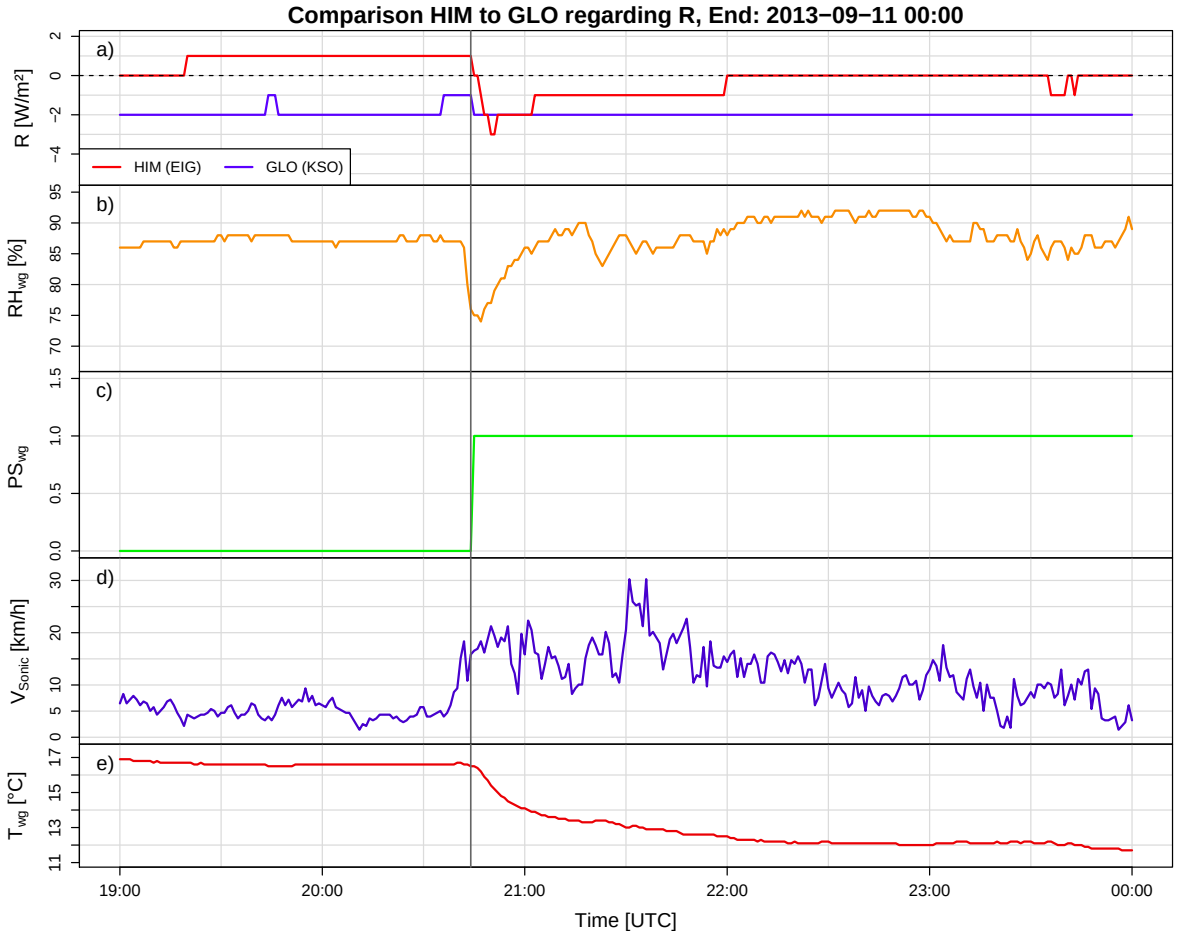

Figure 4.5: As Figure 4.3 but for measurements between 2013-09-10 19:00 UTC and 2013-09-11 00:00 UTC. The dark gray solid line throughout the graph marks 20:40 UTC when *HIM* begins to fall.

Case 4

Figure 4.6 shows radiation and meteorological data between 2013-11-11 00:00 UTC and 06:00 UTC. From 00:00 UTC to 03:03 UTC the diffuse and global radiation sensors showed their common nighttime output signals $R = 0\,\mathrm{W\,m^{-2}}$ (*HIM*) and $R \approx -2\,\mathrm{W\,m^{-2}}$ (*GLO*). Between 02:00 UTC and 03:00 UTC the precipitation sensor PS_{wg} recorded some raindrops, though interestingly *HIM* and *GLO* did not respond to these isolated drops. Only after continuous rain set in at 03:03 UTC the output of *HIM* and *GLO* decreased by about 2 to $3\,\mathrm{W\,m^{-2}}$ until 03:30 UTC. Over the next hours it continued to rain and *HIM* and *GLO* showed continuous deviations from the $0\,\mathrm{W\,m^{-2}}$ line. Once the rain ceased *HIM* and *GLO* started to recover to their corresponding initial states.
Taken together the insights gained in the initial investigations (outlined in the four illustrative cases above) led to the hypothesis that precipitation events have a significant impact on the radiation sensor output. Armed with this insight a set of initial experiments was designed that is described in detail below (Subsection 4.1.3).

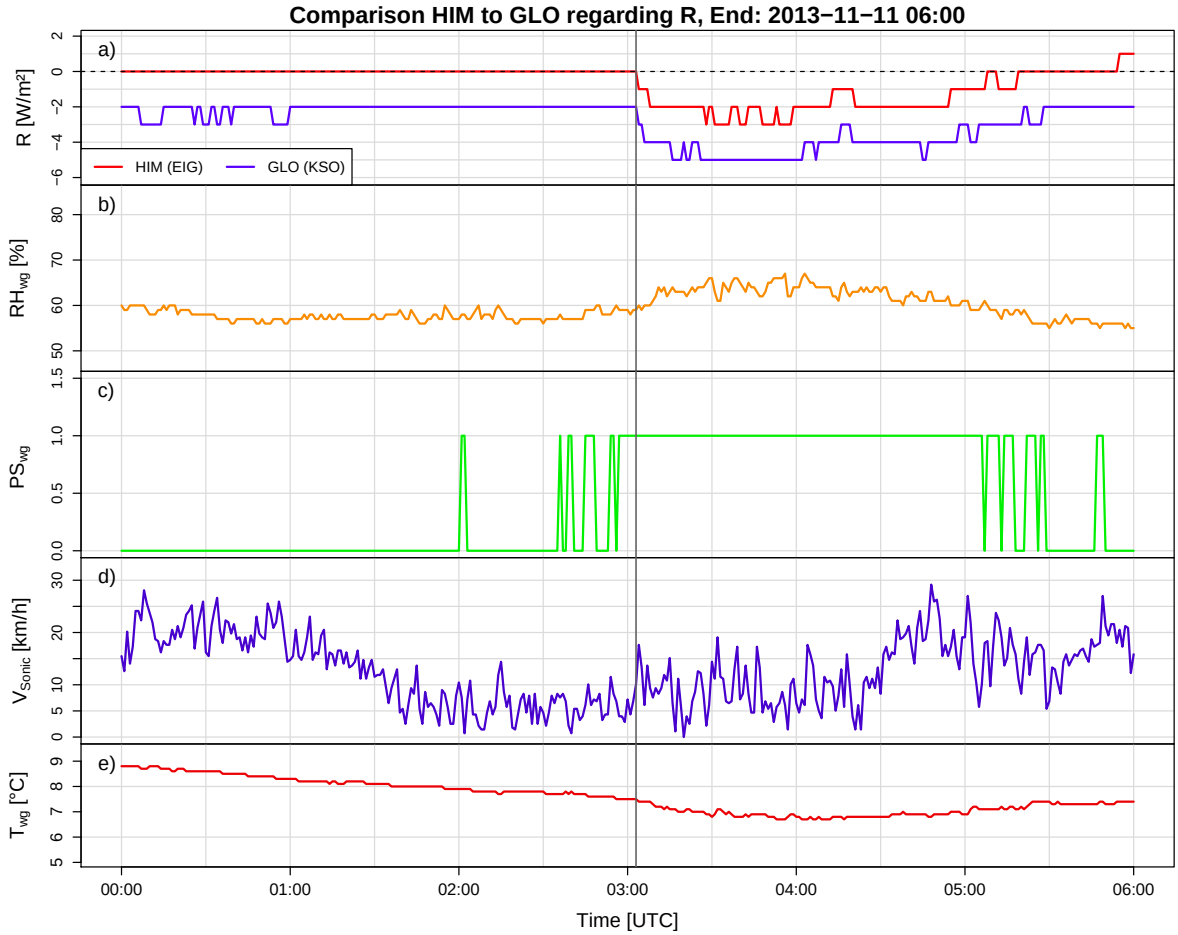

Figure 4.6: As Figure 4.3 but for measurements between 2013-11-11 00:00 UTC and 06:00 UTC. The dark gray solid line throughout the graph marks 03:03 UTC when *HIM* and *GLO* begin to fall.

4.1.2 Statistical investigations

To identify potential causes for the persistent difference $|\Delta R| = 2$ W m^{-2} between *HIM* and *GLO*, a detailed analysis of the instruments body temperatures T_{HIM} and T_{GLO} and ambient air temperature T_{wg} was performed for the period June 2013 to May 2014.

First the average body temperature of the sensor for diffuse radiation $\overline{T}_{\mathrm{HIM}}$ was considered. Figure 4.7(a) shows a box-whisker plot for $\overline{T}_{\mathrm{HIM}}$ on monthly basis for the time period June-December 2013. As expected all metrics (medians, quantiles and whiskers) follow the usual seasonal variation. A similar seasonal pattern (as for $\overline{T}_{\mathrm{HIM}}$) is found for the body temperature of *GLO* $\overline{T}_{\mathrm{GLO}}$ (see Figure 4.7(b)).

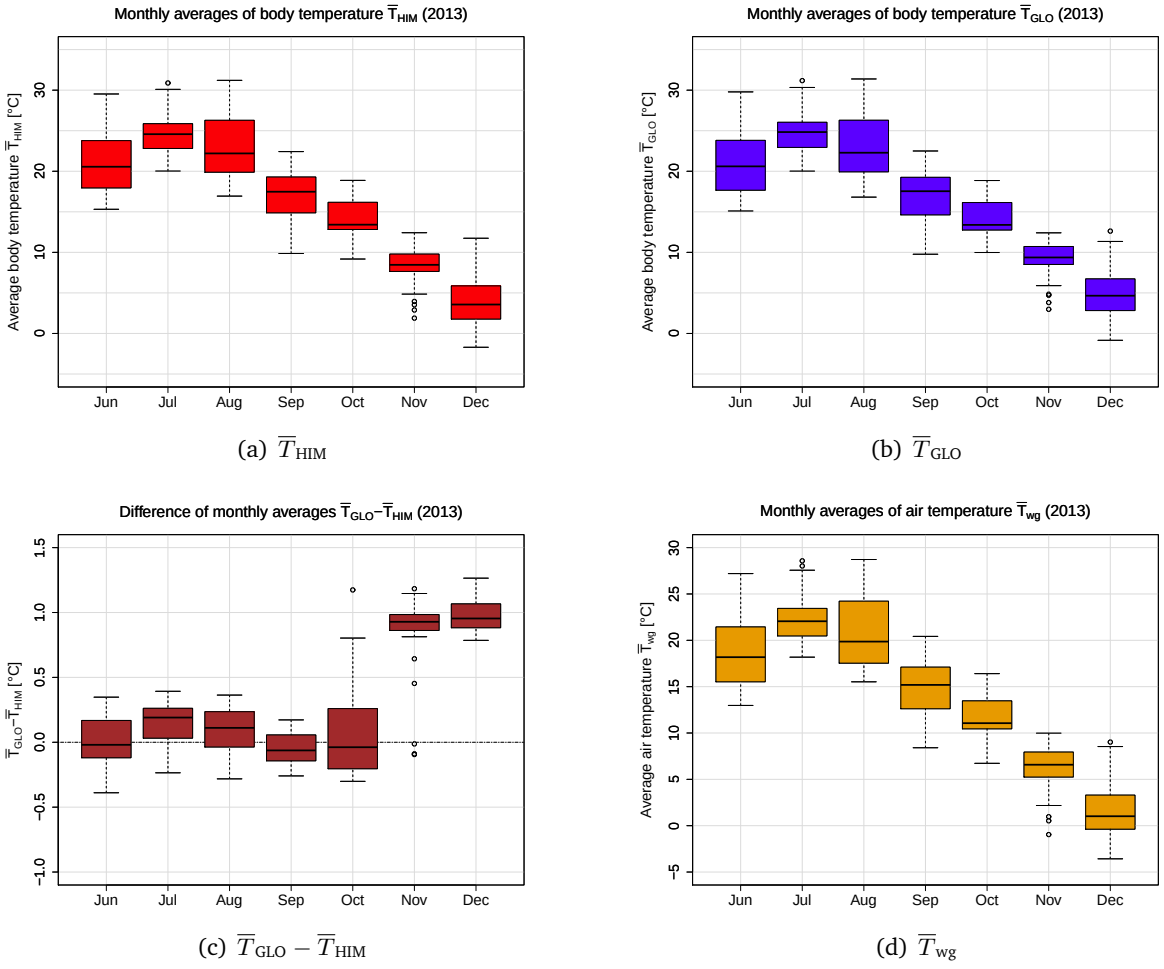

(a) $\overline{T}_{\mathrm{HIM}}$ (b) $\overline{T}_{\mathrm{GLO}}$

(c) $\overline{T}_{\mathrm{GLO}} - \overline{T}_{\mathrm{HIM}}$ (d) $\overline{T}_{\mathrm{wg}}$

Figure 4.7: Monthly Box-Whisker plots of (a) average body temperature $\overline{T}_{\mathrm{HIM}}$ [°C] of the pyranometer measuring diffuse radiation (*HIM*, CMP 21, Eigenbrodt housing), (b) average body temperature $\overline{T}_{\mathrm{GLO}}$ [°C] of the pyranometer measuring global radiation (*GLO*, CMP 21, KSO housing), (c) difference $\overline{T}_{\mathrm{GLO}} - \overline{T}_{\mathrm{HIM}}$ [°C] between the body temperatures of the pyranometers at ARAD site Graz/University and (d) average ambient air temperature $\overline{T}_{\mathrm{wg}}$ [°C] at TAWES site Graz/University for June to December 2013.

Although both amplitude and seasonality of $\overline{T}_{\mathrm{GLO}}$ and $\overline{T}_{\mathrm{HIM}}$ look similar on first sight, their difference $\overline{T}_{\mathrm{GLO}} - \overline{T}_{\mathrm{HIM}}$ (Figure 4.7(c)) shows a remarkable jump from October onwards (particularly in November and December). Median differences of body temperature in June-September range

between -0.06 and $0.19\,°$C; upper and lower quartiles of the difference in this period have been in the range of $-0.39\,°$C to $0.39\,°$C. With the beginning of the cold season of the year this pattern changes dramatically, i.e., the median difference of the body temperatures increases to $1\,°$C and the inner quartile range narrows to $0.9\,°$C to $1.2\,°$C.

One explanation for the jump in body temperature differences could be related to the heating system of the KSO housing, i.e., the change of the heating level in transition periods. The heating system of the KSO housing and the characteristics of the two heating levels HL_1 and HL_2 are detailed in section 3.2.11 above. Figure 4.7(d) displays the average ambient air temperature $\overline{T}_{\text{wg}}$ in a box-whisker plot. Detailed statistical analysis showed that median values of monthly $\overline{T}_{\text{wg}}$ are a little smaller than those of $\overline{T}_{\text{HIM}}$ and $\overline{T}_{\text{GLO}}$ while quantile ranges are of similar magnitude. The most important feature visualized in Figure 4.7(d) is that ambient air temperature in November and December is frequently (for more than 75% of measured values) below $8\,°$C, i.e., allowing the thermal cut-out to switch to the upper heating level. Although amperages are recorded, the structure of the TAWES data acquisition system does not allow to continuously monitor these heating levels at needed resolution/accuracy.

An indirect way to understand the jumps shown in Figure 4.7(c) could be quality flags provided for data in the ARAD framework. Figure 4.8 shows the cumulative sum of *FL* type 2 (measured and incorrect) from June to December 2013. During the first couple months, i.e. June-October, *HIM* and *GLO* showed similarly evolving cumulative *FL* 2 curves (except two cases in early August, see Figure 4.4, and middle October). Starting in November, the number of observations flagged *FL* 2 increases drastically for *GLO*, reaching by the end of the year a cumulative sum three times larger than those of *HIM*.

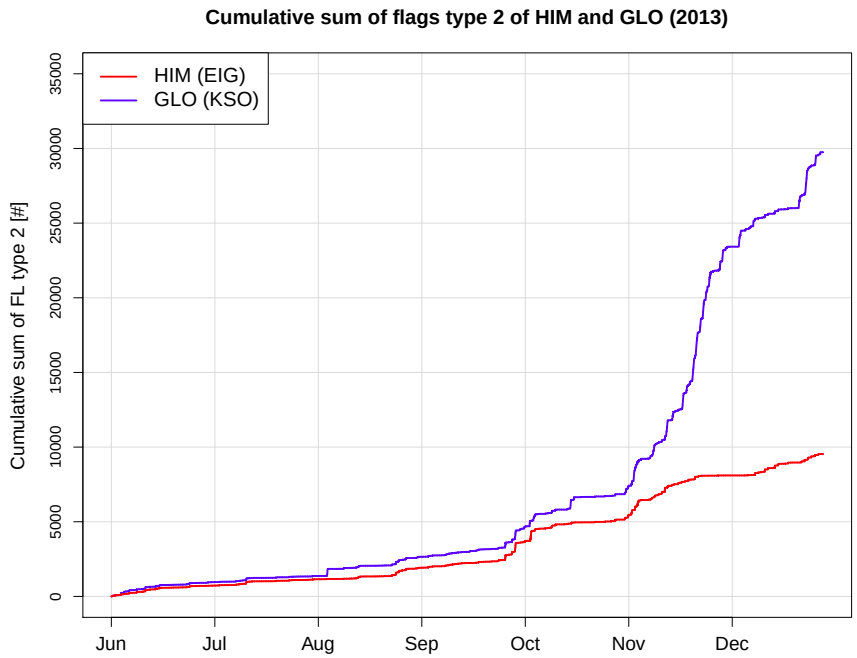

Figure 4.8: Cumulative sum of quality flags of type 2 for measurements of global (*GLO*, CMP 21, KSO housing) and diffuse radiation (*HIM*, CMP 21, Eigenbrodt housing) between June and December 2013.

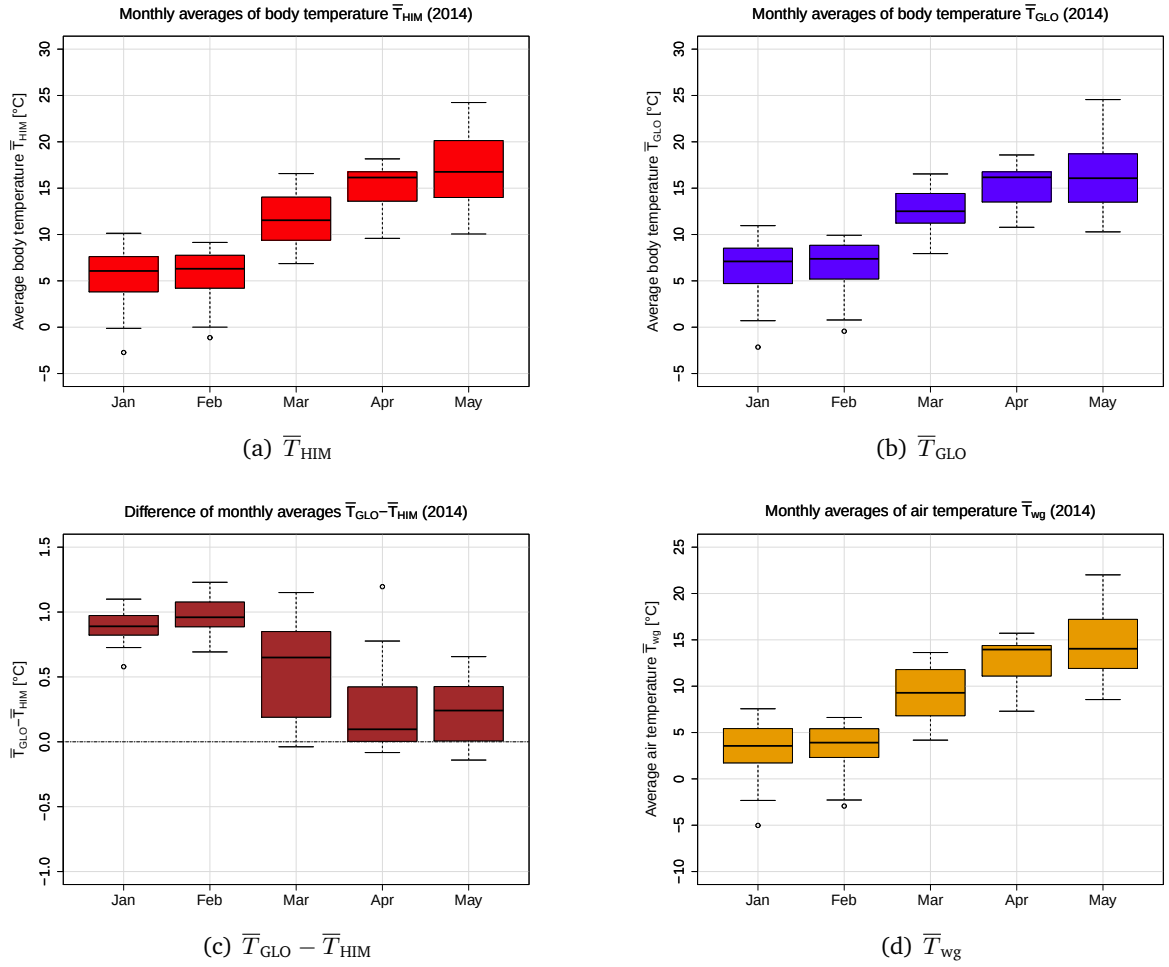

(a) $\overline{T}_{\mathrm{HIM}}$ (b) $\overline{T}_{\mathrm{GLO}}$

(c) $\overline{T}_{\mathrm{GLO}} - \overline{T}_{\mathrm{HIM}}$ (d) $\overline{T}_{\mathrm{wg}}$

Figure 4.9: As Figure 4.7 but for measurements for January to May 2014.

Motivated by the abrupt change in body temperatures with the onset of the cold season, statistical investigations continued for the winter-spring transition. Figure 4.9 shows box-whisker plots of body temperatures of *HIM* (panel a) and *GLO* (panel b), their difference (panel c) as well as the ambient air temperature (panel d) for January to May 2014. In January and February the median difference in the body temperatures of *HIM* and *GLO* is approximately $0.9\,^{\circ}$C, which decreases with the onset of the warm season, reaching median values well below $0.5\,^{\circ}$C in April and May. The large difference between $\overline{T}_{\mathrm{HIM}}$ and $\overline{T}_{\mathrm{GLO}}$ in January and February can be explained by ambient air temperatures, with monthly averages well below $8\,^{\circ}$C, effecting the heating level of *GLO*.

In March 2014 the Box-Whisker of $\overline{T}_{\mathrm{GLO}} - \overline{T}_{\mathrm{HIM}}$ has a huge span width from $0\,^{\circ}$C to $1\,^{\circ}$C, accordingly the averaged ambient air temperature $\overline{T}_{\mathrm{wg}}$ had nearly 50% of measurements under $8\,^{\circ}$C and the cumulative sum of *FL* 2 increased further on. Just in middle April 2014 the blue curve in Figure 4.10 began to mitigate and flatten out.

In conclusion during the colder months of the year, the KSO heating level is regularly at HL_2 thereby raising the body temperature of the global radiation sensor T_{GLO}. Thus heating currents occurring inside the CMP 21 (could) influence the solar radiation measurements.

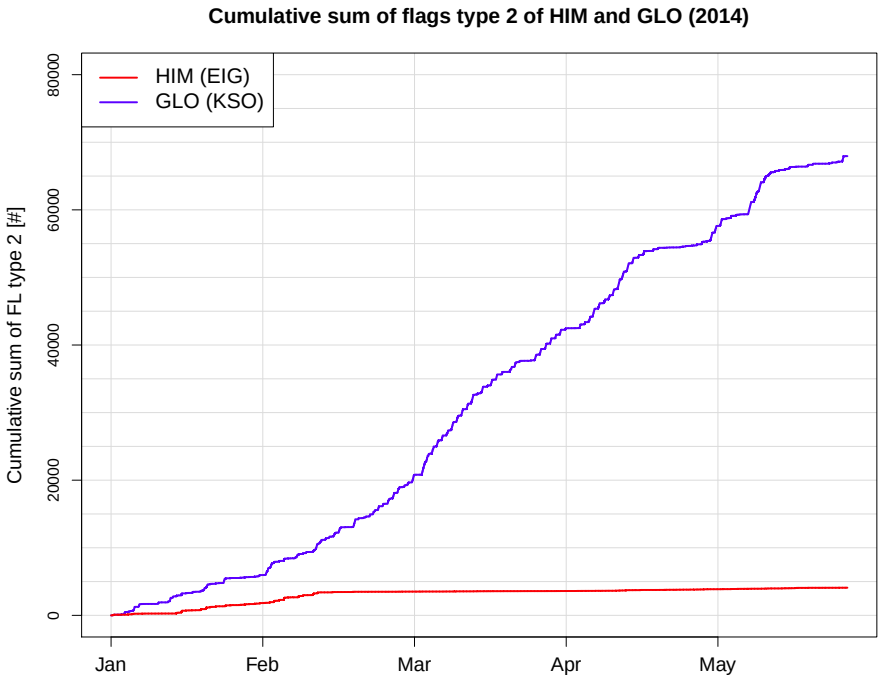

Figure 4.10: As Figure 4.8 but for January to May 2014.

4.1.3 Initial experiments

Motivated by the findings above a series of experiments with *HIM* and *GLO* were conducted. These experiments included: (1) spray-tests, (2) adjustments of the heating level and (3) coverage of pyranometer glass-domes.

To investigate the influence of individual rain drops and precipitation events rain was simulated by spraying distilled water on the glass-domes of the pyranometers during nighttime. The spray bottle used in these experiments was filled with distilled water and kept at approximately ambient temperature. Water was sprayed on glass-domes from short distances ($2 - 4\,\mathrm{cm}$) from above. Besides spray-test experiments with short term dome coverage (to simulate abrupt changes in wind speed) and changes in heating level (to simulate abrupt changes in ambient air temperature) have been performed. Exemplary six experiments ranging from spray-tests with different numbers of strokes and coverage-tests to adjustments in heating level are detailed below.

Experiment 1: Spray-test with 30 strokes

The first experiment discussed was a spray-test with 30 strokes. Figure 4.11 shows the time series of measurements of *HIM* and *GLO* between 2014-10-09 16:00 UTC and 21:00 UTC (left-hand axis); note the absolute difference between the measurements $|\Delta R|$ is shown on the right-hand axis. At dusk the difference between *GLO* and *HIM* was on the common value of $|\Delta R| = 1 - 2\,\mathrm{W\,m^{-2}}$. At 17:55 UTC the spray-test with 30 strokes, marked with the magenta dashed vertical line, was performed and both sensors declined simultaneously by $4\,\mathrm{W\,m^{-2}}$. After a few minutes *HIM* and *GLO* recovered to their initial state.

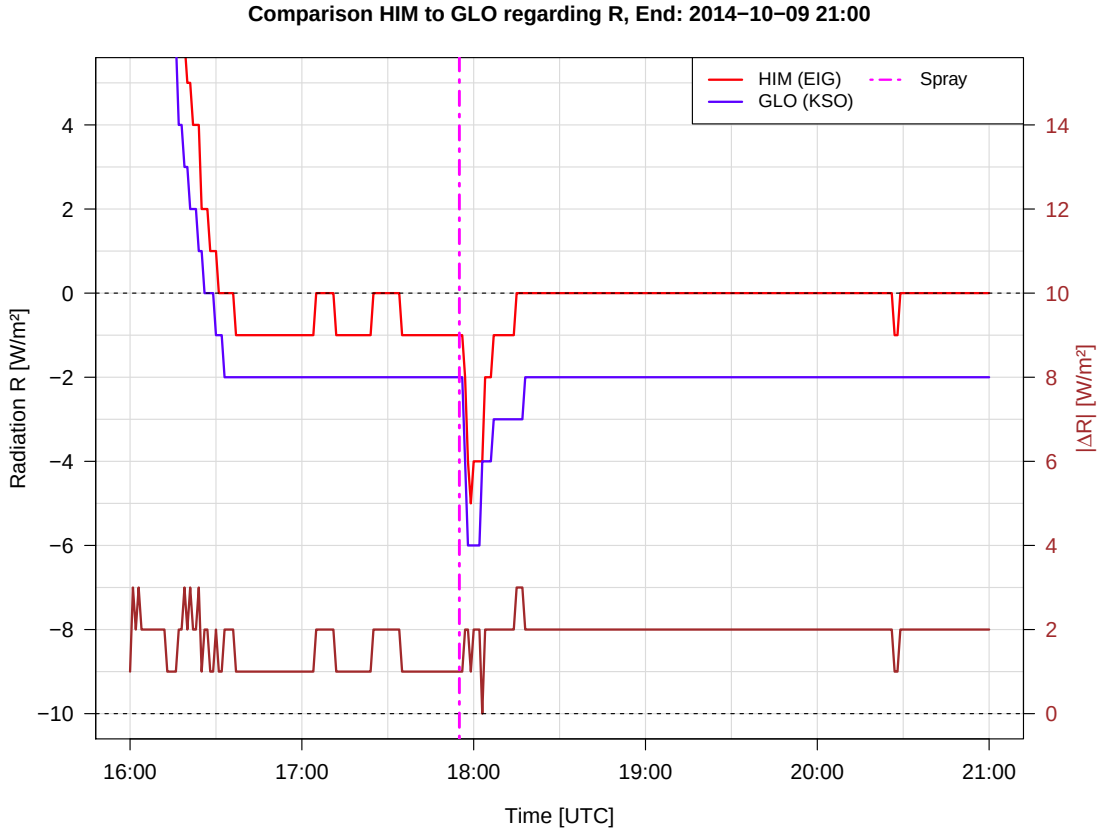

Figure 4.11: As Figure 4.1 but for measurements between 2014-10-09 16:00 UTC and 21:00 UTC. The magenta dashed vertical line marks a spray-test with 30 strokes at 17:55 UTC.

Experiment 2: Spray-test with 10 strokes

Four days later, on October 13, a second experiment, similar to the first but with less strokes, was performed (see Figure 4.12). The spray-test included ten strokes and was performed on 2014-10-13 17:57 UTC. Shortly after the spraying *HIM* and *GLO* output changed: *HIM* declined from $0\,\mathrm{W\,m^{-2}}$ to $-4\,\mathrm{W\,m^{-2}}$ and *GLO* fell about $2\,\mathrm{W\,m^{-2}}$. Two possible reasons for the different response were considered: (1) differences in the actual amount of distilled water sprayed on the domes or (2) differences in the instrument housings. Both sensors recovered within half an hour but *HIM* needed about twice the time of *GLO* to return to its initial state of $R = 0\ \mathrm{W\ m^{-2}}$.

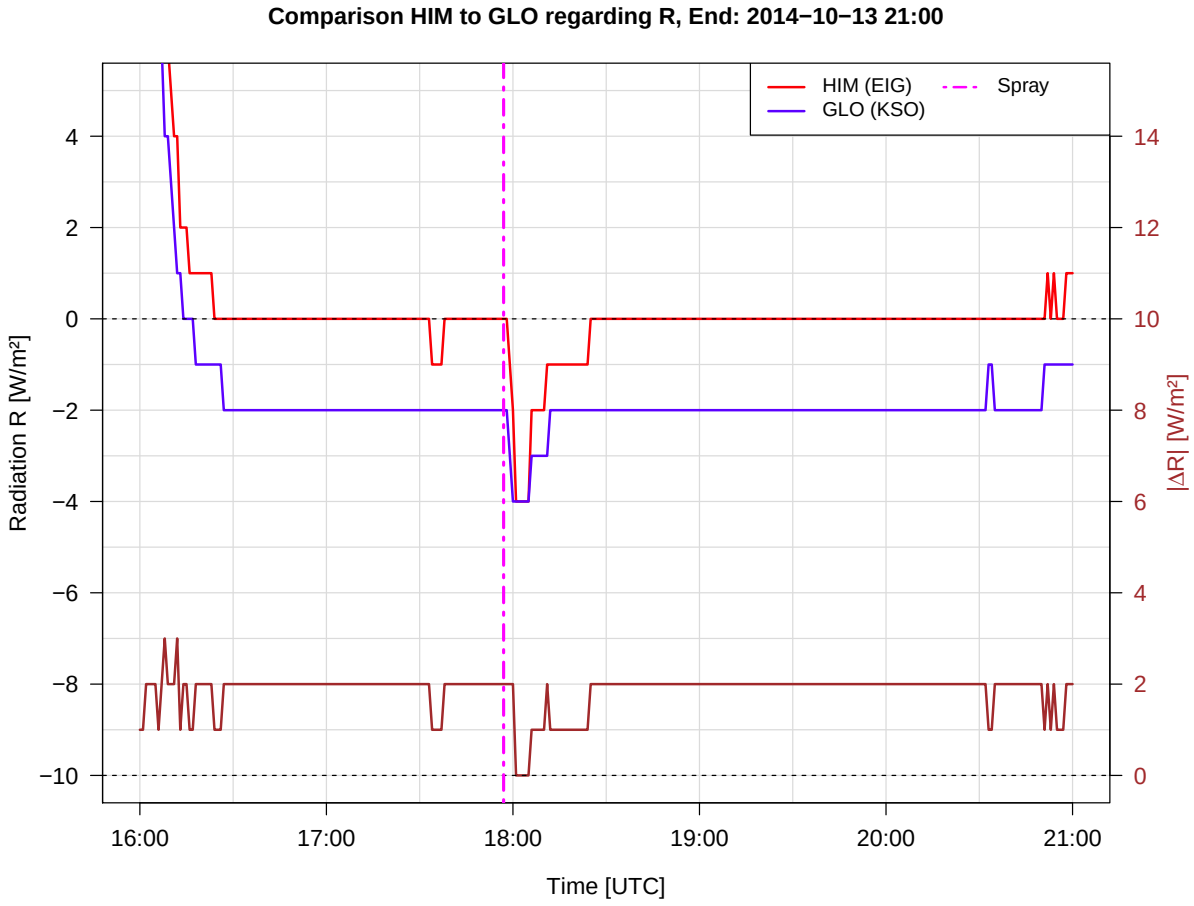

Figure 4.12: As Figure 4.1 but for measurements between 2014-10-13 16:00 UTC and 21:00 UTC. The magenta dashed vertical line marks a spray-test with 10 strokes at 17:57 UTC.

Experiment 3: Spray-test with one stroke

The two spray-tests described above showed similar responses despite significant differences in the amount of water impacting the instruments/housings. Therefore experiment three was designed to test for a possible lower bound in precipitation influence. To test for such a lower bound a spray-test involving a single stroke, indicated in Figure 4.13 by the magenta dashed vertical line marking October 14 2014 at 17:57 UTC, was performed. While *GLO* showed no response to this single spray stroke, *HIM* declined by $1\,\mathrm{W\,m^{-2}}$. However, as visible in Figure 4.13 *HIM* varied before the spray-test, so it is not entirely clear if the $1\,\mathrm{W\,m^{-2}}$ change was a physical response to the spraying or rather instrumentation noise. It is noted that a $1\,\mathrm{W\,m^{-2}}$ response of the radiation sensors at ARAD site Graz/University could also result from rounding effects, because the data acquisition system allows no decimal digits.

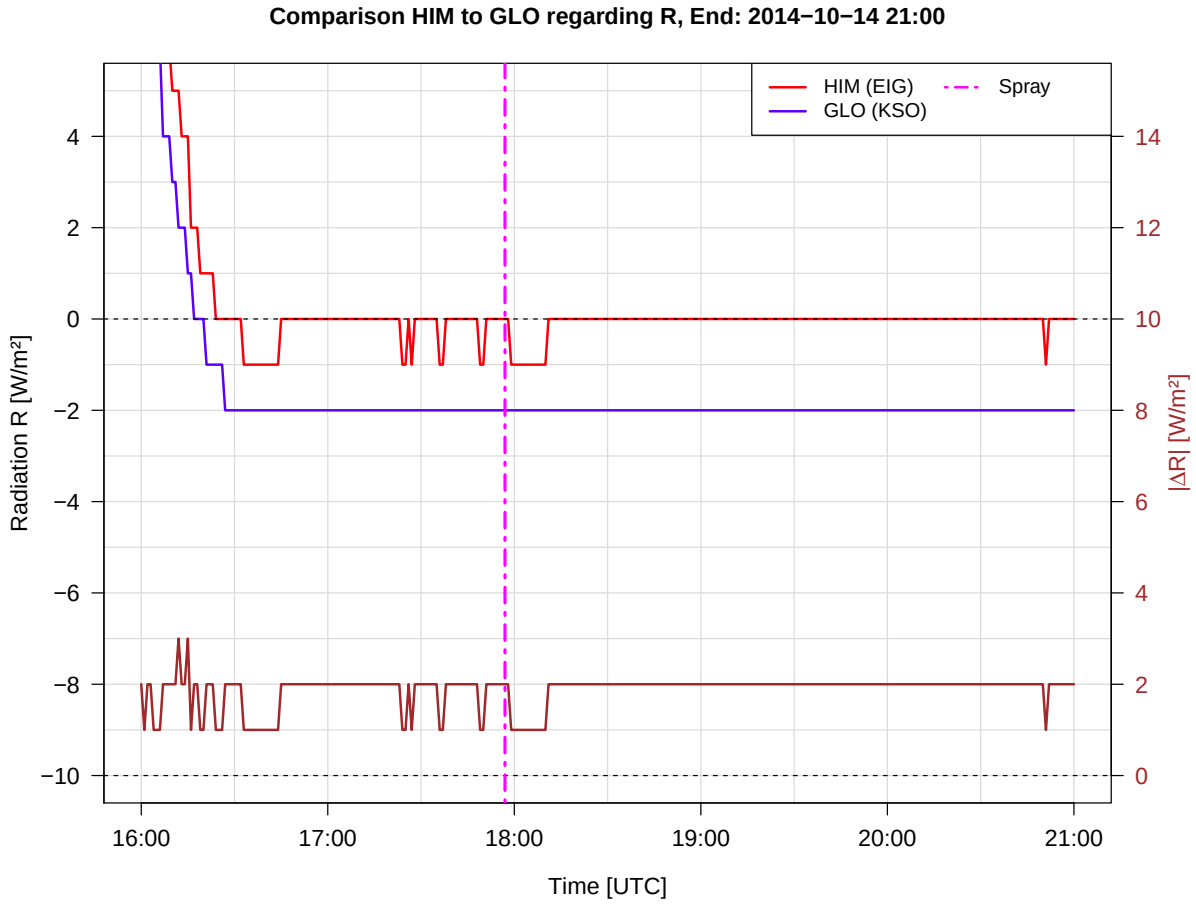

Figure 4.13: As Figure 4.1 but for measurements between 2014-10-14 16:00 UTC and 21:00 UTC. The magenta dashed vertical line marks a spray-test with one stroke at 17:57 UTC.

Experiment 4: Spray-test with five strokes

The fourth spray-test, consisting of five individual strokes, was performed on October 15 2014 at 17:56 UTC. As shown in Figure 4.14 both *HIM* and *GLO* fell simultaneously by $1\,\mathrm{W\,m^{-2}}$. About an hour after the spray-test the radiation sensors co-evolved with at steady offset of $|\Delta R|$ of $2\,\mathrm{W\,m^{-2}}$.

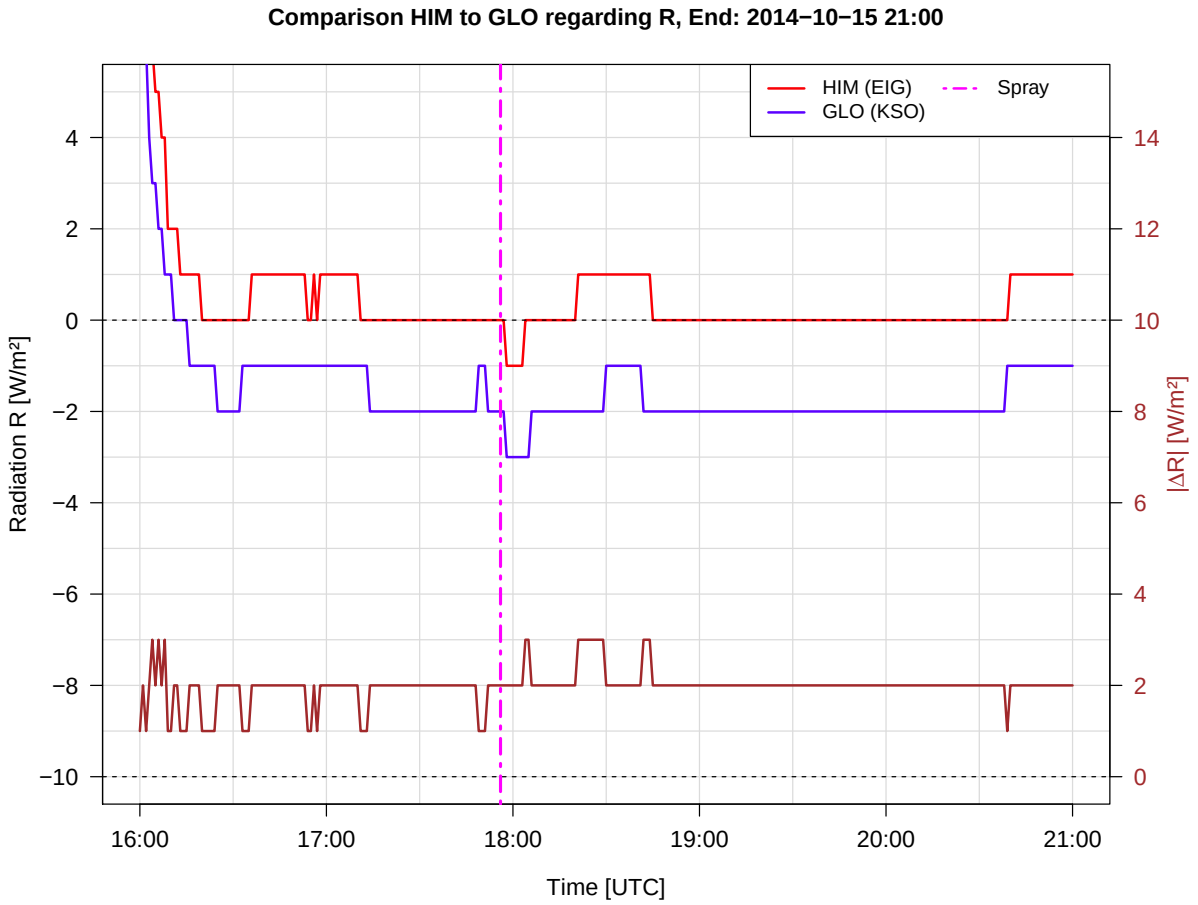

Figure 4.14: As Figure 4.1 but for measurements between 2014-10-15 16:00 UTC and 21:00 UTC. The magenta dashed vertical line marks a spray-test with five strokes at 17:56 UTC.

Experiment 5: Spray-test with 30 strokes followed by a cover-test

The fifth experiment consisted of a spray-test (with 30 strokes) followed by immediate dome coverage (using self-constructed aluminium caps). This test was performed simultaneously for *HIM* and *GLO*. Figure 4.15 shows the time series of diffuse and global radiation sensor output during this experiment on 2014-11-12 16:00 UTC and 21:00 UTC. The spray-test marked with the magenta dashed vertical line started at 17:50 UTC. Immediately after spraying the aluminium cap was fit on each pyranometer for 4 minutes. One can see that *HIM* and *GLO* declined by $2\,\mathrm{W\,m^{-2}}$ during the covering period, compared to experiment one (30 strokes uncovered, see above) where radiation sensors fell by $6\,\mathrm{W\,m^{-2}}$. Despite the smaller net response the instruments took longer to recover than in previous attempts, indicating effects of the coverage on the thermal balance of the glass-domes.

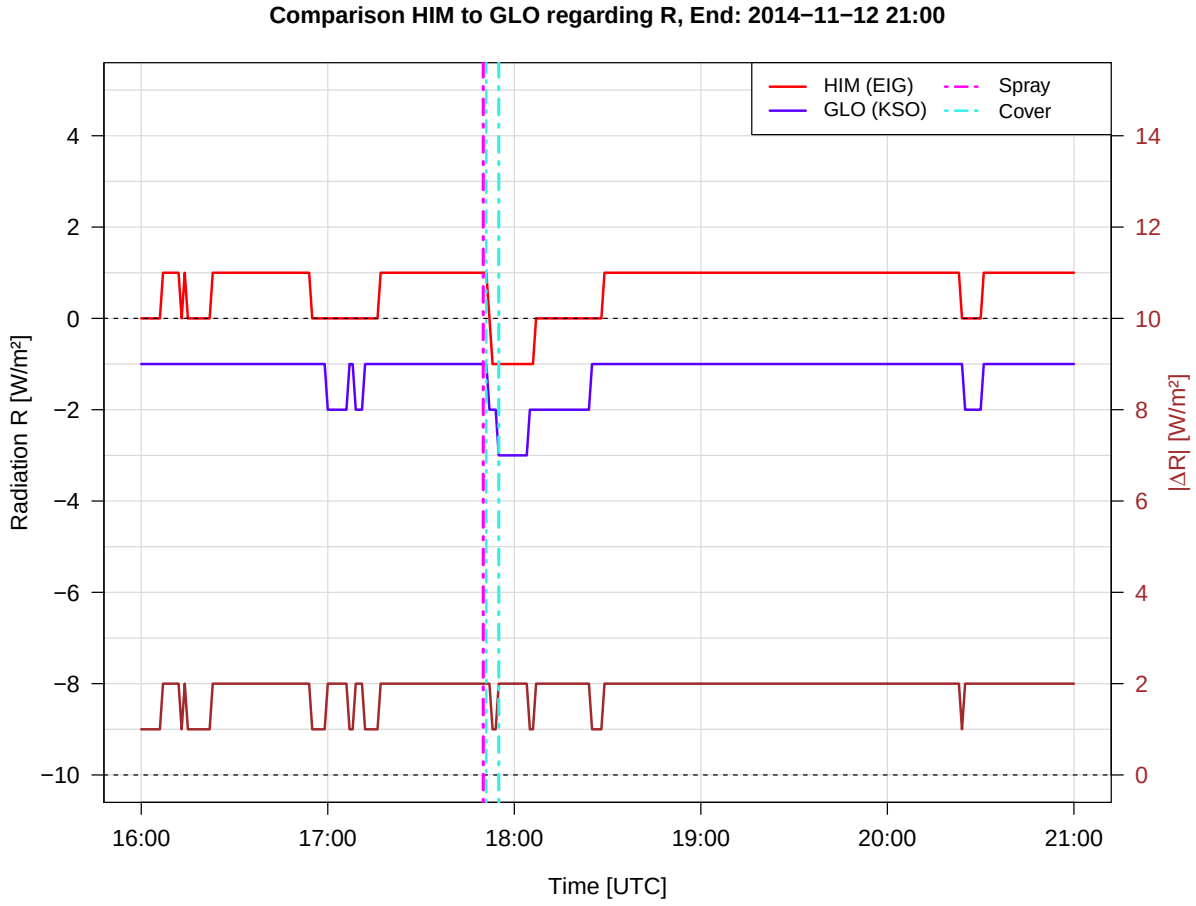

Figure 4.15: As Figure 4.1 but for measurements between 2014-11-12 16:00 UTC and 21:00 UTC. The magenta dashed vertical line marks a spray-test with 30 strokes at 17:50 UTC, the two cyan dashed vertical lines mark a cover-test between 17:51 UTC and 17:55 UTC.

From the five experiments described above it is concluded that any kind of water impact, ranging from individual rain drops to full rain, influences/disturbs the radiative flux measurements at ARAD site Graz/University. Every spray-experiment triggered a decline in the sensor signal though no clear correlation between the number of strokes performed and the change in sensor output could be established due to the combination of a limited number of experiments and limited sensor

output resolution. Therefore further investigations regarding the impact of precipitation events on radiation measurements have been performed in the course of an extensive measurement campaign, described below.

Experiment 6: Adjustment of heating level

As described in subsection 4.1.2, the body temperature of *GLO* was found to be $1\,^{\circ}$C higher than those of *HIM* during the cold season. This difference in body temperature was attributed to changes in the heating level, i.e., frequent occurrence of HL_2, of the KSO housing used for *GLO*. To investigate the role of the heating level on sensor output in the cold season, the heating level was fixed at HL_1 for a two day period in December 2014.

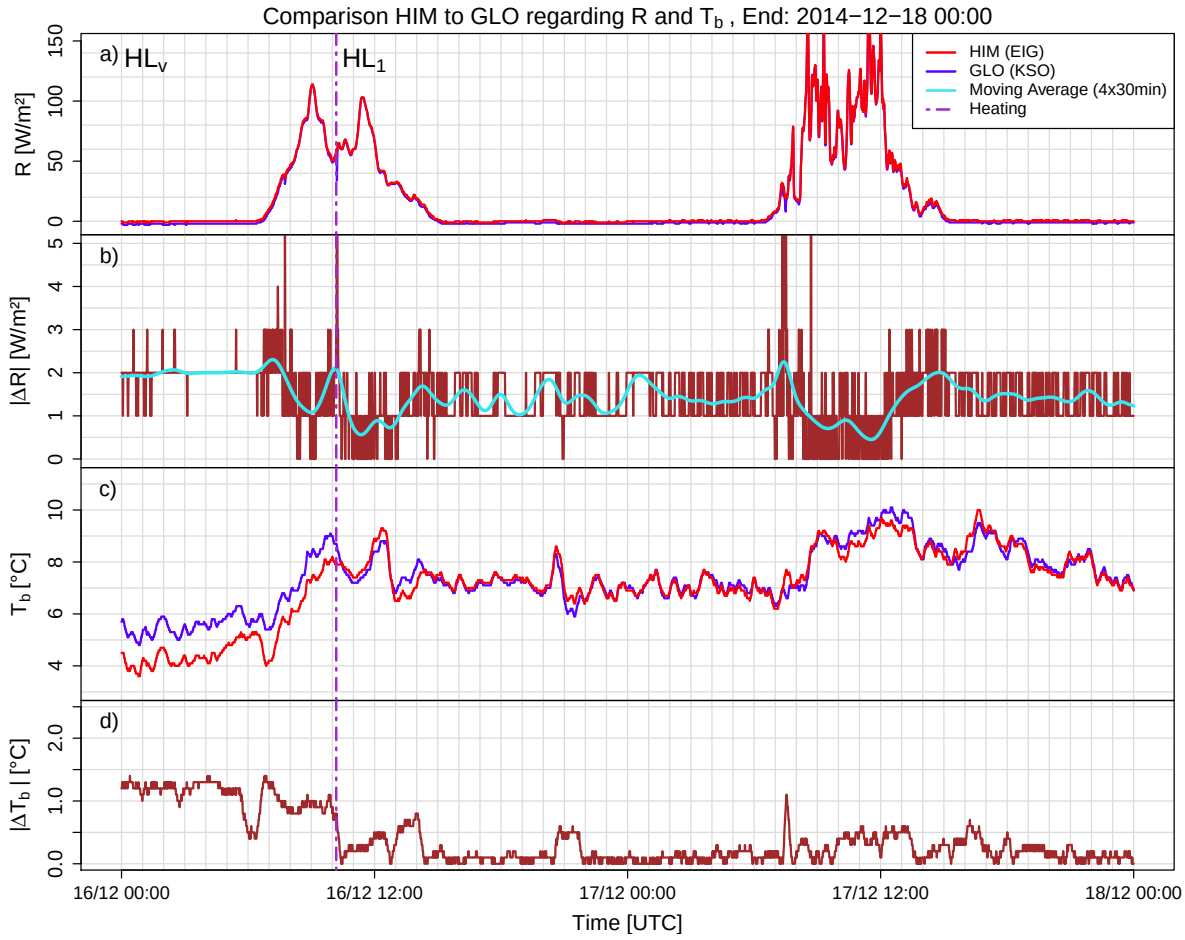

Figure 4.16: Measurements of radiation components and corresponding instrument body temperatures at ARAD site Graz/University between 2014-12-16 00:00 UTC and 2014-12-18 00:00 UTC. (a) Radiation R [W m^{-2}] measured at ARAD site Graz/University with sensors for diffuse (*HIM*: CMP 21, Eigenbrodt housing, red curve) and global radiation (*GLO*: CMP 21, KSO housing, blue curve). (b) Absolute difference between measurements of *HIM* and *GLO* $|\Delta R|$ [W m^{-2}] in 1-minute time resolution (brown curve) and as 4x30 minute symmetrically moving average filter (turquoise curve). (c) Body temperature T_b [°C] of *HIM* (red curve) and *GLO* (blue curve). (d) Absolute difference between body temperatures of *HIM* and *GLO* $|\Delta T_\mathrm{b}|$ [°C]. The purple dashed vertical line throughout the graph indicates a change in heating level from HL_v to HL_1 on 2014-12-16 10:13 UTC.

Figure 4.16 shows radiation output (panels a, b) and body temperatures (panels c, d) of *HIM* and *GLO* between 2014-12-16 00:00 UTC and 2014-12-18 00:00 UTC. Between 2014-12-16 00:00 UTC and 10:13 UTC (marked with purple dashed vertical line) the difference of diffuse and global radiation sensors (panel b) was $|\Delta R| = 2\,\mathrm{W\,m^{-2}}$. As shown in panels c and d, the body temperature of *GLO* was always greater than that of *HIM*; $|\Delta T_\mathrm{b}|$ was about $1\,^\circ$C.

At 2014-12-16 10:13 UTC the thermal cut-out was turned off and the heating level was fixed to HL_1 (marked in panel a). After this adjustment the body temperature of *GLO* dropped to approximately the same level as those of *HIM*, also the constant offset between *HIM* and *GLO* of $2\,\mathrm{W\,m^{-2}}$ almost vanished.

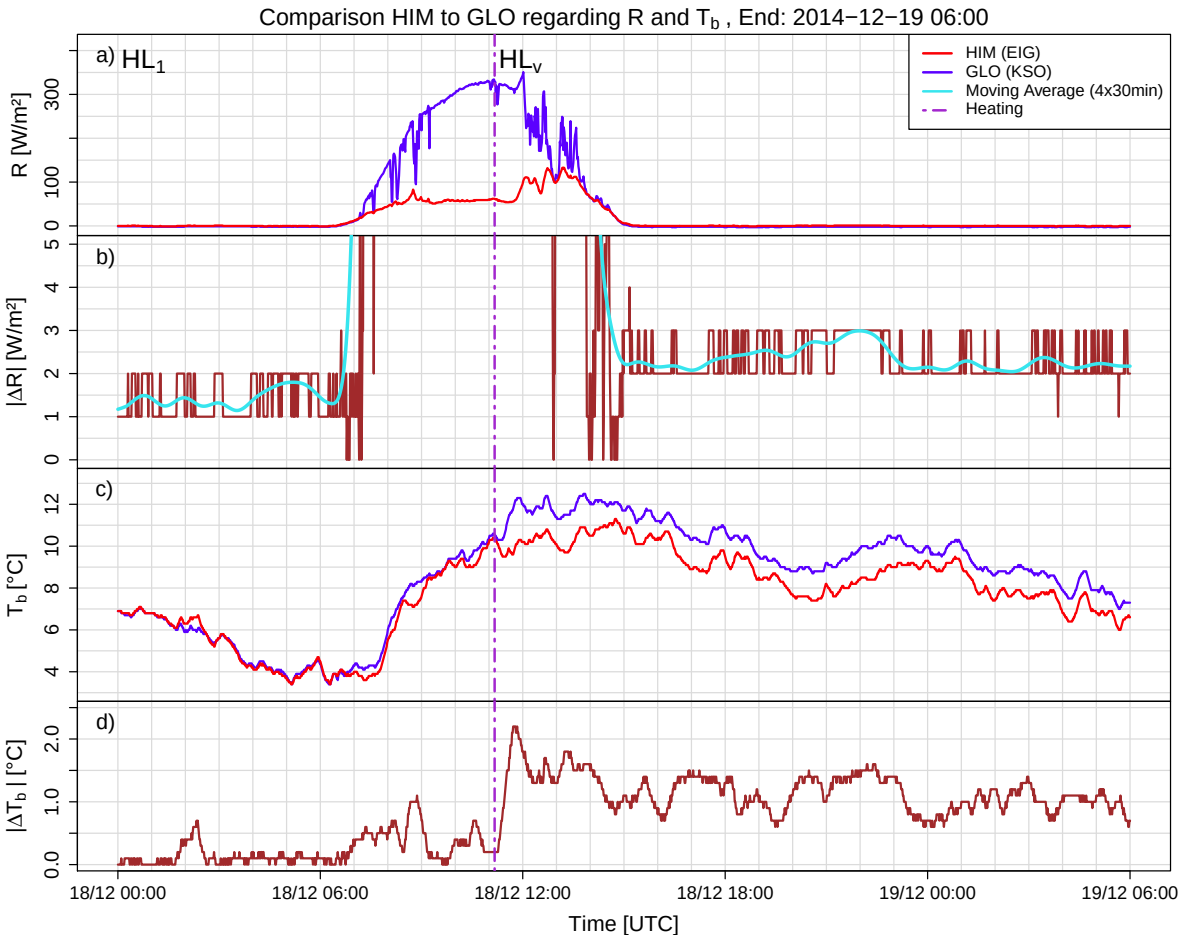

Figure 4.17: As Figure 4.16 but for measurements between 2014-12-18 00:00 UTC and 2014-12-19 06:00 UTC. The purple dashed vertical line throughout the graph indicates a change in heating level from HL_1 to HL_v on 2014-12-18 11:14 UTC.

Figure 4.17 shows the strong increase in body temperature of *GLO* after the thermal cut-out was switched on at 2014-12-18 11:14 UTC (marked with the purple dashed vertical line) leading to a difference $|\Delta T_\mathrm{b}|$ of about $1\,^\circ$C. With time the difference between the output signals $|\Delta R|$ evolved to the ‚common' value of $2\,\mathrm{W\,m^{-2}}$ (2014-12-18 16:00 UTC).

The results of these initial experiments showed that (at least during nighttime conditions):

1. Water, raindrops and maybe snow trigger negative pyranometer output signals with magnitude depending on the amount of water.
2. The heating levels of pyranometer housings (and their stability) influence the radiation measurements.

To further investigate these effects an extensive measurement campaign (see Section 4.2) engaging all housing types used at ARAD site Graz/University, including modifications, has been performed.

4.2 Measurement campaign

In the previous sections the influence of meteorological factors on the radiation measurements, particularly regarding nighttime offsets, at ARAD site Graz/University has been investigated and a first set of hypothesis has been developed. Following this initial investigations an extensive measurement campaign has been performed between 22nd and 29th of January 2015. The aim of this campaign was to 'simulate' meteorological events (e.g., precipitation) outside of a laboratory environment under natural weather conditions.

The campaign was performed during a series of days with steady overcast but precipitation free conditions to allow for a comprehensive set of experiments. Two CMP 21 pyranometers and two Eigenbrodt SBL 480 housings were provided by ZAMG colleagues Dr. Marc Olefs and Dr. Martin Mair for this campaign. Mag. Dietmar Baumgartner of Kanzelhöhe Observatory (University of Graz) provided a self-built KSO housing, a CR300 data logging system (Campbell Scientific, Inc.) and a series of platinum resistance thermometers (hereinafter referred to as PT100 elements) for the campaign. For observations of ambient meteorological conditions an ‚all-in-one' observing system (hereinafter referred to as LUFFT), WS600 UMB by Lufft GmbH, was provided by Prof. Erich Mursch-Radlgruber from the Institute of Meteorology of the University of Natural Resources and Applied Sciences, Vienna (BOKU). A second meteorological observing system (mobile meteorological observing system, hereinafter referred to as MobMet), was provided by the Institute of Geophysics, Astrophysics and Meteorology/Institute of Physics, of the University of Graz (IGAM/IP). Both LUFFT and MobMet measured ambient air temperature, relative humidity, wind speed and wind direction. LUFFT would have been able to observe precipitation (amount and type) as well but fortunately the campaign period remained precipitation free. Table 4.1 provides an overview about the measurement devices and observed meteorological factors during the measurement campaign.

Table 4.1: Overview about measurement devices (and corresponding observed meteorological variables) employed at ARAD site Graz/University in January 2015 [$^{\circledast}$ provided by Marc Olefs and Martin Mair (ZAMG); $^{\circledcirc}$provided by Erich Mursch-Radlgruber (BOKU Vienna); $^{\otimes}$provided by IGAM; $^{\odot}$provided by KSO].

Meteorological factor / **Measurement device**	T_a	RH	V	D	R	PS
LUFFT$^{\circledcirc}$	x	x	x	x		x
MobMet$^{\otimes}$	x	x	x	x		
TAWES	x	x	x	x		x
CMP 21$^{\circledast}$					x	
C3$^{\odot}$	x					

During the campaign the additional pyranometers have been installed on the rooftop of Heinrichstraße 28, aligned in east-west direction approximately four meters north-east of ARAD site Graz/University. During the entire course of the campaign one CMP 21 was employed in an Eigenbrodt SBL 480 housing in standard operational configuration (ventilated, heating level 10 W). This device, hereinafter referred to as *PYRANO A*, served during the campaign as reference device. The second CMP 21, hereinafter referred to as *PYRANO B*, was placed either in an Eigenbrodt SBL 480 or KSO housing during the course of the experiments, thereby allowing to investigate the sensor response to simulated 'meteorological events' under both housing environments.

LUFFT served two purposes during the campaign: (1) to observe ambient meteorological condi-

tions, and (2) to investigate a possible influence of ventilation shafts on the rooftop of Heinrichstraße 28 for ARAD measurements (see Figure 4.18).
A further scope of the campaign was to investigate changes in heat currents and ambient temperatures inside the KSO and Eigenbrodt SBL 480 housings during experiments and relaxation periods. To this aim two PT100 elements were mounted inside the housings fixed on the CMP 21 pyranometer. One PT100 was mounted directly below the outer glass dome, to measure the temperature at the dome base (which is considered equivalent to the temperature inside the glass domes during nighttime and overcast conditions). The second PT100 element was mounted near the bottom of the CMP 21 sensor to characterize the sensors body temperature during experimental and relaxation periods. The location of PT100 elements on the CMP 21 pyranometer is shown in Figures 4.19 and 4.20.

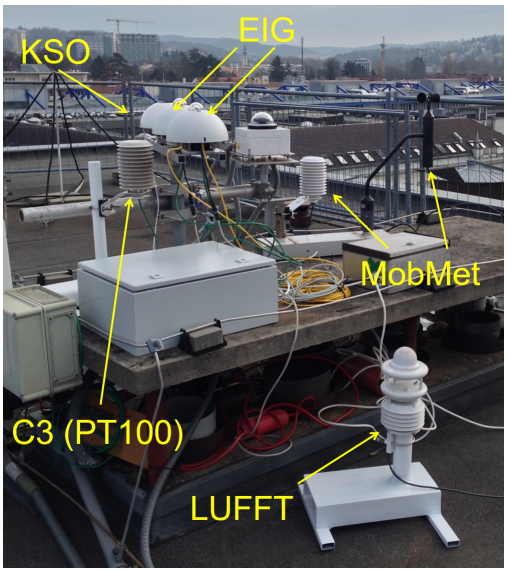

Figure 4.18: Instrumentation used during the measurement campaign at ARAD site Graz/University in January 2015.

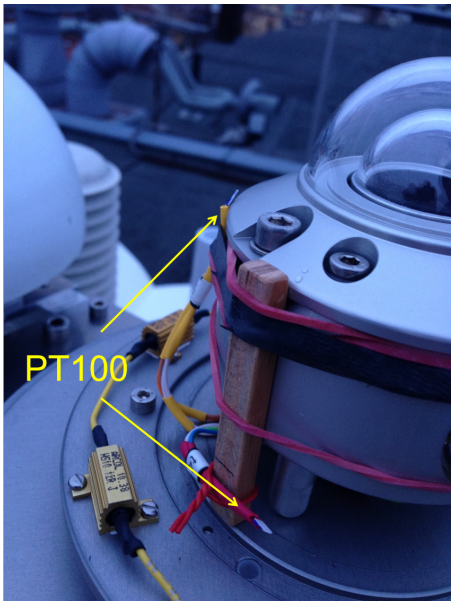

Figure 4.19: Position of the PT100 temperature elements inside the housing (below the outer glass dome and beneath the pyranometer base).

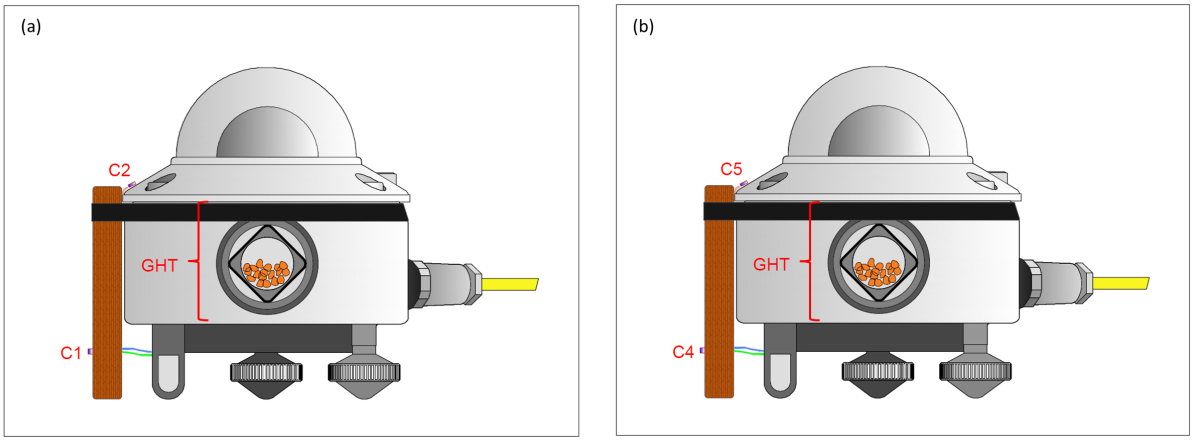

Figure 4.20: Position of the PT100 temperature elements inside the housings. (a) shows C1 and C2 at the reference (*PYRANO A*) and (b) C4 and C5 at the experimental pyranometer (*PYRANO B*). The curly bracket at GHT indicates the non defined position of the measured body temperature T_b.

Figures 4.21 shows a zoomed view on the individual PT100 elements. It was important to ensure that the upper PT100 element (hereinafter referred to as C2 or T_{C2} in the reference pyranometer *PYRANO A* and C5 or T_{C5} in the experimental pyranometer *PYRANO B*) did not contact the body of the CMP 21 and/or the housing walls (see Figure 4.21(a)), otherwise one would measure ambient temperature (as the pyranometer body and housing walls are considered to be in thermodynamic equilibrium with ambient air) instead of the temperature inside the individual pyranometer housings.

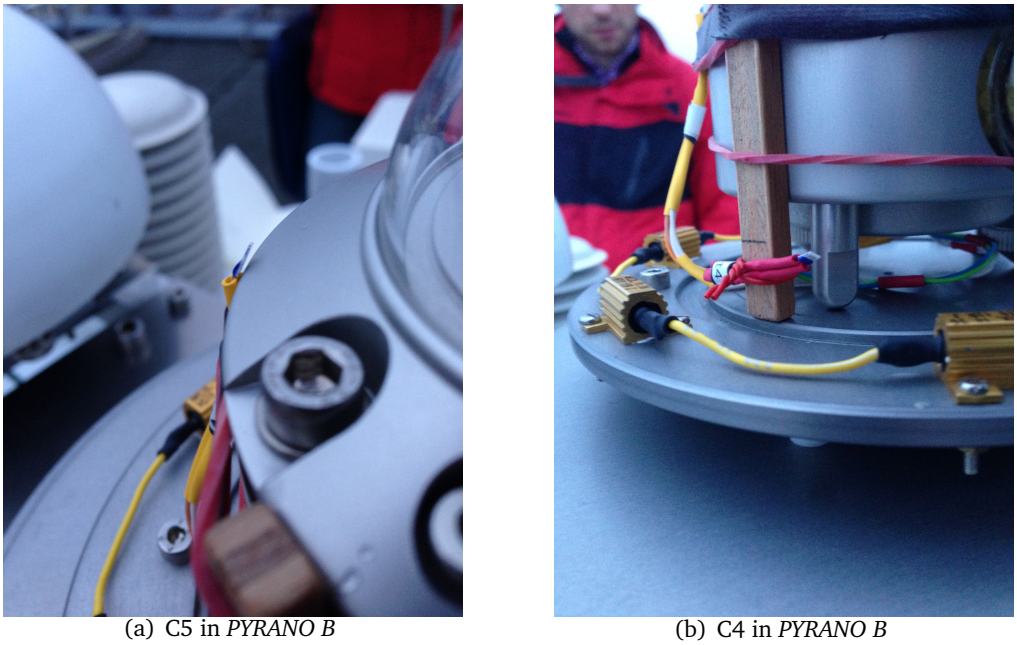

(a) C5 in *PYRANO B* (b) C4 in *PYRANO B*

Figure 4.21: A zoomed view on the individual PT100 elements inside the experimental pyranometer *PYRANO B* (CMP 21, KSO housing). (a) shows the upper PT100 element C5 and (b) shows the lower PT100 element C4.

The second PT100 element was fixed to each pyranometer with a little piece of wood, rubber band and wire (see Figure 4.21(b)). Further the lower PT100 elements (hereinafter referred to as C1 or T_{C1} in the reference pyranometer *PYRANO A* and C4 or T_{C4} in the experimental pyranometer *PYRANO B*) was ensured to be placed in the middle of the distance between two heating elements to avoid over-proportional heating compared to ambient air.

The main set of experiments during the campaign was comprised of a set of standardized spray-tests, simulating effects of natural precipitation on the radiation sensor output. Figure 4.22(a) indicates a person (the author of this thesis) performing a spray-test. Spray-tests have been performed at certain distance to the pyranometer glass-dome ($2 - 4\,\text{cm}$) and 30 pumps of distilled water have been brought onto the sensor dome. To simulate ‚realistic precipitation' the spray bottle was kept outside at all times ensuring that the simulated precipitation occurred at ambient air temperature.
After almost every spray-test a few water drops remained on the outer glass-dome. Sometimes even the drops stayed at the rim to the body of CMP 21 because the velocity of the emanating air from the housing was high enough to prevent water drops from flowing off (see Figure 4.22(b)).

(a) Example for a spray-test

(b) Example for water drops remaining on the outer glass-dome after a spray-test

Figure 4.22: Illustration of spray-tests: (a) shows a person (the author of this thesis) which performs a spray-test at certain distance to the pyranometer glass-dome ($2 - 4\,\text{cm}$) with 30 pumps of distilled water. (b) shows an example for water drops remaining on the outer glass-dome after a spray-test as the velocity of the air emanating from the housing was high enough to prevent water drops from flowing off (clearly visible at the left and right rim to the body of the CMP 21).

4.2.1 The whole time series of the measurement campaign

An overview about the radiation time series measured during the entire campaign (with reference in standard setup and including experimental and relaxation periods) lasting from 2015-01-23 15:00 UTC till 2015-01-29 08:25 UTC is shown in Figure 4.23.
The radiation measurements R of *PYRANO A* (green curve) and *PYRANO B* (orange curve) are shown on the left-hand axis, while the right-hand axis presents their absolute difference $|\Delta R|$ in 1-minute resolution (brown) and smoothed with a symmetric, multi-step moving average filter (four times 30 minutes, turquoise curve). In the upper part of this Figure one can see the current instrument housing of the experimental pyranometer: EIG (as defined above), $\mathrm{KSO_{orig.}}$ (original KSO housing as used for the global radiation sensor at ARAD site Graz/University), $\mathrm{KSO_{5\ mm}}$ (KSO housing with heating elements elevated by 5 mm), $\mathrm{KSO_{10\ mm}}$ (KSO housing with heating elements elevated by 10 mm) and $\mathrm{KSO_{15\ mm}}$ (KSO housing with heating elements elevated by 15 mm). Changes in housing configurations during the campaign are marked with a goldenrod dashed vertical lines.

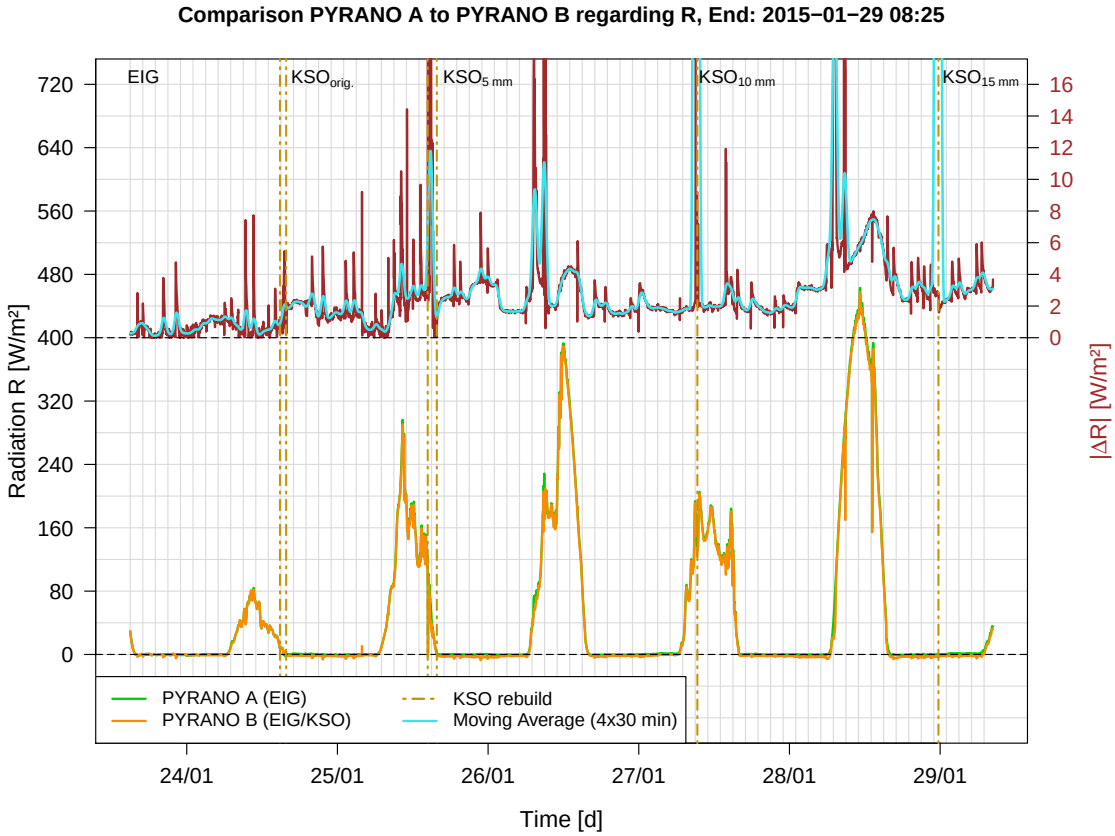

Figure 4.23: Comparison of radiation R [W m^{-2}] measured with reference (*PYRANO A*, CMP 21, Eigenbrodt housing, green) and experimental pyranometers (*PYRANO B*, CMP 21, Eigenbrodt or KSO housing, orange) between 2015-01-23 15:00 UTC and 2015-01-29 08:25 UTC. For convenience the absolute difference between measurements of *PYRANO A* and *PYRANO B* $|\Delta R|$ [W m^{-2}] is shown along with the individual instrument measurements as 1-minute average (brown curve) and four times 30 minute symmetric, multi-step moving average filter (turquoise curve) on right-hand axis. The black dashed horizontal lines mark 0 W m^{-2} for R and $|\Delta R|$, respectively. Goldenrod dashed vertical lines indicate changes in instrument housing between Eigenbrodt and KSO as well as height adjustments in the heating elements within the KSO housing; heating element adjustments for individual periods are detailed in the top of the graph.

Figure 4.23 contains many interesting details outlined below. For now two interesting cases shall be considered: (1) At the beginning of the time series both pyranometer were placed in Eigenbrodt SBL 480 housings and the difference $|\Delta R|$ was at/close to $0\,\mathrm{W\,m^{-2}}$. Small differences (which have been expected) are described in subsection 4.2.2. Shortly after the instrumentation setup was changed to the $\mathrm{KSO_{orig.}}$ housing $|\Delta R|$ jumped to a value of $2\,\mathrm{W\,m^{-2}}$, indicating the observed offset between pyranometers in Eigenbrodt and KSO housings (as observed at ARAD site Graz/University) is repeatable with independent sensors and housing units. (2) In the early morning of the 25$^{\mathrm{th}}$ of January the heating power of the KSO housing was turned off and $|\Delta R|$ decreased towards $1\,\mathrm{W\,m^{-2}}$, as observed during preliminary investigations described in subsection 4.1.3.

The following subsections provide a detailed analysis of radiation measurements during experimental conditions and relaxation periods using the individual housing setups described above.

4.2.2 Analysis of measurements with both pyranometers contained in Eigenbrodt SBL 480 housings

Figure 4.24 shows the first eleven hours of the field campaign. During this period both CMP 21 pyranometers were contained in Eigenbrodt SBL 480 housings and the heating level was set to 25 W, the standard heating configuration for pyranometer operation in high alpine environments within the ARAD network (e.g., at ARAD site Sonnblick). Although this heating level exceeds the one recommended by the manufacturer for moderate environmental conditions (10 W), as commonly present at ARAD site Graz/University, this did not affect pyranometer performance as seen in the parallel evolution of sensor output from *PYRANO A* (reference) and *PYRANO B* (experimental). Throughout the eleven hour operational period $|\Delta R|$ was close to $0\,\mathrm{W\,m^{-2}}$, highlighting the stability of sensors contained in Eigenbrodt SBL 480 housings.

At 20:37 UTC the heating power for the experimental pyranometer *PYRANO B* was switched off (0 W). Following the change in heating level, the thermal environment for the pyranometer changed and its output signal decreased within ten minutes to a value of $-2.5\,\mathrm{W\,m^{-2}}$. Twenty minutes later the pyranometer had stabilized in its new thermal environment and its output plateaued at around $-1\,\mathrm{W\,m^{-2}}$. $|\Delta R|$ was about $3\,\mathrm{W\,m^{-2}}$, illustrating the difference in pyranometer output when operated in strongly heated (25 W) or unheated (0 W) housing configuration.
At 22:18 UTC the heating level of *PYRANO B* was set to 25 W and shortly thereafter the pyranometer's output signal increased by $4\,\mathrm{W\,m^{-2}}$, which is the same amount it had decreased after switching the heating system off. After about one hour both radiation sensors (reference and experimental) reached similar output levels illustrated by $|\Delta R|$ varying around $0\,\mathrm{W\,m^{-2}}$. This simple experiment with ‚brute-force' adjustments in heating levels illustrates the large influence of the thermal environment inside the housing for pyranometer performance.

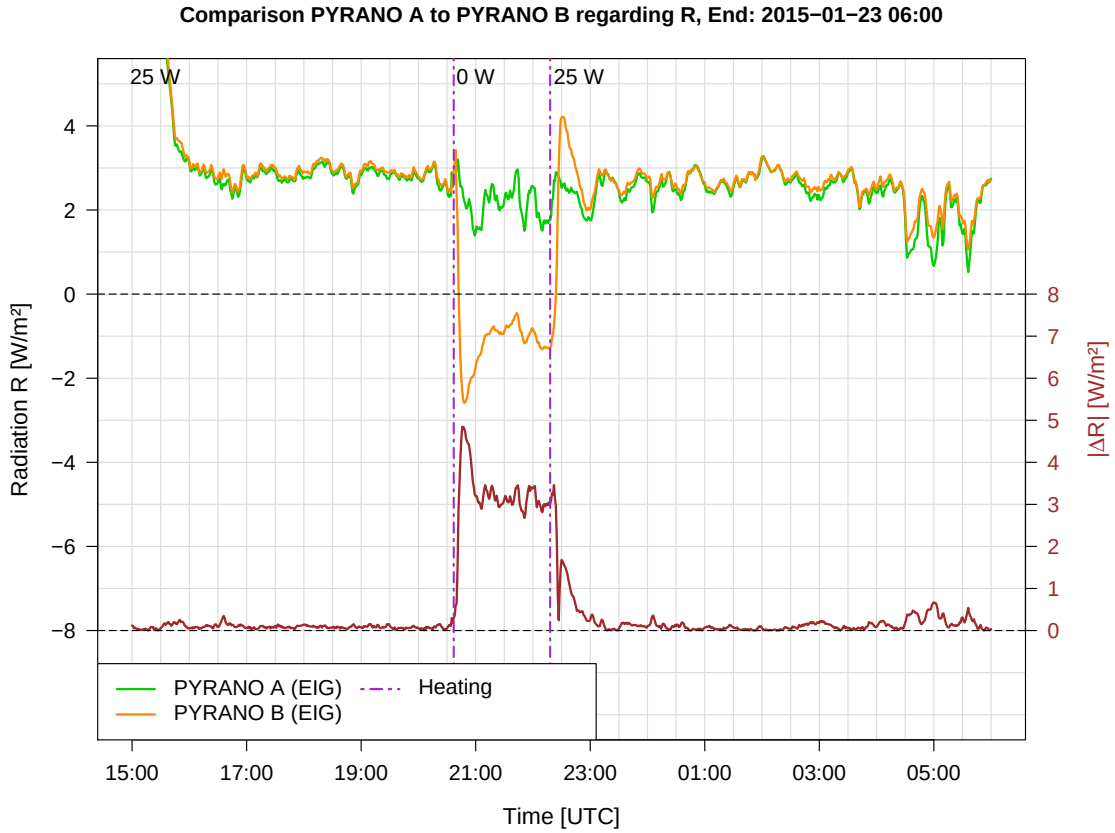

Figure 4.24: Comparison of radiation R [W m^{-2}] measured with reference (*PYRANO A*, CMP 21, Eigenbrodt housing, green) and experimental pyranometers (*PYRANO B*, CMP 21, Eigenbrodt housing, orange) between 2015-01-22 15:00 UTC and 2015-01-23 06:00 UTC. For convenience the absolute difference between measurements of *PYRANO A* and *PYRANO B* $|\Delta R|$ [W m^{-2}] is shown along with the individual instrument measurements as 1-minute average (brown curve) on right-hand axis. The black dashed horizontal lines mark $0\,\mathrm{W\,m^{-2}}$ for R and $|\Delta R|$, respectively. Dark orchid dashed vertical lines indicate changes in heating power for *PYRANO B* between 2015-01-22 20:37 UTC and 2015-01-22 22:18 UTC; heating power [W] for individual periods is detailed at the top of the graph.

Next the body temperatures T_b of *PYRANO A* and *PYRANO B* during the course of the experiment illustrated above are compared (see Figure 4.25). In the beginning the body temperatures of the pyranometers evolve in parallel with a quasi-constant offset of $0.6\,°\mathrm{C}$. Once the heating power of *PYRANO B* was switched off the body temperature curves diverge. The shape of the body temperature adjustment between 2015-01-22 20:37 UTC and 22:18 UTC follows an exponential form, which is the known form of adjustment towards a temperature equilibrium according to the *Maxwell-Boltzmann distribution*. Shortly after the heating power got turned on again (at 22:18 UTC) the experimental pyranometer reached temperature equilibrium with an offset to the reference sensor of approximately $0.8\,°\mathrm{C}$.

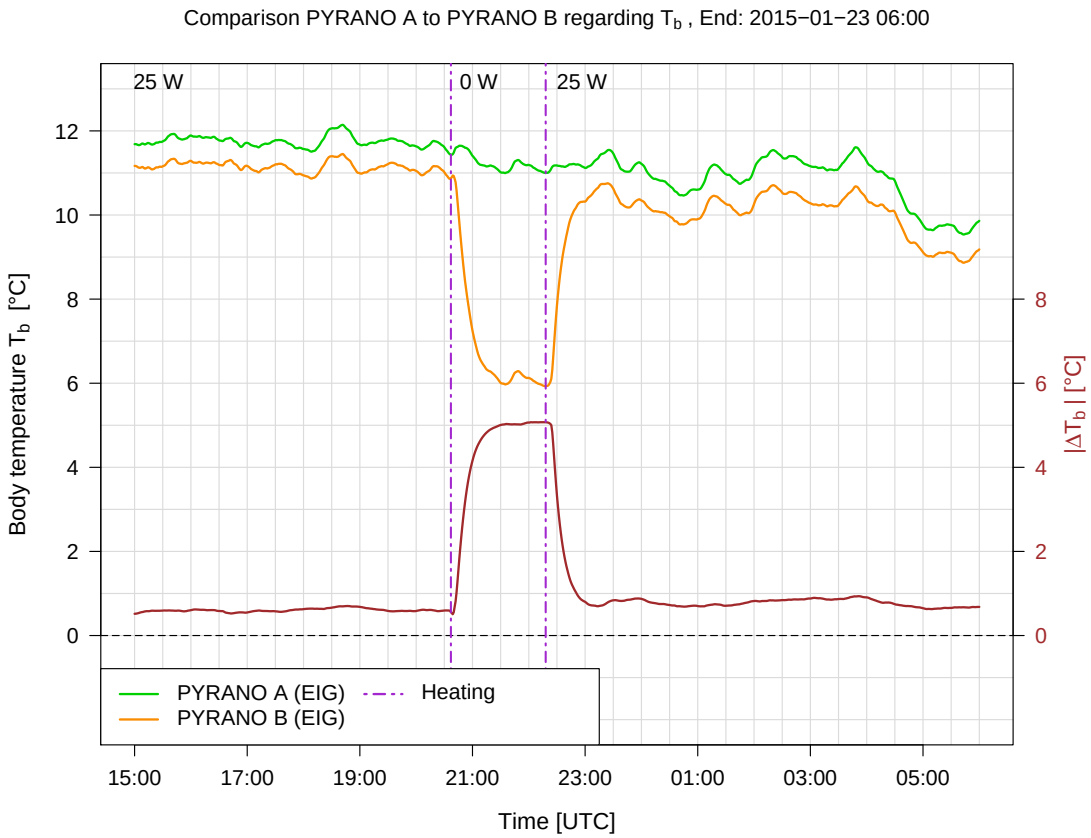

Figure 4.25: Comparison of body temperatures T_b [°C] of reference (*PYRANO A*, CMP 21, Eigenbrodt housing, green) and experimental pyranometers (*PYRANO B*, CMP 21, Eigenbrodt housing, orange) between 2015-01-22 15:00 UTC and 2015-01-23 06:00 UTC. For convenience the absolute difference between body temperatures of *PYRANO A* and *PYRANO B* $|\Delta T_\mathrm{b}|$ [°C] is shown along with the individual instrument measurements on right-hand axis. The black dashed horizontal line marks $0\,°\mathrm{C}$ for $|\Delta T_\mathrm{b}|$. Dark orchid dashed vertical lines indicate changes in heating power for *PYRANO B* between 2015-01-22 20:37 UTC and 2015-01-22 22:18 UTC; heating power [W] for individual periods is detailed at the top of the graph.

Between 2015-01-23 14:00 UTC and 2015-01-23 14:30 UTC the heating power of the pyranometers was set from $25\,\mathrm{W}$ to $10\,\mathrm{W}$, which is the heating level during routine operation at ARAD site Graz/University. The next paragraphs detail analyses for experiments performed during this ‚standard' configuration.

Figure 4.26 shows radiation output of *PYRANO A* and *PYRANO B* and their difference $|\Delta R|$ between 2015-01-23 15:00 UTC and 2015-01-24 05:00 UTC; the heating power for individual periods is detailed at the top of the graph. As one can see $|\Delta R|$ was almost $0\,\mathrm{W\,m^{-2}}$ until the the first spray-test for *PYRANO B* (at 16:05 UTC, marked with the first magenta dashed vertical line in Figure 4.26) was performed. Right after the spray-test the output signal decreased by about $3\,\mathrm{W\,m^{-2}}$, comparable to the spray-test detailed in section 4.1.3. Almost one hour later (at 16:56 UTC) another spray-test was performed, which showed similar results. Here an interesting effect gets visible, that was not detectable in the preliminary experiments due to the resolution of the logging system, radiation overshooting. Already after half an hour *PYRANO B* reached an approximately constant level of radiation and varied in parallel to *PYRANO A*.

For the next experiment the heating power of *PYRANO B* (in standard Eigenbrodt configuration) was reduced to $5\,\mathrm{W}$ at 2015-01-23 18:03 UTC. Despite this change in heating level no major effects on the output of the pyranometer have been found and therefore both instruments evolved parallel and in close proximity ($|\Delta R|$ close to $0\,\mathrm{W\,m^{-2}}$). Two hours after the heating level was adjusted the first spray-test at a $5\,\mathrm{W}$ heating level was performed. *PYRANO B* declined by about $3.5\,\mathrm{W\,m^{-2}}$ and recovered to its initial baseline within 30 minutes as seen in previous experiments with $10\,\mathrm{W}$ heating level.

Between 2015-01-23 21:48 UTC and 2015-01-23 22:08 UTC the next experiment, involving covering of the glass-domes of both instruments, the reference (*PYRANO A*) and experimental (*PYRANO B*), with fitted aluminium caps (see Figure 4.27), was performed (see cyan dashed vertical lines in Figure 4.26). *PYRANO A* and *PYRANO B* output increased rapidly due to thermal blocking but recovered instantly to their baseline values after the caps have been removed. After removing the caps, another spray-test was performed on the experimental pyranometer and the output signal declined, stronger than before; reaching a value $|\Delta R| > 4.5\,\mathrm{W\,m^{-2}}$. In summary, no matter how much R dropped after the spray-tests, it recovered to its original baseline value within $30 - 40$ minutes.

A second cover-test was performed between 23:33 UTC and 23:49 UTC. The curves of both pyranometers in- and decreased around $1\,\mathrm{W\,m^{-2}}$ within 16 minutes (see Figure 4.26). After this attempt, the heating system of *PYRANO B* was turned off ($0\,\mathrm{W}$ at 23:49 UTC) for the rest of this series. Following this change in housing setup *PYRANO B* output remained at an almost steady level though $|\Delta R|$ to *PYRANO A* increased, indicating the strong dependence of pyranometer stability on the heating system (see Figure 4.26).

Now the focus turns to the body temperatures T_b during and after/before spray-tests. Figure 4.28 shows the body temperature T_b of *PYRANO A* and *PYRANO B* (left-hand axis) and their difference $|\Delta T_\mathrm{b}|$ (right-hand axis) between 2015-01-22 15:00 UTC and 2015-01-23 06:00 UTC. At the beginning of the time series both pyranometers had a similar body temperature ($|\Delta T_\mathrm{b}| = 0.3\,^\circ\mathrm{C}$). After each individual spray-test (performed at 16:05 UTC, 16:56 UTC, 20:09 UTC, and 22:10 UTC) $|\Delta T_\mathrm{b}|$ rose exponential for at least 10 minutes. The body temperature of *PYRANO B* needed more time to recover to its initial value than the radiation R, not less than an hour. Further a clear cooling of the body temperature of the experimental pyranometer is visible in Figure 4.26 following reductions in heating power to $5\,\mathrm{W}$ at 18:03 UTC and to $0\,\mathrm{W}$ at 23:49 UTC.

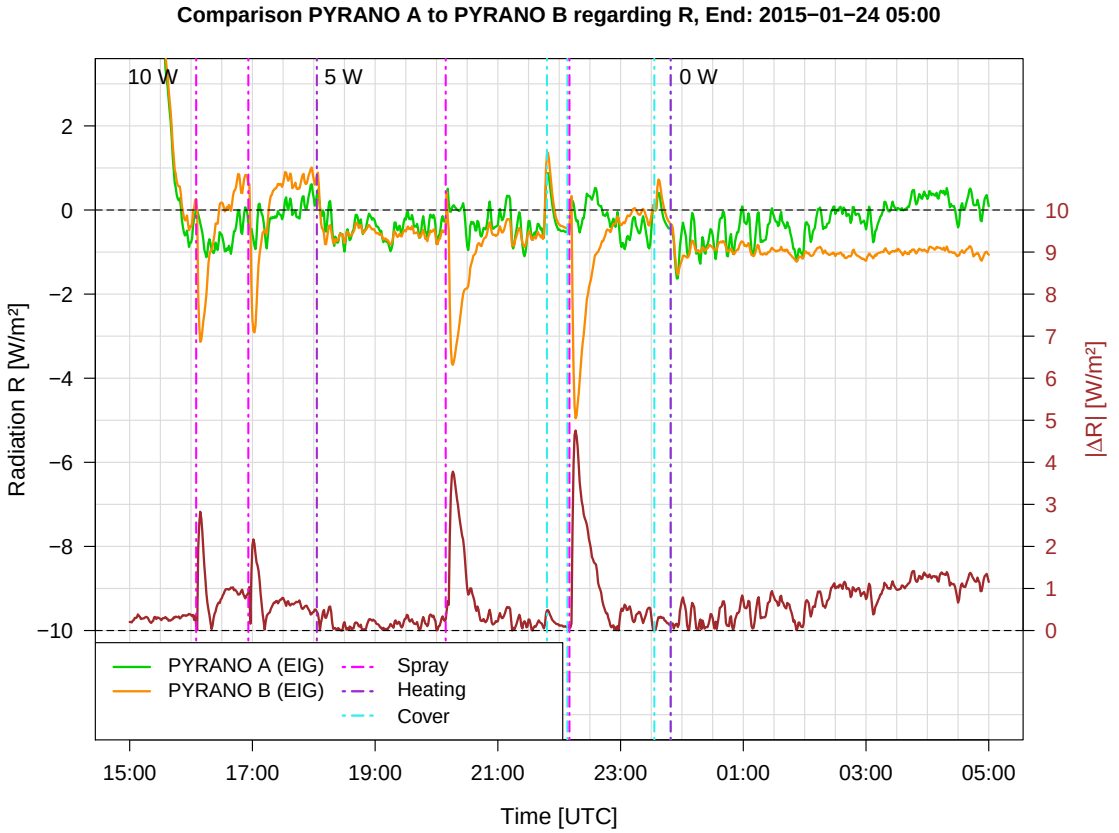

Figure 4.26: Comparison of radiation R [W m^{-2}] measured with reference (*PYRANO A*, CMP 21, Eigenbrodt housing, green) and experimental pyranometers (*PYRANO B*, CMP 21, Eigenbrodt housing, orange) between 2015-01-23 15:00 UTC and 2015-01-24 05:00 UTC. For convenience the absolute difference between measurements of *PYRANO A* and *PYRANO B* $|\Delta R|$ [W m^{-2}] is shown along with the individual instrument measurements as 1-minute average (brown curve) on right-hand axis. The black dashed horizontal lines mark $0\,\mathrm{W\,m^{-2}}$ for R and $|\Delta R|$, respectively. Dark orchid dashed vertical lines indicate changes in heating power for *PYRANO B* at 2015-01-23 18:03 UTC and at 2015-01-23 23:49 UTC; heating power [W] for individual periods is detailed at the top of the graph. The magenta dashed vertical lines mark spray-tests at 2015-01-23 16:05 UTC, at 16:56 UTC, at 20:09 UTC and at 22:10 UTC. The cyan dashed vertical lines mark cover-tests between 2015-01-23 21:48 UTC and 2015-01-23 22:08 UTC and between 2015-01-23 23:33 UTC and 2015-01-23 23:49 UTC.

Figure 4.27: Picture of a cover-test on the glass-domes of the reference (*PYRANO A*, CMP 21, Eigenbrodt housing, right) and experimental (*PYRANO B*, CMP 21, KSO housing, left) instruments with fitted aluminium caps.

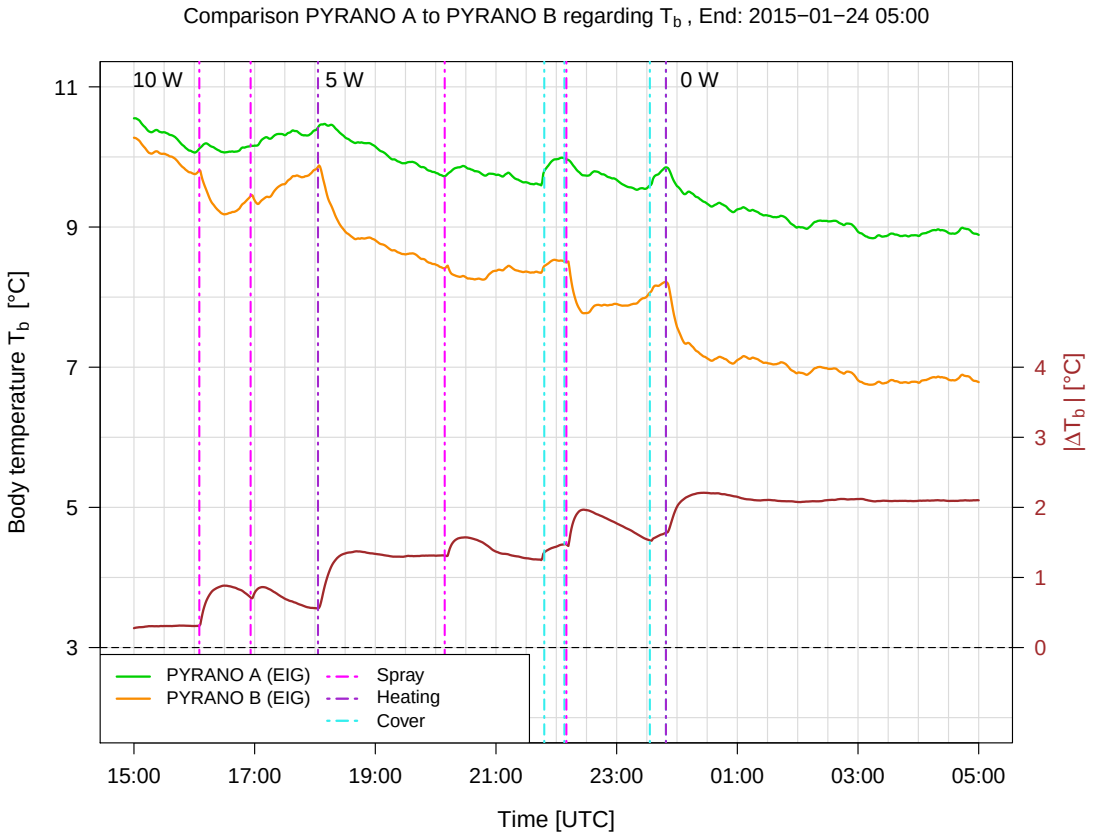

Figure 4.28: Comparison of body temperatures T_b [°C] of reference (*PYRANO A*, CMP 21, Eigenbrodt housing, green) and experimental pyranometers (*PYRANO B*, CMP 21, Eigenbrodt housing, orange) between 2015-01-22 15:00 UTC and 2015-01-23 06:00 UTC. For convenience the absolute difference between body temperatures of *PYRANO A* and *PYRANO B* $|\Delta T_\mathrm{b}|$ [°C] is shown along with the individual instrument measurements on right-hand axis. The black dashed horizontal line marks $0\,°\mathrm{C}$ for $|\Delta T_\mathrm{b}|$. Dark orchid dashed vertical lines indicate changes in heating power for *PYRANO B* at 2015-01-23 18:03 UTC and at 2015-01-23 23:49 UTC; heating power [W] for individual periods is detailed at the top of the graph. The magenta dashed vertical lines mark spray-tests at 2015-01-23 16:05 UTC, at 16:56 UTC, at 20:09 UTC and at 22:10 UTC. The cyan dashed vertical lines mark cover-tests between 2015-01-23 21:48 UTC and 2015-01-23 22:08 UTC and between 2015-01-23 23:33 UTC and 2015-01-23 23:49 UTC.

The analysis of the temperature time series of the PT100 elements mounted inside each housing, shown in Figure 4.29 (C1 (bottom, orange curve) and C2 (top, green curve) in the reference (*PYRANO A*), C4 (bottom, red curve) and C5 (top, blue curve) inside the experimental pyranometer (*PYRANO B*)) provided important insights on what had happened during the whole set of experiments described above.

C1 and C2 showed almost the entire time series a difference of $0.9\,°\mathrm{C}$, except during the two cover-tests (between 21:48 UTC and 22:08 UTC and between 23:33 UTC and 23:49 UTC) where C2 increased strikingly by around $0.7\,°\mathrm{C}$ and remained high until the cap was removed again. A similar result is found for C5, although with a slightly weaker increase ($\approx 0.4\,°\mathrm{C}$). Panels (a) and (b) in Figure 4.29 show the most interesting curve progressions. At the beginning of the time series C4 and C5 had a similar difference as C1 and C2 below ($\approx 0.7\,°\mathrm{C}$). At 16:05 the difference between C5 an C4 decreased a little which was possible caused by a water drop impacting C5

during/after the spray test. Further spray-tests performed later (at 16:56 UTC, 20:09 UTC and 22:10 UTC) did not show any noticeable changes in the difference. Interestingly after the first change in heating level ($10\,\mathrm{W}$ to $5\,\mathrm{W}$ at 18:03 UTC) the temperature of C5 declined by about $0.5\,^{\circ}\mathrm{C}$, whereas C4 remained almost at the same temperature level, i.e., C5 was still higher than C4. Remembering Figure 4.26, the output signals of *PYRANO A* and *PYRANO B* were close to each other. At 23:49 UTC the heating power was turned off and C5 decreased as seen before and the difference C5-C4 turned negative and remained at roughly $-0.2\,^{\circ}\mathrm{C}$. At the same time the sensor output of *PYRANO B* dropped to a nearly constant value of $-1\,\mathrm{W\,m^{-2}}$ and remained there until the end of the series.

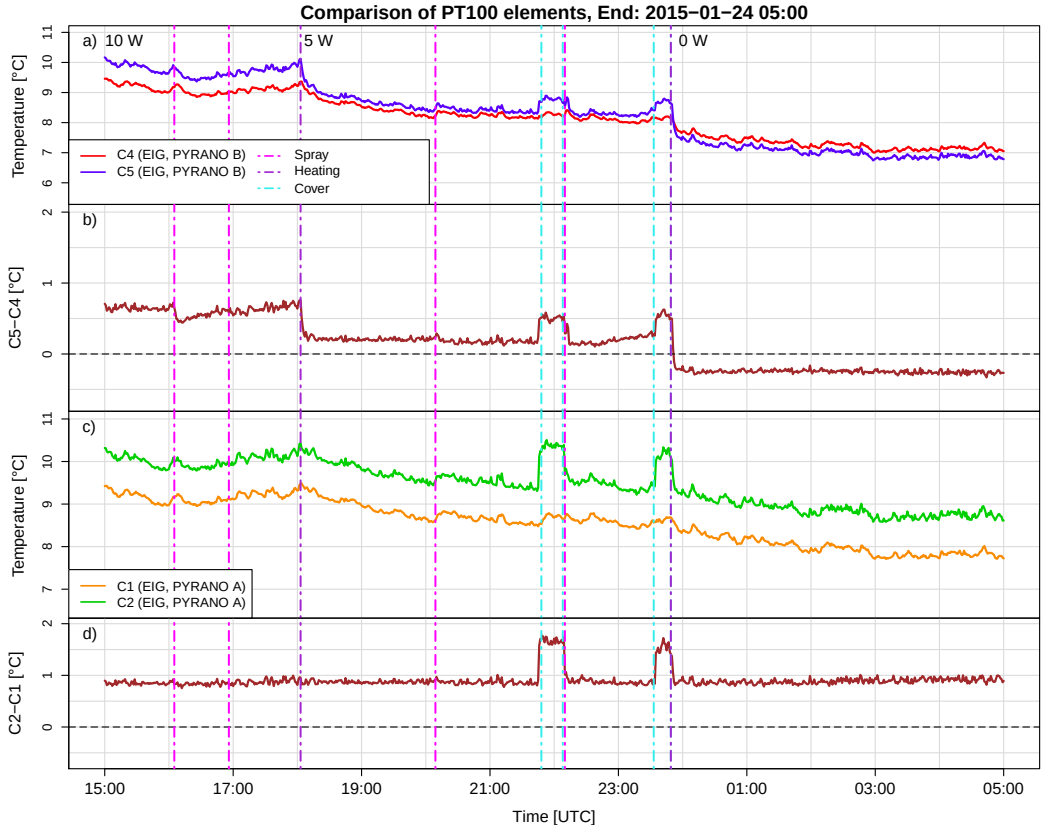

Figure 4.29: Comparison of temperatures [°C] measured by the PT100 elements C2, C3, C4 and C5 inside reference and experimental housing systems: (a) C4 (lower mounted, red curve) and C5 (upper mounted, blue curve) represent temperatures inside the experimental setup (*PYRANO B*, CMP 21, Eigenbrodt housing); (b) temperature difference C5-C4; (c) C1 (lower mounted, orange curve) and C2 (upper mounted, green curve) inside the reference system (*PYRANO A*, CMP 21, Eigenbrodt housing); (d) temperature difference C2-C1. All panels for observations between 2015-01-23 15:00 UTC and 2015-01-24 05:00 UTC. The black dashed horizontal lines in panels (b) and (d) mark $0\,^{\circ}\mathrm{C}$ for C2-C1 or C5-C4. Dark orchid dashed vertical lines indicate changes in heating power for *PYRANO B* at 2015-01-23 18:03 UTC and at 2015-01-23 23:49 UTC; heating power [W] for individual periods is detailed at the top of the graph. The magenta dashed vertical lines mark spray-tests at 2015-01-23 16:05 UTC, at 16:56 UTC, at 20:09 UTC and at 22:10 UTC. The cyan dashed vertical lines mark cover-tests between 2015-01-23 21:48 UTC and 2015-01-23 22:08 UTC and between 2015-01-23 23:33 UTC and 2015-01-23 23:49 UTC.

After switching off the heating system of *PYRANO B*, $|\Delta R|$ was around a value of $1\,\mathrm{W\ m^{-2}}$ (see in Figure 4.30). At 05:57 UTC the first spray-test at a heating power of $0\,\mathrm{W\,m^{-2}}$ was performed. It is worth mentioning that the distilled water used in this attempt had room temperature due to refilling the bottle only a couple minutes before. Thus the difference of the pyranometers

decreased, approximately $1\,\mathrm{W\,m^{-2}}$ in the first couple of seconds. Shortly after this decline $|\Delta R|$ rose to over $2\,\mathrm{W\,m^{-2}}$ and returned to its initial value within 30 minutes. The second attempt, performed at 07:01 UTC, showed nearly the same. At 08:11 UTC heating was switched on, back to $5\,\mathrm{W}$. Simultaneously $|\Delta R|$ declined and plateaued around $0.3\,\mathrm{W\,m^{-2}}$.

At 09:18 UTC and at 10:36 UTC spray-tests have been performed and the difference between *PYRANO A* and *PYRANO B* increased to about $7.5\,\mathrm{W\ m^{-2}}$. The reason for this large change in sensor output is not entirely clear, though it is very likely that higher radiation R levels (around $50\,\mathrm{W\ m^{-2}}$ and $80\,\mathrm{W\,m^{-2}}$) triggered this larger response as spray-tests have been performed during the day but at overcast conditions. Another potential explanation would be wind speed, which influences evaporation, though this factor can be excluded as average and maximum wind velocity V_{MM} shown in Figure 4.31 didn't change/vary strikingly.

At 12:05 UTC the heating power was changed to $10\,\mathrm{W}$ and two final spray-tests for *PYRANO B* in standard Eigenbrodt configuration have been performed. These spray-test showed similar increased values of $|\Delta R|$ ($2\,\mathrm{W\,m^{-2}}$ at 12:57 UTC and $3\,\mathrm{W\,m^{-2}}$ at 13:59 UTC) as the other spray-tests performed in this configuration before.

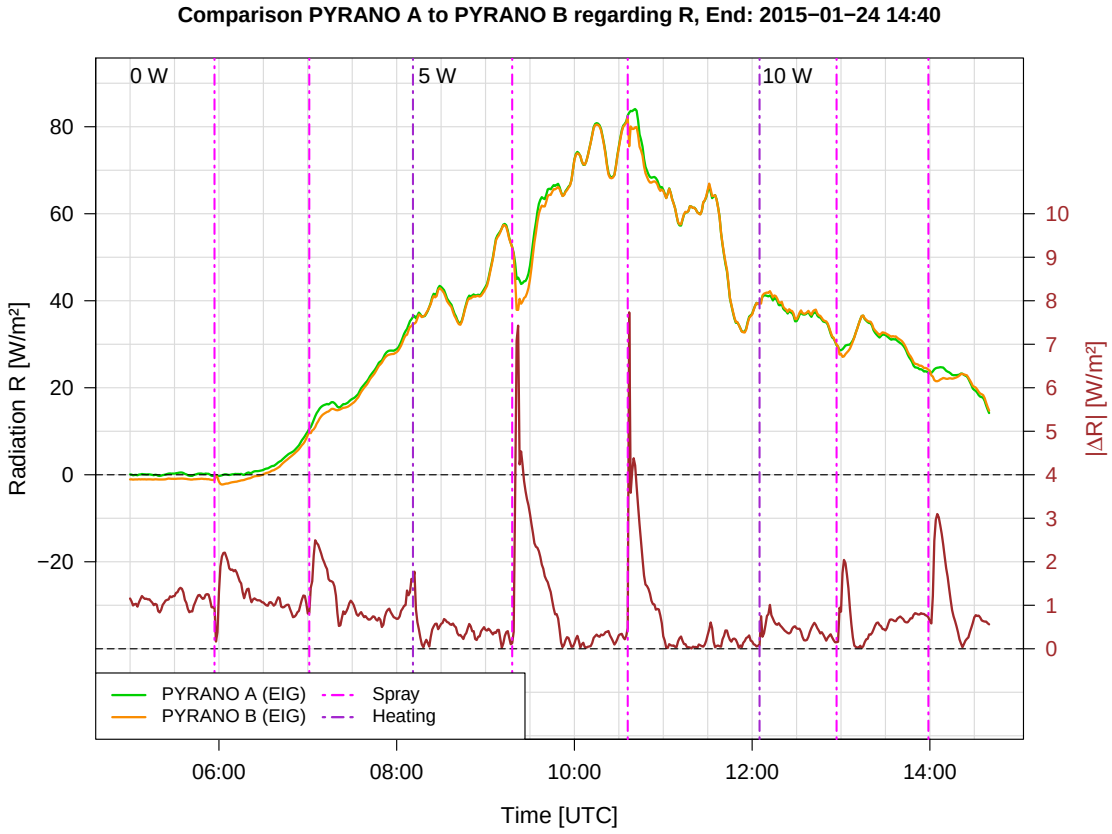

Figure 4.30: As Figure 4.26 but for comparison of radiation R [W m^{-2}] measured with reference (*PYRANO A*, CMP 21, Eigenbrodt housing, green) and experimental pyranometers (*PYRANO B*, CMP 21, Eigenbrodt housing, orange) between 2015-01-24 05:00 UTC and 2015-01-24 14:40 UTC. Dark orchid dashed vertical lines indicate changes in heating power for *PYRANO B* at 2015-01-24 08:11 UTC and at 2015-01-24 12:05 UTC; heating power [W] for individual periods is detailed at the top of the graph. The magenta dashed vertical lines mark spray-tests at 2015-01-24 05:57 UTC, at 07:01 UTC, at 09:18 UTC, at 10:36 UTC, at 12:57 UTC and at 13:59 UTC.

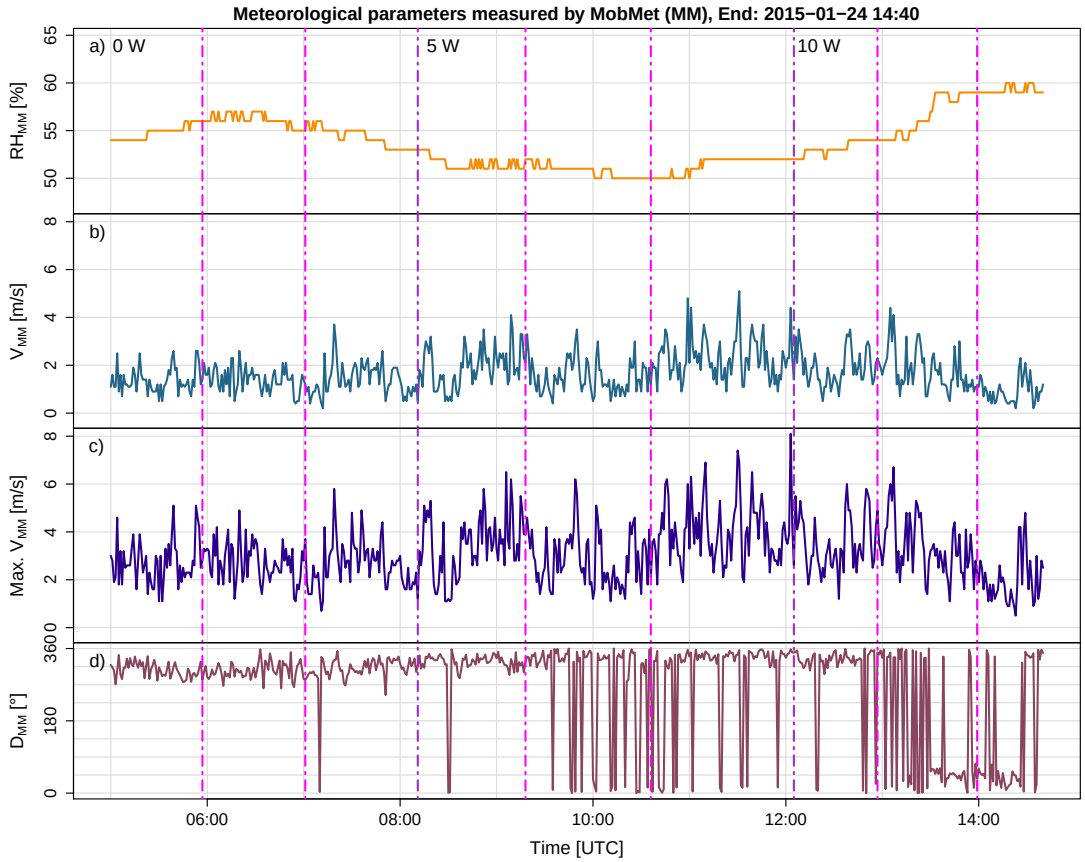

Figure 4.31: Meteorological parameters (a) relative humidity RH_{MM} [%], (b) wind speed V_{MM} [m s^{-1}], (c) maximum wind speed Max.V_{MM} [m s^{-1}] and (d) wind direction D_{MM} [°] measured by MobMet between 2015-01-24 05:00 UTC and 2015-01-24 14:40 UTC.

Figure 4.32 shows the body temperatures of both pyranometers (reference, experimental) and their difference between 2015-01-24 05:00 UTC and 2015-01-24 14:40 UTC. The constant offset of $|\Delta T_{\mathrm{b}}| \approx 2\,^{\circ}\mathrm{C}$ was disturbed by individual spray tests, but after most spray-tests $|\Delta T_{\mathrm{b}}|$ returned to its baseline value within 30 minutes. At 08:11 UTC and 12:05 UTC the heating power was increased by $+5$ W in each case. Following both heating changes the difference between *PYRANO A* and *PYRANO B* decreased exponentially, highlighting the importance of the heating level for instrument stability/performance.

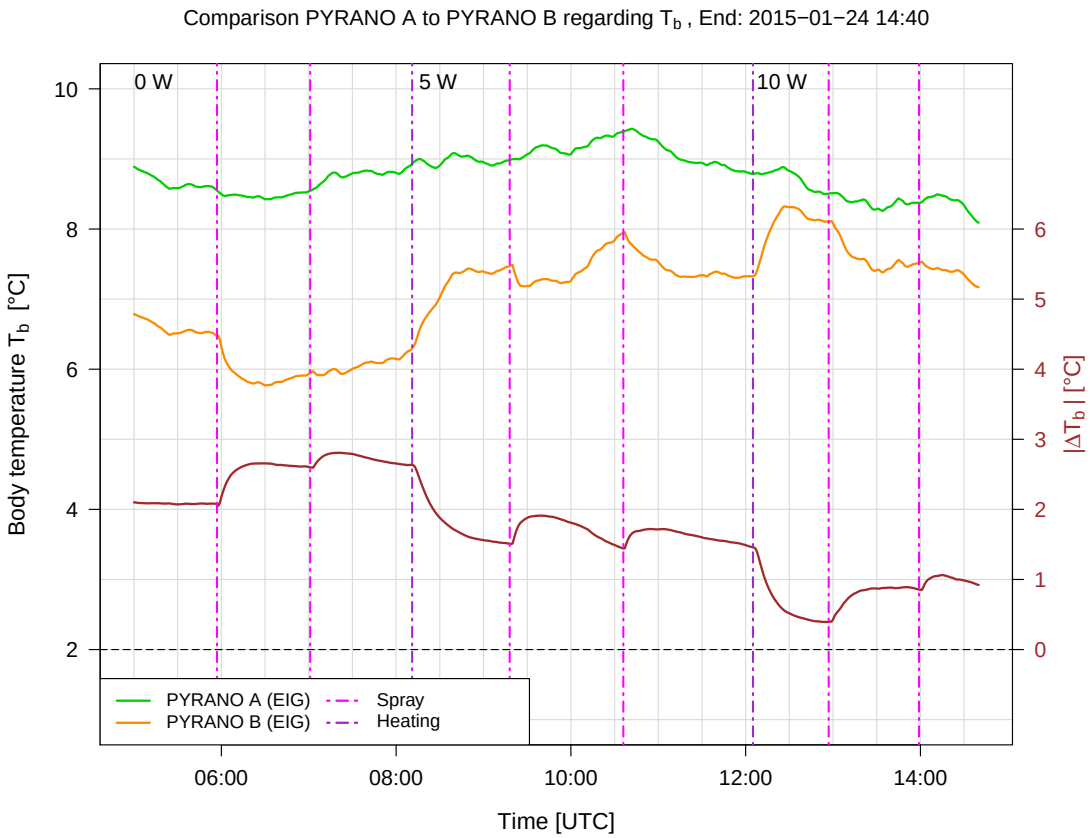

Figure 4.32: As Figure 4.28 but for comparison of body temperatures T_b [°C] measured with reference (*PYRANO A*, CMP 21, Eigenbrodt housing, green) and experimental pyranometers (*PYRANO B*, CMP 21, Eigenbrodt housing, orange) between 2015-01-24 05:00 UTC and 2015-01-24 14:40 UTC. Dark orchid dashed vertical lines indicate changes in heating power for *PYRANO B* at 2015-01-24 08:11 UTC and at 2015-01-24 12:05 UTC; heating power [W] for individual periods is detailed at the top of the graph. The magenta dashed vertical lines mark spray-tests at 2015-01-24 05:57 UTC, at 07:01 UTC, at 09:18 UTC, at 10:36 UTC, at 12:57 UTC and at 13:59 UTC.

In a nutshell the comparison of two Eigenbrodt SBL 480 housings showed that different pyranometers operate very similar, no matter of the heating power is $5\,\mathrm{W}$, $10\,\mathrm{W}$ or $25\,\mathrm{W}$. Only disabling the heating power (i.e., $0\,\mathrm{W}$ heating) showed a larger deviating response. Individual heating level adjustments beyond the $0\,\mathrm{W}$ line triggered small exponential changes which recovered to baseline values between disturbed and undisturbed sensors of around $1\,\mathrm{W\,m^{-2}}$ within 30 minutes.

Following this ‚proof' of stability for Kipp&Zonen sensors operated in Eigenbrodt SLB 480 housings the campaign continued to investigate effects of spray-tests and other experiments on the KSO housing (in standard and modified configuration) which, as indicated by preliminary results from ARAD site Graz/University, shows a constant offset to sensors operated in SLB 480 housings.

4.2.3 Analysis of measurements for pyranometers contained in an Eigenbrodt SBL 480 (reference) and KSO original (experimental) housing

Following the experimental work with two CMP 21 sensors placed in Eigenbrodt SBL 480 housings (one reference, one experimental instrument) the experimental setup was repeated with a KSO housing (as experimental instrument). In this configuration the experimental setup is identical to the setup for *GLO* and *HIM* at ARAD site Graz/University.

Figure 4.33 shows the time series of joint measurements of the reference instrument (*PYRANO A*, Eigenbrodt SBL 480, heating level 10 W) with the experimental instrument in $KSO_{orig.}$ setup (*PYRANO B*, KSO housing, heating level 10 W, heating elements at default position) between 2015-01-24 16:00 UTC and 2015-01-25 05:00 UTC. Already 10 minutes after *PYRANO B* was rebuilt to the $KSO_{orig.}$ setup the difference between *PYRANO A* and *PYRANO B* reached a value of around 2 W m^{-2}, indicating that the offset identified at ARAD site Graz/University during preliminary investigations is reproducible with a different sensor of the same type.

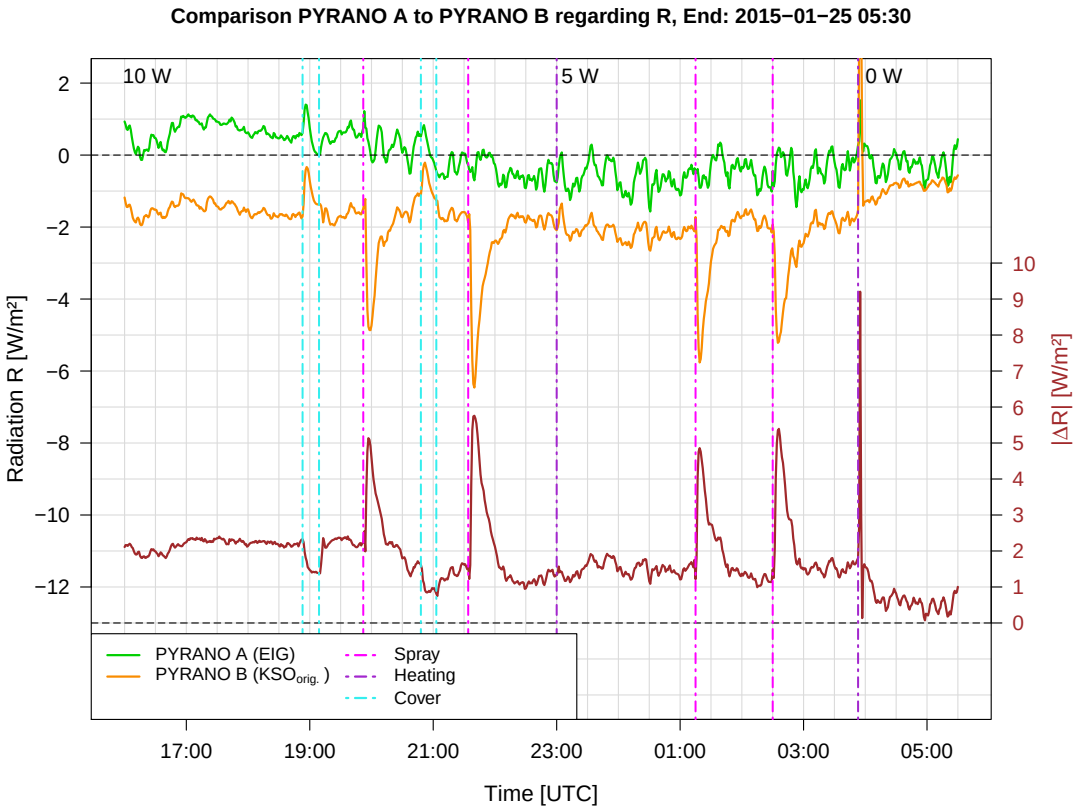

Figure 4.33: As Figure 4.26 but for comparison of radiation R [W m^{-2}] measured with reference (*PYRANO A*, CMP 21, Eigenbrodt housing, green) and experimental pyranometers (*PYRANO B*, CMP 21, KSO original housing, orange) between 2015-01-24 16:00 UTC and 2015-01-25 05:00 UTC. Dark orchid dashed vertical lines indicate changes in heating power for *PYRANO B* at 2015-01-24 23:00 UTC and at 2015-01-25 03:53 UTC; heating power [W] for individual periods is detailed at the top of the graph. The magenta dashed vertical lines mark spray-tests at 2015-01-24 19:52 UTC, at 21:34 UTC, at 2015-01-25 01:15 UTC and at 02:30 UTC. The cyan dashed vertical lines mark cover-tests between 2015-01-24 18:53 UTC and 2015-01-24 19:09 UTC and between 2015-01-24 20:48 UTC and 2015-01-24 21:03 UTC.

The first experiment performed in this instrumentation setup was a cover-test (see Figure 4.33) which started at 18:53 UTC and ended at 19:09 UTC. Radiation output of both pyranometers (PYRANO A and B) increased simultaneously and declined within 16 minutes after the cover-test to its initial baseline value. A second cover-test performed between 20:48 UTC and 21:03 UTC brought similar results (see Figure 4.33).

As during the comparison of pyranometers contained in Eigenbrodt SBL 480 housings a series of spray-tests (four tests, see Figure 4.33) was performed during the comparison of the reference pyranometer with the pyranometer contained in a ‚standard' KSO housing. During all four spray-tests, performed between 19:52 UTC and 03:00 UTC, approximately equal deflections of $|\Delta R|$ around $5\,\mathrm{W\ m^{-2}}$, were found.

On 2015-01-25 at 03:53 UTC the heating power of the KSO housing was turned off. Following this change in heating the radiation measurements of *PYRANO B* converged towards the reference (*PYRANO A*). After changing the heating power $|\Delta R|$ varied between 0 and $1\,\mathrm{W\ m^{-2}}$ until the end of the time series shown in Figure 4.33. It is important to note that the large deflection visible in Figure 4.33 is due to an artificial signal, caused by a headlamp during work near the measurement platform between 03:50 UTC and 03:54 UTC on 2015-01-25.

The results of the experiments with the KSO housing in standard configuration indicate that the internal heating system is very likely contributing to the offset between pyranometers operated with Eigenbrodt and KSO standard housings. In the following different configurations of the KSO housing regarding the magnitude of the heating level (and height of the heating elements within the housing) are considered. Overall it is noted that the limited number of experiments possible during the measurement campaign does not allow statistically significant conclusions regarding the influence of the heating system (and heating level). Nevertheless results summarized in this thesis indicate that further investigations of these effects should be prioritized in future work.

Next the focus is turned to the body temperatures of *PYRANO A* (EIG) und *PYRANO B* ($\mathrm{KSO_{orig.}}$) between 2015-01-24 16:00 UTC and 2015-01-25 05:30 UTC, illustrated in Figure 4.34. The first feature of interest in this time series is the almost constant difference $|\Delta T_\mathrm{b}| \approx 0.8\,^\circ\mathrm{C}$ during periods where both ventilation units have been heated with $10\,\mathrm{W}$ (from 17:00 UTC to 18:53 UTC) and $5\,\mathrm{W}$ (from 23:30 UTC to 01:15 UTC). Preliminary investigations showed that the body temperature of the pyranometer contained in the KSO housing should be $1\,^\circ\mathrm{C}$ higher than those of the pyranometer contained in the Eigenbrodt SBL 480 housing. The smaller difference in body temperatures during the comparison period is attributed to the base temperature of the $\mathrm{KSO_{orig.}}$ housing. As the $\mathrm{KSO_{orig.}}$ housing was kept at ambient temperature (ventilated but not heated until installation) it needed more time to reach thermal equilibrium at a heating power of $10\,\mathrm{W}$. Thus the $10\,\mathrm{W}$ heating can be considered more like a $5\,\mathrm{W}$ heating during this period.

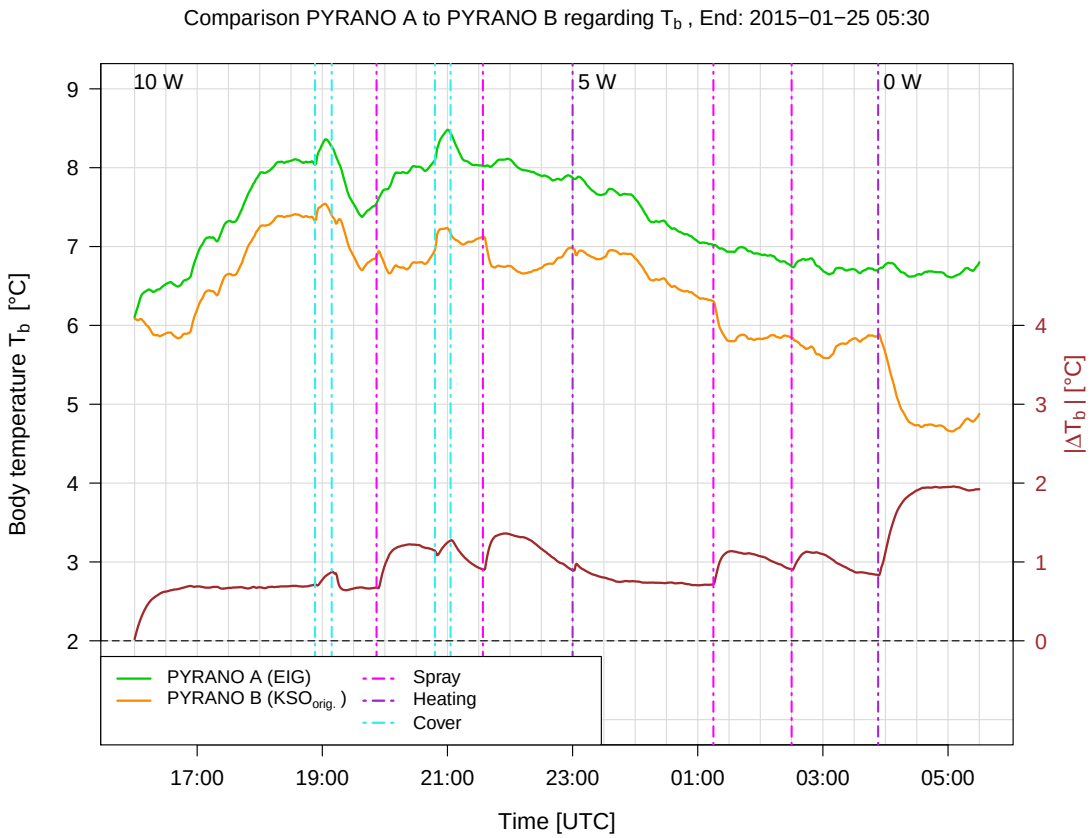

Figure 4.34: As Figure 4.28 but for comparison of body temperatures T_b [°C] measured with reference (*PYRANO A*, CMP 21, Eigenbrodt housing, green) and experimental pyranometers (*PYRANO B*, CMP 21, KSO original housing, orange) between 2015-01-24 16:00 UTC and 2015-01-25 05:00 UTC. Dark orchid dashed vertical lines indicate changes in heating power for *PYRANO B* at 2015-01-24 23:00 UTC and at 2015-01-25 03:53 UTC; heating power [W] for individual periods is detailed at the top of the graph. The magenta dashed vertical lines mark spray-tests at 2015-01-24 19:52 UTC, at 21:34 UTC, at 2015-01-25 01:15 UTC and at 02:30 UTC. The cyan dashed vertical lines mark cover-tests between 2015-01-24 18:53 UTC and 2015-01-24 19:09 UTC and between 2015-01-24 20:48 UTC and 2015-01-24 21:03 UTC.

During the cover-tests performed between 18:53 UTC and 19:09 UTC and 20:48 UTC and 21:03 UTC slight increases in pyranometer body temperatures have been observed, similar in magnitude as observed for the Eigenbrodt SBL 480 housings. Further T_b of *PYRANO B* declined following each spray-test (marked with magenta dashed vertical lines in Figure 4.34) and the difference in body temperature $|\Delta T_\mathrm{b}|$ between the two pyranometers shows exponential behaviour. At 03:53 UTC the body temperature of *PYRANO B* decreased strongly as the heating level of the housing was set to $0\,\mathrm{W}$.

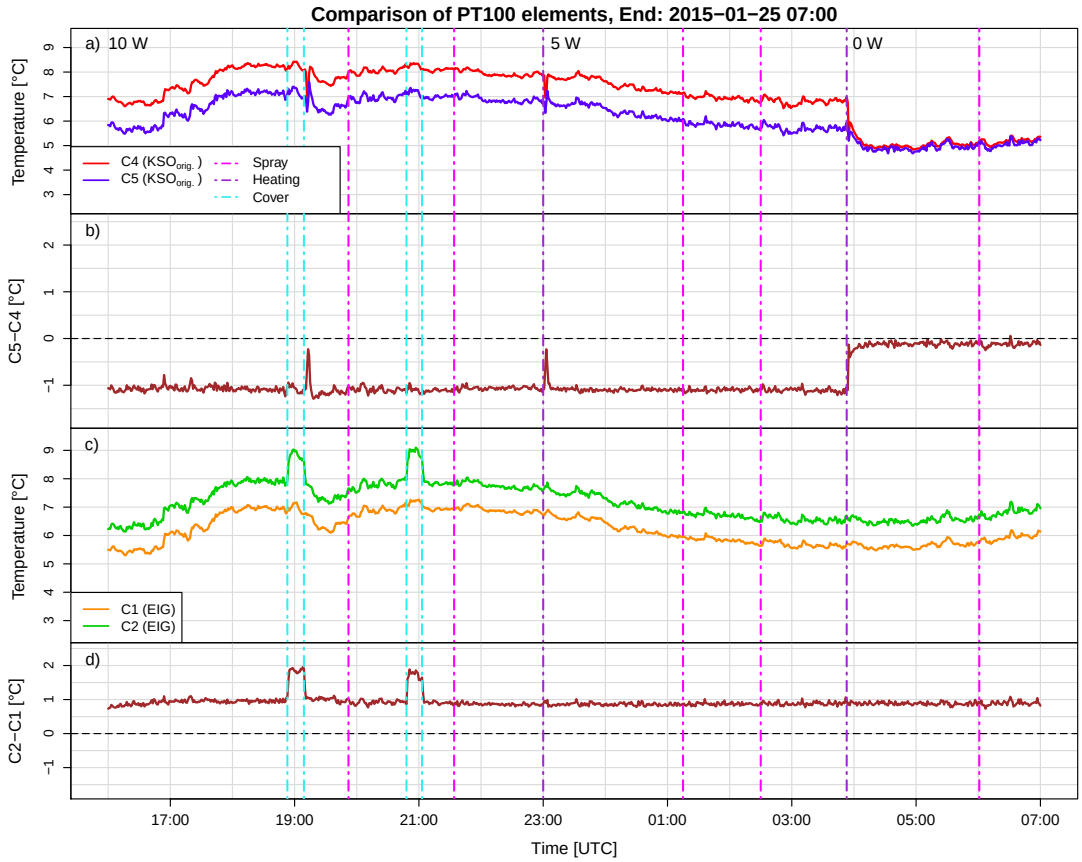

Figure 4.35: As Figure 4.29 but for comparison of C4 and C5 in the experimental pyranometer housing (*PYRANO B*, CMP 21, KSO original housing) between 2015-01-24 16:00 UTC and 2015-01-25 07:00 UTC. Dark orchid dashed vertical lines indicate changes in heating power for *PYRANO B* at 2015-01-24 23:00 UTC and at 2015-01-25 03:53 UTC; heating power [W] for individual periods is detailed at the top of the graph. The magenta dashed vertical lines mark spray-tests at 2015-01-24 19:52 UTC, at 21:34 UTC, at 2015-01-25 01:15 UTC and at 02:30 UTC. The cyan dashed vertical lines mark cover-tests between 2015-01-24 18:53 UTC and 2015-01-24 19:09 UTC and between 2015-01-24 20:48 UTC and 2015-01-24 21:03 UTC.

Figure 4.35 shows the time series of the four PT100 elements, two each mounted inside the reference and experimental housings, between 2015-01-25 16:00 UTC and 2015-01-26 07:00 UTC. PT100 elements C1 (bottom) and C2 (top) have been mounted inside the reference housing while C4 (bottom) and C5 (top) have been mounted inside the KSO housing. From this graph it is obvious that the glass-domes of the pyranometer contained in a KSO$_{orig.}$ housing (represented by C5) are colder than the sensors body temperature (represented by C4), while its the opposite for sensors contained in Eigenbrodt SBL 480 housings. Interestingly *PYRANO B* seems to deviate slightly from thermodynamic equilibrium while being heated (with either 5 or $10\,$W) as at both heating levels a difference between T_{C4} and T_{C5} of about $1\,^{\circ}$C occurred. A similar absolute difference is found for the temperature elements mounted inside the Eigenbrodt SBL 480 housing, indicating that also this device is slightly off thermodynamic equilibrium. As expected once the heating system of the KSO$_{orig.}$ housing was switched off the pyranometer obtained thermodynamic equilibrium as the difference between T_{C4} and T_{C5} converged close to $0\,^{\circ}$C.

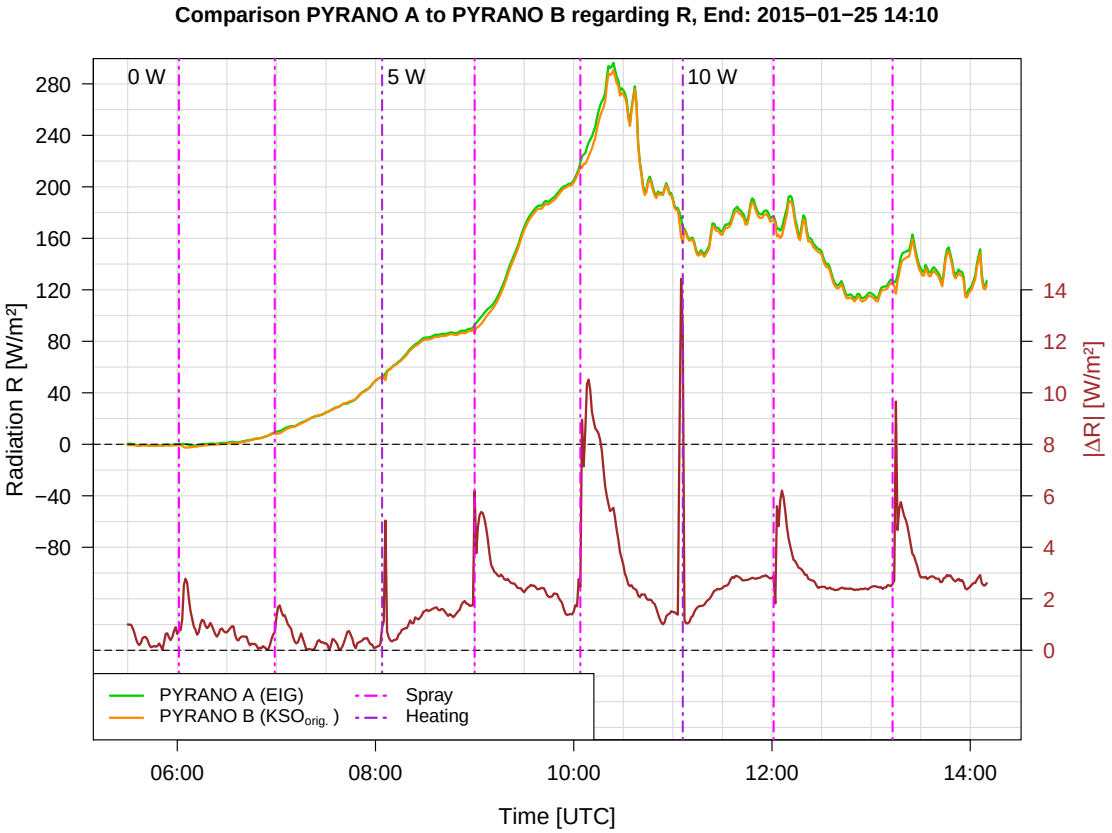

Figure 4.36: As Figure 4.26 but for comparison of radiation R [W m^{-2}] measured with reference (*PYRANO A*, CMP 21, Eigenbrodt housing, green) and experimental pyranometers (*PYRANO B*, CMP 21, KSO original housing, orange) between 2015-01-25 05:00 UTC and 2015-01-25 14:10 UTC. Dark orchid dashed vertical lines indicate changes in heating power for *PYRANO B* at 2015-01-25 08:04 UTC and at 2015-01-25 11:06 UTC; heating power [W] for individual periods is detailed at the top of the graph. The magenta dashed vertical lines mark spray-tests at 2015-01-25 06:01 UTC, at 06:59 UTC, at 09:00 UTC, at 10:04 UTC, at 12:01 UTC and at 13:13 UTC.

The second part of the comparison time period between pyranometers contained in Eigenbrodt SBL 480 (reference setup) and KSO original housings (experimental setup) is shown in Figures 4.36 (regarding R) and 4.37 (regarding T_b). The beginning of the time series in Figure 4.36 shows that $|\Delta R|$ varied between 0 and $1\,\mathrm{W\,m^{-2}}$. The first two spray-tests, performed during nighttime conditions, resulted in increased differences among pyranometer outputs of $3\,\mathrm{W\,m^{-2}}$ at 06:01 UTC and $2\,\mathrm{W\,m^{-2}}$ at 06:59 UTC). As after previous spray-tests observed, $|\Delta R|$ between *PYRANO A* and *PYRANO B* rebound within few minutes to its baseline values.

At 08:04 UTC the heating system of the KSO$_{\mathrm{orig.}}$ housing was switched back to heating level $5\,\mathrm{W}$, resulting in a strong increase in R output of *PYRANO B* in the order of $1.5\,\mathrm{W\,m^{-2}}$. Furthermore $|\Delta R|$ increased to almost $3\,\mathrm{W\,m^{-2}}$ after the heating level was restored to its default level of $10\,\mathrm{W}$ at 11:06 UTC.

Daytime spray-tests (at 09:00 UTC and at 12:01 UTC) resulted in $|\Delta R| \approx 6\,\mathrm{W\,m^{-2}}$ while those at 10:04 UTC and 13:13 UTC triggered values of $|\Delta R| \approx 10\,\mathrm{W\,m^{-2}}$. It is assumed that these large differences in radiation sensor output are a result of generally larger baseline radiation levels due to day time conditions. Meteorological variables such as wind velocity are excluded as cause

given the dependence of evaporation on both radiation and wind speed discussed above (see Section 2.10).
After radiation signals have been addressed the discussion is turned to the effect of individual experiments on the body temperature of the pyranometers. At 08:04 UTC the heating power of the experimental pyranometer was changed to 5 W and the difference $|\Delta T_b|$ reduced to roughly $0.8\,°C$ as the day before. After changing the heating power to 10 W at 11:06 UTC T_b of the experimental pyranometer (*PYRANO B*) exceeded the body temperature of the reference instrument (*PYRANO A*), indicating the strong influence of the heating system on thermal properties of and inside the $KSO_{orig.}$ housing (see Figure 4.37). Further each spray-test triggered a decrease in $|\Delta T_b|$ following an exponential form for about 30 minutes.

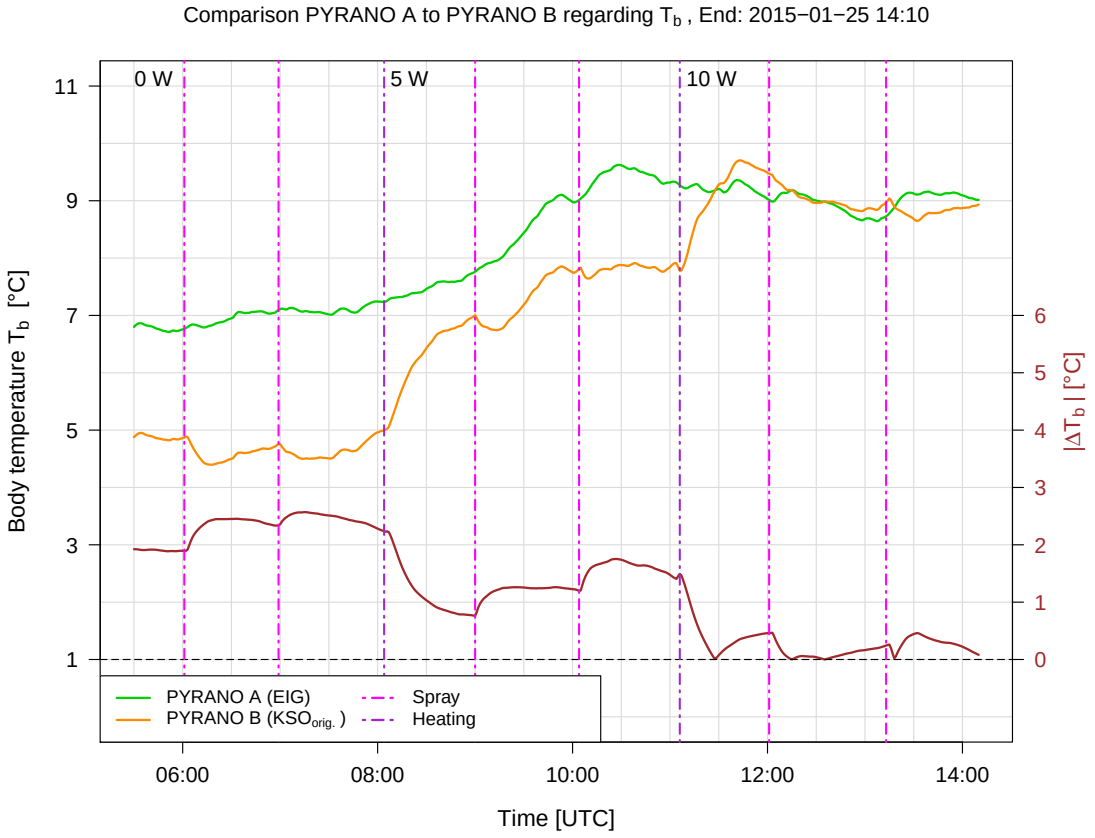

Figure 4.37: As Figure 4.28 but for comparison of body temperatures T_b [°C] measured with reference (*PYRANO A*, CMP 21, Eigenbrodt housing, green) and experimental pyranometers (*PYRANO B*, CMP 21, KSO original housing, orange) between 2015-01-25 05:00 UTC and 2015-01-25 14:10 UTC. Dark orchid dashed vertical lines indicate changes in heating power for *PYRANO B* at 2015-01-25 08:04 UTC and at 2015-01-25 11:06 UTC; heating power [W] for individual periods is detailed at the top of the graph. The magenta dashed vertical lines mark spray-tests at 2015-01-25 06:01 UTC, at 06:59 UTC, at 09:00 UTC, at 10:04 UTC, at 12:01 UTC and at 13:13 UTC.

4.2.4 Analysis of measurements for pyranometers contained in an Eigenbrodt SBL 480 (reference) and KSO modified (experimental) housing

To investigate if a different setup of the heating system inside the KSO housing would mitigate nighttime offsets relative to the Eigenbrodt SBL 480 reference a series of experiments with slightly raised heating elements (5 mm, 10 mm and 15 mm above standard configuration height) was performed.

The first modification occurred between 2015-01-25 14:23 UTC and 2015-01-25 15:50 UTC when the heating ring of the KSO housing was raised 5 mm using a self-built (by Mag. Dietmar Baumgartner and KSO colleagues) 20 mm wide aluminium ring with the same diameter as the upper base plate and four distance sleeves (made of plastic for insulation) which were mounted between the base plate and the ring (see Figure 4.38). This configuration of the KSO housing is hereinafter referred to as $KSO_{5\,mm}$.

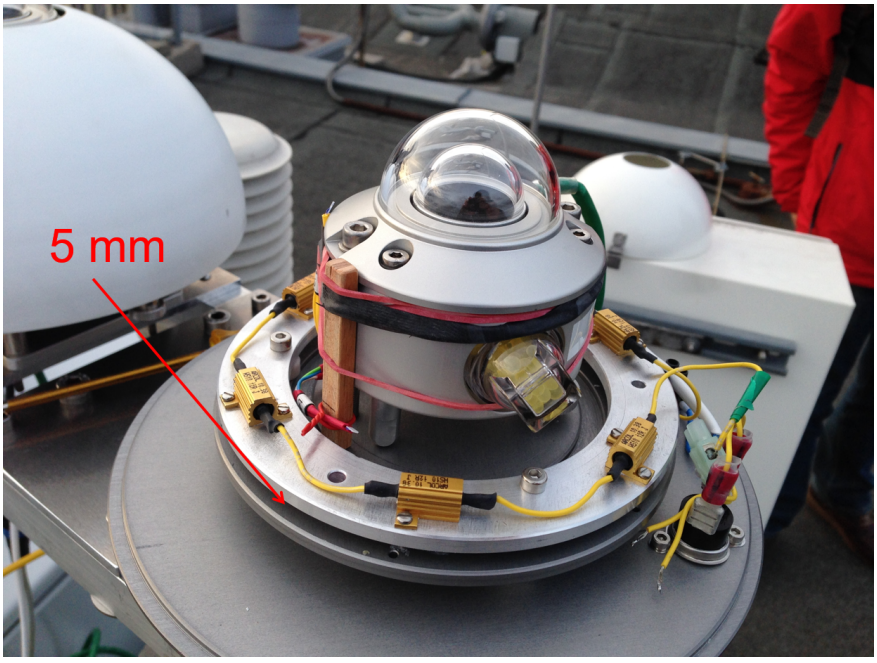

Figure 4.38: Experimental radiation sensor *PYRANO B* and its modification of the heating elements elevated by 5 mm (marked with the red arrow) realized by an aluminium ring with a width of 20 mm and four distance sleeves.

The time series of radiation output from the pyranometer contained in the $KSO_{5\,mm}$ housing between 2015-01-25 16:00 UTC and 2015-01-26 05:00 UTC is shown in Figure 4.39. Against expectation the raised heating system did not improve instrument performance as $|\Delta R|$ varied around 2.5 W m^{-2} at a heating power of only 5 W. At 20:54 UTC the heating level of *PYRANO B* was raised to 10 W and shortly after $|\Delta R|$ increased by an additional 1 W m^{-2}. Interestingly switching off the heating system did not stabilize the sensor mounted in $KSO_{5\,mm}$ over the time period considered as $|\Delta R|$ remained at roughly 1.7 W m^{-2} over several hours, and thus slightly larger than during operation of the $KSO_{orig.}$ housing. Spray-tests showed effects similar to those seen for other housing configurations before ($KSO_{orig.}$ and Eigenbrodt SBL 480), with values of $|\Delta R|$ between 5.6 W m^{-2} (23:53 UTC) and 8 W m^{-2} (22:45 UTC).

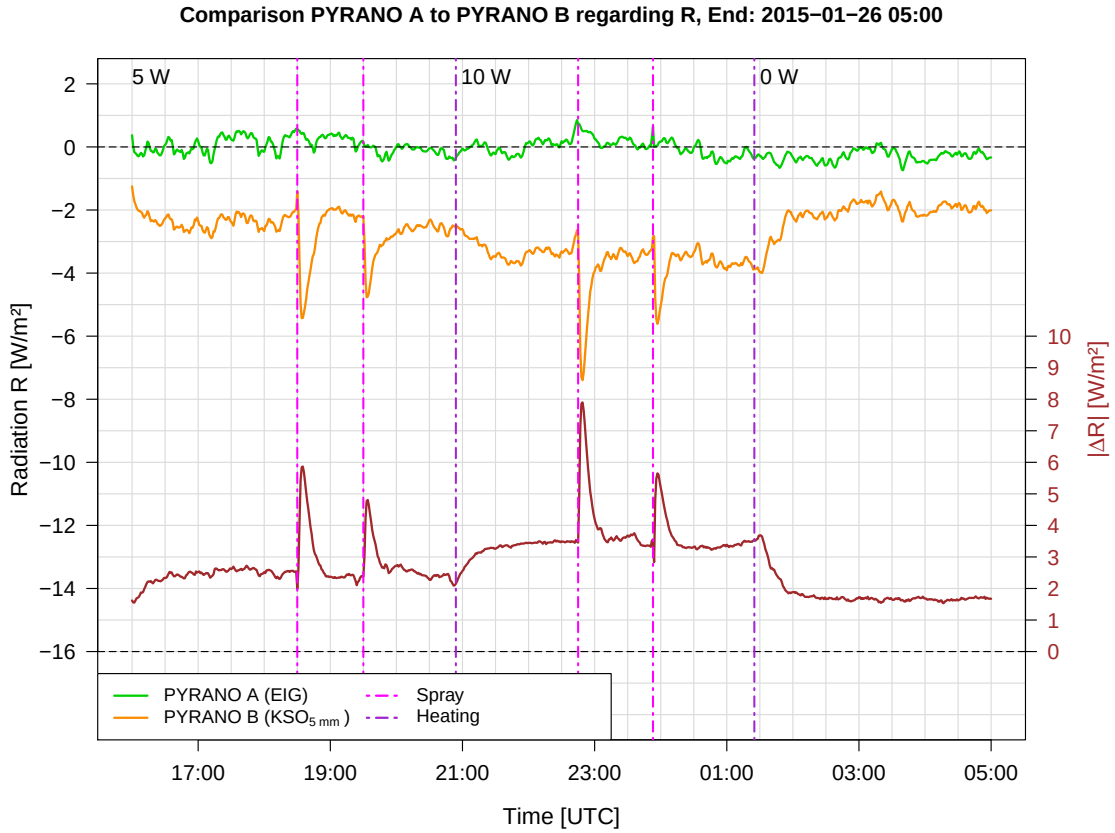

Figure 4.39: As Figure 4.26 but for comparison of radiation R [W m^{-2}] measured with reference (*PYRANO A*, CMP 21, Eigenbrodt housing, green) and experimental pyranometers (*PYRANO B*, CMP 21, KSO housing, heating elements elevated by 5 mm, orange) between 2015-01-25 16:00 UTC and 2015-01-26 05:00 UTC. Dark orchid dashed vertical lines indicate changes in heating power for *PYRANO B*on 2015-01-25 20:54 UTC and on 2015-01-26 01:25 UTC; heating power [W] for individual periods is detailed at the top of the graph. The magenta dashed vertical lines mark spray-tests at 2015-01-25 18:30 UTC, at 19:30 UTC, at 22:45 UTC and at 23:53 UTC.

The body temperatures for the reference pyranometer and the sensor mounted in the $KSO_{5\,mm}$ housing are shown in Figure 4.40 for the period between 2015-01-25 16:00 UTC and 2015-01-26 05:00 UTC). At the beginning of the time series $|\Delta T_b|$ plateaued at a value of $0.4\,°C$. Spray-tests have been performed at 18:30 UTC and 19:30 UTC triggering a decline of the body temperature of *PYRANO B*. Further, once the heating power was raised from 5 to $10\,W$ shortly before 21:00 UTC, T_b of the experimental pyranometer increased strongly compared to the body temperature of *PYRANO A*. As the body temperature of *PYRANO B* exceeded those of *PYRANO A* the difference $|\Delta T_b|$ followed a reverse exponential curve after the spray-tests at 22:45 UTC and 23:53 UTC. After the heating power of *PYRANO B* was turned off, the difference between the body temperature of the two pyranometers reached about $1.8\,°C$.

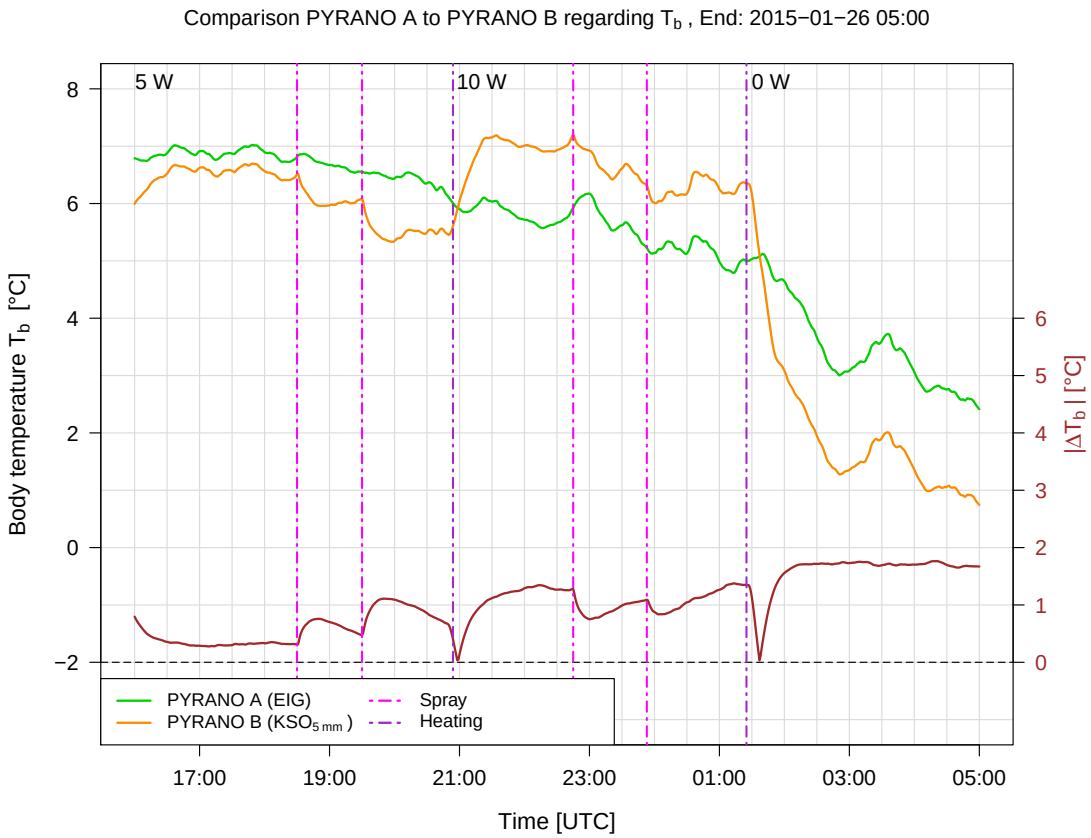

Figure 4.40: As Figure 4.28 but for comparison of body temperatures T_b [°C] measured with reference (*PYRANO A*, CMP 21, Eigenbrodt housing, green) and experimental pyranometers (*PYRANO B*, CMP 21, KSO housing, heating elements elevated by 5 mm, orange) between 2015-01-25 16:00 UTC and 2015-01-26 05:00 UTC. Dark orchid dashed vertical lines indicate changes in heating power for *PYRANO B* on 2015-01-25 20:54 UTC and on 2015-01-26 01:25 UTC; heating power [W] for individual periods is detailed at the top of the graph. The magenta dashed vertical lines mark spray-tests on 2015-01-25 18:30 UTC, at 19:30 UTC, at 22:45 UTC and at 23:53 UTC.

Figure 4.41 shows a comparison of temperatures recorded with PT100 elements in the Eigenbrodt SBL 480 (reference) and $\mathrm{KSO}_{5\,\mathrm{mm}}$ (experimental) housings. PT100 elements C4 and C5 characterize temperatures inside the housing (C4) and glass-dome temperatures (C5) of *PYRANO B*. Interestingly the difference between these two temperatures increased compared to the $\mathrm{KSO}_{\mathrm{orig.}}$ configuration by about $0.5\,°\mathrm{C}$ (see Figure 4.35). The difference between housing temperature (represented by C4) and glass-dome temperature (represented by C5) grew with increased heating level, as seen in Figure 4.41, reaching a difference to the reference pyranometer of $|\Delta R| \approx 3.5\,\mathrm{W\,m^{-2}}$ (see Figure 4.39).

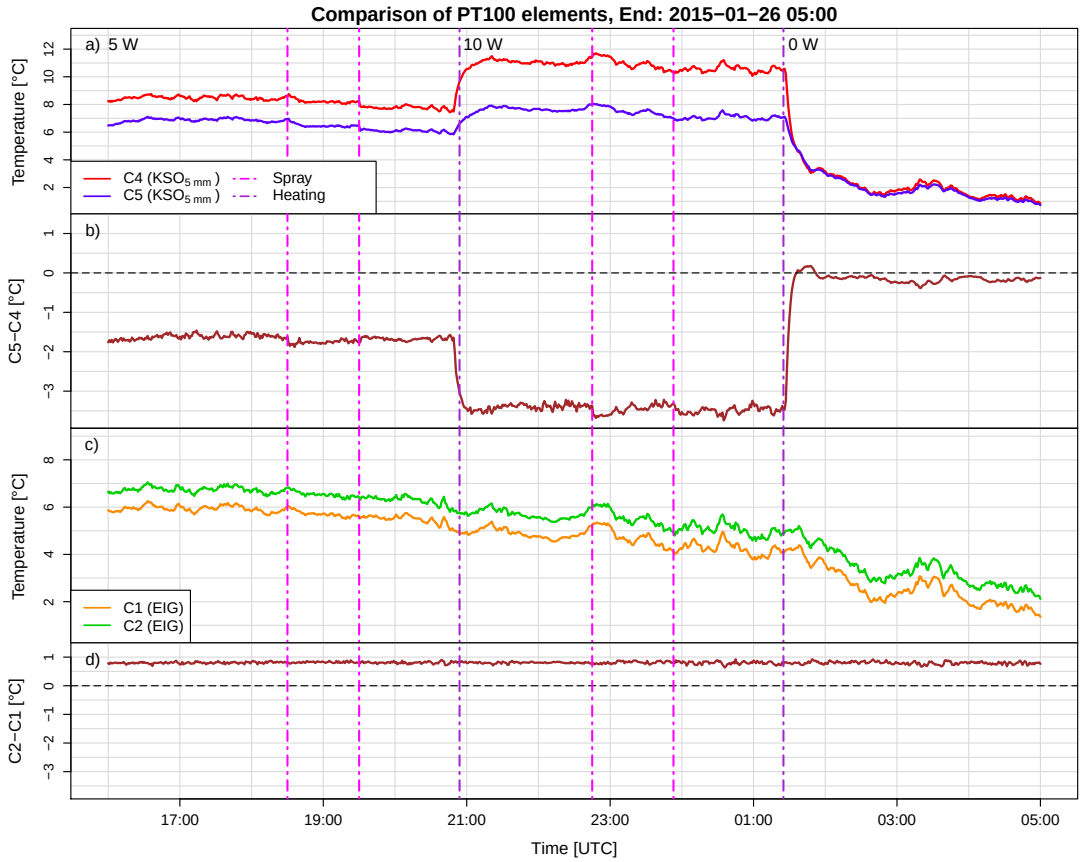

Figure 4.41: As Figure 4.29 but for comparison of C4 and C5 inside the experimental pyranometer (*PYRANO B*, CMP 21, KSO housing, heating elements elevated by 5 mm) between 2015-01-25 16:00 UTC and 2015-01-26 05:00 UTC. Dark orchid dashed vertical lines indicate changes in heating power for *PYRANO B* on 2015-01-25 20:54 UTC and on 2015-01-26 01:25 UTC; heating power [W] for individual periods is detailed at the top of the graph. The magenta dashed vertical lines mark spray-tests on 2015-01-25 18:30 UTC, at 19:30 UTC, at 22:45 UTC and at 23:53 UTC.

The next few paragraphs detail sensor evolution (R and T_b) during periods with heating level $0\,\mathrm{W}$ for the $\mathrm{KSO}_{5\,\mathrm{mm}}$ housing.

Figure 4.42 indicates radiation output of *PYRANO A* and *PYRANO B* and their difference $|\Delta R|$ at a steady heating power of $0\,\mathrm{W}$ for *PYRANO B* during which a series of three spray tests was performed. While two of this spray tests (at 06:01 UTC and 14:11 UTC) triggered similar responses, the third (at 07:07 UTC) resulted in a large $|\Delta R|$ close to $18\,\mathrm{W\,m^{-2}}$. The reason for this striking response is believed to be a change of ambient air temperature below freezing levels, thus the water impacting the dome during the spray-test froze on contact and caused a cold-shock response of the pyranometer.

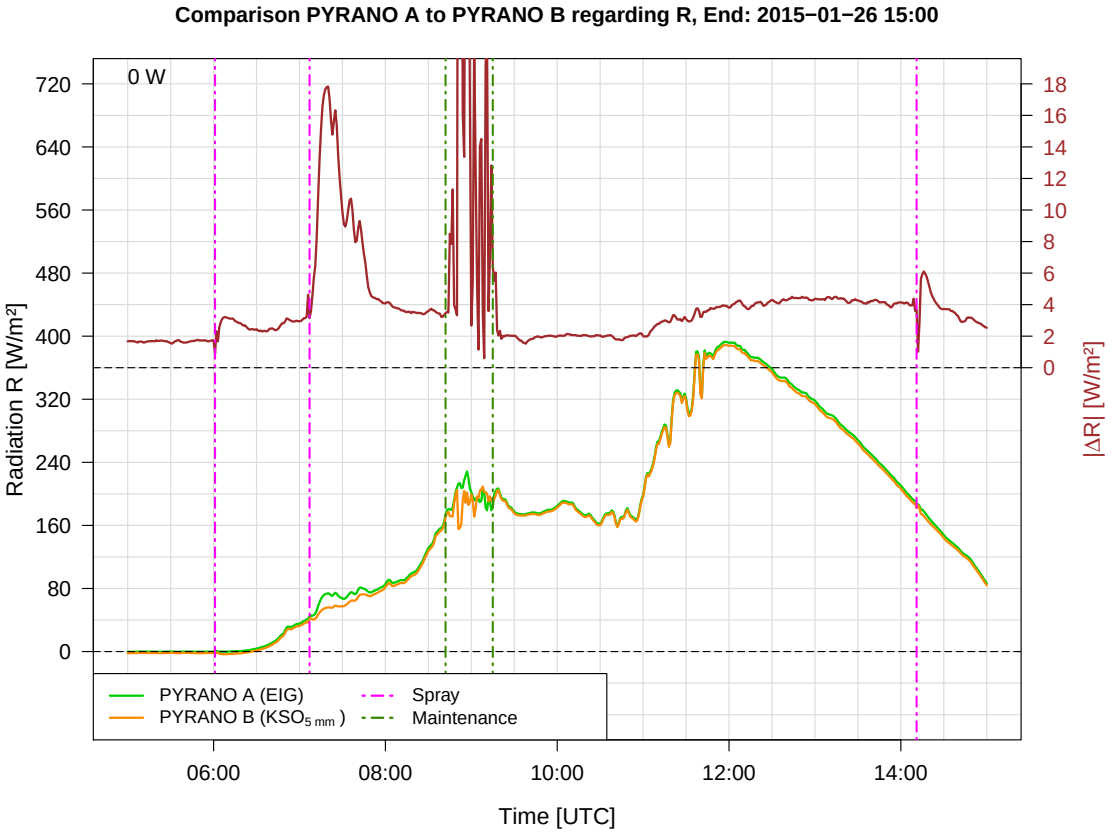

Figure 4.42: As Figure 4.39 but for comparison of radiation R [W m^{-2}] measured with reference (*PYRANO A*, CMP 21, Eigenbrodt housing, green) and experimental pyranometers (*PYRANO B*, CMP 21, KSO housing, heating elements elevated by 5 mm, orange) between 2015-01-26 05:00 UTC and 2015-01-26 15:00 UTC. The magenta dashed vertical lines mark spray-tests on 2015-01-26 06:01 UTC, at 07:07 UTC and at 14:11 UTC. The dark green dashed vertical lines mark a period of instrument maintenance between 2015-01-26 08:42 UTC and 2015-01-26 09:15 UTC.

The 07:07 UTC spray-test on *PYRANO B* is hardly visible in the time series of body temperatures shown in Figure 4.43, indicating that contact freezing did primarily influence glass-dome temperatures and not thermal stability inside the $\mathrm{KSO}_{5\,\mathrm{mm}}$ housing unit.

The second interesting case is shown in Figure 4.44 between 2015-01-26 15:00 UTC and 2015-01-27 05:00 UTC during which the heating level of *PYRANO B* was 0 W, i.e. heating has been manually switched off. Initially R of the reference and the experimental sensors showed an approximately constant offset of $\approx 1.5\,\mathrm{W\ m^{-2}}$. Over time four spray-tests (at 16:52 UTC, 18:37 UTC, 22:36 UTC and 23:56 UTC) have been performed resulting in values of $|\Delta R|$ between $\approx 2-3\,\mathrm{W\ m^{-2}}$. The most interesting feature of this time series occurred after the fourth spray-test, where both radiation sensors, disturbed (*PYRANO B*) and undisturbed (*PYRANO A*), increased slowly their output signal. *PYRANO A* reached values above $1.5\,\mathrm{W\ m^{-2}}$ for a few minutes and the experimental device progressed towards $0\,\mathrm{W\ m^{-2}}$; $|\Delta R|$ remained constant around $1.9\,\mathrm{W\ m^{-2}}$, indicating that an external effect must have impacted both devices.

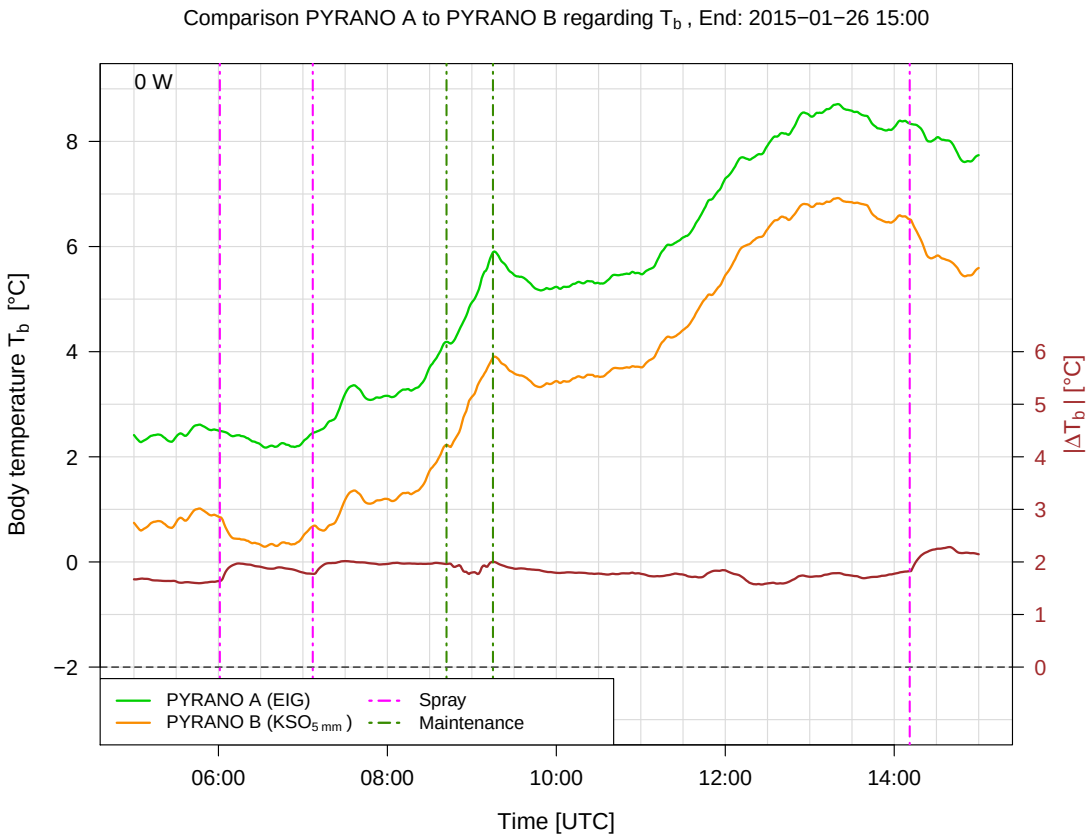

Figure 4.43: As Figure 4.40 but for comparison of body temperatures T_b [°C] measured with reference (*PYRANO A*, CMP 21, Eigenbrodt housing, green) and experimental pyranometers (*PYRANO B*, CMP 21, KSO housing, heating elements elevated by 5 mm, orange) between 2015-01-26 05:00 UTC and 2015-01-26 15:00 UTC. The magenta dashed vertical lines mark spray-tests on 2015-01-26 06:01 UTC, at 07:07 UTC and at 14:11 UTC. The dark green dashed vertical lines mark a period of instrument maintenance between 2015-01-26 08:42 UTC and 2015-01-26 09:15 UTC.

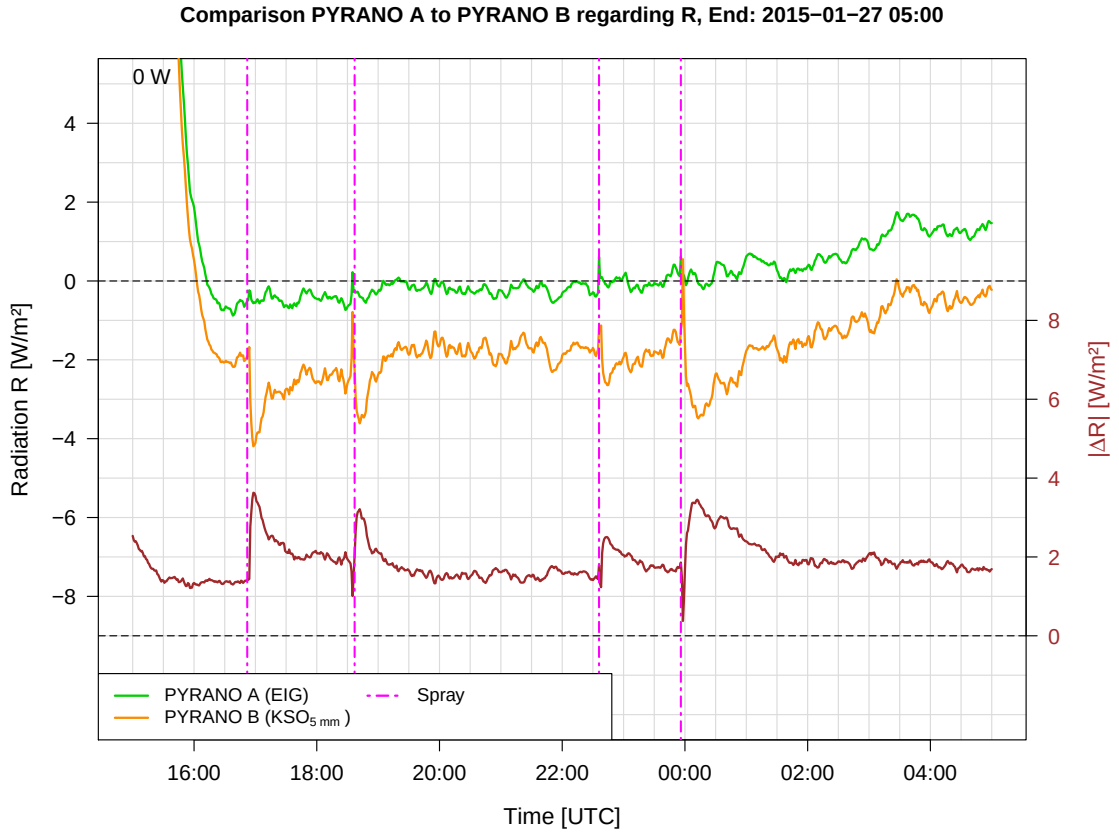

Figure 4.44: As Figure 4.39 but for comparison of radiation R [W m^{-2}] measured with reference (*PYRANO A*, CMP 21, Eigenbrodt housing, green) and experimental pyranometers (*PYRANO B*, CMP 21, KSO housing, heating elements elevated by 5 mm, orange) between 2015-01-26 15:00 UTC and 2015-01-27 05:00 UTC. The magenta dashed vertical lines mark spray-tests on 2015-01-26 16:52 UTC, at 18:37 UTC, at 22:36 UTC and at 23:56 UTC.

A little bit lagged (around 20 minutes) to the radiation response the body temperatures of both pyranometers began to increase by about $1.5\,^{\circ}$C within 30 minutes (see Figure 4.45). The body temperature of *PYRANO B* varied more or less after every experiment (at 16:52 UTC, 18:37 UTC, 22:36 UTC and 23:56 UTC) but the influence of water drops occurred mainly at the glass-dome.

The reason for the enhanced output signal of the reference and the experimental radiation sensors as well of *HIM* and *GLO* (see Figure 4.46) after 2015-01-27 02:00 UTC was found to be influence of net long-wave radiation (measured at the ARAD site Graz/University), shown in Figure 4.46. The radiation R measured by the pyrgeometer at ARAD site Graz/University increased steadily from 23:00 UTC to 02:30 UTC. Afterwards within 40 minutes the output signal of *LONG* (net) reached a value around -30 W m^{-2}. Over the same time period *PYRANO A* and *PYRANO B* and ARAD site Graz/University sensors *HIM* and *GLO* increased their output signals.

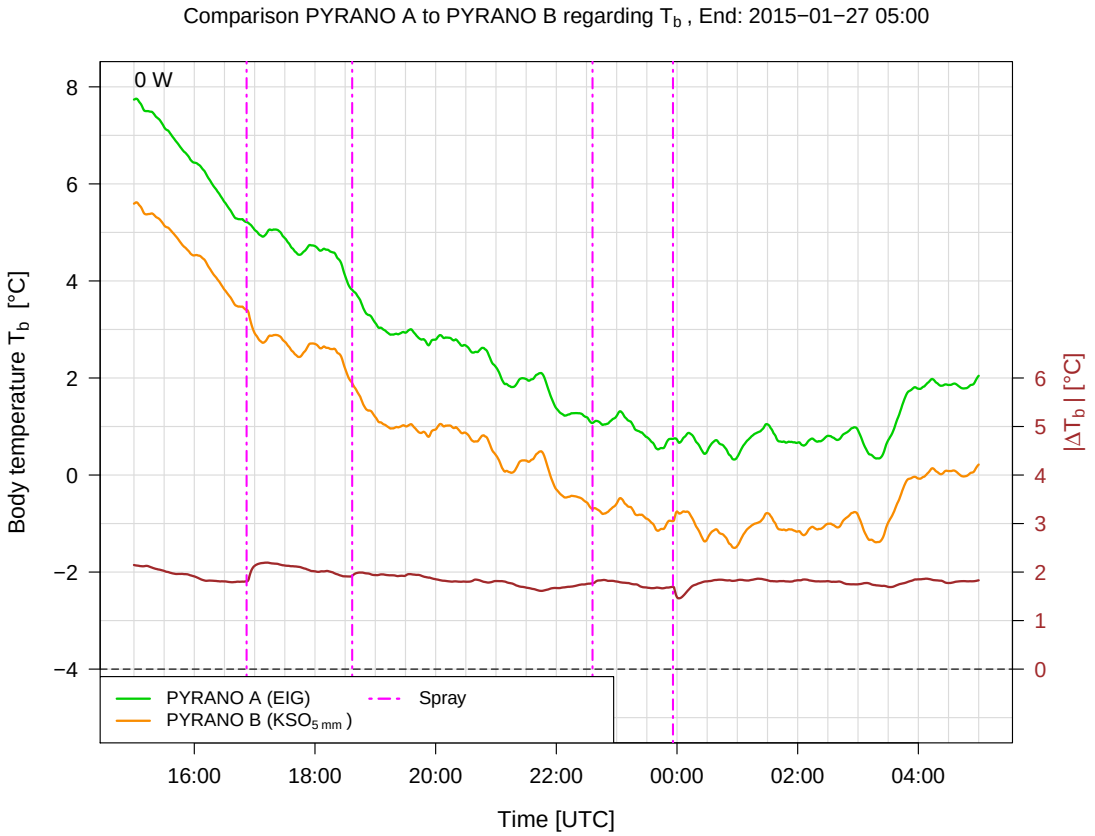

Figure 4.45: As Figure 4.40 but for comparison of radiation body temperatures T_b [°C] measured with reference (*PYRANO A*, CMP 21, Eigenbrodt housing, green) and experimental pyranometers (*PYRANO B*, CMP 21, KSO housing, heating elements elevated by 5 mm, orange) between 2015-01-26 15:00 UTC and 2015-01-27 05:00 UTC. The magenta dashed vertical lines mark spray-tests on 2015-01-26 16:52 UTC, at 18:37 UTC, at 22:36 UTC and at 23:56 UTC.

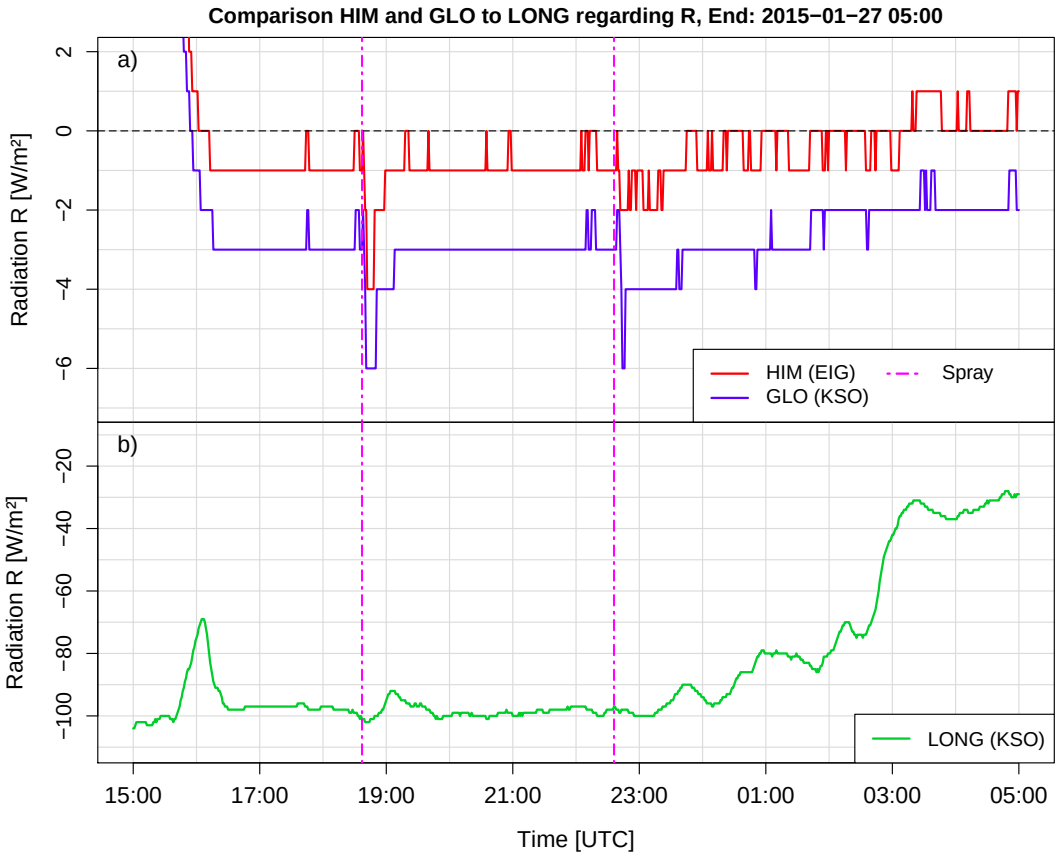

Figure 4.46: Comparison of radiation R [$\mathrm{W\,m^{-2}}$] measured at ARAD site Graz/University with sensors for diffuse (*HIM*: CMP 21, Eigenbrodt housing, red curve), global (*GLO*: CMP 21, KSO housing, blue curve) (both in panel a) and net long-wave radiation (*LONG*: CRG 4, KSO housing, lime-green curve) (panel b) between 2015-01-26 15:00 UTC and 2015-01-27 05:00 UTC. The magenta dashed vertical lines mark spray-tests on 2015-01-26 18:37 UTC and at 22:36 UTC.

Following the experiments with the $\mathrm{KSO_{5\,mm}}$ housing additional experiments have been performed with further raised distance of the heating ring to the upper base plate. The aim of the modifications to the experimental housing was to reduce the distance between heating elements and the glass-dome and to increase the temperature of the air flow without adjusting the heating level.

Thus the heating ring was elevated by additional $5\,\mathrm{mm}$ in the morning of January 27, 2015 (construction between 09:00 UTC and 09:20 UTC). On January 28, 2015 the heating ring got elevated another 5 mm (construction between 23:31 UTC and 23:44 UTC). These setups, referred to as $\mathrm{KSO_{10\,mm}}$ and $\mathrm{KSO_{15\,mm}}$ housings did unfortunately not improve the performance of *PYRANO B* compared to the reference pyranometer (*PYRANO A*) and original KSO housing. Therefore time series of sensor output during $\mathrm{KSO_{10\,mm}}$ and $\mathrm{KSO_{15\,mm}}$ operation are not further discussed here but shown for completeness in Appendices A and B (see Figures A.1 to B.3).

Overall the results of the experiments with modified KSO housings indicate that the general setup of the heating system (number of heating elements and/or their alignment, and/or their position in the air flow and/or their position (distance) around (to) the pyranometer body) might be responsible for the offset observed in comparison to the reference pyranometer.

Subsections 4.2.1 to 4.2.4 above provide a detailed discussion of effects observed during experiments with different pyranometer housings during the measurement campaign. A graphical protocol of all performed experiments is shown in Figure C.1 regarding the radiation R and in Figure C.2 regarding T_{b} (see Appendix C). The following subsections (4.2.5 to 4.2.8) focus on statistical investigations regarding the impact of spray-tests, the comparison of pyranometer body and glass-dome temperatures with ambient air temperature (during both relaxation and experimental periods), theoretical considerations/calculations based on sensor temperature and radiation records as well as comparisons of meteorological records obtained with different instruments during the measurement campaign.

4.2.5 Statistical analysis of spray-tests

As outlined in subsection 3.5.2 the amount of water impacting the glass-dome of pyranometers during standardized spray-tests (i.e., 30 strokes from $2-4$ cm distance) was determined as 3.35 g in laboratory analysis. This section discusses the statistical analysis regarding the impact of spray-tests on sensor output while contained in the Eigenbrodt SBL 480 and $\mathrm{KSO}_{\mathrm{orig.}}$ housing, respectively.

Tables 4.2 - 4.7 summarize information on ΔR^* the maximum difference between sensor output of *PYRANO B* and *PYRANO A* within 30 minutes following each spray-test; $\overline{\Delta R_{i=1}}$ the mean difference between sensor *PYRANO B* and *PYRANO A* during the 10 minutes prior the spray-test; $\overline{\Delta R_{i=2}}$ the mean difference between sensor *PYRANO B* and *PYRANO A* $30-39$ minutes after the spray-test; $\overline{\Delta R^* - \overline{\Delta R_i}}$, the average over differences of ΔR^* and $\overline{\Delta R_{i=1}}$ and ΔR^* and $\overline{\Delta R_{i=2}}$, respectively; as well as $\left|\overline{\Delta R_f}\right|$ the average over all values for $\overline{\Delta R^* - \overline{\Delta R_i}}$ in specific configurations .

Comparing these benchmark numbers for experiments using Eigenbrodt SBL 480 housings with different heating configurations indicates that the 10 W configuration (recommended by the manufacturer) as well as the 0 W configuration (unheated) seem to provide a more stable thermal environment for the experimental pyranometer than a heating level of 5 W. As obvious from Tables 4.2 - 4.4 differences in pyranometer response during individual spray-tests performed under the same heating level configuration occurred, most likely representing an overlying signal of ambient conditions.

Tables 4.5 - 4.7 provide information on the analysis for spray-tests during operation of the $\mathrm{KSO}_{\mathrm{orig.}}$ housing. In comparison to the Eigenbrodt SBL 480 housing, sensor output responses have been quite similar during operation at 10 and 5 W heating levels. As one might expect given the results outlined in the previous sections the pyranometer contained in the $\mathrm{KSO}_{\mathrm{orig.}}$ housing showed (compared to the reference pyranometer) the smallest response while ventilated but unheated.

In general the impact of spray-tests on pyranometers has been smallest, for both housings, under unheated conditions. Although, an important caveat, limited sample size for 0 W experiments (two vs. four each for 10 and 5 W, respectively) needs to be considered. Further, due to time constraints during the campaign only a limited number of spray-tests has been performed with the modified KSO housings (i.e, with the heating ring raised by 5, 10, 15 mm), which allow only limited comparison and are therefore not further addressed here.

Table 4.2: Statistical analysis of spray-tests regarding experimental pyranometer *PYRANO B* contained in Eigenbrodt SBL 480 housing at heating level of 10 W.

Time [UTC] / **Difference [W m^{-2}]**	16:05	16:56	12:57	13:59
Min. ΔR^*	-2.83	-2.17	-2.04	-3.10
$\overline{\Delta R_{i=1}}$ (10 minutes before)	0.36	0.86	0.26	0.79
$\overline{\Delta R_{i=2}}$ (30 − 39 minutes after)	0.99	0.70	0.56	0.69
$\overline{\Delta R^* - \overline{\Delta R_i}}$	-3.50	-2.95	-2.45	-3.84
$\lvert\overline{\Delta R_f}\rvert$	3.18			

Table 4.3: Statistical analysis of spray-tests regarding experimental pyranometer *PYRANO B* contained in Eigenbrodt SBL 480 housing at heating level of 5 W.

Time [UTC] / **Difference [W m^{-2}]**	20:09	22:10	09:18	10:36
Min. ΔR^*	-3.78	-4.76	-7.43	-7.73
$\overline{\Delta R_{i=1}}$	-0.18	0.11	-0.27	-0.24
$\overline{\Delta R_{i=2}}$	-0.33	-0.56	-0.31	0.10
$\overline{\Delta R^* - \overline{\Delta R_i}}$	-3.53	-4.53	-7.14	-7.66
$\lvert\overline{\Delta R_f}\rvert$	5.72			

Table 4.4: Statistical analysis of spray-tests regarding experimental pyranometer *PYRANO B* contained in Eigenbrodt SBL 480 housing at heating level of 0 W.

Time [UTC] / **Difference [W m^{-2}]**	05:57	07:01
Min. ΔR^*	-2.21	-2.49
$\overline{\Delta R_{i=1}}$	-1.15	-0.96
$\overline{\Delta R_{i=2}}$	-1.06	-0.81
$\overline{\Delta R^* - \overline{\Delta R_i}}$	-1.15	-1.61
$\lvert\overline{\Delta R_f}\rvert$	1.38	

Table 4.5: Statistical analysis of spray-tests regarding experimental pyranometer *PYRANO B* contained in KSO original housing at heating level of 10 W.

Time [UTC] / **Difference [W m^{-2}]**	19:52	21:34	12:01	13:13
Min. ΔR^*	-5.13	-5.76	-6.20	-9.66
$\overline{\Delta R_{i=1}}$	-2.16	-1.54	-2.84	-2.46
$\overline{\Delta R_{i=2}}$	-2.03	-1.40	-2.40	-2.79
$\overline{\Delta R^* - \overline{\Delta R_i}}$	-3.04	-4.29	-3.58	-7.03
$\left\lvert\overline{\Delta R_f}\right\rvert$	4.49			

Table 4.6: Statistical analysis of spray-tests regarding experimental pyranometer *PYRANO B* contained in KSO original housing at heating level of 5 W.

Time [UTC] / **Difference [W m^{-2}]**	01:15	02:30	09:00	10:04
Min. ΔR^*	-4.86	-5.39	-6.18	-10.51
$\overline{\Delta R_{i=1}}$	-1.59	-1.22	-1.74	-1.63
$\overline{\Delta R_{i=2}}$	-1.47	-1.47	-2.43	-2.28
$\overline{\Delta R^* - \overline{\Delta R_i}}$	-3.33	-4.05	-4.09	-8.56
$\left\lvert\overline{\Delta R_f}\right\rvert$	5.00			

Table 4.7: Statistical analysis of spray-tests regarding experimental pyranometer *PYRANO B* contained in KSO original housing at heating level of 0 W.

Time [UTC] / **Difference [W m^{-2}]**	06:01	06:59
Min. ΔR^*	-2.78	-1.74
$\overline{\Delta R_{i=1}}$	-0.53	-0.08
$\overline{\Delta R_{i=2}}$	-0.64	-0.08
$\overline{\Delta R^* - \overline{\Delta R_i}}$	-2.19	-1.66
$\left\lvert\overline{\Delta R_f}\right\rvert$	1.93	

4.2.6 Comparison of pyranometer body temperature(s) with ambient air temperature

As described in Kipp&Zonen (2010) the body temperature T_{b} of pyranometers depends (strongly) on ambient air temperature T_a. To determine the relationship between pyranometer body temperatures and ambient air temperature data obtained with PT 100 element C3 (co-located at experimental platform, mounted in a multi-plate radiation shield) and MobMet (thermistor, co-located in vicinity of the experimental platform) have been used. The relationship between individual temperature pairs was determined using the Kendall rank correlation coefficient (Cor) and a coefficient of determination (Var), which is Cor squared (Schönwiese, 2006). Calculations have been performed using the ‚base' package within R (R Core Team, 2014).

First the focus is drawn to the comparison between the body temperature of the reference pyranometer ($T_{\mathrm{b,PA}}$) and ambient air temperature. To this aim Figure 4.47 shows the time series of $T_{\mathrm{b,PA}}$, C3 and MobMet (both T_a) obtained during the measurement campaign. To account for short-term fluctuations of individual sensor recordings, which could occur simply due to sensor noise, all three time series have been smoothed with a symmetric 30 minute moving average filter. Panel (a) of Figure 4.47 provides a comparison of the time series of $T_{\mathrm{b,PA}}$ to C3. The two temperature curves are evolving parallel but show a constant offset of a few °C. The rank correlation after Kendall yields a value of Cor $= 0.93$, with a coefficient of determination Var $= 0.87$. The comparison of $T_{\mathrm{b,PA}}$ to MobMet yields slightly lower values, Cor $= 0.85$ and Var $= 0.73$ (see Figure 4.47b). Panel (c) provides a comparison of ambient air temperature measurements of C3 and MobMet. Between 2015-01-23 and 2015-01-25 hardly any difference in ambient air temperature readings is found among the two sensors. From 2015-01-26 and 2015-01-29 the temperature curves diverge a little with generally lower readings for MobMet than C3. The reason for this diverging tendency can be explained by different positions and height levels on the rooftop, exposing sensors slightly different to changes in wind direction and wind speed.

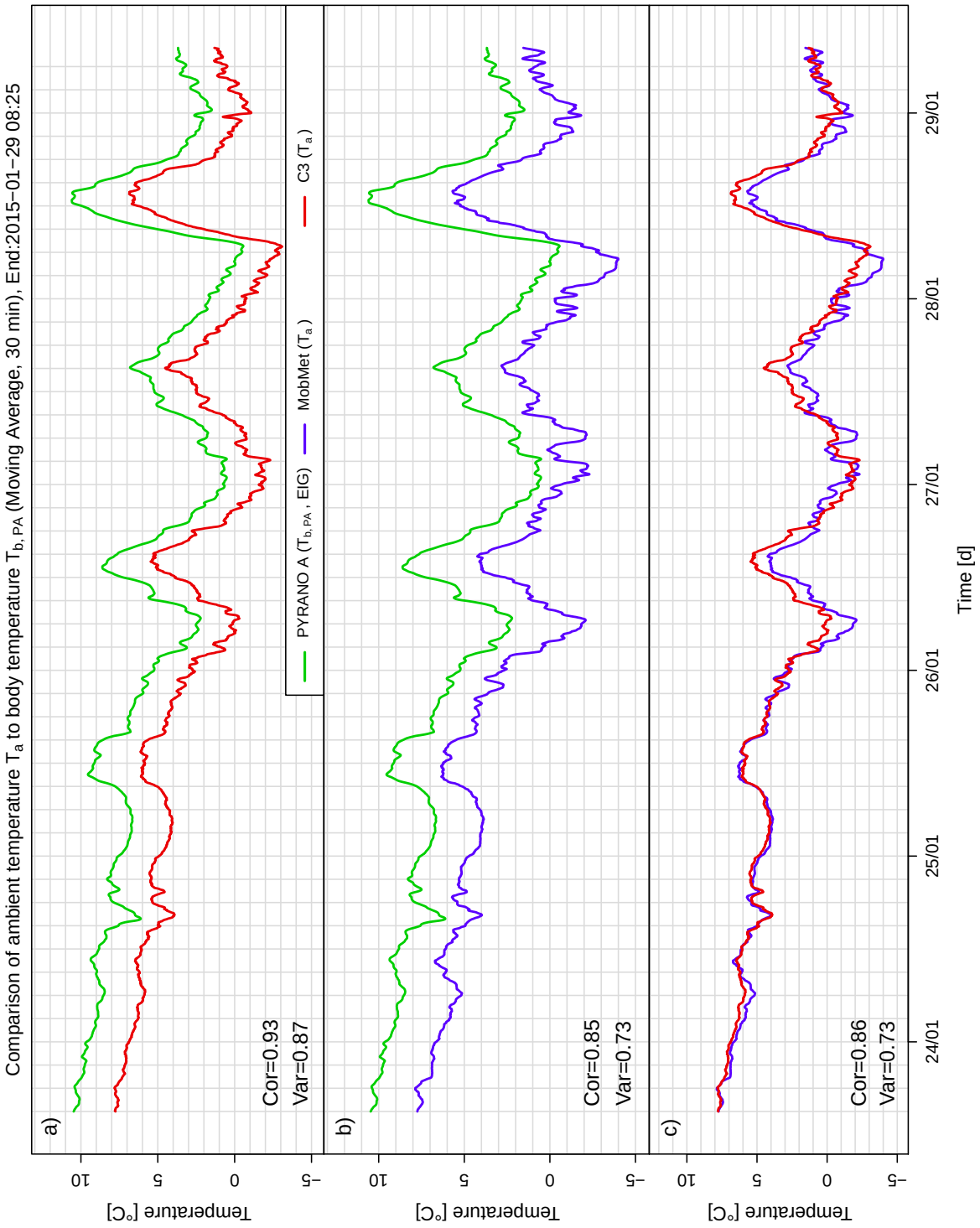

Figure 4.47: Comparison of ambient air temperature T_a [°C] measured with two instruments (C3 and MobMet) and body temperature $T_{\mathrm{b,PA}}$ [°C] measured with reference (*PYRANO A*, CMP 21, Eigenbrodt housing, green) between 2015-01-23 15:00 UTC and 2015-01-29 08:25 UTC. For convenience C3 and MobMet are compared with each other in the third sub-figure (c). Kendall rank correlation coefficient (Cor) and coefficient of determination ($\mathrm{Cor}^2 = \mathrm{Var}$) indicate the degree of association between two measured quantities, state in lower left-hand corner of each sub-figure.

Figure 4.48 shows a scatterplot of temperature readings of $T_{\mathrm{b,PA}}$ and C3. In total N $= 8246$ observational points (1 minute averages, green open dots) are compared. The red line is the regression line indicating a strong linear relationship of $T_{\mathrm{b,PA}}$ and C3 and on offset $T_{\mathrm{b,PA}} - \mathrm{C3} \approx 2.6\,^{\circ}\mathrm{C}$. Statistics for 1 minute data are Cor $= 0.90$ and Var $= 0.81$, which are, as expected, slightly lower than those for the smoothed time series.

As similar difference as for $T_{\mathrm{b,PA}}$ and C3 was found for $\overline{T}_{\mathrm{HIM}}$ and $\overline{T}_{\mathrm{wg}}$ from June 2013 to May 2014 (see Figures 4.49(a) and 4.49(c)) confirming the strong relationship between pyranometer body temperature and ambient air temperature. Differences between $\overline{T}_{\mathrm{GLO}}$ and $\overline{T}_{\mathrm{wg}}$ showed a similar pattern but slightly more seasonal variation (see Figures 4.49(b) and 4.49(d)).

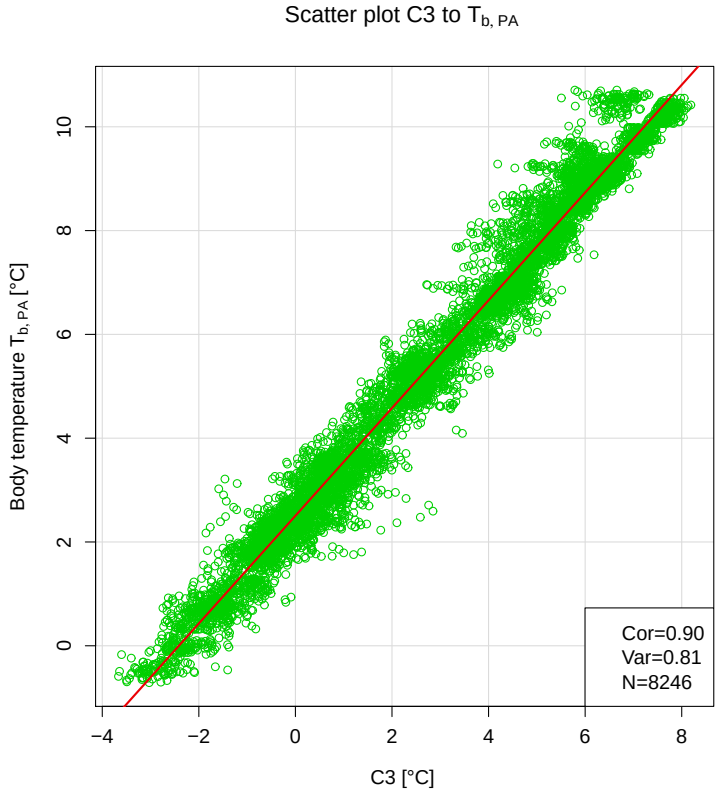

Figure 4.48: Scatter plot between the PT100 element C3 [°C] and the body temperature of the reference pyranometer $T_{\mathrm{b,PA}}$ [°C] (*PYRANO A*, CMP 21, Eigenbrodt housing) between 2015-01-23 15:00 UTC and 2015-01-29 08:25 UTC. Kendall rank correlation coefficient (Cor) and coefficient of determination ($\mathrm{Cor}^2 = \mathrm{Var}$) indicate the degree of association between the two measured quantities, N represents the number of values; all three variables are indicated in lower right-hand corner.

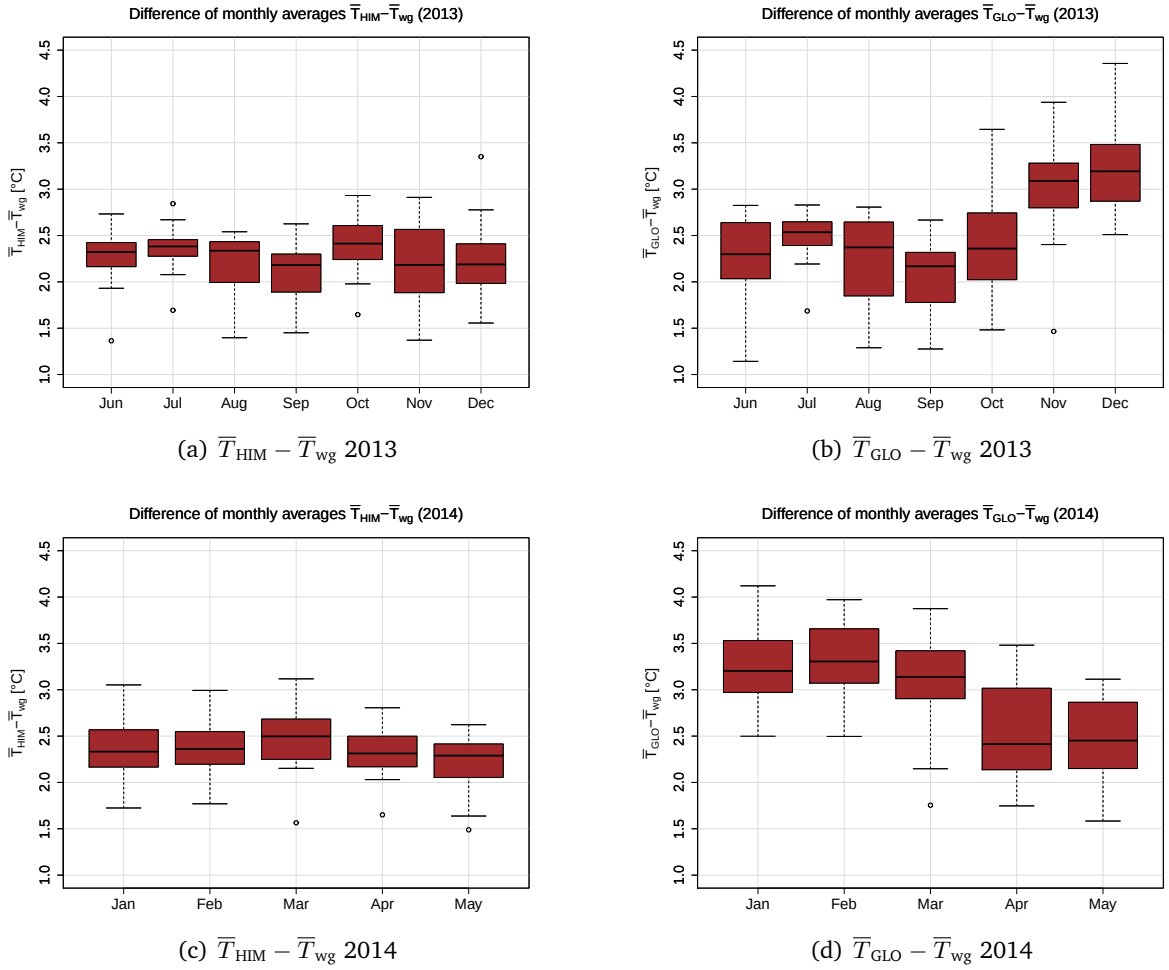

(a) $\overline{T}_{\mathrm{HIM}} - \overline{T}_{\mathrm{wg}}$ 2013

(b) $\overline{T}_{\mathrm{GLO}} - \overline{T}_{\mathrm{wg}}$ 2013

(c) $\overline{T}_{\mathrm{HIM}} - \overline{T}_{\mathrm{wg}}$ 2014

(d) $\overline{T}_{\mathrm{GLO}} - \overline{T}_{\mathrm{wg}}$ 2014

Figure 4.49: Monthly Box-Whisker plots of (a) difference [°C] between the body temperature of the pyranometer measuring diffuse radiation (*HIM*) at ARAD site Graz/University $\overline{T}_{\mathrm{HIM}}$ and average ambient air temperature at TAWES site Graz/University $\overline{T}_{\mathrm{wg}}$, (b) difference [°C] between the body temperature of the pyranometer measuring global radiation (*GLO*) at ARAD site Graz/University $\overline{T}_{\mathrm{GLO}}$ and average ambient air temperature at TAWES site Graz/University $\overline{T}_{\mathrm{wg}}$; (a)-(b) for June to December 2013; (c) as (a) and (d) as (b); but for January to May 2014.

Next the ambient air temperature measurements of C3 and MobMet are compared with the body temperature of *PYRANO B* (see Figure 4.50). Despite various changes in housings, heating levels and reoccurring influence by experiments (spray-tests and capping experiments) $T_{\mathrm{b,PB}}$ and ambient sensors (C3 and MobMet) show joint patterns and co-evolvement. Statistics are: Cor $= 0.75$ and Var $= 0.57$ for C3 and Cor $= 0.73$ and Var $= 0.53$ for MobMet, respectively. $T_{\mathrm{b,PB}}$ shows largest difference to C3 and MobMet during periods where *PYRANO B* was contained in a KSO housing with a heating power of $10\,\mathrm{W}$.

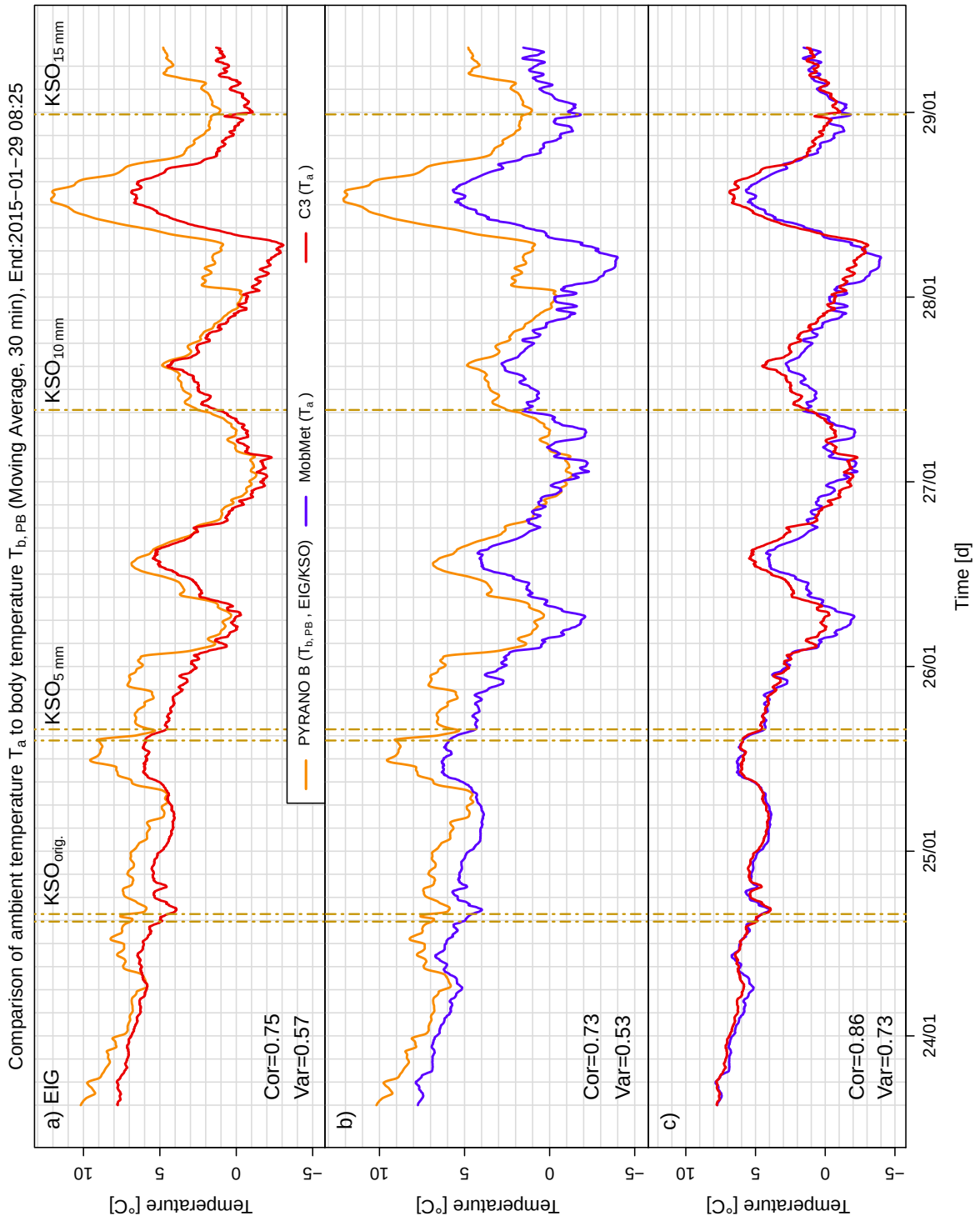

Figure 4.50: As Figure 4.47 but for comparison of body temperature $T_{b,PB}$ [°C] measured with experimental pyranometer (*PYRANO B*, CMP 21, EIG or KSO housing, heating elements elevated by different hight, orange) between 2015-01-23 15:00 UTC and 2015-01-29 08:25 UTC. Goldenrod dashed vertical lines indicate changes in instrument housing between Eigenbrodt and KSO as well as height adjustments in the heating elements within the KSO housing; heating element adjustments for individual periods are detailed in the top of the graph.

Observations with $T_{\mathrm{b,PB}}$ way higher/lower or approximately equal to ambient air temperature T_a are easier identified in Figure 4.51. The regression line of $T_{\mathrm{b,PB}}$ and C3 splits the data cloud into two parts: data points left of the regression line stem (in majority) from periods with heating power at $10\,\mathrm{W}$, (note: the difference $T_{\mathrm{b,PB}} - \mathrm{C3}$ varied between 3.5 and $5.5\,°\mathrm{C}$), while data points right of the regression line stem (in majority) from periods where the heating power was turned off.

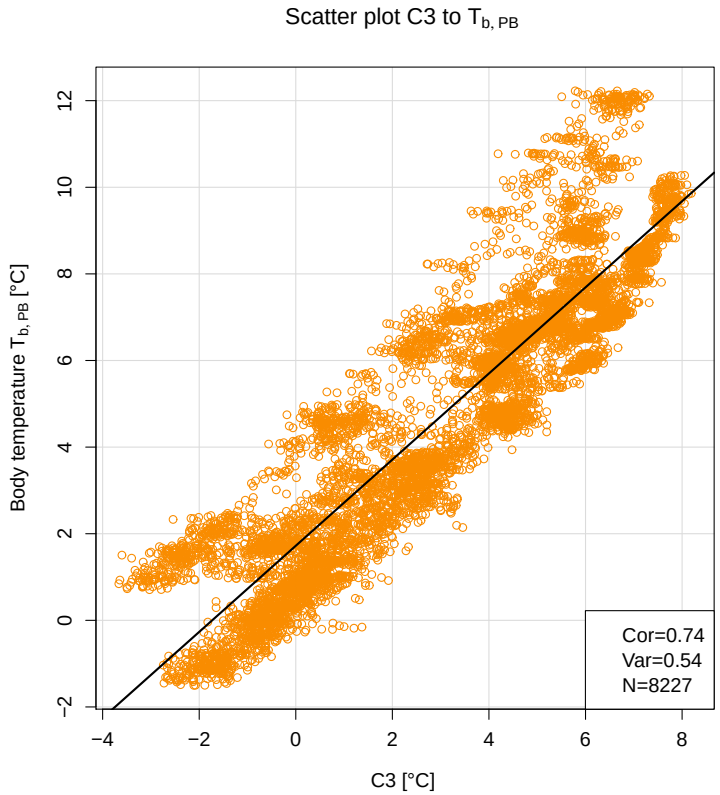

Figure 4.51: As Figure 4.48 but with measurements of the body temperature of the experimental pyranometer $T_{\mathrm{b,PB}}$ [°C] (*PYRANO B*, CMP 21, EIG or KSO housing, heating elements elevated by different mm).

4.2.7 Theoretical black body radiative exchange

The question arises if the thermal offset of a pyranometer, arising by radiative heat exchange between the instruments glass-dome and the sensing element, can be empirically corrected? An extensive literature review revealed that although the problem of thermal offsets is well known (Kipp&Zonen, 2010) its empirical correction is hardly addressed in the scientific literature. The master thesis of Bernando C. A. Domínguez titled ‚Characterization of Pyranometer Thermal Offset and Correction of Historical Data‘, supervised by M. P. Haeffelin, J. R. Mahan and E. P. Scott provides to date the only theoretical and empirical guidance on this problem. Domínguez (2001) investigated thermal offsets for a Eppley precision spectral pyranometers (PSP). To correct for this thermal offset the temperature gradient between the pyranometer's inner glass-dome and the detector was measured (invasively) with thermistors. The observational series of temperature gradients was then used to establish empirical correlations between the theoretical black body radiative exchange and the PSP output signal, yielding an empirical correction function for the offset.
The offset can be expressed as

$$\text{Offset} = G\,\sigma\left(T_\text{d}^4 - T_\text{b}^4\right) + H \tag{4.1}$$

where G and H are the slope and T_d is the temperature of the glass-dome.

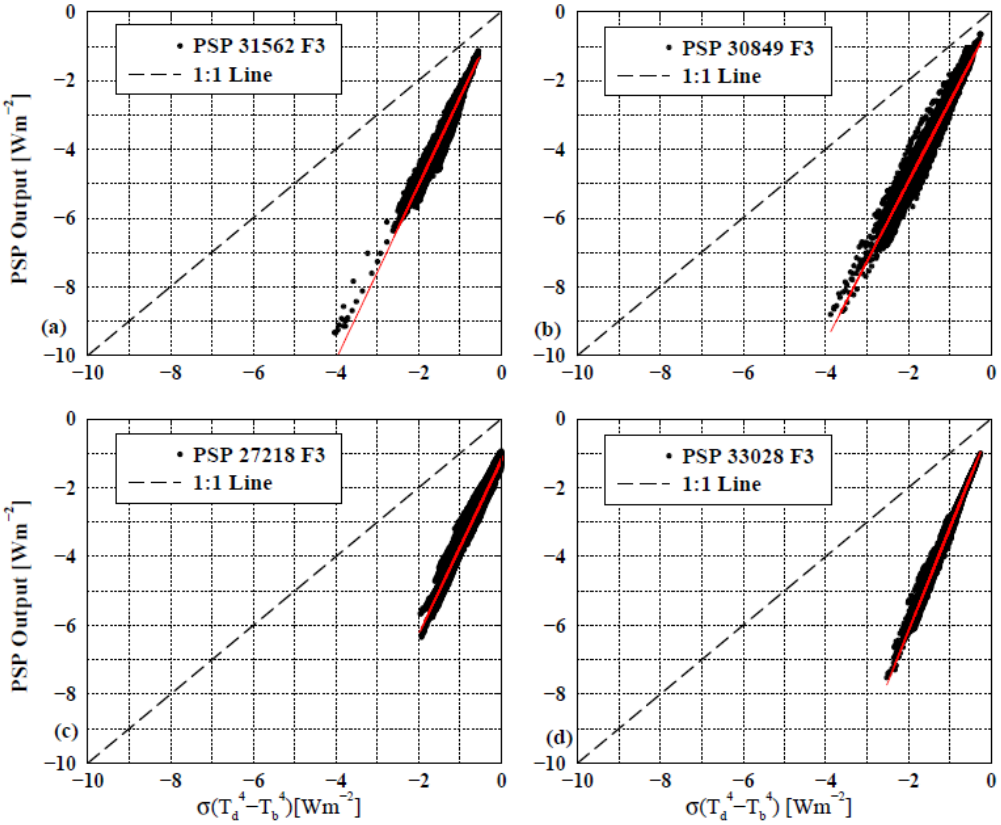

Figure 4.52: Theoretical blackbody radiative exchange between the glass-dome T_d [K] and the body temperature T_b [K] versus the output signal of the precision spectral pyranometer (PSP) [W m^{-2}]. The numbers near PSP in the figure legend indicate instrument serial numbers. The black dashed diagonal lines mark the identity lines while the solid red lines are regression lines. Source: (Domínguez, 2001)

As shown in Figure 4.52 of the nighttime output (thermal offset) with the theoretical black body radiative exchange represented by $\sigma\,(T_{\mathrm{d}}^4 - T_{\mathrm{b}}^4)$ [W m^{-2}] could be identified (explained variance ranged between Var $= 0.97$ and Var $= 0.99$ among PSPs). Thus Eq. 4.1 was used by Domínguez for the correction of the thermal offset during nighttime conditions. After correction all nighttime radiation values have been above $0\,\mathrm{W\,m^{-2}}$ (see Figure 4.53), proving the effectiveness of the correction method (Domínguez, 2001).

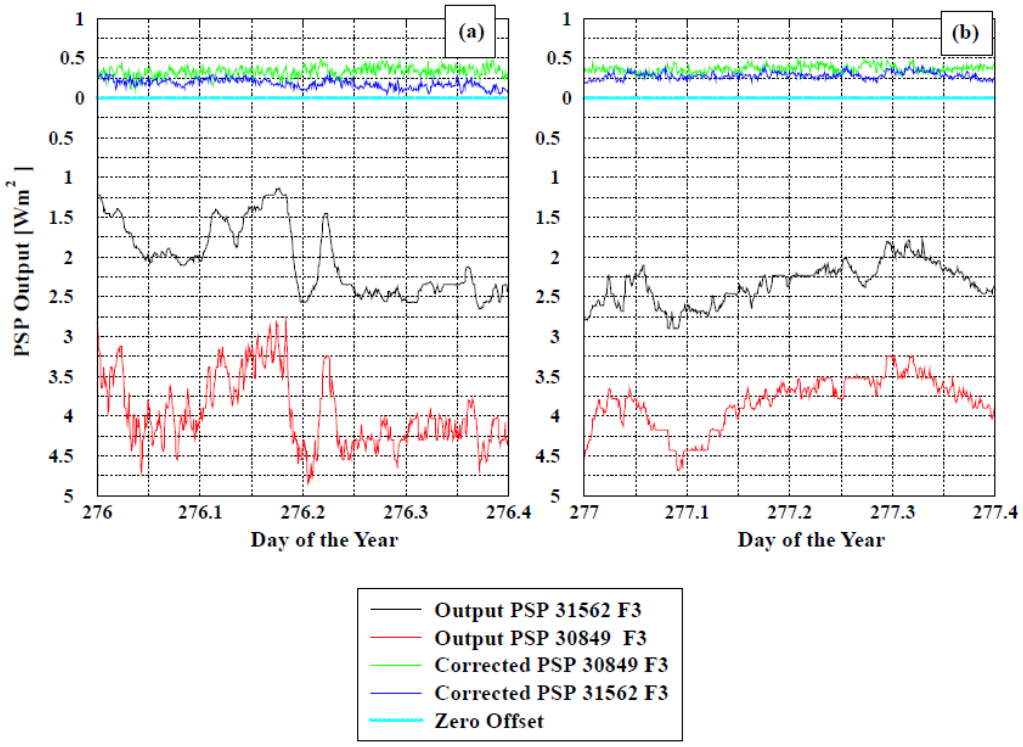

Figure 4.53: Time Series of standard (black and red curve) and corrected (green and blue curve) PSP output [W m^{-2}] for (a) October 2, 2000 (day of the year 276) and (b) October 3, 2000 (day of the year 277). The cyan horizontal lines mark $0\,\mathrm{W\,m^{-2}}$ for PSP Output. Source: (Domínguez, 2001)

A major caveat of the proposed methodology by Domínguez (2001) is that it is invasive, i.e. the outer glass-dome of the PSPs needed to be drilled to allow for direct temperature measurements of the inner glass-dome. As such invasive procedure could not be pursued in this thesis work, due to the costs expected for the replacement of damaged instruments, a slightly different approach generally following the methodology of Domínguez (2001) was chosen. As outlined above PT100 elements C2 (*PYRANO A*) and C5 (*PYRANO B*) have been considered to represent the temperature of the inner glass-dome in close approximation. Therefore the theoretical black body radiative exchange was calculated using measurements of C2 T_{C2} and the body temperature of the reference pyranometer $T_{\mathrm{b,PA}}$ in relationship to its output signal. It is noted that only the reference pyranometer is used for calculations as output of *PYRANO B* was the majority of the time impacted by experiments.

Figure 4.54 shows the theoretical black body radiative exchange calculated by the measurements of C2 T_{C2} and the body temperature of the reference pyranometer $T_{\mathrm{b,PA}}$ in relationship to the output signal of *PYRANO A* between 18:00 UTC and 04:00 UTC for all campaign days expect the January

22, 2015. The scatter plot shows a large bandwidth of the night values, $\sigma(T_{C2}^4 - T_{b,PA}^4)$ ranged from $-4\,W\,m^{-2}$ to $5.5\,W\,m^{-2}$ while *PYRANO A* radiation output varied between $-1.6\,W\,m^{-2}$ and $2\,W\,m^{-2}$. Statistical calculations yield a low explained variance of the output signal of only 14%. Such weak statistical relationship allows unfortunately not for a correction of the nighttime thermal offset observed.

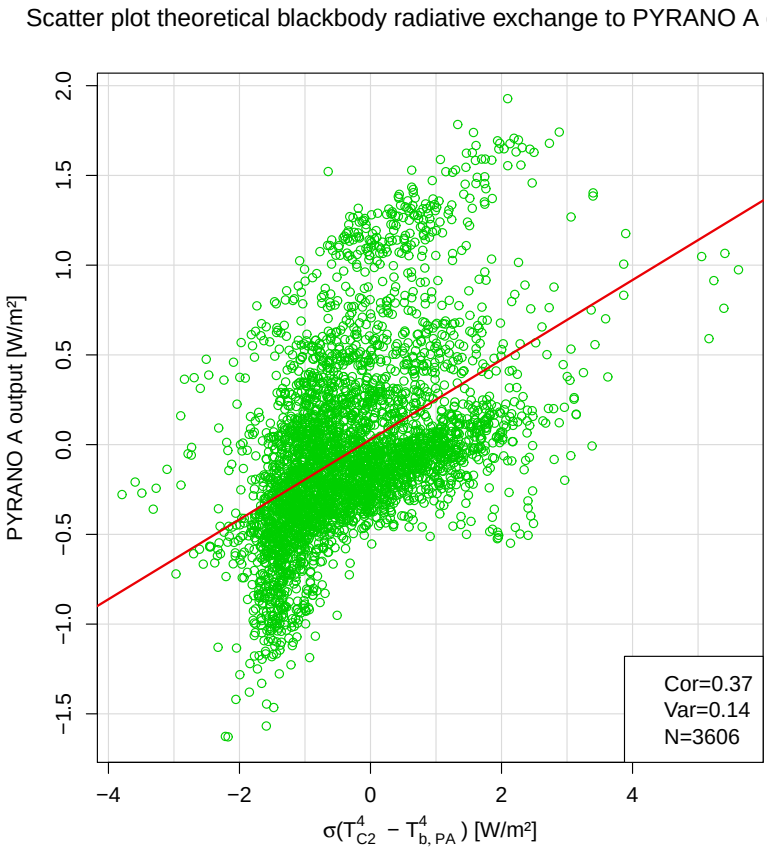

Figure 4.54: Scatter plot of the theoretical blackbody radiative exchange between the PT100 element C2 (mounted as closely as possible to the glass-dome of the pyranometer) and the body temperature of the reference pyranometer (*PYRANO A*, CMP 21, Eigenbrodt housing), calculated with $\sigma(T_{C2}^4 - T_{b,PA}^4)$ [$W\,m^{-2}$], to the output signal of the reference pyranometer between 18:00 UTC and 04:00 UTC of every day of measurement campaign expect the January 22 2015. Kendall rank correlation coefficient (Cor) and coefficient of determination ($Cor^2 = Var$) indicate the degree of association between two measured quantities, state in lower left-hand corner of each sub-figure. N represents the number of values.

In a further correction attempt the data used was restricted to output signals equal or below $0\,W\,m^{-2}$ (see Figure 4.55). Three interesting segments, separated by vertical lines at $-2\,W\,m^{-2}$ and $0\,W\,m^{-2}$ for the output signals, can be identified in this plot. The majority of data points $N = 1612$ is found for the middle segment, while the number of data points in the right hand segment is significantly lower ($N = 599$) and hardly any data points are found in the left hand segment ($N = 45$). In summary Figure 4.55 shows that both theoretical black body exchange for negative pyranometer output and pyranometer output are for most parts of the time series within $-2\,W\,m^{-2}$ and $0\,W\,m^{-2}$ though no robust and meaningful relationship for correction can be established due to large variability within this bandwidth. Therefore it is concluded, comparing

results shown here with those of Domínguez (2001), that temperatures recorded with the PT100 element C2 T_{C2} are not accurately enough representing the real temperature of the glass-dome to establish a comprehensive correction function. Further investigations (using different approaches) have not been possible within the framework of this master thesis as invasive approaches could not be pursued due to limitations by instrument costs as outlined above.

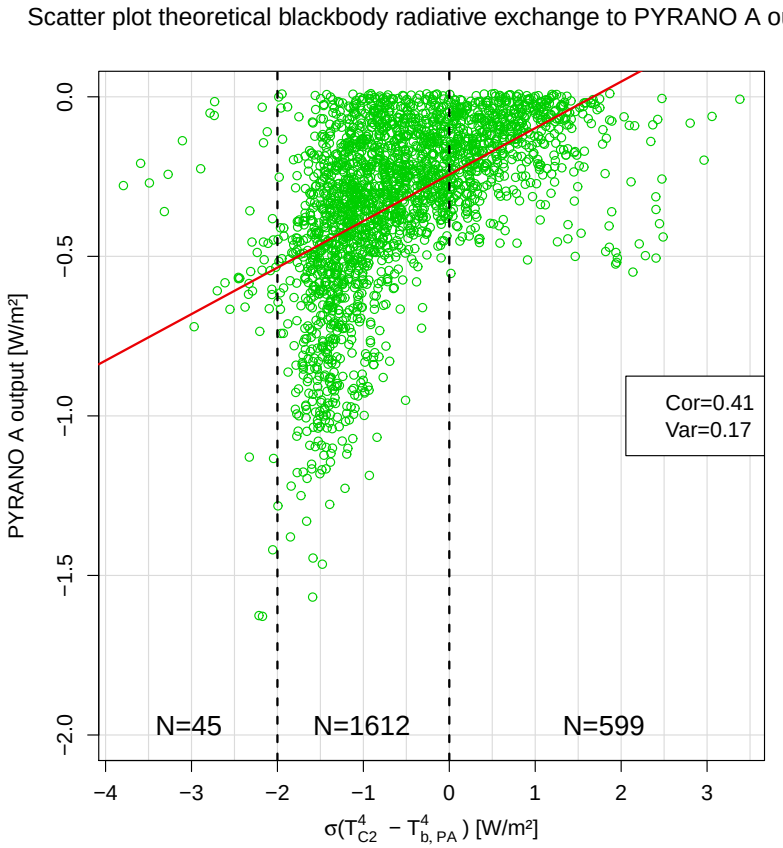

Figure 4.55: As Figure 4.54 but the output signals with values above $0\,\mathrm{W\,m^{-2}}$ cut off. The two vertical, black dashed lines mark the bandwidth of $\sigma(T_{C2}^4 - T_{b,PA}^4)$ which corresponds to the range of *PYRANO A* output (y-axis).

4.2.8 Comparison of meteorological records obtained during the measurement campaign

Meteorological observations from mobile platforms (LUFFT and MobMet, placed near the experimental platform on the rooftop of Heinrichstraße 28) and the continuously operating TAWES system have been used for the analysis of ambient conditions during the measurement campaign. The operation of multiple platforms allowed: (1) to assess the uncertainty of obtained meteorological records and (2) to investigate research questions regarding external influences on radiation measurements at ARAD site Graz/University, i.e. a potential influence of ventilation shafts located in vicinity to the ARAD platform on the rooftop of Heinrichstraße 28.

A potential influence of air emitted (at room temperature) by ventilation shafts on the rooftop of Heinrichstraße 28 was discussed in section 4.1. During the course of the measurement campaign the position of LUFFT (on the rooftop) has been varied (see Figure 4.56) to investigate if air emitted by the ventilation shafts influences temperature, relative humidity and/or wind speed near ARAD site Graz/University. Comparison of readings of LUFFT and MobMet further allowed to investigate if air emitted by ventilation shafts flows solely horizontal or if upward turbulent motions occur.

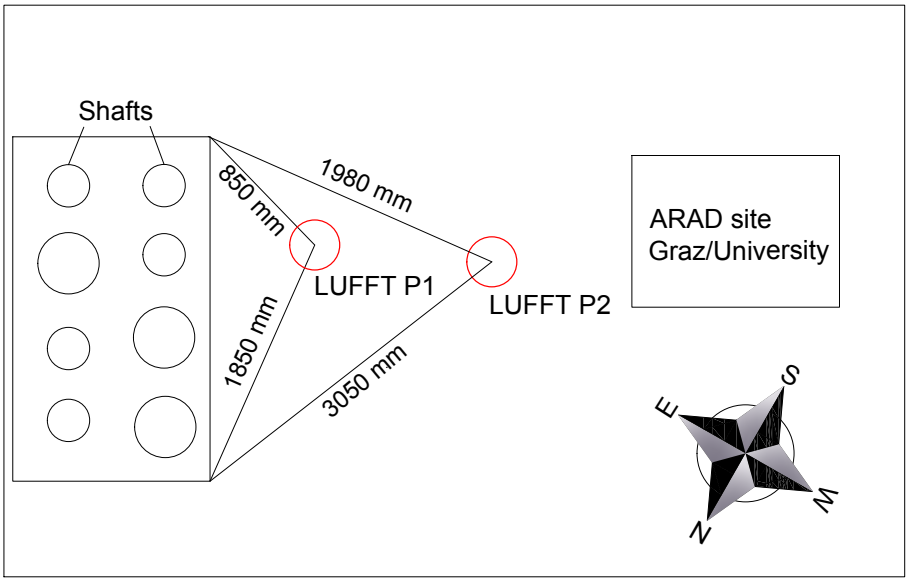

Figure 4.56: Exemplary illustration of two positions (close to the ventilation shafts (LUFFT P1); in vicinity of ARAD site Graz/University (LUFFT P2)) of the all-in-one meteorological device LUFFT during the measurement campaign. The left-hand side rectangle symbolises the concrete slab directly above the ventilation shafts (black circles). The right-hand side rectangle symbolises ARAD site Graz/University.

Figure 4.57 shows the smoothed (by a symmetric two times 30 minutes moving average filter) time series of air temperature measured by LUFFT and MobMet. Position changes of LUFFT are marked in this figure with goldenrod dashed vertical lines. At the beginning of the time series (2015-01-23 00:00 UTC) LUFFT was located near the shafts and $|\Delta T_a|$ with a value of about $8\,°$C has been observed. Seven hours later, on 2015-01-23 07:00 UTC LUFFT was moved about 30 cm closer to the shafts. Following this change in position a further increase of $|\Delta T_a| = 2\,°$C was observed.

Roughly two hours later (2015-01-23 08:56 UTC) the position of LUFFT was adjusted again. Now LUFFT was placed in close vicinity of the ARAD site and a pronounced decrease of $|\Delta T_a|$ from ≈ 10 to $\approx 0\,°$C was observed. About 2.5 hours later the position of LUFFT was adjusted again, this time the instrument was relocated to its initial position (nearby the shafts) and T_a of LUFFT increased to $\approx 14\,°$C which, is $\approx 6\,°$C higher than T_a measured by MobMet. This pronounced jump in temperature clearly indicates the influence of air emitted by the ventilation shafts on ambient air temperature.

In the afternoon (16:05 UTC) LUFFT was moved 1900 mm away from the shafts towards the ARAD site. Following this position change $|\Delta T_a|$ dropped to roughly $1\,°$C. Given this large drop in T_a of LUFFT between the positions near the ventilation shafts and the ARAD site it is assumed that air emitted by the ventilation shafts might not (significantly) effect ambient air temperatures near the ARAD site. To investigate this further LUFFT was elevated 620 mm (at the same position) to obtain temperature readings closer to the inlet tubes of ARAD pyranometers. T_a of LUFFT decreased slightly but as $|\Delta T_a|$ remained almost constant this change is rather attributed to ambient cooling than influence of air emitted by the ventilation shafts. To test this hypothesis LUFFT was moved once again closer (500 mm distance) to the ventilation shafts at 2015-01-24 12:05 UTC. Immediately $|\Delta T_a|$ increased by about $4\,°$C, indicating the influence of air emitted on ambient air in close vicinity to the shafts. Changes in T_a of LUFFT following additional position changes illustrated in Figure 4.57 align with the observations described above and are therefore not further detailed here.

Extending the analysis from ambient air temperature to wind speed confirms the hypothesis that air emitted by ventilation shafts influences ambient air in close vicinity of the shafts but does not influence ambient conditions in vicinity of the ARAD platform. When placed in distance of the ventilation shafts (periods following the 2nd, 4th, 5th and 6th goldenrod dashed vertical line in Figure 4.58) LUFFT showed approximately the same wind speed V_i as MobMet. In contrary, when placed in vicinity of the shafts (marked with 1st and 3rd goldenrod dashed vertical line in Figure 4.58) $|\Delta V_\mathrm{i}|$ between LUFFT and MobMet increased.

Although an effect of air emitted by the shafts on the ARAD sensors could not be found during campaign measurements, well-founded conclusions in this case would require additional and longer investigations beyond this thesis work.

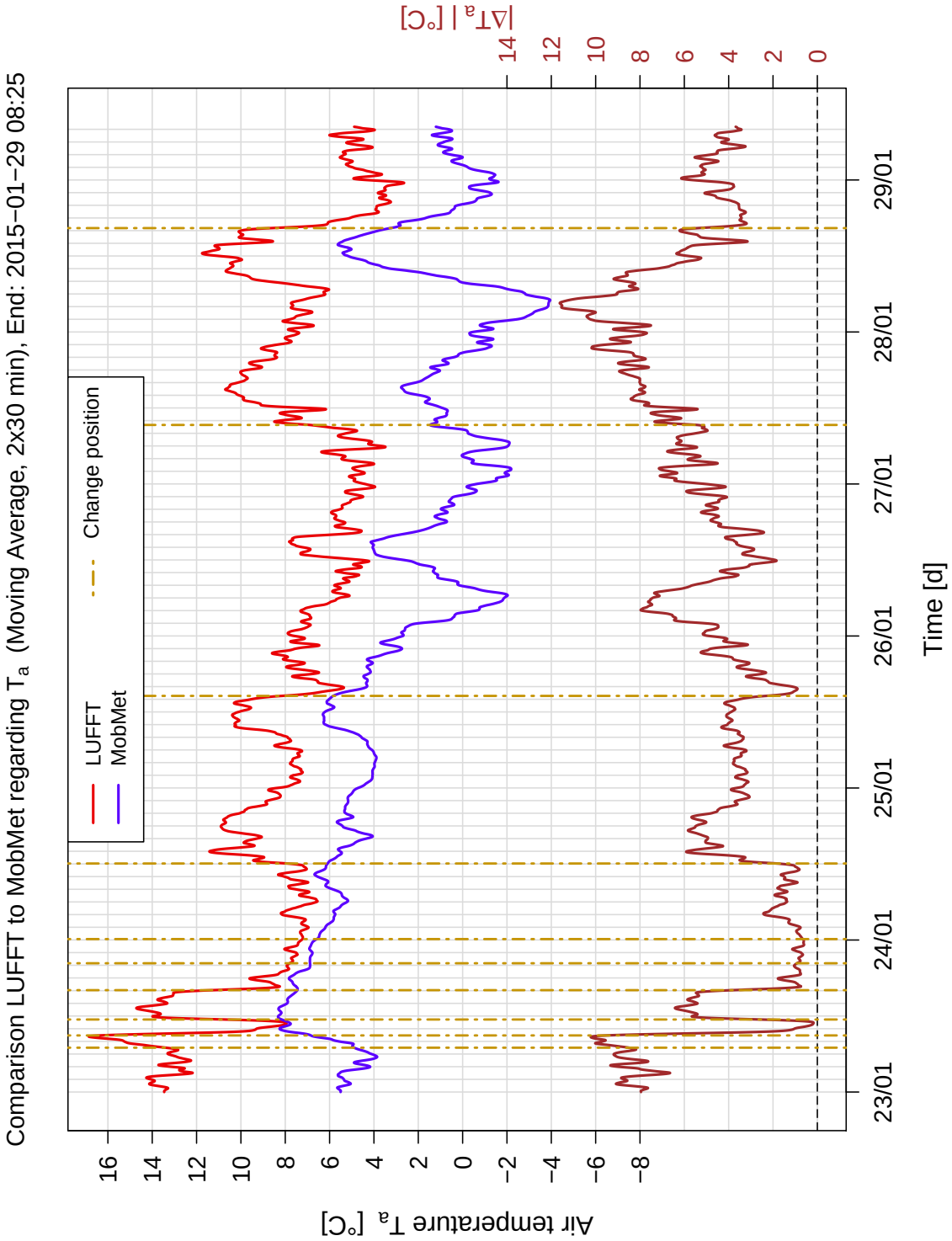

Figure 4.57: Comparison of the ambient air temperature T_a [°C] measured with the all-in-one meteorological system LUFFT and the mobile meteorological measurement device MobMet between 2015-01-23 00:00 UTC and 2015-01-29 08:25 UTC. Goldenrod dashed vertical lines indicate changes in position of LUFFT during the measurement campaign.

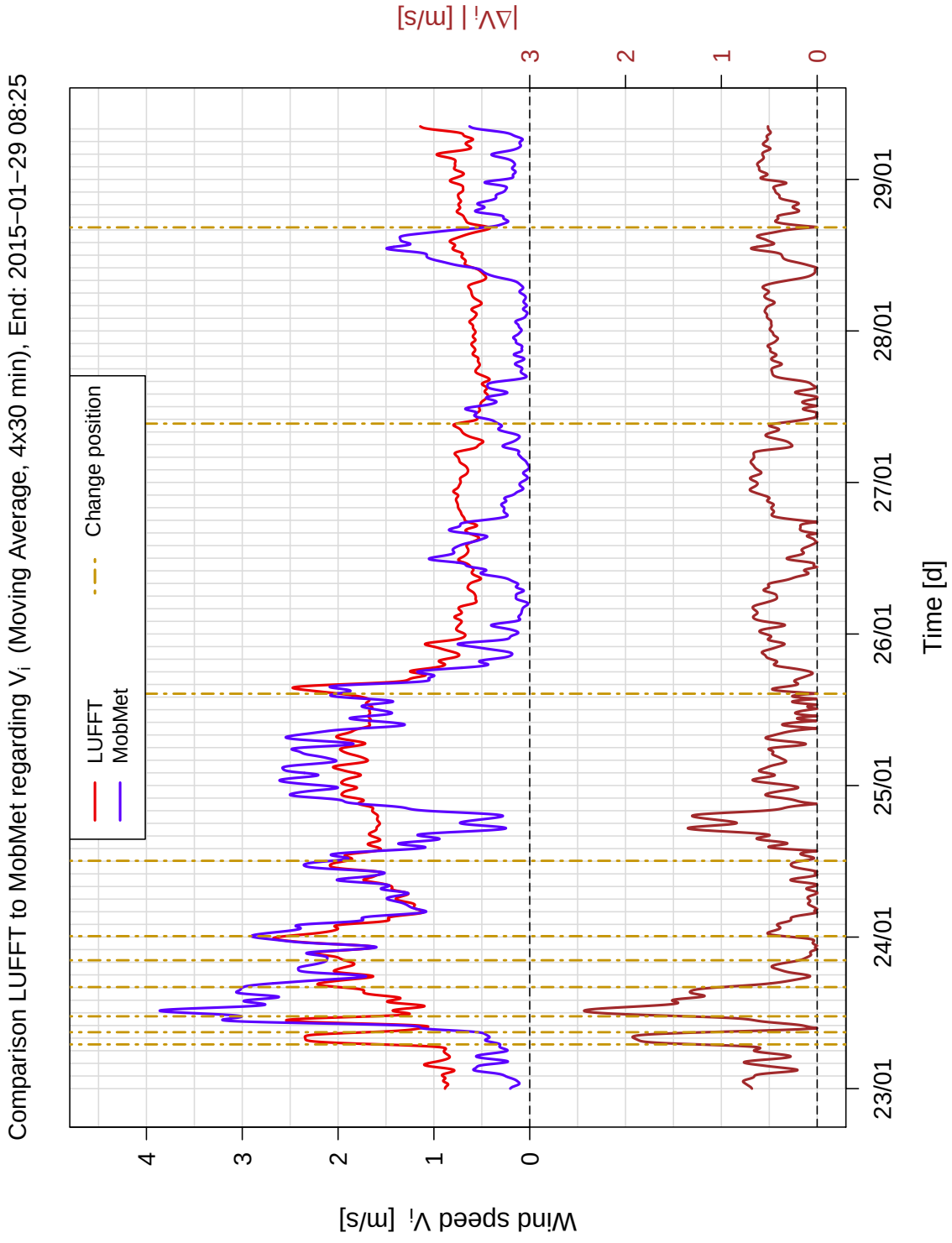

Figure 4.58: Comparison of the wind speed V_i [m s^{-1}] measured with the all-in-one meteorological system LUFFT and the mobile meteorological measurement device MobMet between 2015-01-23 00:00 UTC and 2015-01-29 08:25 UTC. Goldenrod dashed vertical lines indicate changes in position of LUFFT during the measurement campaign.

A comprehensive statistical analysis of wind measurements (wind speed V_i and wind direction D_i) by LUFFT, MobMet and TAWES (Sonic) is provided below. Figures 4.59 to Figure 4.61 show contour plots relating hourly wind frequencies [%] and wind direction D_L as well as box-whisker plots for hourly winds speed V_L for these devices.

Figures 4.59 shows that wind measurements by LUFFT show much weaker diurnal variation than corresponding MobMet or Sonic measurements. This is not surprising given the frequent location change of LUFFT on the rooftop of Heinrichstraße 28 exposing the sensor to both undisturbed ambient conditions and air (temperature and flow) streaming out of the ventilation shafts. MobMet and Sonic show very similar patterns in wind quantities with a pronounced frequency component of wind direction between 315 and 360 degrees and a pronounced diurnal cycle in wind speed (maxima around local noon).

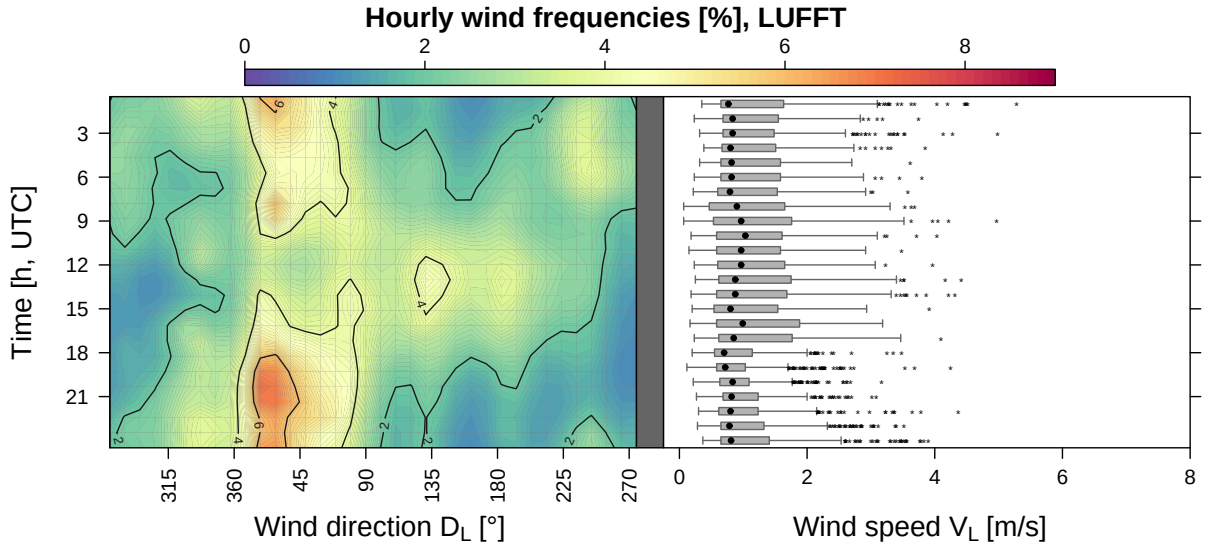

Figure 4.59: (left) Contour plot of hourly wind frequencies [%] for wind direction D_L [°] (resolution 1°). (right) Whisker plot of hourly aggregated wind speed V_L [m s^{-1}]. All data are observations by LUFFT between 2015-01-23 00:00 UTC and 2015-01-29 08:25 UTC.

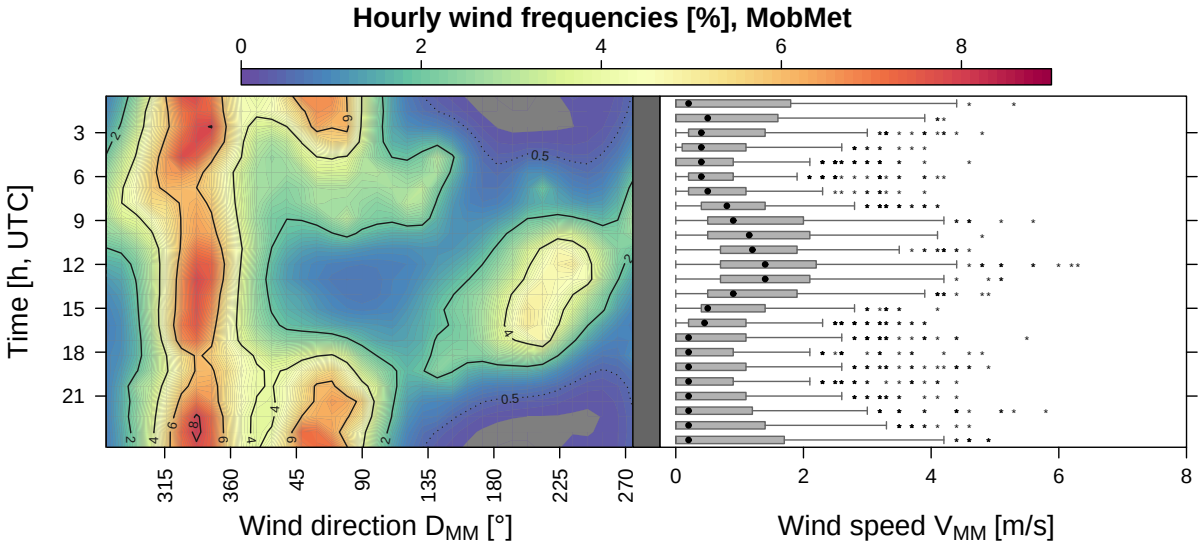

Figure 4.60: As Figure 4.59 but for observations by MobMet (MM) between 2015-01-23 00:00 UTC and 2015-01-29 08:25 UTC.

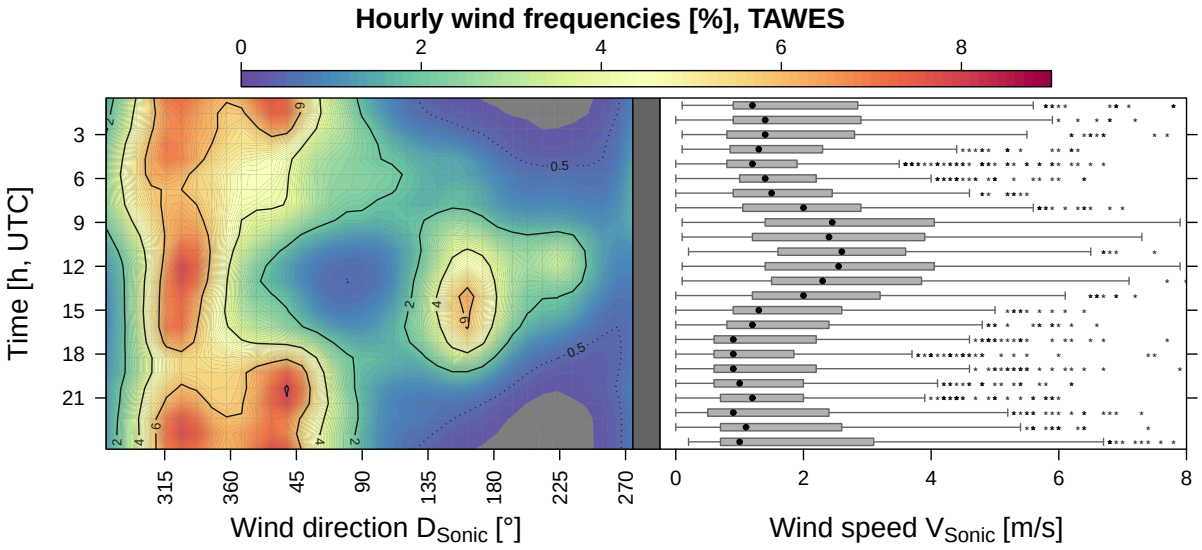

Figure 4.61: As Figure 4.59 but for observations by TAWES (Sonic) between 2015-01-23 00:00 UTC and 2015-01-29 08:25 UTC.

In summary analysis of ambient air temperature and wind records by meteorological sensors indicates that it is unlikely that air emitted by ventilation shafts on the rooftop of Heinrichstraße 28 is (significantly) influencing radiation measurements at the ARAD site. Wind related quantities observed during the campaign period agreed well among ‚permanently installed sensors' and changes in wind speed and wind direction recorded by the mobile device LUFFT represent its distance/proximity to the ventilation shafts. Although no significant influence of air emitted by the ventilation shafts could be found near the ARAD platform, it is important to note that ambient air in proximity to the shafts carried a clear signal of the emitted air which one might need to consider if additional instruments would be mounted on the platform above/near the ventilation shafts.

5 Summary and Conclusions

A precise knowledge of the surface energy budget, which includes the solar and terrestrial radiation fluxes, is needed to accurately characterize the global energy balance which is largely determining Earth's climate (Ramanathan, 1987; Augustine and Dutton, 2013; Wild et al., 2015).

As in-situ observations are sparse and restricted to land areas, satellite measurements of radiative fluxes are needed to characterize the global energy balance. Precise information on radiation budget components from ground-based networks is needed for retrieval optimization and satellite product validation (Gupta et al., 2003; Zhang et al., 2010; Yan et al., 2011; Wang et al., 2014) and the evaluation and/or parametrization of radiative fluxes in global and regional climate models (Wild et al., 1998; Marty et al., 2003; Freidenreich and Ramaswamy, 2011) and reanalysis products (Allan, 1999).

To this aim national and global monitoring networks for surface radiative fluxes have been established in recent decades. The most prominent among these networks is the so-called Baseline Surface Radiation Network (BSRN) operating under the auspices of the World Climate Research Programme (WCRP) (Ohmura et al., 1998). BSRN sites are equipped with state-of-the art instruments of highest accuracy and to date more than 50 anchor sites are operational worldwide.

National monitoring networks such as the Austrian RADiation Monitoring Network (ARAD), which has been established in 2010 by a consortium of the Central Agency of Meteorology and Geodynamics (ZAMG), the University of Graz, the University of Innsbruck, and the University of Natural Resources and Applied Sciences, Vienna (BOKU), orient themselves on BSRN standards (McArthur, 2005). ARAD comprises to date five sites (Wien Hohe Warte, Graz/University, Innsbruck/University, Kanzelhöhe Observatory and Sonnblick (which is also a BSRN site)) and aims to provide long-term monitoring of radiation budget components at highest accuracy and to capture the spatial patterns of radiation climate in Austria (Olefs et al., 2015).

Given the accuracy requirement for the local monitoring of radiative fluxes instrument offsets, triggered by meteorological factors and/or instrumentation, pose a major challenge in radiation monitoring. Recently a nighttime offset between two pyranometers, monitoring global and diffuse radiation, has been identified at ARAD site Graz/University. Although nighttime pyranometer measurements are of no particular importance by themselves, they provide a reference for instrument performance according to BSRN standards (McArthur, 2005) and are indicators for possible changed offsets during daylight conditions. The two pyranometers concerned are of same type (CMP 21 by manufacturer Kipp&Zonen) but contained in different housing systems (one Eigenbrodt SBL 480 housing, one self-built cost-effective KSO housing). Therefore besides external factors i.e., meteorological factors such as precipitation, ambient temperature and wind, the instrumentation itself might be the cause of the observed offset.

The main focus of this master thesis has been to investigate the influence of meteorological factors and instrumentation on radiation measurements at ARAD site Graz/University and to possibly determine the root cause for the observed instrument offset.

Within the scope of this thesis data from ARAD site Graz/University between June 2013 and May 2014 has been analyzed. In addition to the analysis of routine ARAD data a series of experiments has been performed at ARAD site Graz/University to ‚simulate' meteorological effects (e.g., precipitation) under stable nighttime conditions. The results of this series of preliminary experiments indicated that precipitation events and changes in ambient conditions (temperature and/or wind speed) influence radiation measurements.

To further characterize instrument responses and differences in these responses among different instrumentation setups, i.e., different housing units and heating levels and/or heating ring positions inside the housings, an extensive measurement campaign has been performed in January 2015. During this campaign more than 60 experiments, including standardized spray-tests (30 strokes from $2-4$ cm distance) to simulate precipitation events, coverage-tests to simulate abrupt changes in wind speed, rapid adjustments in heating levels to simulate abrupt changes in ambient air temperature and to investigate instrument performance/robustness under different heating levels, and combinations of those listed above, have been performed.

As ARAD site Graz/University is a routine monitoring site, experiments could not be performed at the site to not disturb the monitoring series. Therefore two additional pyranometers (of the same type as the ARAD sensors, provided by Dr. Marc Olefs and Dr. Martin Mair (both ZAMG)) have been installed in vicinity of the ARAD site for the campaign. These pyranometers have been placed during experiments in the same type of housings as operated at the ARAD site. While the housing of the experimental pyranometer was changed during the campaign, the reference pyranometer was contained the whole period in a housing of type Eigenbrodt SBL 480. During the campaign pyranometer body temperature has been recorded and additional temperature measurements (using standard PT100 elements) inside the housing systems and near the pyranometers outer glass-domes have been performed to characterize thermal environments and heat flow. Additional measurements - characterizing ambient meteorological conditions - have been performed with two mobile meteorological observation platforms, WS600 UMB by Lufft GmbH (provided by Prof. Dr. Erich Mursch-Radlgruber from BOKU) and a self-built mobile observation platform (MobMet, provided by the Institute of Physics, of the University of Graz), during the measurement campaign.

The key finding of this thesis is that both, instrumentation applied, and ambient meteorological conditions significantly influence pyranometer performance and thus measurement accuracy at ARAD site Graz/University.

First the focus is turned to the influence of instrumentation on radiation measurements. The offset between the output of two pyranometers of the same type, originally observed at ARAD site Graz/University, is repeatable for pyranometers operated in different housing systems as shown by the results of the measurement campaign. In contrary if instruments are operated in housing systems of the same type, the offset is strongly reduced. Additionally it was found that the operational heating level strongly influences pyranometer stability independent of the housing. The campaign experiments showed that independent of the housing system, pyranometer output changed no matter if the housing systems heating power was enhanced, reduced or eliminated. The analysis presented shows further that sensors needed about 30 to 60 minutes to stabilize in

the ‚new' thermal environment after changes in the heating level have been performed. Changes in pyranometer output varied among heating levels and housing systems used. Interestingly it was found by comparing output from instruments contained in different housing systems during undisturbed conditions that sensor output of pyranometers contained in the Eigenbrodt SBL 480 housing in standard configuration (10 W heating level, ventilated) and an unheated but ventilated KSO housing showed the best agreement. This is a surprising result given that BSRN guidelines recommend an operational heating level of 10 W (or higher depending on ambient conditions). Given the good agreement of two pyranometers (of the same type) when operated in housing systems of the same type such setup appears preferential for routine observations. Nevertheless the accuracy of such ‚stable setup' needs to be taken with caution - given instruments might be at same levels but still not accurately represent ‚real world' radiative fluxes - as indicated by the observed offset among pyranometers (of same type) operated in different housing systems.

Now the focus is turned to the influence of ambient meteorology on radiation measurements. A series of spray-tests performed during preliminary analyses indicated that water impacting on the pyranometer's glass dome affects instrument stability. Throughout the campaign a series of ‚standardized' spray-tests has been performed. During these spray-tests 30 strokes of distilled water (from a distance of $2-4$ cm) have impacted on the pyranometer glass-dome(s). Laboratory analysis showed that the 30 strokes applied equal an average amount of 3.35 g of distilled water - which corresponds roughly to 3.35 ml - a quantity released within short-term moderate precipitation events. Each of these spray-tests triggered a response in instrument output and body temperature, lasting about 30 minutes. This result indicates that precipitation (as simulated by the spray-tests) affects the thermal environment of the instrument and thus its stability. Statistical analyses showed that instrument responses are smallest when contained in an unheated KSO housing or the Eigenbrodt SBL 480 housing in standard configuration. Spray-tests performed on pyranometers contained in the Eigenbrodt SBL 480 housing at 5 or 0 W heating level resulted in larger output responses than observed during standard operational conditions (10 W). Output responses of pyranometers contained in the KSO housing have been about a factor two larger following spray-tests if the housing was heated (heating level of 10 or 5 W). In summary instrument response (output and body temperature) following spray-tests varied among housing systems and their configuration though a general (negative) sensor response was found throughout all trials.

Besides spray-tests a series of coverage experiments has been performed to simulate abrupt changes in wind speed. These experiments showed in general hardly any impact on pyranometer performance, although larger responses were found for combinations of spray- and cover-tests than spray-tests alone. This result indicates that under ambient conditions pyranometers might be slightly less affected by stratiform than convective precipitation as the later accounts (normally) for larger precipitation amounts with concurrent enhanced wind speeds (storminess).

Adjustments of the heating levels of instrument housings have been described above in the context of spray-tests. A second series of heating level adjustments (without concurrent spray-tests) has been performed during the measurement campaign to simulate abrupt changes in ambient temperature. These experiments showed that reductions in heating level instantaneously affect pyranometers, i.e. pyranometer output and body temperature declined following reductions of the heating levels independent of the housing system used. This result indicates that abrupt changes in ambient conditions, or failures in the heating system of a housing, can significantly influence measurement performance and accuracy. Pyranometer output and body temperature remained disturbed following spray-tests and/or adjustments in heating level for about 30 minutes.

Instrument response and recovery followed a quasi-exponential form towards equilibrium, as expected according to the Maxwell-Boltzmann distribution.

A secondary research question addressed in this thesis was the potential influence of air emitted (at room temperature) by ventilation shafts in vicinity of the platform of ARAD site Graz/University. To this aim ambient air temperature measurements from the mobile meteorological observation platforms deployed during the measurement campaign (MobMet (fixed location) and LUFFT (mobile)) have been compared. This comparison indicates that air emitted from the shafts affects ambient air in direct vicinity of the ARAD platform. An effect on the ARAD sensors could not be found during campaign measurements, but well-founded conclusions in this case would require additional investigations beyond this thesis work.

In summary the results of this thesis indicate that: (1) measurements during/after precipitation events and/or highly variable ambient conditions need to be taken with care due to possible instrument disturbance; (2) offsets observed between pyranometers of the same type when operated in different housing systems have been repeatable under ambient conditions suggesting that the operation of one housing system is preferential for routine monitoring sites; (3) offsets between pyranometers operated in the KSO and Eigenbrodt housing, reduced if the KSO housing was ventilated but unheated, indicating that further modifications of the self-built KSO housing system should be considered to improve system performance; (4) a detailed comparison of pyranometer performance throughout all types of housing systems used within the ARAD framework is suggested for future work to determine possible offsets and improve the overall accuracy of ARAD measurements.

List of Figures

2.1 Illustration of the *Lambert's cosine law*. 4
2.2 The spectral radiance of a black body as a function of wavelength for different temperatures in linear (top) and double-logarithmic scale (bottom). 7
2.3 Extinction of the spectral radiance L_λ^I in a medium (grey rectangle) with the density ρ and the mass-specific extinction coefficient k. Source: (Hantel, 2013) 10
2.4 The atmosphere and the Earth's surface should be two infinitely thin areas (for illustrative purposes they are drawn extensive) and can't save any form of physical energy. The variables T_E and T_s besides represent their temperatures. In analogy to (Hantel, 2013, p. 21). 14
2.5 Calculated surface radiation budget components at ARAD site Graz/University for 2015-06-19. 18
2.6 Cross-section of a pyranometer. 19
2.7 Conceptional model for partial pressure p_i with the mass m_i, the side-length L_m and an area A of a cube. Every particle has its own velocity v_i and moves along the six directions parallel to the side edge. Source: (Hantel, 2013) 22

3.1 Overview of the Austrian RADiation (ARAD) station locations. 28
3.2 Cross section of the CMP 21, indicated are the outer and inner glass-dome, the sensing element with the thermopile, the drying cartridge, the subframe and the white sun-shield. Source: (Kipp&Zonen, 2010) 29
3.3 Schematic outside illustration of a CMP 21 with two glass-domes. The orange pellets represent the silica-gel in the drying cartridge to regulate the humidity level inside the radiometer. The yellow cable is a low noise type cable for signal transmission. In analogy to (Kipp&Zonen, 2010) 29
3.4 Illustration of the solar irradiance spectrum at the Earth's surface with specific absorption lines of diverse molecules in the atmosphere and corresponding pyranometer response. Note: the spectral response of a thermopile-type pyranometer shows a large range of possible absorption wavelengths for short-wave radiation. Source: (Kipp&Zonen, 2010) 31
3.5 Schematic illustration of the upper half space as seen from a pyranometer at ARAD site Graz/University. This geometric horizon was designed with a high-resolution digital elevation model by staff of Kanzelhöhe Observatory. 31
3.6 Illustration of the radiative transfer between the CMP 21 and the (‚cold') atmosphere. Source: (Kipp&Zonen, 2010) 32
3.7 ARAD monitoring site Graz/University on top of the roof of Heinrichstraße 28, 8010 Graz. 34
3.8 Heating elements of *HIM* and *GLO*. 35

4.1 Comparison of radiation R measured at ARAD site Graz/University, 2013-07-16 19:00 UTC and 2013-07-17 04:00 UTC 42

4.2 As Figure 4.1 but for measurements between 2013-08-04 18:00 UTC and 2013-08-05 04:00 UTC. 43
4.3 Measurements of radiation components at ARAD site Graz/University and meteorological variables (co-located) between 2013-06-15 20:00 UTC and 2013-06-16 02:00 UTC. 45
4.4 As Figure 4.3 but for measurements between 2013-08-04 18:00 UTC and 2013-08-05 00:00 UTC. 46
4.5 As Figure 4.3 but for measurements between 2013-09-10 19:00 UTC and 2013-09-11 00:00 UTC. 47
4.6 As Figure 4.3 but for measurements between 2013-11-11 00:00 UTC and 06:00 UTC. 48
4.7 Monthly Box-Whisker plots of (a) average body temperature $\overline{T}_{\mathrm{HIM}}$ [°C] of the pyranometer measuring diffuse radiation (*HIM*, CMP 21, Eigenbrodt housing), (b) average body temperature $\overline{T}_{\mathrm{GLO}}$ [°C] of the pyranometer measuring global radiation (*GLO*, CMP 21, KSO housing), (c) difference $\overline{T}_{\mathrm{GLO}} - \overline{T}_{\mathrm{HIM}}$ [°C] between the body temperatures of the pyranometers at ARAD site Graz/University and (d) average ambient air temperature $\overline{T}_{\mathrm{wg}}$ [°C] at TAWES site Graz/University for June to December 2013. 49
4.8 Cumulative sum of quality flags of type 2 for measurements of global (*GLO*, CMP 21, KSO housing) and diffuse radiation (*HIM*, CMP 21, Eigenbrodt housing) between June and December 2013. 50
4.9 As Figure 4.7 but for measurements for January to May 2014. 51
4.10 As Figure 4.8 but for January to May 2014. 52
4.11 As Figure 4.1 but for measurements between 2014-10-09 16:00 UTC and 21:00 UTC. 53
4.12 As Figure 4.1 but for measurements between 2014-10-13 16:00 UTC and 21:00 UTC. 54
4.13 As Figure 4.1 but for measurements between 2014-10-14 16:00 UTC and 21:00 UTC. 55
4.14 As Figure 4.1 but for measurements between 2014-10-15 16:00 UTC and 21:00 UTC. 56
4.15 As Figure 4.1 but for measurements between 2014-11-12 16:00 UTC and 21:00 UTC. 57
4.16 Measurements of radiation components and corresponding instrument body temperatures at ARAD site Graz/University between 2014-12-16 00:00 UTC and 2014-12-18 00:00 UTC. 58
4.17 As Figure 4.16 but for measurements between 2014-12-18 00:00 UTC and 2014-12-19 06:00 UTC. 59
4.18 Instrumentation used during the measurement campaign at ARAD site Graz/University in January 2015. 62
4.19 Position of the PT100 temperature elements inside the housing (below the outer glass dome and beneath the pyranometer base). 62
4.20 Position of the PT100 temperature elements inside the housing (below the outer glass dome and beneath the pyranometer base). 63
4.21 A zoomed view on the individual PT100 elements inside the experimental pyranometer *PYRANO B* (CMP 21, KSO housing). 63
4.22 Illustration of spray-tests. 64
4.23 Comparison of radiation R measured with reference (*PYRANO A*, CMP 21, Eigenbrodt housing, green) and experimental pyranometers (*PYRANO B*, CMP 21, Eigenbrodt or KSO housing, orange) between 2015-01-23 15:00 UTC and 2015-01-29 08:25 UTC. 65

4.24 Comparison of radiation R measured with reference (*PYRANO A*, CMP 21, Eigenbrodt housing, green) and experimental pyranometers (*PYRANO B*, CMP 21, Eigenbrodt housing, orange) between 2015-01-22 15:00 UTC and 2015-01-23 06:00 UTC. 67
4.25 Comparison of body temperatures T_{b} of reference (*PYRANO A*, CMP 21, Eigenbrodt housing, green) and experimental pyranometers (*PYRANO B*, CMP 21, Eigenbrodt housing, orange) between 2015-01-22 15:00 UTC and 2015-01-23 06:00 UTC. . . 68
4.26 Comparison of radiation R measured with reference (*PYRANO A*, CMP 21, Eigenbrodt housing, green) and experimental pyranometers (*PYRANO B*, CMP 21, Eigenbrodt housing, orange) between 2015-01-23 15:00 UTC and 2015-01-24 05:00 UTC. 70
4.27 Picture of a cover-test on the glass-domes of the reference (*PYRANO A*, CMP 21, Eigenbrodt housing, right) and experimental (*PYRANO B*, CMP 21, KSO housing, left) instruments with fitted aluminium caps. 70
4.28 Comparison of body temperatures T_{b} of reference (*PYRANO A*, CMP 21, Eigenbrodt housing, green) and experimental pyranometers (*PYRANO B*, CMP 21, Eigenbrodt housing, orange) between 2015-01-22 15:00 UTC and 2015-01-23 06:00 UTC. . . 71
4.29 Comparison of temperatures measured by the PT100 elements C2, C3, C4 and C5 inside reference and experimental housing systems between 2015-01-23 15:00 UTC and 2015-01-24 05:00 UTC. 72
4.30 As Figure 4.26 but for comparison of radiation R measured with reference (*PYRANO A*, CMP 21, Eigenbrodt housing, green) and experimental pyranometers (*PYRANO B*, CMP 21, Eigenbrodt housing, orange) between 2015-01-24 05:00 UTC and 2015-01-24 14:40 UTC. 73
4.31 Meteorological parameters (a) relative humidity RH_{MM}, (b) wind speed V_{MM}, (c) maximum wind speed Max.V_{MM} and (d) wind direction D_{MM} measured by MobMet between 2015-01-24 05:00 UTC and 2015-01-24 14:40 UTC. 74
4.32 As Figure 4.28 but for comparison of body temperatures T_{b} measured with reference (*PYRANO A*, CMP 21, Eigenbrodt housing, green) and experimental pyranometers (*PYRANO B*, CMP 21, Eigenbrodt housing, orange) between 2015-01-24 05:00 UTC and 2015-01-24 14:40 UTC. 75
4.33 As Figure 4.26 but for comparison of radiation R measured with reference (*PYRANO A*, CMP 21, Eigenbrodt housing, green) and experimental pyranometers (*PYRANO B*, CMP 21, KSO original housing, orange) between 2015-01-24 16:00 UTC and 2015-01-25 05:00 UTC. 76
4.34 As Figure 4.28 but for comparison of body temperatures T_{b} measured with reference (*PYRANO A*, CMP 21, Eigenbrodt housing, green) and experimental pyranometers (*PYRANO B*, CMP 21, KSO original housing, orange) between 2015-01-24 16:00 UTC and 2015-01-25 05:00 UTC. 78
4.35 As Figure 4.29 but for comparison of C4 and C5 in the experimental pyranometer housing (*PYRANO B*, CMP 21, KSO original housing) between 2015-01-24 16:00 UTC and 2015-01-25 07:00 UTC. 79
4.36 As Figure 4.26 but for comparison of radiation R measured with reference (*PYRANO A*, CMP 21, Eigenbrodt housing, green) and experimental pyranometers (*PYRANO B*, CMP 21, KSO original housing, orange) between 2015-01-25 05:00 UTC and 2015-01-25 14:10 UTC. 80

4.37 As Figure 4.28 but for comparison of body temperatures T_b measured with reference (*PYRANO A*, CMP 21, Eigenbrodt housing, green) and experimental pyranometers (*PYRANO B*, CMP 21, KSO original housing, orange) between 2015-01-25 05:00 UTC and 2015-01-25 14:10 UTC. 81

4.38 Experimental radiation sensor *PYRANO B* and its modification of the heating elements elevated by $5\,\mathrm{mm}$. 82

4.39 As Figure 4.26 but for comparison of radiation R measured with reference (*PYRANO A*, CMP 21, Eigenbrodt housing, green) and experimental pyranometers (*PYRANO B*, CMP 21, KSO housing, heating elements elevated by 5 mm, orange) between 2015-01-25 16:00 UTC and 2015-01-26 05:00 UTC. 83

4.40 As Figure 4.28 but for comparison of body temperatures T_b measured with reference (*PYRANO A*, CMP 21, Eigenbrodt housing, green) and experimental pyranometers (*PYRANO B*, CMP 21, KSO housing, heating elements elevated by 5 mm, orange) between 2015-01-25 16:00 UTC and 2015-01-26 05:00 UTC. 84

4.41 As Figure 4.29 but for comparison of C4 and C5 in the experimental pyranometer housing (*PYRANO B*, CMP 21, KSO housing, heating elements elevated by 5 mm) between 2015-01-25 16:00 UTC and 2015-01-26 05:00 UTC. 85

4.42 As Figure 4.39 but for comparison of radiation R measured with reference (*PYRANO A*, CMP 21, Eigenbrodt housing, green) and experimental pyranometers (*PYRANO B*, CMP 21, KSO housing, heating elements elevated by 5 mm, orange) between 2015-01-26 05:00 UTC and 2015-01-26 15:00 UTC. 86

4.43 As Figure 4.40 but for comparison of body temperatures T_b measured with reference (*PYRANO A*, CMP 21, Eigenbrodt housing, green) and experimental pyranometers (*PYRANO B*, CMP 21, KSO housing, heating elements elevated by 5 mm, orange) between 2015-01-26 05:00 UTC and 2015-01-26 15:00 UTC. 87

4.44 As Figure 4.39 but for comparison of radiation R measured with reference (*PYRANO A*, CMP 21, Eigenbrodt housing, green) and experimental pyranometers (*PYRANO B*, CMP 21, KSO housing, heating elements elevated by 5 mm, orange) between 2015-01-26 15:00 UTC and 2015-01-27 05:00 UTC. 88

4.45 As Figure 4.40 but for comparison of radiation body temperatures T_b measured with reference (*PYRANO A*, CMP 21, Eigenbrodt housing, green) and experimental pyranometers (*PYRANO B*, CMP 21, KSO housing, heating elements elevated by 5 mm, orange) between 2015-01-26 15:00 UTC and 2015-01-27 05:00 UTC. 89

4.46 Comparison of radiation R measured at ARAD site Graz/University with sensors for diffuse (*HIM*: CMP 21, Eigenbrodt housing, red curve), global (*GLO*: CMP 21, KSO housing, blue curve) and net long-wave radiation (*LONG*: CRG 4, KSO housing, lime-green curve) between 2015-01-26 15:00 UTC and 2015-01-27 05:00 UTC. . . 90

4.47 Comparison of ambient air temperature T_a measured with two instruments (C3 and MobMet) and body temperature $T_{\mathrm{b,PA}}$ measured with reference pyranometer (*PYRANO A*, CMP 21, Eigenbrodt housing, green) between 2015-01-23 15:00 UTC and 2015-01-29 08:25 UTC. 95

4.48 Scatter plot between the PT100 element C3 and the body temperature of the reference pyranometer $T_{\mathrm{b,PA}}$ (*PYRANO A*, CMP 21, Eigenbrodt housing) between 2015-01-23 15:00 UTC and 2015-01-29 08:25 UTC. 96

4.49 Monthly Box-Whisker plots of (a) difference [°C] between the body temperature of the pyranometer measuring diffuse radiation (*HIM*) at ARAD site Graz/University $\overline{T}_{\mathrm{HIM}}$ and average ambient air temperature at TAWES site Graz/University $\overline{T}_{\mathrm{wg}}$, (b) difference [°C] between the body temperature of the pyranometer measuring global radiation (*GLO*) at ARAD site Graz/University $\overline{T}_{\mathrm{GLO}}$ and average ambient air temperature at TAWES site Graz/University $\overline{T}_{\mathrm{wg}}$; (a)-(b) for June to December 2013; (c) as (a) and (d) as (b); but for January to May 2014. 97

4.50 As Figure 4.47 but for comparison of body temperature $T_{\mathrm{b,PB}}$ measured with experimental pyranometer (*PYRANO B*, CMP 21, EIG or KSO housing, heating elements elevated by different hight, orange) between 2015-01-23 15:00 UTC and 2015-01-29 08:25 UTC. 98

4.51 As Figure 4.48 but with measurements of the body temperature of the experimental pyranometer $T_{\mathrm{b,PB}}$ (*PYRANO B*, CMP 21, EIG or KSO housing, heating elements elevated by different mm). 99

4.52 Theoretical blackbody radiative exchange between the glass-dome T_{d} and the body temperature T_{b} versus the output signal of the Precision Spectral Pyranometer (PSP).100

4.53 Time Series of standard and corrected PSP output for (a) October 2, 2000 (day of the year 276) and (b) October 3, 2000 (day of the year 277). Source: (Domínguez, 2001) 101

4.54 Scatter plot of the theoretical blackbody radiative exchange between the PT100 element C2 and the body temperature of the reference pyranometer (*PYRANO A*, CMP 21, Eigenbrodt housing), calculated with $\sigma(T_{\mathrm{C2}}^4 - T_{\mathrm{b,PA}}^4)$, to the output signal of the reference pyranometer between 18:00 UTC and 04:00 UTC of every day of measurement campaign expect the January 22 2015. 102

4.55 As Figure 4.54 but the output signals with values above $0\,\mathrm{W\,m^{-2}}$ cut off. 103

4.56 Comparison of the ambient air temperature T_a measured with the all-in-one meteorological system LUFFT and the mobile meteorological measurement device MobMet between 2015-01-23 00:00 UTC and 2015-01-29 08:25 UTC. 104

4.57 Comparison of the ambient air temperature T_a measured with the all-in-one meteorological system LUFFT and the mobile meteorological measurement device MobMet between 2015-01-23 00:00 UTC and 2015-01-29 08:25 UTC. 106

4.58 Comparison of the wind speed V_{i} measured with the all-in-one meteorological system LUFFT and the mobile meteorological measurement device MobMet between 2015-01-23 00:00 UTC and 2015-01-29 08:25 UTC. 107

4.59 Contour plot of hourly wind frequencies observed by LUFFT. 108

4.60 As Figure 4.59 but for observations by MobMet (MM) between 2015-01-23 15:00 UTC and 2015-01-29 08:25 UTC. 109

4.61 As Figure 4.59 but for observations by TAWES (Sonic) between 2015-01-23 15:00 UTC and 2015-01-29 08:25 UTC. 109

A.1 Comparison of radiation R measured with reference (*PYRANO A*, CMP 21, Eigenbrodt housing, green) and experimental pyranometers (*PYRANO B*, CMP 21, KSO housing, heating elements elevated by 10 mm, orange) between 2015-01-27 16:30 UTC and 2015-01-28 05:00 UTC. 137

A.2 Comparison of body temperatures T_b of reference (*PYRANO A*, CMP 21, Eigenbrodt housing, green) and experimental pyranometers (*PYRANO B*, CMP 21, KSO housing, heating elements elevated by 10 mm, orange) between 2015-01-27 16:30 UTC and 2015-01-28 05:00 UTC. 138
A.3 Comparison of temperatures measured by the PT100 elements C2, C3, C4 and C5 inside reference and experimental housing systems: (a) C4 and C5 represent temperatures inside the experimental housing system (*PYRANO B*, CMP 21, KSO housing, heating elements elevated by 10 mm); (b) temperature difference C5-C4; (c) C1 and C2 inside the reference housing system (*PYRANO A*, CMP 21, Eigenbrodt housing); (d) temperature difference C2-C1. All panels for observations between 2015-01-27 16:30 UTC and 2015-01-28 05:00 UTC. 139
B.1 As Figure A.1 but for comparison of radiation R measured with reference reference (*PYRANO A*, CMP 21, Eigenbrodt housing, green) and experimental pyranometers (*PYRANO B*, CMP 21, KSO housing, heating elements elevated by 10 mm, later by 15 mm, orange) between 2015-01-28 16:00 UTC and 2015-01-29 08:00 UTC. . . . 140
B.2 As Figure A.2 but for comparison of body temperatures T_b of reference (*PYRANO A*, CMP 21, Eigenbrodt housing, green) and experimental pyranometers (*PYRANO B*, CMP 21, KSO housing, heating elements elevated by 10 mm, later by 15 mm, orange) between 2015-01-28 16:00 UTC and 2015-01-29 08:00 UTC. 141
B.3 As Figure A.3 but for comparison of temperatures measured inside the reference (*PYRANO A*, CMP 21, Eigenbrodt housing) and experimental housing systems (*PYRANO B*, CMP 21, KSO housing, heating elements elevated by 10 mm or 15 mm) between 2015-01-27 16:30 UTC and 2015-01-28 05:00 UTC. 142
C.1 Comparison of radiation R measured with reference (*PYRANO A*, CMP 21, Eigenbrodt housing, green) and experimental pyranometers (*PYRANO B*, CMP 21, KSO housing, orange) between 2015-01-23 15:00 UTC and 2015-01-29 08:25 UTC. . . 143
C.2 Comparison of body temperatures T_b measured with reference (*PYRANO A*, CMP 21, Eigenbrodt housing, green) and experimental pyranometers (*PYRANO B*, CMP 21, KSO housing, orange) between 2015-01-23 15:00 UTC and 2015-01-29 08:25 UTC. 144

List of Tables

3.1 Technical specifics of the CMP 21 pyranometer. Source:(Kipp&Zonen, 2010) 30
3.2 Housing properties of *HIM* and *GLO*. 34
3.3 Statistical summary (average, standard deviation, absolute error and relative error) of laboratory trials for five spray tests x_i, each performed with 30 strokes of distilled water. 38

4.1 Overview about measurement devices (and corresponding observed meteorological variables) employed at ARAD site Graz/University in January 2015. 61
4.2 Statistical analysis of spray-tests regarding experimental pyranometer *PYRANO B* contained in Eigenbrodt SBL 480 housing at heating level of $10\,\mathrm{W}$. 92
4.3 Statistical analysis of spray-tests regarding experimental pyranometer *PYRANO B* contained in Eigenbrodt SBL 480 housing at heating level of $5\,\mathrm{W}$. 92
4.4 Statistical analysis of spray-tests regarding experimental pyranometer *PYRANO B* contained in Eigenbrodt SBL 480 housing at heating level of $0\,\mathrm{W}$. 92
4.5 Statistical analysis of spray-tests regarding experimental pyranometer *PYRANO B* contained in KSO original housing at heating level of $10\,\mathrm{W}$. 93
4.6 Statistical analysis of spray-tests regarding experimental pyranometer *PYRANO B* contained in KSO original housing at heating level of $5\,\mathrm{W}$. 93
4.7 Statistical analysis of spray-tests regarding experimental pyranometer *PYRANO B* contained in KSO original housing at heating level of $0\,\mathrm{W}$. 93

Abbreviations

ARAD	Austrian RADiation Monitoring Network
BOKU	University of Natural Resource and Applied Sciences, Vienna
BSRN	Baseline Surface Radiation Network
C1, **C2**, **C3**, **C4**, **C5**	PT100 thermoelements
CRS	Coarse-Resolution Subregions defined within the **HISTALP** project
EIG	Synonym for Eigenbrodt SBL 480 housing
FL	Quality flags of semi-automatically weather monitoring system (**TAWES**)
GLO	Pyranometer measuring global radiation at ARAD site Graz/University
HIM	Pyranometer measuring diffuse radiation at ARAD site Graz/University
HISTALP	Historical Instrumental climatological Surface Time series
IGAM	Institute of Geophysics, Astrophysics and Meteorology
IP	Institute of Physics
IPCC	Intergovernmental Panel on Climate Change
KSO	Kanzelhöhe Observatory
LUFFT	Meteorological observation platform by Lufft GmbH
MobMet	Meteorological observation platform of Institute for Physics
PYRANO A	Reference radiation sensor during the measurement campaign
PYRANO B	Experimental radiation sensor during the measurement campaign

RTE	Radiative transfer equation
TAWES	Semi-automatically weather monitoring system of **ZAMG**
TOA	Top of the atmosphere
WCRP	World Climate Research Programme
WMO	World Meteorological Organization
ZAMG	Austrian Central Institute for Meteorology and Geodynamics

Symbols

A	Area
$\mathrm{d}A$	Differential area or radiation receiver
$\mathrm{d}A'$	Radiation source
AU	Astronomical unit
a	Albedo
B	Radiance of a blackbody
B_λ	Spectral radiance of a blackbody
c	Speed of light
c_p	Specific heat capacity at constant pressure
D	Wind direction (with various suffixes, see below)
D_{L}	Wind direction measured by meteorological observation platform LUFFT
D_{MM}	Wind direction measured by meteorological observation platform MobMet
D_{Sonic}	Wind direction measured by TAWES site Graz/University
d	Distance
d_P	Diameter of particles
d_y	Day of year
E_{Solar}	Solar energy bulk
e	Partial pressure of water vapour

e_s	Saturation vapour pressure
F	Irradiance (with various suffixes, see below)
$\mathrm{d}F$	Differential irradiance
F_A	Force
F_G	Ground heat flux
F_{iso}	Isotropic irradiance
F_L	Latent heat flux
F_{lw}	Long-wave solar radiation
$F_{lw}^{\downarrow}$	Incoming long-wave solar radiation
$F_{lw}^{\uparrow}$	Outgoing long-wave solar radiation
F_N	Net radiative flux
F_S	Sensible heat flux
F_{Solar}	Solar irradiance
F_{sw}	Short-wave solar radiation
$F_{sw}^{\downarrow}$	Incoming short-wave solar radiation
$F_{sw}^{\uparrow}$	Outgoing short-wave solar radiation
G	Slope
g	Gravitational acceleration
H	Slope
HL_1	Heating level 1 ($5\,$W)
HL_2	Heating level ($10\,$W)

HL_v	Heating level (varying)
h	Planck's constant
I	Momentum
J_λ	Source function
K_z	Eddy diffusion coefficient
k_B	Boltzmann constant
L	Radiance (with various suffixes, see below)
L_{iso}	Isotropic radiance
L_m	Side-length of a cube
L_{Solar}	Solar radiance
L_w	Heat of vaporisation for water
L_λ	Spectral radiance of a random body
M	Mass
M^*	Amount of substance
m	Mass of a single molecule
m^*	Molar mass
m_d^*	Molar mass of dry air
$m_{O_2}^*$	Molar mass of molecular oxygen
N	Number of particles
N_A	Avogadro constant
n	Concentration of particles

p	Pressure
p_d	Partial pressure of dry air
p_i	Partial pressure
PS_{wg}	Precipitation sensor measured by TAWES site Graz/University in weather garden
q	Specific humidity
q_0	Specific humidity at the surface
q_a	Specific humidity of air
R	Radiation
R^*	Universal gas constant
R_d	Specific gas constant of dry air
R_v	Specific gas constant of water vapour
r	Radius
$\mathbf{r}$	Vector of the distance
r_E	Radius of the Earth
r_{Solar}	Radius of the Sun
RH	Relative humidity (with various suffixes, see below)
RH_{MM}	Relative humidity measured by meteorological observation platform MobMet
S	Sensitivity of a radiometer
S_0	Solar constant
s	Distance through a medium
$\mathrm{d}s$	Differential distance through a medium

T	Temperature (with various suffixes, see below)
T_a	Ambient air temperature
$T_{\text{b,PA}}$	Body temperature of *PYRANO A*
$T_{\text{b,PB}}$	Body temperature of *PYRANO B*
T_C	Temperature of the compensation element
T_{C1}	Temperature of PT100 element C1
T_{C2}	Temperature of PT100 element C2
T_{C4}	Temperature of PT100 element C4
T_{C5}	Temperature of PT100 element C5
T_d	Temperature of the glass-dome
T_E	Radiative equilibrium temperature of the Earth
T_{GLO}	Body temperature of the pyranometer measuring global radiation
T_{HIM}	Body temperature of the pyranometer measuring diffuse radiation
T_{L}	Temperature measured by meteorological observation platform LUFFT
T_{MM}	Temperature measured by meteorological observation platform MobMet
T_{RA}	Temperature of the receiving area
T_s	Earth's surface temperature
T_{Solar}	Temperature of the Sun
T_{wg}	Temperature measured at TAWES site Graz/University in weather garden
T_λ	Transmittance
T_Ψ	Transmittance of atmosphere

t	Time
t_h	Time of day in UTC
U	Voltage
U_{out}	Output voltage
V	Wind speed
V_c	Volume
V_{L}	Wind speed measured by meteorological observation platform LUFFT
V_{MM}	Wind speed measured by meteorological observation platform MobMet
V_{Sonic}	Wind speed measured by at TAWES site Graz/University
v	Velocity of a particle
x	Spray process
Δx	Absolute error
δx	Relative error
z	Height above the surface
$\alpha(\lambda)$	Absorptivity (wavelength dependent)
α_a	Heat transfer coefficient between receiving area and air
β	Heat transfer coefficient between receiving area and compensation element
δ_{Solar}	Declination angle of the Sun
$\varepsilon(\lambda)$	Emissivity (wavelength dependent)
ε_o	Orbital eccentricity
ϑ	Altitude or zenith angle

κ	Thermal conductivity
λ	Wavelength
λ_g	Geographical longitude angle
ν	Frequency
ρ	Density of particles
ρ^*	Amount concentration
ρ_v	Amount concentration of water vapour
$\varrho(\lambda)$	Reflectivity (wavelength dependent)
σ	Stefan-Boltzmann constant
σ_a	Absorption cross section
$\sigma_{c_{\mathrm{H}}}$	Cloud coverage high
$\sigma_{c_{\mathrm{L}}}$	Cloud coverage low
$\sigma_{c_{\mathrm{M}}}$	Cloud coverage middle
σ_{scat}	Scattering diameter
σ_x	Standard deviation
ς	Thermoelectric power
τ	Optical depth
τ_o	Absorption coefficient of ozone
τ_{wv}	Absorption coefficient of water vapour
Φ	Radiative flux
$\mathrm{d}\Phi$	Differential radiative flux

Φ_{in}	Incoming radiative flux
Φ_{out}	Outgoing radiative flux
φ	Azimuth or latitude angle
φ_g	Geographical latitude angle
Ψ	Angle of entry of the Sun
Ω	Electrical resistance
ω	Solid angle
$\mathrm{d}\omega$	Differential solid angle
$\Delta\omega$	Change of solid angle

Bibliography

Allan R. P.: *Evaluation of Simulated Clear-Sky Longwave Radiation Using Ground-Based Observations*, Journal of Climate, 13: 1951-1964, 1999.

Anderson D. E., Cahalan R. F.: *The solar radiation and climate experiment (SORCE) mission for the NASA earth observing system (eos)*, Solar Physics, 230(1-2): 3-6, doi:10.1007/S11207-005-1592-6, 2005.

Auer I., Böhm R., Jurkovic A., Lipa W., Orlik A., Potzmann R., Schöner W., Ungersböck M., Matulla C., Briffa K., Jones P., Efthymiadis D., Brunetti M., Nanni T., Maugeri M., Mercalli L., Mestre O., Moisselin J.-M., Begert M., Müller-Westermeier G., Kveton V., Bochnicek O., Stastny P., Lapin M., Szalai S., Szentimrey T., Cegnar T., Dolinar M., Gajic-Capka M., Zaninovic K., Majstorovic Z., Nieplova E.: *HISTALP - historical instrumental climatological surface time series of the Greater Alpine Region*, International Journal of Climatology, 27, 17-46, doi:10.1002/joc.1337, 2007.

Augustine J. A., Hodges G. B., Cornwall C. R., Michalsky J. J., Medina C. I.: *An Update on SURFRAD-The GCOS Surface Radiation Budget Network for the Continental United States*, Journal of Atmospheric and Oceanic Technology, 22: 1460-1472, 2005.

Augustine J. A., Dutton E. G.: *Variability of the surface radiation budget over the United States from 1996 through 2011 from high-quality measurements*, Journal of Geophysical Research, 118, doi:10.1029/2012JD018551, 2013.

Burridge D. M., Gadd A. J.: *The Meteorological Office operational 10 level numerical weather prediction model*, British Meteorological Office Tech Notes 12 and 48, RG122SZ, 1974.

Darmstaedter L.: *Handbuch zur Geschichte der Naturwissenschaften und der Technik*, Berlin-Heidelberg: Springer-Verlag, 1908

Domínguez B. C. A.: *Characterization of Pyranometer Thermal Offset and Correction of Historical Data*, Blacksburg/Virginia: Master Thesis, 2001.

Donner L. J., Wyman B. L., Hemler R. S., Horowitz L. W., Ming Y., Zhao M., Golaz J.-C., Ginoux P., Lin S.-J., Schwarzkopf M. D., Austin J., Alaka G., Cooke W. F., Delworth T. L., Freidenreich S. M., Gordon C. T., Griffies S. M., Held I. M., Hurlin W. J., Klein S. A., Knutson T. R., Langenhorst A. R., Lee H.-C., Lin Y., Magi B. I., Malyshev S. L., Milly P. C. D., Naik V., Nath M. J., Pincus R., Ploshay J. J., Ramaswamy V., Seman C. J., Shevliakova E., Sirutis J. J., Stern W. F., Stouffer R. J., Wilson R. J., Winton M., Wittenberg A. T., Zeng F.: *The Dynamical Core, Physical Parameterizations, and Basic Simulation Characteristics of the Atmospheric Component AM3 of the GFDL Global Coupled Model CM3*, Journal of Climate, 24: 3484-3519, 2011.

Dutton E. G., Stone R. S., Nelson D. W., Mendonca B. G.: *Recent Interannual Variations in Solar Radiation, Cloudiness, and Surface Temperature at the South Pole*, Journal of Climate, 4, 848, 1991.

Farnell GmbH: *Technical sheet Multicomp 03EN15T044 thermal cut-out, NC V1.0*, Salzburg/Hallwang: Farnell GmbH, 2013.

Freidenreich S. M., Ramaswamy V.: *Analysis of the biases in the downward shortwave surface flux in the GFDL CM2.1 general circulation model*, Journal of Geophysical Research, 116, D08208, doi:10.1029/2010JD014930, 2011.

Gilgen H., Wild M., Ohmura A.: *Means and trends of shortwave incoming radiation at the surface estimated from Global Energy Balance Archive data*, Journal of Climate, 11, 2042, 1998.

Gupta S. K., Kratz D. P., Wilber A. C., Nguyen L. C.: *Validation of Parameterized Algorithms Used to Derive TRMM-CERES Surface Radiative Fluxes*, Journal of Atmospheric and Oceanic Technology, 21: 742-752, 2003.

Hantel M.: *Einführung Theoretische Meteorologie*, Berlin-Heidelberg: Springer-Verlag, 2013

IPCC, 2014: *Climate Change 2014: Synthesis Report.* Contribution of Working Groups I, II and III to the Fifth Assessment Report of the Intergovernmental Panel on Climate Change [Core Writing Team, R.K. Pachauri and L.A. Meyer (eds.)]. IPCC, Geneva, Switzerland, 151 pp.

Kipp&Zonen B.V.: *CMA series CMP series Instruction Manual Version 1007*, Delft (Netherlands): Kipp&Zonen, 2010.

Kraus H.: *Die Atmosphäre der Erde*, Berlin-Heidelberg: Springer-Verlag, 2004

Kuipers Munneke P., van den Broeke M. R., Lenaerts J. T. M., Flanner M. G., Gardner A. S., van de Berg W. J.: *A new albedo parameterization for use in climate models over the Antarctic ice sheet*, Journal of Geophysical Research, 116, D05114, doi:10.1029/2010JD015113, 2011.

Lange H. J.: *Die Physik des Wetters und des Klimas*, Berlin: Dietrich Reimer Verlag GmbH, 2002.

Liepert B. G.: *Observed reductions of surface solar radiation at sites in the United States and worldwide from 1961 to 1990*, Geophysical Research Letters, 29, 2002GL014910, 2002.

Liljequist G. H., Cehak K.: *Allgemeine Meteorologie*, Braunschweig/Wiesbaden: Friedr. Vieweg & Sohn Verlagsgesellschaft mbH, 1984.

Loeb N. G., Lyman J. M., Johnson G. C., Allan R. P., Doelling D. R., Wong T., Soden B. J., Stephens G. L.: *Observed changes in top-of-the-atmosphere radiation and upper-ocean heating consistent within uncertainty*, Nature Geoscience, 5(2): 110-113, doi:10.1038/Ngeo1375, 2012.

Marty C., Philipona R., Delamere J., Dutton E. G., Michalsky J., Stamnes K., Storvold R., Stoffel T., Clough S. A., Mlawer E. J.: *Downward longwave irradiance uncertainty under arctic atmospheres: Measurements and modeling*, Journal of Geophysical Research, 108, D12, 4358, doi:10.1029/2002JD002937, 2003.

McArthur L. J. B.: *World Climate Research Programme-Baseline Surface Radiation Network (BSRN) - Operations Manual Version 2.1*, Experimental Studies Division, Atmospheric Environment Service, Downsview, Ontario, Canada, 2005.

Olefs M., Baumgartner D. J., Obleitner F., Bichler C., Foelsche U., Pietsch H., Rieder H. E., Weihs P., Geyer F., Haiden T., Schöner W.: *The Austrian radiation monitoring network ARAD - best practice and added value*, Atmospheric Measurement Techniques Discussions, 8: 10663-10710, 2015.

Ohmura A., Dutton E. G., Forgan B., Frohlich C., Gilgen H., Hegner H., Heimo A., Stephens G. L., König-Langlo G., McArthur B., Müller G., Philipona R., Pinker R., Whitlock C. H., Dehne K., Wild M.: *Baseline surface radiation network (bsrn/wcrp): new precision radiometry for climate research*, Bulletin of the American Meteorological Society, 79(10): 2115-2136, 1998.

Petty G. W.: *A First Course In Atmospheric Radiation*, Madison/Wisconsin: Sundog Publishing, 2006.

Pinker R. T., Zhang B., Dutton E. G.: *Do Satellites Detect Trends in Surface Solar Radiation?*, Science, 308: 850-854, 2005.

Ramanathan V.: *The Role of Earth Radiation Budget Studies in Climate and General Circulation Research*, Journal of Geophysical Research, 92, D4, 4075-4095, 1987.

R Core Team: *R: A Language and Environment for Statistical Computing*, Vienna, Austria: R Foundation for Statistical Computing, 2014.

Schönwiese C.-D.: *Praktische Statistik für Meteorologen und Geowissenschaftler*, Stuttgart: Gebrüder Borntraeger Verlagsbuchhandlung, 2006.

Stanhill G., Cohen S.: *Global dimming: a review of the evidence for a widespread and significant reduction in global radiation with discussion of its probable causes and possible agricultural consequences*, Agricultural and Forest Meteorology, 107, 255, 2001.

Stull R. B.: *An Introduction to Boundary Layer Meteorology*, Dordrecht: Kluwer Academic Publishers, 1988.

Wang P., Sneep M., Veefkind J. P., Stammes P., Levelt P. F.: *Evaluation of broadband surface solar irradiance derived from the Ozone Monitoring Instrument*, Remote Sensing of the Environment, 149: 88-99, 2014.

Wielicki B. A., Barkstrom B. R., Harrison E. F., Lee R. B., Smith G. L., Cooper J. E.: *Clouds and the earth's radiant energy system (CERES): an earth observing system experiment*, Bulletin of the American Meteorological Society, 77(5): 853-868, 1996.

Wild M., Ohmura A., Gilgen H., Roeckner E., Giorgetta M., Morcrette J.-J.: *The disposition of radiative energy in the global climate system: GCM-calculated versus observational estimates*, Climate Dynamics, 14: 853-869, 1998.

Wild M., Gilgen H., Roesch A., Ohmura A., Long C. N., Dutton E. G., Forgan B., Kallis A., Russak V., Tsvetkov A.: *From Dimming to Brightening: Decadal Changes in Solar Radiation at Earth's Surface*, Science, 308: 847-850, 2005.

Wild M.: *Global dimming and brightening: A review*, Journal of Geophysical Research, 114, D00D16, doi:10.1029/2008JD011470, 2009.

Wild M., Folini D., Schär C., Loeb N., Dutton E. G., König-Langlo G.: *The global energy balance from a surface perspective*, Climate Dynamics, 40: 3107-3134, 2013.

Wild M., Folini D., Hakuba M. Z., Schär C., Senevirante S. I., Kato S., Rutan D., Ammann C., Wood E. F., König-Langlo G.: *The energy balance over land and oceans: an assessment based on direct observations and CMIP5 climate models*, Climate Dynamics, 44: 3393-3429, 2015.

Williams L. D., Barry R. G., Andrews J. T.: *Application of computed global radiation for areas of high relief*, Journal of Applied Meteorology, 11, 526–533 1972.

Yan H., Huang J., Minnis P., Wang T., Bi J.: *Comparison of CERES surface radiation fluxes with surface observations over Loess Plateau*, Remote Sensing of the Environment, 115: 1489-1500, 2011.

Zentralanstalt für Meteorologie und Geodynamik (ZAMG): *Wetterstationen*, https://www.zamg.ac.at/cms/de/images/klima/bild_messnetze/tawes-messinstrumente (access on October 2015)

Zhang Y., Long C. N., Rossow W. B., Dutton E. G.: *Exploiting diurnal variations to evaluate the ISCCP-FD flux calculations and radiative-flux-analysis-processed surface observations from BSRN, ARM, and SURFRAD*, Journal of Geophysical Research, 115, D15105, doi:10.1029/2009JD012743, 2010.

Zhou Y., Kratz D. P., Wilber A. C., Gupta S. K., Cess R. D.: *An improved algorithm for retrieving surface downwelling longwave radiation from satellite measurements*, Journal of Geophysical Research, 112, D15102, doi:10.1029/2006JD008159, 2007.

Zmarsly E., Kuttler W., Pethe H.: *Meteorologisch-klimatologisches Grundwissen*, Stuttgart: Verlag Eugen Ulmer GmbH & Co., 2002.

Appendices

Appendix A

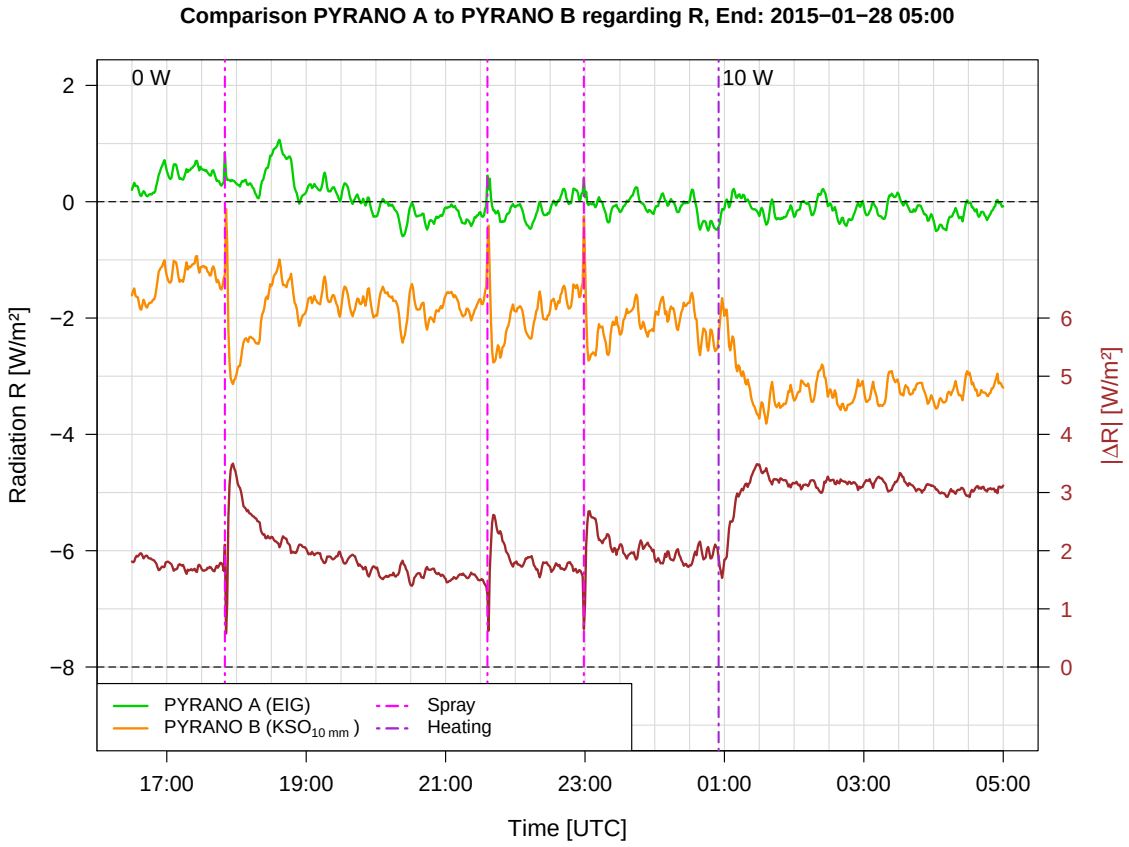

Figure A.1: Comparison of radiation R [W m^{-2}] measured with reference (*PYRANO A*, CMP 21, Eigenbrodt housing, green) and experimental pyranometers (*PYRANO B*, CMP 21, KSO housing, heating elements elevated by 10 mm, orange) between 2015-01-27 16:30 UTC and 2015-01-28 05:00 UTC. For convenience the absolute difference between measurements of *PYRANO A* and *PYRANO B* $|\Delta R|$ [W m^{-2}] is shown along with the individual instrument measurements as 1-minute average (brown curve) on right-hand axis. The black dashed horizontal lines mark $0\,$W m^{-2} for R and $|\Delta R|$, respectively. Dark orchid dashed vertical lines indicate changes in heating power for *PYRANO B* at 2015-01-28 00:55 UTC; heating power [W] for individual periods is detailed at the top of the graph. The magenta dashed vertical lines mark spray-tests at 2015-01-27 17:50 UTC, at 21:36 UTC and at 22:59 UTC.

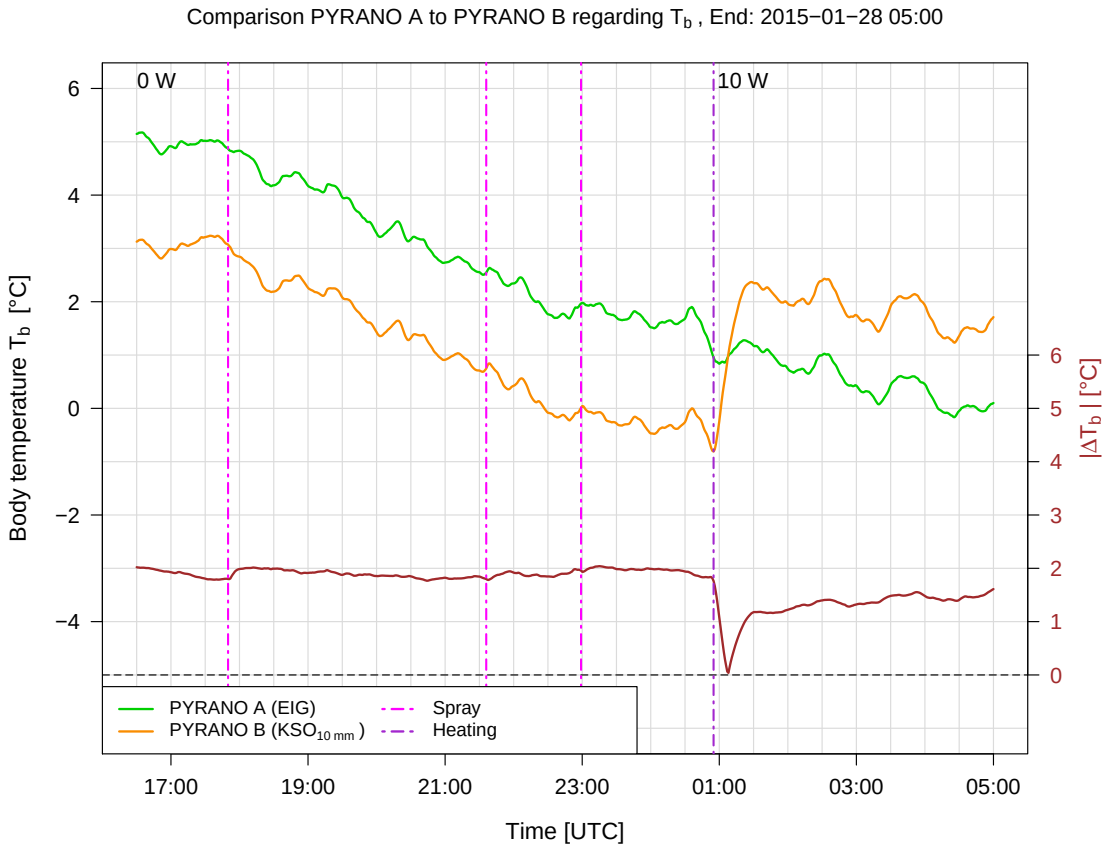

Figure A.2: Comparison of body temperatures T_b [°C] of reference (*PYRANO A*, CMP 21, Eigenbrodt housing, green) and experimental pyranometers (*PYRANO B*, CMP 21, KSO housing, heating elements elevated by 10 mm, orange) between 2015-01-27 16:30 UTC and 2015-01-28 05:00 UTC. For convenience the absolute difference between body temperatures of *PYRANO A* and *PYRANO B* $|\Delta T_\mathrm{b}|$ [°C] is shown along with the individual instrument measurements on right-hand axis. The black dashed horizontal line marks 0 °C for $|\Delta T_\mathrm{b}|$. Dark orchid dashed vertical lines indicate changes in heating power for *PYRANO B* at 2015-01-28 00:55 UTC; heating power [W] for individual periods is detailed at the top of the graph. The magenta dashed vertical lines mark spray-tests at 2015-01-27 17:50 UTC, at 21:36 UTC and at 22:59 UTC.

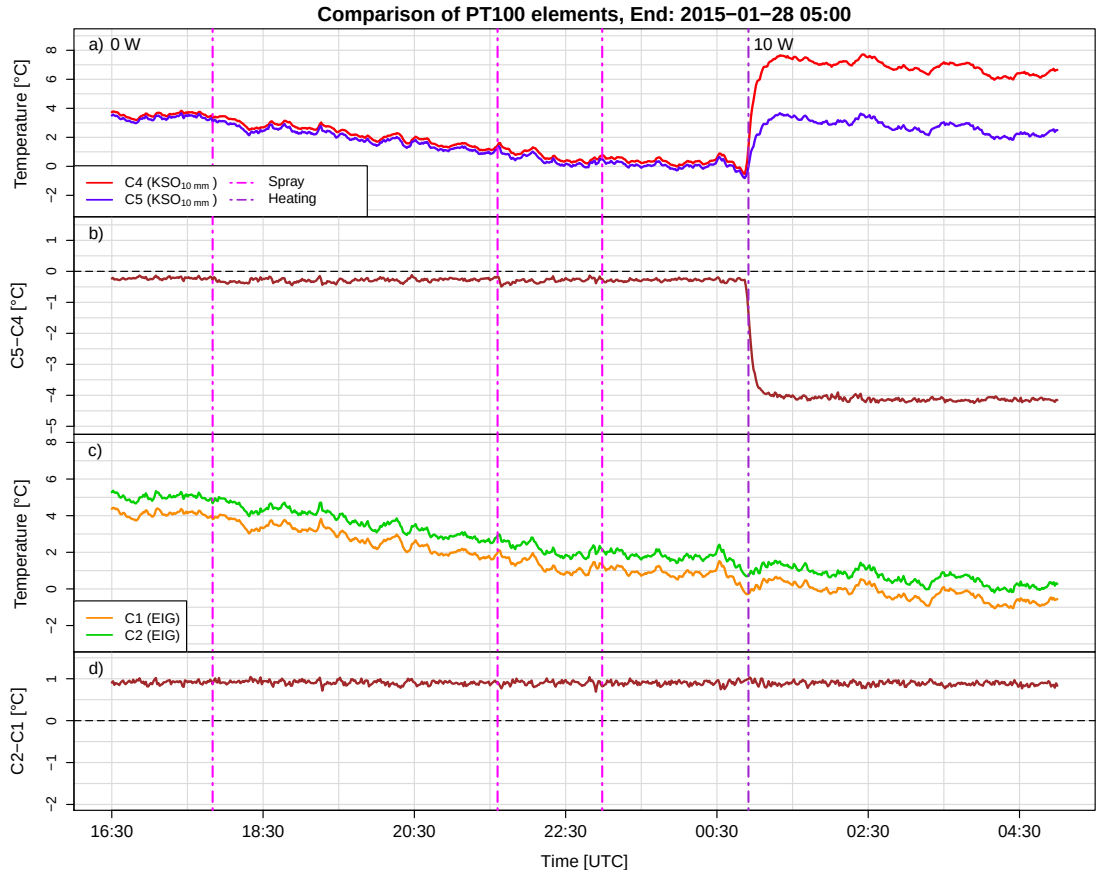

Figure A.3: Comparison of temperatures [°C] measured by the PT100 elements C2, C3, C4 and C5 inside reference and experimental housing systems: (a) C4 (lower mounted, red curve) and C5 (upper mounted, blue curve) represent temperatures inside the experimental housing system (*PYRANO B*, CMP 21, KSO housing, heating elements elevated by 10 mm); (b) temperature difference C5-C4; (c) C1 (lower mounted, orange curve) and C2 (upper mounted, green curve) inside the reference housing system (*PYRANO A*, CMP 21, Eigenbrodt housing); (d) temperature difference C2-C1. All panels for observations between 2015-01-27 16:30 UTC and 2015-01-28 05:00 UTC. The black dashed horizontal lines in panels (b) and (d) marks $0\,^{\circ}$C for C2-C1 or C5-C4. Dark orchid dashed vertical lines indicate changes in heating power for *PYRANO B* at 2015-01-28 00:55 UTC; heating power [W] for individual periods is detailed at the top of the graph. The magenta dashed vertical lines mark spray-tests at 2015-01-27 17:50 UTC, at 21:36 UTC and at 22:59 UTC.

Appendix B

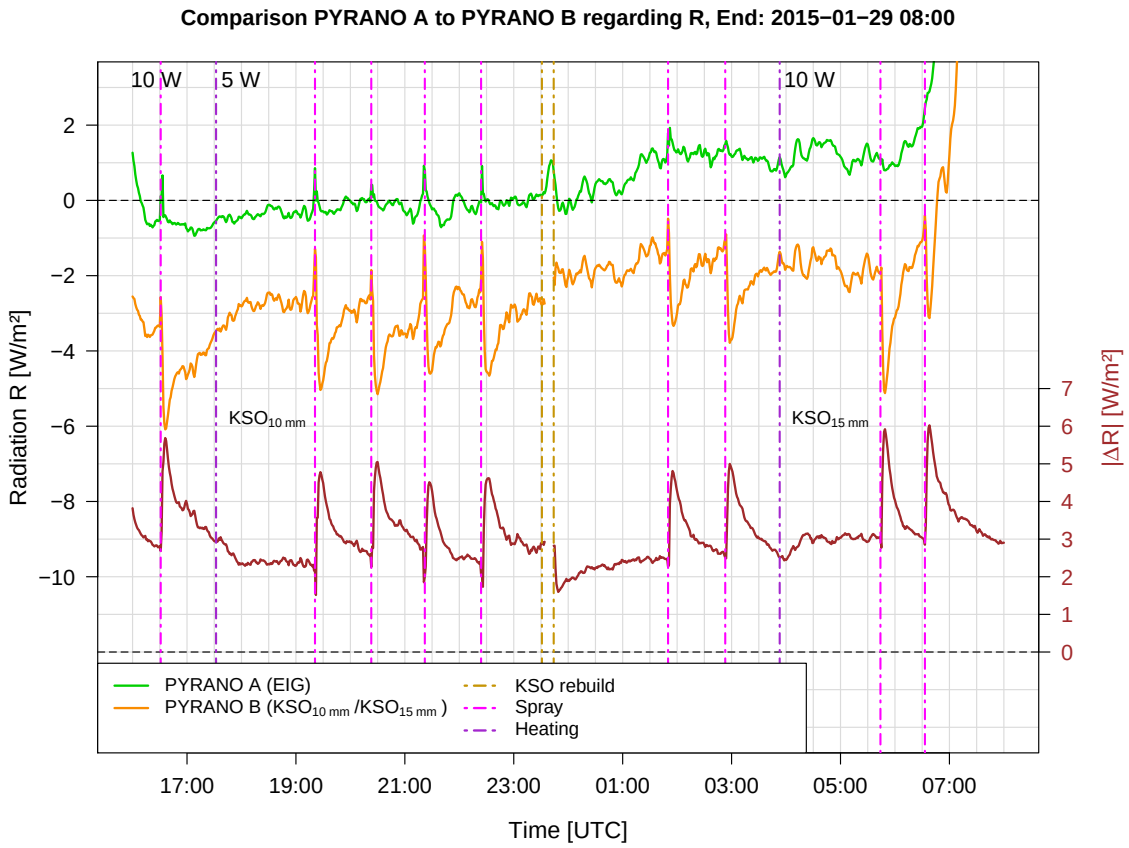

Figure B.1: As Figure A.1 but for comparison of radiation R measured with reference (*PYRANO A*, CMP 21, Eigenbrodt housing, green) and experimental pyranometers (*PYRANO B*, CMP 21, KSO housing, heating elements elevated by 10 mm, later by 15 mm, orange) between 2015-01-28 16:00 UTC and 2015-01-29 08:00 UTC. Dark orchid dashed vertical lines indicate changes in heating power for *PYRANO B* at 2015-01-28 17:32 UTC and at 2015-01-29 03:53 UTC. The magenta dashed vertical lines mark spray-tests at 2015-01-28 16:31 UTC, at 19:21 UTC, at 20:23 UTC, at 21:22 UTC, at 22:24 UTC, at 2015-01-29 01:50 UTC, at 02:53 UTC, at 05:44 UTC and at 06:33 UTC. Goldenrod dashed vertical lines indicate the change in elevated heating elements between $KSO_{10\,mm}$ and $KSO_{15\,mm}$.

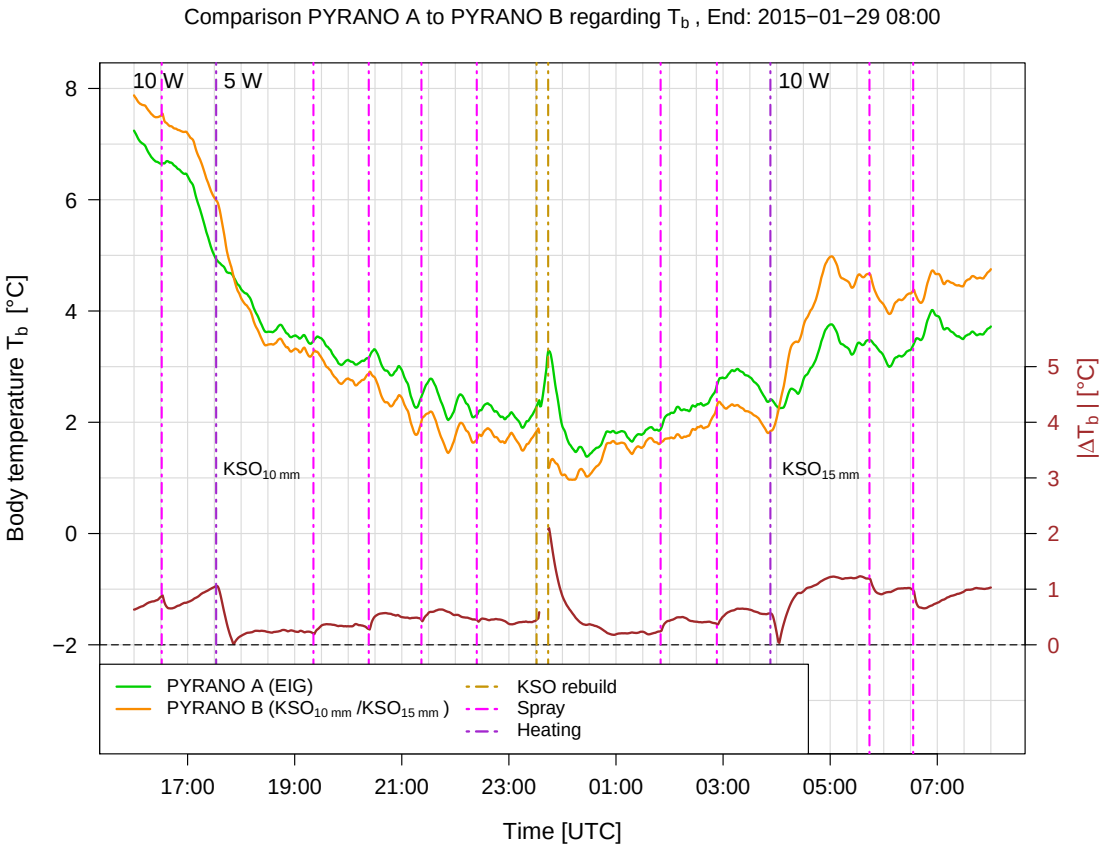

Figure B.2: As Figure A.2 but for comparison of body temperatures T_b of reference (*PYRANO A*, CMP 21, Eigenbrodt housing, green) and experimental pyranometers (*PYRANO B*, CMP 21, KSO housing, heating elements elevated by 10 mm, later by 15 mm, orange) between 2015-01-28 16:00 UTC and 2015-01-29 08:00 UTC. Dark orchid dashed vertical lines indicate changes in heating power for *PYRANO B* at 2015-01-28 17:32 UTC and at 2015-01-29 03:53 UTC. The magenta dashed vertical lines mark spray-tests at 2015-01-28 16:31 UTC, at 19:21 UTC, at 20:23 UTC, at 21:22 UTC, at 22:24 UTC, at 2015-01-29 01:50 UTC, at 02:53 UTC, at 05:44 UTC and at 06:33 UTC. Goldenrod dashed vertical lines indicate the change in elevated heating elements between $KSO_{10\,mm}$ and $KSO_{15\,mm}$.

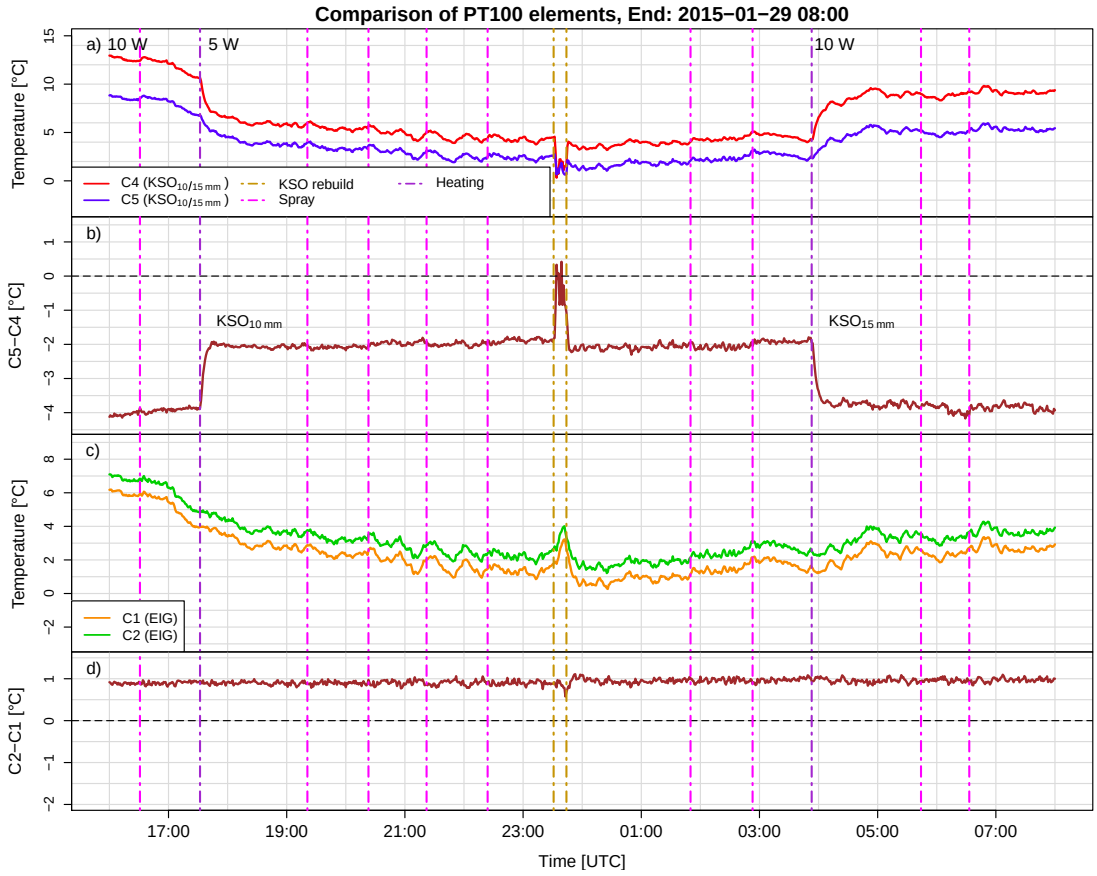

Figure B.3: As Figure A.3 but for comparison of temperatures measured inside the reference (*PYRANO A*, CMP 21, Eigenbrodt housing) and experimental housing systems (*PYRANO B*, CMP 21, KSO housing, heating elements elevated by 10 mm or 15 mm) between 2015-01-27 16:30 UTC and 2015-01-28 05:00 UTC. Dark orchid dashed vertical lines indicate changes in heating power for *PYRANO B* at 2015-01-28 17:32 UTC and at 2015-01-29 03:53 UTC. The magenta dashed vertical lines mark spray-tests at 2015-01-28 16:31 UTC, at 19:21 UTC, at 20:23 UTC, at 21:22 UTC, at 22:24 UTC, at 2015-01-29 01:50 UTC, at 02:53 UTC, at 05:44 UTC and at 06:33 UTC. Goldenrod dashed vertical lines indicate the change in elevated heating elements between $KSO_{10\,mm}$ and $KSO_{15\,mm}$.

Appendix C

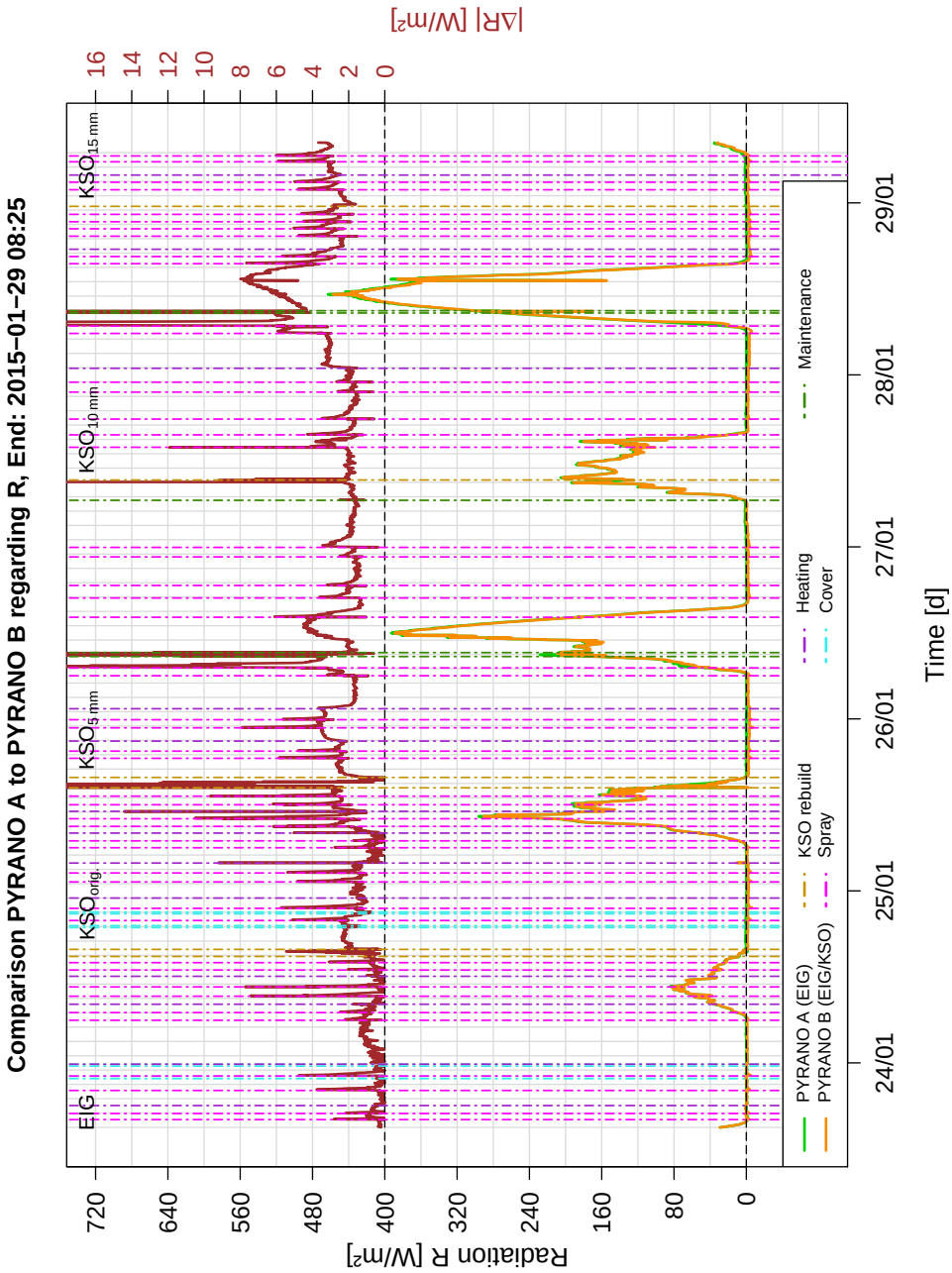

Figure C.1: Comparison of radiation R [W m^{-2}] measured with reference (*PYRANO A*, CMP 21, Eigenbrodt housing, green) and experimental pyranometers (*PYRANO B*, CMP 21, KSO housing, heating elements elevated by 10 mm, orange) between 2015-01-23 15:00 UTC and 2015-01-29 08:25 UTC. For convenience the absolute difference between measurements of *PYRANO A* and *PYRANO B* $|\Delta R|$ [W m^{-2}] is shown along with the individual instrument measurements as 1-minute average (brown curve) on right-hand axis. The black dashed horizontal lines mark $0\,\mathrm{W\ m^{-2}}$ for R and $|\Delta R|$, respectively. Dark orchid dashed vertical lines indicate changes in heating power for *PYRANO B*. The magenta dashed vertical lines mark spray-tests. Goldenrod dashed vertical lines indicate the change in elevated heating elements between $\mathrm{KSO_{orig.}}$, $\mathrm{KSO_{5\,mm}}$, $\mathrm{KSO_{10\,mm}}$ and $\mathrm{KSO_{15\,mm}}$. The cyan dashed vertical lines mark cover-tests. The dark green dashed vertical lines mark periods of instrument maintenance.

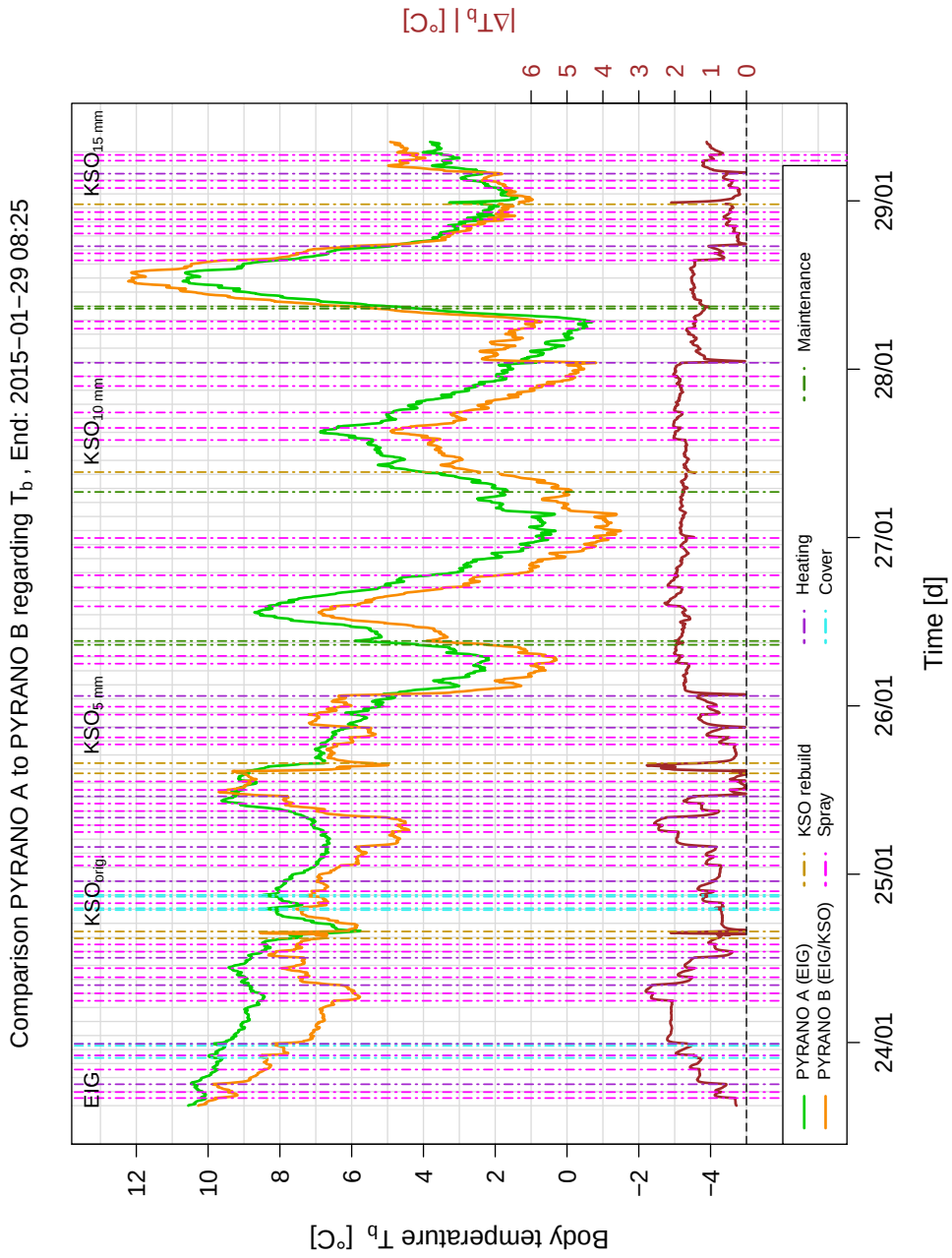

Figure C.2: Comparison of body temperatures T_b [°C] measured with reference (*PYRANO A*, CMP 21, Eigenbrodt housing, green) and experimental pyranometers (*PYRANO B*, CMP 21, KSO housing, heating elements elevated by 10 mm, orange) between 2015-01-23 15:00 UTC and 2015-01-29 08:25 UTC. For convenience the absolute difference between measurements of *PYRANO A* and *PYRANO B* $|\Delta T_\mathrm{b}|$ [°C] is shown along with the individual instrument measurements as 1-minute average (brown curve) on right-hand axis. The black dashed horizontal lines mark $0\,^\circ$C for $|\Delta T_\mathrm{b}|$. Dark orchid dashed vertical lines indicate changes in heating power for *PYRANO B*. The magenta dashed vertical lines mark spray-tests. Goldenrod dashed vertical lines indicate the change in elevated heating elements between $\mathrm{KSO_{orig.}}$, $\mathrm{KSO_{5\,mm}}$, $\mathrm{KSO_{10\,mm}}$ and $\mathrm{KSO_{15\,mm}}$. The cyan dashed vertical lines mark cover-tests. The dark green dashed vertical lines mark periods of instrument maintenance.